Process Development and Optimisation for Efficient and Cost-effective Cu(In,Ga)Se_2 Thin Film Solar Cells

Zhengfei Wei

Submitted for the degree of Doctor of Philosophy

Heriot-Watt University

School of Engineering and Physical Sciences

October 2014

ABSTRACT

Chalcopyrite copper indium gallium diselenide ($Cu(In,Ga)Se_2$ or CIGS) solar cells have achieved the highest laboratory power conversion efficiency among thin film PV technologies, and have the potential to be manufactured cost-effectively at large scale. In this thesis, detailed studies on the growth of CIGS solar cells by means of a pilot scale inline co-evaporation system have been performed to explore the beneficial deposition techniques to successfully transfer the research achievements into cost-effective industrial production. The work involved the development and optimisation of several new processes along with the design of the inline pilot scale system. Effects of the thin absorber layers (with thickness of ~1 μm) on material quality and the device performance have been investigated using (i) a two-step process with room temperature evaporated metal precursors, (ii) a three-stage process at constant substrate temperature and (iii) a three-stage process at varied substrate temperatures. Changing the copper and gallium compositions of the CIGS layers was observed to have a strong impact on the structural and electronic properties and hence on the performance of the solar cells. In one study, simple mechanical compression was employed on a batch of low quality porous CIGS films to significantly improve the surface morphological and the optoelectronic properties. Photoluminescence measurements revealed the band-to-tail defect-related recombination that was detrimental to the quality of as-grown and compressed films. In another study, rapid thermal processing (RTP) was applied to the low temperature Cu-In-Ga-Se precursor layers in an attempt to reduce the cost and optimise the reaction mechanism of the chalcopyrite material. After fine tuning of the process conditions, the CIGS layers with larger grain size exhibited power conversion efficiencies up to 10.8%. While these results are promising, the device performance was mainly limited by the low open circuit voltage and the low fill factor. It has been found that the Cu-In-Ga-Se precursors doped with low concentrations of sodium were beneficial for re-crystallisation of the CIGS films due to the reduced grain size and crystallinity of the precursors. An *in-situ* X-ray diffraction technique was used to investigate the phase evaluation in both Na-free and Na-doped Cu-In-Ga-Se precursor layers as a function of temperature. The results confirmed that the formation of both CIGS as well as secondary phases in the layer with the Na-doped precursors started at higher temperatures compared to Na-free precursors. It is therefore expected that further improvements in the solar cell efficiency might be achieved following this RTP and low-temperature precursor process.

In Memory of My Dear Grandfather

ACKNOWLEDGEMENTS

First and foremost I would like to thank Prof. Hari Upadhyaya of Heriot-Watt University for accepting me as his PhD student and for all of the advice, encouragement opportunities that he has given me during my PhD studies both at Loughborough University and Heriot-Watt University. I would like to thank Prof. Ayodhya Tiwari and Dr. Stephan Bucheler of the Swiss Federal Laboratories for Materials Science and Technology (Empa, Switzerland) for allowing me to work in their labs, gain a great amount of knowledge and guide me to find the novelties of my work. I would like to thank Prof. Stuart Irvine of Glyndŵr University and Dr. Nick Bennett of Heriot-Watt University for agreeing to examine this thesis.

Several colleagues provided substantial contributions of time and understanding in supporting this work, in particular Dr. Chris Hibberd, Dr. Jiang Zhu, Ben Grew, Shiva Beharrysingh and Prof. Ralph Gottschalg of Loughborough University for my understanding of CIGS research in my initial PhD stages. I would like to thank Terry Shimell and Phil Eames of Scientific Vacuum Systems Ltd. for their technical support during my visits in their company to help to design and test the inline pilot scale co-evaporation CIGS system. Further thanks go Dr. S. Senthilarasu, Dr. Prabhakara Bobbili, Dr. Aruna Ivaturi, Jonathan Morton and many other colleagues in the Energy Conversion Lab of Heriot-Watt University for their assistance on some of experimental work and reviewing some of the publications. I would like to thank Dr. Shiro Nishiwaki, Peter Fuchs, Dr. Alex Uhl, Patrick Reinhard, Dr. Caroline Sutter, Fan Fu, Dr. Yaroslav Romanyuk and Dr. Songhak Yoon of Empa, Switzerland for very useful discussion on preparation and characterising of CIGS solar cells.

For specific measurements, thanks go to Dr. Michael Yakushev of University of Strathclyde for PL measurements, Dr. Jim Buckman of Heriot-Watt University for EDX measurements, Dr. Ali Abbas of Loughborough University for EDX and SEM measurements, Neil Ross of Heriot-Watt University for profilometer measurements.
In addition, this work would not have been possible without all of those named above.
I must thank my entire family especially my grandfathers Yuming and Ruilin, my parents Guohua and Ying, my younger brother Jiahan for all your support for last five years throughout all my PhD studies.

TABLE OF CONTENTS

LIST OF PUBLICATIONS

1. **Zhengfei Wei**, S. Senthilarasu, Michael V. Yakushev, Robert W. Martin and Hari M. Upadhyaya, "Effect of mechanical compression on Cu(In,Ga)Se_2 films: micro-structural and photoluminescence analysis," *RSC Advances*, vol. 4, pp. 5141-5147, 2014.
2. **Zhengfei Wei**, Prabhakara R. Bobbili, S. Senthilarasu, Terry Shimell, and Hari M. Upadhyaya, *"*Design and optimisation of process parameters in an in-line CIGS evaporation pilot system,*" Surface and Coatings Technology*, vol. 241, pp. 159-167, 2014.
3. **Zhengfei Wei**, Prabhakara R. Bobbili, Terry Shimell, and Hari M. Upadhyaya, *"*Development of an Efficient Substrate Heating Assembly for High Efficiency CIGS Solar Cells over 30cmx30cm-area using an In-line Pilot Evaporation System,*" Conference Record of 39th IEEE Conference Photovoltaic Specialists*, Tampa, pp. 2060-2063, 2013.
4. **Zhengfei Wei**, Terry Shimell and Hari M. Upadhyaya, *"*Studies on Optoelectronic Properties of Vacuum and Non-Vacuum Processed Cu(In,Ga)Se_2 Solar Cells,*" Conference Record of 27th European Photovoltaic Solar Energy Conference*, Frankfurt, pp. 2798-2801, 2012.
5. **Zhengfei Wei**, Terry Shimell and Hari M. Upadhyaya, "Optimisation Towards High-Efficiency 30cmx30cm-Size Cu(In,Ga)Se_2 Solar Cells Using an In-Line Co-Evaporation System," *Conference Record of 26th European Photovoltaic Solar Energy Conference*, Hamburg, pp. 2840-2844, 2011.
6. **Zhengfei Wei**, Jake W. Bowers, Terry Shimell and Hari M. Upadhyaya, "Advance in-line deposition system and process development for high efficiency Cu(In,Ga)Se_2 solar cells," *Conference Record of 6th Photovoltaic Science and Applications and Technology*, Southampton, pp. 25-28, 2010.

Chapter 1 – Introduction

1.1 Photovoltaic technologies

The world-wide severe climate changes and the increasing global energy demand urge us to take actions immediately to develop clean technologies in delivering secure, sustainable, and affordable energy sources. Under the banner of "20-20-20 by 2020", the climate and energy priorities for Europe are to: a) reduce the greenhouse gas emissions by 20%; b) increase the share of renewables to 20% ; and c) reduce the energy consumption by 20% [1.1]. While the rapid growth of renewable energy productions in recent years continues with good promise, the photovoltaic (PV) industry has been one of fastest growing energy areas with a growth rate over 40% per year for over a decade [1.2]. This growth rate is driven not only by the progress in the materials and processing technologies, but also by the market introduction programmes in many countries all over the world and increased fossil energy prices [1.2]. Photovoltaics can directly convert the solar radiation into electricity without any greenhouse gas emissions. As solar energy is the most abundant energy source, cost-effective photovoltaic technologies have emerged as one of most promising candidates in renewable energy productions.

About 80% of the current photovoltaic production uses wafer-based crystalline silicon technology. A major advantage of this technology is that complete production lines can be bought, installed and up and running within a relatively short time frame. This production is mature and with a low-risk placement on return of investments [1.2]. These cells are based on mono-crystalline (c-Si) or multi-crystalline silicon (mc-Si) wafers. In the laboratory, the external verified record power conversion efficiency is 25.6% for c-Si and 20.4% for multi-Si solar cells [1.3]. However, further cost reductions are predicted to be limited. A number of factors account for this, the first factor is the thicker wafers of high purity grade silicon (~200 μm), which are required to absorb all the photons from the solar spectrum. Secondly, the rigid and brittle silicon wafers are required to be encapsulated with glass laminations to avoid damage during installation and operation. These encapsulation materials lead to extra material costs and their weight makes them expensive to transport and install [1.4].

Commercial thin film technologies include amorphous silicon (a-Si) solar cells, polycrystalline copper indium gallium diselenide disulphide ($Cu(In,Ga)(Se,S)_2$ or CIGSeS) and cadmium telluride (CdTe) have grown significantly in recent years. The temporary shortage in silicon feedstock and a few companies offering turn-key production lines for thin-film solar cells have resulted in huge investments into thin film technologies since 2005 [1.2, 1.5]. Research efforts on a-Si have successfully lowered the impact of light-induced degradation to achieve around 10% efficiency [1.6]. Another approach to increase the efficiency of a-Si solar cells is making a multi-junction device consisting of nano-crystalline silicon (nc-Si) and a-Si. This multi-junction design increased the efficiency up to 13.4% [1.3]. CdTe solar cells offer small area device efficiency of over 21% [1.7], and can be deposited on a large scale with relatively inexpensive deposition equipment, compared to silicon solar cell production. CIGSeS solar cells offer the highest power conversion efficiencies of over 21.7% [1.8], which will be introduced in detail in *Section 1.2*.

Emerging technologies are based on low-cost materials or processes such as dye-sensitised solar cells (DSSC), organic solar cells, perovskite solar cells and copper zinc tin diselenide disulphide (CZTSeS), which has the potential to further lower the manufacturing cost of solar cells. State-of-the-art DSSC devices have achieved a conversion efficiency of 13% [1.9]. However, long-term stability with a reasonable efficiency requires further improvements towards commercialising these DSSCs. For organic solar cells, the bulk hetero-junction structure helps to improve the efficiency up to 10.7% [1.3]. A sufficiently high stability with an acceptable efficiency of organic solar cells is the key challenge for the further development. The performance of solar cell newcomer materials named perovskites have soared up to 17.9% in the last a few years [1.3]. Replacing lead (Pb) without losing the device efficiency significantly could help perovskites into a more favourable marketplace. The absorber material – CZTSeS – is a cheaper option from the point of view of material cost as compared to CIGSeS. By using earth-abundant, nontoxic and low-cost zinc and tin replacing indium and gallium in CIGSeS, researchers have put a vast amount of interest in this emerging material and have pushed the energy efficiency to rapidly reach 12.6% [1.10].

1.1.1 Introduction to photovoltaic operating principles

A solar cell typically consists of a semiconductor p-n junction and two contacts. The p-n junction is to absorb light and separate the generated electron-hole pairs. Thus, the

photo-generated electrons and holes (charge carriers) transfer into an external circuit through two contacts. For the contacts, at least one of which is transparent to let light into solar cells. The basic structure and electronic band diagram of such a device is shown in Fig. 1.1.

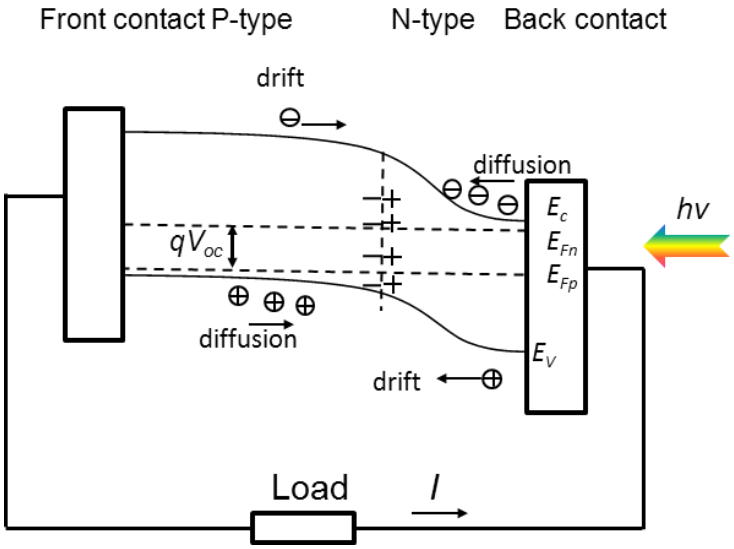

Figure 1.1: *Electron energy band diagram of a p-n junction solar cell, showing a semiconductor junction for separating photo-generated electron-hole pair, E_C represents the conduction band minimum, E_{Fn} and E_{Fp} represent the Fermi energy level in n and p-type semiconductors and E_V represents the valence band maximum.*

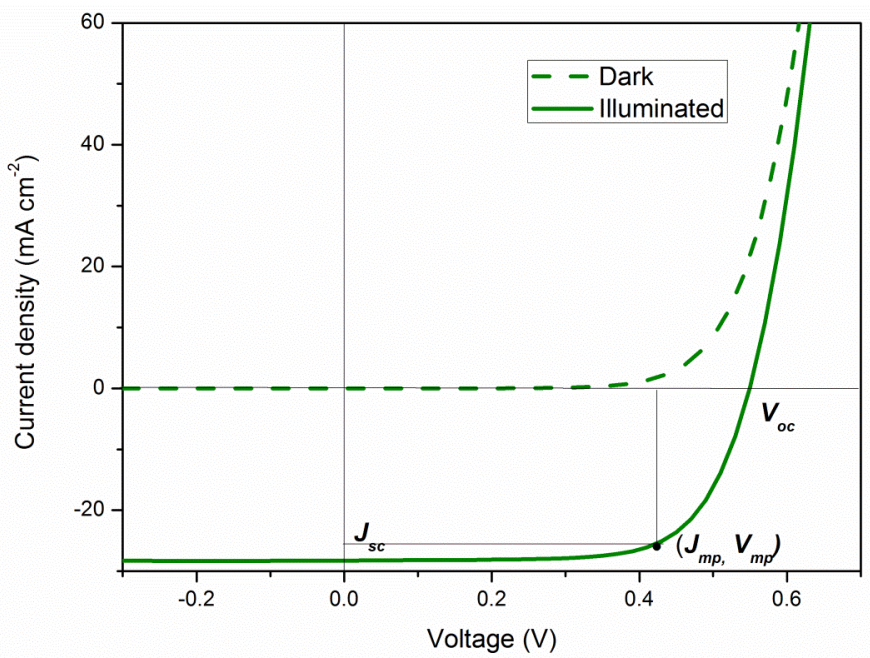

Figure 1.2: *J-V characteristics of a p-n junction solar cell. In the dark condition, the solar cell behaves like a rectifying diode.*

When a photon (hv) with energy larger than the semiconductor band gap is absorbed by the p-n junction, it generates an electron-hole pair. The electron and hole are separated by the built-in electrical field at the p-n junction and ideally only recombine after travelling around an external circuit. The more photons absorbed by the junction, the greater the current that the device generates, while the greater the band gap energy of the absorber material the greater the potential of the electrons moving around the external circuit and hence the greater the voltage across the device.

The current-voltage characteristics of a model solar cell are shown in Fig. 1.2, along with the current density and voltage parameters used for describing them. These parameters include the short circuit current density (J_{sc}), open circuit voltage (V_{oc}) and the current density and voltage at the maximum power point (J_{mpp} and V_{mpp}, respectively).

The power conversion efficiency of solar cells is calculated by equation (1.1), where P_{in} is the irradiance illuminating the solar cells and the fill factor (FF) is derived from equation (1.2).

$$\eta = \frac{J_{mpp}V_{mpp}}{P_{in}} = \frac{FF \cdot J_{sc} \cdot V_{oc}}{P_{in}} \tag{1.1}$$

$$FF = \frac{J_{mpp}V_{mpp}}{J_{sc}V_{oc}} \tag{1.2}$$

The electrical properties of solar cells are conveniently described by an equivalent circuit, shown in Fig. 1.3. The illuminated p-n junction is represented by a photo-generated current density (J_{ph}) in parallel with a diode and a resistance (R_{sh}) and in series with another resistance, R_s. An approximation of magnitude of the series and parallel resistances may be calculated from the slope of the *J-V* curve at open and short circuit, respectively.

$$J = J_0 \left(\exp\left(\frac{V - IR_S}{akT}\right) - 1 \right) + \frac{V - IR_S}{R_{sh}} - J_{ph} \tag{1.3}$$

where J_0 is the saturation current density. The k is the Boltzmann constant, T is the absolute temperature, a is diode ideality factor and J_L is the leakage current density can be expressed by $(V\text{-}IR_s)/R_{sh}$.

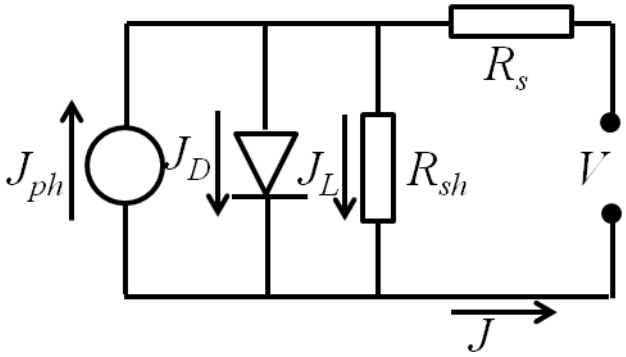

Figure 1.3: *Equivalent circuit of a p-n junction solar cell. The cell is indicated by a current source J_{ph} in parallel with a diode current density J_D, a series resistance R_s and a parallel resistance R_{sh}.*

1.1.2 State of the art of Cu(In,Ga)(Se,S)$_2$ solar cells - their applications and challenges

The processing of silicon wafer based modules typically uses the metal fingers and busbars to connect individual solar cells. Patterning module contacts during deposition utilises so-called monolithic interconnection of solar cells in the CIGSeS or CdTe solar modules [1.11, 1.12]. The monolithic integration approach can significantly reduce the cost of processing the modules and potentially increase the active area of the modules.

Since CIGSeS thin films are not rigid as compared to wafers, they are perfectly suitable to coat onto flexible substrates such as metal or polymer foils. In recent years, the manufacturing of flexible solar cells and modules has become feasible and enables potential roll-to-roll production [1.13]. The application of flexible solar cells also offers potential for further cost reductions by less material usage, reduced transport cost due to less weight and reduced installation time and hence the cost. It could be well suited to building integrated photovoltaic (BIPV) systems [1.4, 1.11] where it provides more design options for architects.

If chalcopyrite CIGSeS photovoltaics can effectively contribute to the future energy supply, they will need to enter into the range of terawatts of installed capacity. Currently, the largest CIGSeS manufacturer, Solar Frontier, expects their capacity for module production to grow to the gigawatts/year range [1.14]. It appears realistic that CIGS technology needs further cost reduction and efficiency increase for future expansion. The future cost of CIGSeS modules assuming gigawatts/year has been estimated to be 0.51 \$/W_p at an efficiency of 15.5% [1.15]. de Wild-Scholten reported

the energy payback time and carbon footprint are 1.02 years and 21.4 g CO_2-eq/kWh respectively for CIGSeS roof-top photovoltaic systems. These values are lower than the silicon based technologies [1.16]. It is a very positive prospect for CIGSeS technology expansion in terms of costs and energy payback time.

However, CIGSeS thin film technologies do suffer with some challenges. Towards the terawatt-scale installation, the availability of indium has been addressed as the most critical point. As the limited reserves of indium are the by-product of zinc mining, the maximum possible installation using CIGSeS based photovoltaic with absorber thickness 1 μm would be around 10 terawatts [1.2, 1.15].

1.2 Cu(In,Ga)Se_2 thin film photovoltaics

Developing from the previous section, the following section describes the CIGS technology in detail, which happens to be the central focus studied in this investigation. Highest power conversion efficiencies exceeding 20% have been obtained with a p-CIGS/n-CdS or n-Zn(O,S,OH) junction semiconductor structure [1.17-1.19], where the Cu(In,Ga)$(Se,S)_2$ alloy has been deposited into p-type conductivity with an adjustable band gap energy E_g. By precisely controlling the ratio of the group III elements In and Ga as well as the group VI elements S and Se can be used to engineer the band gap of CIGS in the range of 1.01 ($CuInSe_2$) - 2.43 ($CuGaS_2$) eV [1.20]. A non-linear empirical formula to express the changes in E_g (CIGSe) for different x = [Ga]/([In]+[Ga]) values as [1.21]:

$$E_g = (1-x)\cdot 1.01\ eV + 1.70\cdot x\ eV - bx(1-x) \qquad (1.4)$$

where the value for the bowing parameter b is $0.15 \leq b \leq 0.24$. It has been found that increasing Ga content leads to an increase in the conduction band energy minimum but the valence band energy maximum remains nearly unchanged, and consequently increases the CIGS band gap [1.22]. A double grading (Fig. 1.4) of the [Ga]/([Ga]+[In]) (GGI) ratio is normally obtained in the high efficiency CIGS solar cells deposited using the three-stage co-evaporation process. The explanation and the application of the double-grading will be introduced in Chapter 3. Another compositional parameter Cu content also slightly affects the band gap. An increase of E_g is mainly caused by the reduction of Cu content, which mainly reduces the valance band energy maximum [1.23].

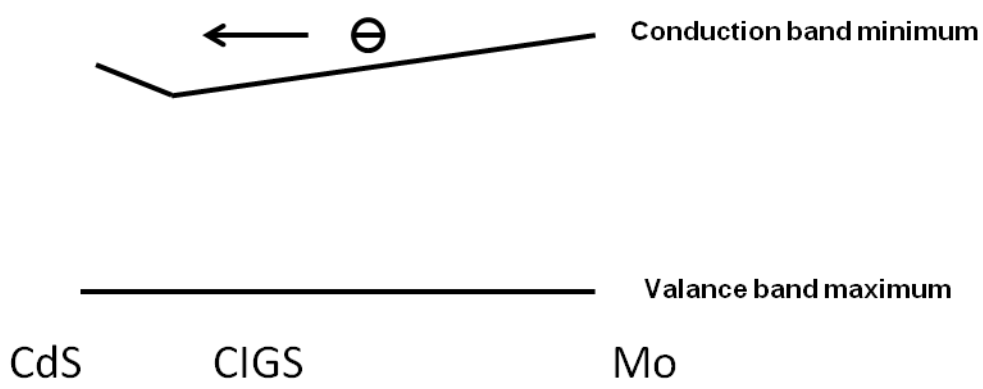

Figure 1.4: *Schematic of a double grading profile for CIGS absorber, induced by the variation of GGI ratio. A photo-generated electron moving towards space-charge region is indicated.*

The phase diagram of the Cu-In-Se system (Fig. 1.5) describes the compositional range of the p-type α-CIS that extends into the Cu-poor region. The composition and temperature dependence of the ternary compounds presents along the molar% of In_2Se_3 line in a mixture of Cu_2Se and In_2Se_3. The existence range of single phase α-CIS is narrow and slightly off-stoichiometric composition. The temperature and composition phase relations of binary compounds are also important to understand the reaction mechanisms of CIGS. A number of metal selenides along with ternary compounds CIS and CGS in the CIGS formation process will be discussed in Chapter 5. The band gap engineering and conductivity depend on the intrinsic doping of the materials. More Cu-poor stoichiometry can result in a n-type β-phases such as $CuIn_5Se_8$ and $Cu_2In_4Se_7$ which are known as ordered defect compounds (ODC) [1.24]. The average composition of the CIGS layer used for high efficiency solar cell application is typically $0.3 \leq$ [Ga]/([Ga]+[In]) (CGI) ≤ 0.4 and $0.7 \leq$ [Cu]/([Ga]+[In]) (CGI) ≤ 0.93 [1.25]. A lateral composition variation leads to a band gap grading.

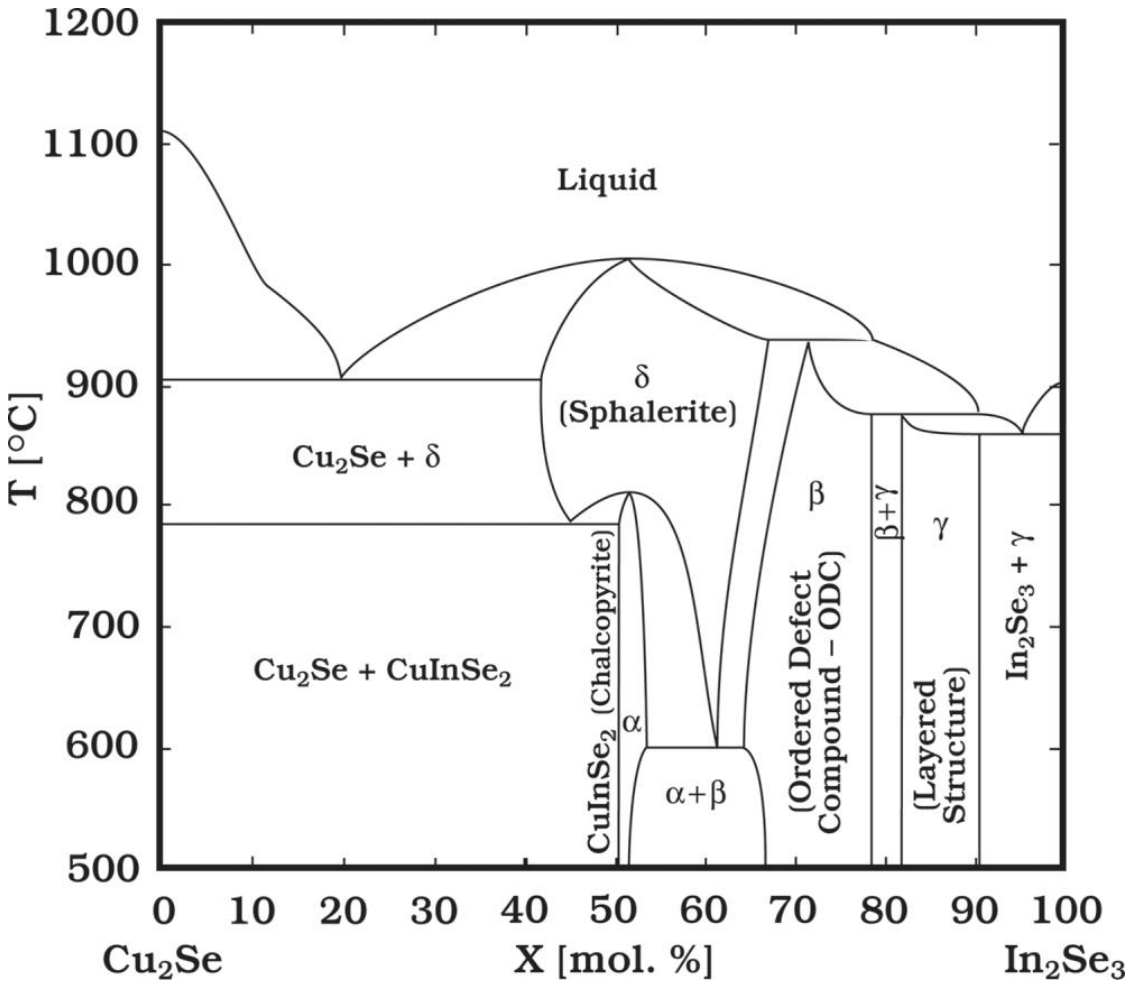

Figure 1.5: Temperature dependence of the phase diagram along the Cu_2Se-In_2Se_3 pseudo-binary tie line of the Cu-In-Se chemical system [1.24].

1.2.1 Device structure

CIGS solar cells in this thesis were fabricated with the typical layer sequence of substrate/Mo/CIGS/CdS/iZnO/ZnO:Al without a top grid and an anti-reflection coating (Fig. 1.6). The CIGS absorber layer is a complex system, because of its distinct intrinsic doping nature and possible doping impurities from other layers. This puts a requirement that all these layers need to be optimised to eliminate the possible losses towards an efficient solar cell device. To grow five layers stack on top of soda lime glass, various deposition equipment including sputtering, co-evaporation, and chemical bath set-up were employed.

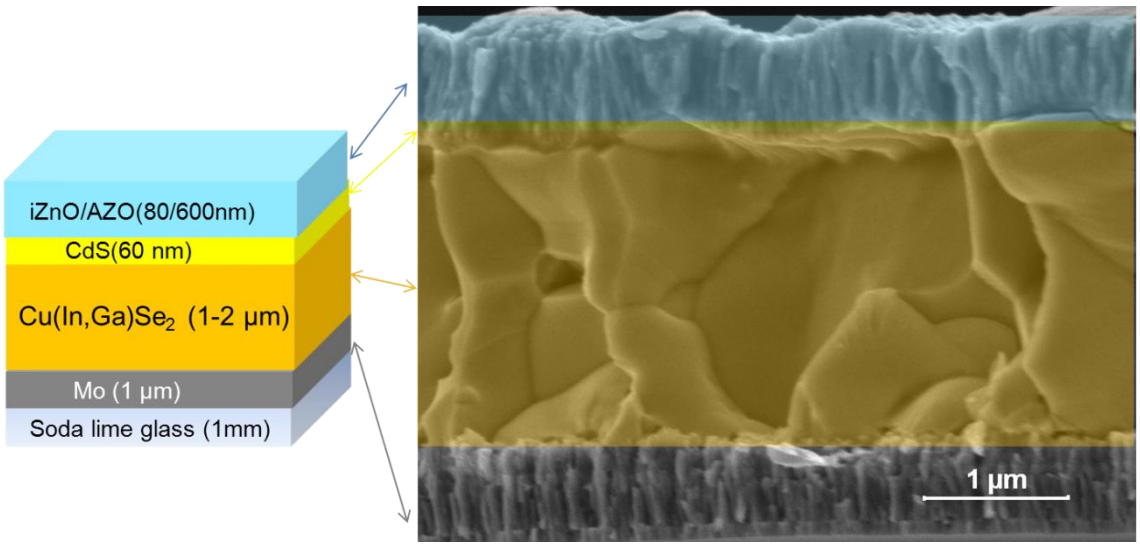

Figure 1.6: *Illustration of a typical CIGS device structure. The thickness of the different layers is also indicated using a schematic.*

First of all, soda lime glass (SLG) is chosen as the substrate for CIGS solar cells mainly because it can provide the beneficial sodium (~0.1 at%) [1.15] and withstand necessary high processing temperature of around 600°C for the α-phase CIGS formation. Other possible substrates for CIGS application such as metal or polymer foils [1.26] were not explored in this thesis. The back contact layer is molybdenum (Mo) grown using DC sputtering on SLG substrates. The good adhesion and low conductivity are required to resist the delamination of layers during the high-temperature processing, and also reduce resistive losses.

The next layer is the CIGS absorber (no sulphurisation process was used in this thesis work), which is the main focus of investigation in this thesis. The two industrially favourable processes, three-stage evaporation process and two-step process, were utilised in this research work. Whilst the two-step process was developed (detailed in Chapter 4), an inline pilot deposition system for the three-stage CIGS process, which is capable of processing 30 cm × 30 cm modules, was designed and built throughout this thesis work during the phase of its development in conjunction with Scientific Vacuum Systems Ltd. (SVS) funded by the Technology Strategy Board (TSB) and Engineering and Physical Science Research Council (EPSRC). Three pairs of Cu, In, Ga point effusion cells and one linear Se effusion cell are equipped into the main deposition chamber to grow the CIGS layer. Because these effusion cells are linearly arranged, a moveable substrate holder with a built-in heater, used for localised heating, traverses forwards and backwards to achieve the three-stage process. A shield was used to

separate Cu effusion cells with Ga and In effusion cells to avoid cross contaminations between each stage. Continuously testing and optimisation of the processes for the CIGS absorber in the inline system are not trivial and require the precise control on the complex temperature and the flux of various elements reaching the substrate at various stages. Modification of a highly complex deposition recipe is very time consuming and involves many steps and sequences. There are no direct and accurate flux measurement provisions in the chamber, therefore an evaporation model was built using MATLAB software package to predict the flux variation of the metal elements. The modelling results were validated by *ex-situ* thickness and composition measurements using profilometry, scanning electron microscopy and X-ray fluorescence. The design and modelling works are described in Chapter 2. The specific recipes for adequate CIGS materials formation are discussed in Chapter 3 of this thesis.

The novel contribution to the thesis work comes from the work carried out at the Swiss Federal Laboratories for Materials Science and Technology (Empa), Switzerland, in collaboration with Heriot-Watt University, UK. In this study, the CIGS absorbers were grown with the low temperature Cu-In-Ga-Se precursor using a co-evaporation system and a rapid thermal processing system for annealing of the samples to fabricate CIGS solar cells with Empa's state-of-the-art facilities. Chapter 5 describes in detail the studies carried out along with the required material and device analysis.

After CIGS deposition, a thin n-type buffer layer of CdS is grown on top of CIGS to form a p-n junction. The CdS were deposited using chemical bath method by using high quality deionised water (18 MΩ-cm), ammonia (14.5 M), cadmium acetate (0.026 M) and thiourea (0.55M) at bath temperature of 70 ℃.

Then, a bi-layer of transparent conducting oxide (TCO) is radio frequency (RF) sputtered on the buffer layer. The TCO layer is composed of a thin highly insulating intrinsic zinc oxide (iZnO) and conductive aluminium doped zinc oxide (ZnO:Al). Depending on the required thicknesses, sputtering conditions were varied and sheet resistance is in the range of 20-60 Ω/square.

1.2.2 Absorber: vacuum and non-vacuum processes

The aim of this thesis is to develop a process for efficient and cost-effective CIGS based thin film solar cells. The challenge is that the process, especially CIGS absorber growth,

should allow inline compatibility and scalability. Understanding various growth processes is important for improvement of absorber properties and hence solar cell efficiency. Here, a brief and selective overview of the current leading vacuum and non-vacuum based CIGS technologies is presented in table 1.1 and 1.2.The most obvious difference between vacuum and non-vacuum processed CIGS absorber materials are the manufacturing cost. The cost-effective non-vacuum processes normally result in a worse power conversion efficiency compared to the vacuum processed devices. Although low-cost non-vacuum processed industrial production of CIGS is very attractive, successful photovoltaic companies are still in favour of vacuum deposition routines which are more feasible due to their superior efficiency, reproducibility and stability for the inline production. To obtain a high quality CIGS material, there are a few requirements that need to be fulfilled: Cu and Ga compositional ranges (*Section 1.2*), control of substrate temperature above 500 ℃, oversupply of selenium/sulphur, and sodium doping [1.15].

For the vacuum deposition processes, a complex deposition method so called "three-stage" co-evaporation process was developed by National Renewable Energy Laboratory (NREL), USA and held the record efficiency since 1994 until early this year [1.18, 1.27]. In the first stage, an $(In,Ga)_2Se_3$ precursor layer is grown at a substrate temperature of 300-400 ℃. In the second stage, Cu and Se are co-evaporated at a substrate temperature of 450-600 ℃ depending on the substrate type (e.g. polyimide, SLG, stainless steel) and additions of extra alkaline layer (e.g. NaF, KF) [1.13, 1.28, 1.29]. During this stage, a quasi-liquid $Cu_{2-x}Se$ phase formed with high Cu mobility, which helps the re-crystallisation of material. As a result, the film turns to Cu-rich, appears with large grains and has high surface roughness [1.15]. In the third stage, the co-evaporation of In, Ga and Se takes place at the same substrate temperature as the second stage until a desired final Cu-poor composition of the film is obtained. During all three stages, the Se vapour is supplied in excess to avoid the insufficient supply of Se for the reaction due to high vapour pressure and low sticking coefficient of the Se at the high substrate temperature [1.30]. More detail about the deposition process can be found in Chapter 2 and 3. The stationary substrate system is used to deposit small area CIGS layers in the most leading laboratories globally, which requires the shutters on top of the effusion cells to achieve the three-stage sequence. Alternatively, moving substrates can be coated as a function of position and speed in the inline system to perform the three-stage process towards the large area application. To conquer the non-

uniformity problem, line sources (which is beyond the scope of this thesis) or multiple-point source can be applied. In this work, the multiple sources approach was taken to design and develop the inline system with a two-point source configuration to improve the uniformity of the layers. The advantages of the three-stage co-evaporation process are ease of control for the beneficial Ga grading and a highly reproducible Na incorporation in the absorber layer. This in turn provides the handle to obtain the superior quality of absorber materials. The disadvantage is the high complexity of a three-stage process recipe. It requires the real-time monitoring and the adjustment of all the process parameters during three stages.

The two-step process is another important CIGS absorber growth method, which separates Cu, In, Ga and Se deposition and formation of CIGS into two steps. Firstly, a stack of precursor layers can be metals, metal oxides, or metal selenides typically deposited at room temperature or very low substrate temperature viz. sputtering, evaporation [1.19, 1.31]. In the second step, the precursor stack is placed into an annealing furnace in the presence of Se, S, H_2Se, or H_2S at a substrate temperature above 500 ℃. The annealing process can be performed in N_2/Ar atmosphere if Se/S has been added into precursor layer itself. Another approach of annealing process uses the rapid thermal processing to improve the CIGS formation [1.32], which significantly reduces the thermal budget. An efficiency up to 20.9% were achieved by Solar Frontier, Japan using a two-step process that employs a sputtered precursor layer and subsequent annealing with highly toxic H_2Se and H_2S gases [1.19]. Utilising their expertise, their production capacity is on a gigawatt scale [1.33]. Furthermore, a newcomer Hanergy, China started to build a production base of CIGS solar modules with a total production capacity of 3 GW at Caofeidian earlier this year [1.34].

Non-vacuum process is normally under two-step process routine. The difference is on the preparation methods of the precursors which include electro-deposition [1.14] and direct liquid coating [1.35, 1.36]. The annealing process of these methods would require decomposing the complexing agents or additional compounds. A hybrid process has been reported combining electro-deposition of a Cu-rich $CuInSe_2$ film and subsequent evaporation of In and Se at a substrate temperature of 550 ℃ [1.37]. All the non-vacuum method requires a high temperature annealing for CIGS formation. More detail about non-vacuum process can be found in literature [1.4, 1.38].

Table 1.1: Selection of institutes and companies that prepare or manufacture high efficiency $Cu(In,Ga)(Se,S)_2$ solar cells and modules using **vacuum** based processes.

Institute	Efficiency (%) (area cm^2)	Deposition technique	Substrates (T ℃)	Notes	Ref.
ZSW	20.8, 19.1 (0.5), 16.8 (61 aperture)	Co-evaporation CIGSe	Glass (610-620)	CdS, Zn(O,S) Sub-module	[1.8, 1.39] [1.25, 1.28]
EMPA	20.4 (0.52) 14.8(13 aperture)	Co-evaporation CIGSe	Polyimide (450)	& Flisom Sub-module	[1.17] [1.14]
NREL	19.9 (0.419) 15.8 (0.42)	Co-evaporation CIGSe	Glass (600)	Wide band gap	[1.29] [1.40]
HZB	19.4 (0.492)	Co-evaporation CIGSe	Glass (610)	-	[1.41]
AIST	19.4(0.515) 15.9(69.6) 18.39(3.6)	Co-evaporation CIGSe	Glass Metal foil Glass	Sub-module Sub-module	[1.42] [1.12] [1.43]
Uppsala	18.6(0.491), 18.6(0.5) 17.4 (16 aperture)	Co-evaporation CIGSe Inline	Glass (520)	CdS, Zn(O,S) & Solibro	[1.44] [1.45]
AGU	18.4 (0.497)	Co-evaporation CIGSe	Glass (540)	ZnS(O,OH)	[1.46] [1.47]
Delaware	17.9	Co-evaporation AgCIGSe	Polyimide	Wide band gap	[1.48]
Company					
Solibro (Hanergy)	20.5 (0.988 aperture) 18.7 (15.89 aperture)	Co-evaporation CIGSe	Glass	Record sub-module	[1.3, 1.49] [1.50]
Manz & Wurth Solar	14.6(module), 15.9(aperture)	Co-evaporation CIGSe	Glass	Module	[1.51]
XsunX	16.4	Multi-area Co-evaporation CIGSe	Stainless steel	Cells with dimension of Si cells	[1.52]
Solarion	15.7	Ion-beam assisted Co-evaporation CIGSe	Polyimide	-	[1.14]
Global Solar Energy (Hanergy)	15.5 (0.4 aperture) 13.2 (3883 aperture)	Co-evaporation CIGSe	Stainless steel	R2R, flexible and rigid module	[1.53]
Fujifilm	15.9 (69.6)	Co-evaporation CIGSe	Stainless steel	Insulating coating	[1.12]
Ascent Solar (FFG Radiant)	14 11.7	Co-evaporation CIGSe	Polyimide	-	[1.54]
Sivapower	18.8	Co-evaporation CIGSe	Glass	-	[1.55]
Solar Frontier	20.9 (0.5) 17.8 (819)	Sputtering,selenisation sulphurisation,CIGSeS	Glass	CdS, Zn(O,S) (H_2Se,H_2S) Sub-module	[1.19] [1.46]
Avancis	16.6	Suputtering and RTP CIGSeS	Glass	SEL-RTP (Se,H_2S)	[1.56]
Miasolé (Hanergy)	17.3 (aperture) 15.7 (9703 aperture)	Sputtering and selenization CIGSe	Stainless steel	R2R, all-sputtering (Se)	[1.50] [1.14]
TSMC	15.7 (10900)	Sputtering,selenisation sulphurisation,CIGSeS	Glass	Stion licensed	[1.57]
Stion	23.2 (65x165)	Sputtering,selenisation sulphurisation,CIGSeS	Glass	Tandem	[1.58]

Table 1.2: Selection of institutes and companies that prepare or manufacture **non-vacuum** based high efficiency $Cu(In,Ga)(Se,S)_2$ solar cells and modules.

Institute	Efficiency (%) (area cm^2)	Deposition technique	Substrates (T ℃)	Notes	Ref.
NREL	11.7(0.4268) 14.1 (0.411)	Electro-deposition&selenisation, hydride (ED+evapor.) CIGSe	Glass (550)	Solution based precursor (Se)	[1.59] [1.60]
IRDEP	9.4(0.1) 11.6 (0.1)	Electro-deposition& selenisation ED & RTP	Glass (550)	Mixed metal oxides,H_2&Se,S	[1.61] [1.62]
Purdue	12 (0.5)	Knife coating & selenisation CIGSeS	Glass (500)	Nanoparticle Se	[1.63]
CIAC	10.1 (0.4)	Spin coating CIS & annealing	Glass (360)	Metal oxides hydroxides, CS_2	[1.64]
Oregon	8.01 (0.1)	Spin coating & selenisation CIGSe	Glass (530)	Solution based precursor,H_2,Se	[1.65]
KIST	8.28 (0.4)	Spin coating & selenisation CIGS	Glass (500)	Solution based precursor, H_2S	[1.66]
Company					
Nanosolar	17.12 (0.5)	Printing & selenisation CIGSe	Al	Nanoparicle & RTP	[1.35]
ISET	13.6 (0.1) 12 (9 × 29.8)	Printing & selenisation CIGSe	Glass	Metal oxides, H_2, H_2Se	[1.67] [1.68]
Nexcis	15.9 12.2	Electro-deposition & RTP CIGSeS	Glass	-	[1.14]
IBM	15.2 (1.5)	Spin coating, hydrazine-based CIGSeS	Glass	Metal selenides precursor	[1.36]

1.2.3 Characterisation techniques

Apart from the deposition process, the proper characterisation techniques are crucial for this thesis work. All the layers in the CIGS solar cell need to be properly designed to obtain an efficient device. Especially, the CIGS absorber is very complex material and required optimising compositional and structural properties for the solar cell application.

1.2.3.1 Material characterisation

Scanning electron microscope (SEM) images were used to investigate structural and morphological properties of the CIGS layers. It is very common to analyse the cross-section and surface of the layers to gather visualised information such as grain size, grain boundaries, film structure and film compactness. Although the grain sizes are not directly related to the device performance [1.25], it is still necessary to have large and compacted grains which are comparable to the film thickness. This is due to grain boundaries are potential recombination centres for photo-generated electron-hole pairs.

X-ray diffraction (XRD) is the other important technique to investigate the orientation of the grains in the polycrystalline CIGS films. There are normally two high intensity

grain orientations, which are along (112) and (220)/(204) crystal planes for high efficiency CIGS solar cells [1.13, 1.25, 1.69]. The intensity ratio between these two main orientations were varied depending on the preparation method of CIGS film [1.25]. However, some lower intensity peaks observed from the XRD pattern for instance (101), (211) and (105)/(213) notations can be considered as indications for the formation of the chalcopyrite phases of CIGS. *In-situ* glancing incident XRD was employed to gather the reaction mechanism information as a function of temperature. The measurements performed at small angles (5 ° and 10 °) of incidence to ensure the best signal to noise ratio. It combines a glancing incident XRD with a vacuum chamber with a heater to complete the conversion of the precursor into the CIGS film.

Composition analysis provides the most important information to grow chalcopyrite CIGS films. The band gap of the CIGS film can be normally varied by the Ga composition. Energy dispersive X-ray spectroscopy (EDX) is one straightforward method to determine the composition of each element. However, the energy of the electrons used is generally 20 kV which can only penetrate 1.0-1.5 μm of the CIGS film depth. EDX can help to obtain an approximate bulk composition of the CIGS absorber, and it requires only absorber grown under very similar conditions can be compared with each other. It is not advisable to quantify the composition of the common impurities such as carbon and oxygen, which can be easily detected from chamber surface.

X-ray fluorescence measurements (XRF) are performed at 45 kV which results in much higher penetration depths than actual film thickness. This enables to quantify the average bulk composition in a very limited error margin. This method is a highly accurate measure and recommended for day to day uses for the optimisation of layer composition.

Secondary ion mass spectroscopy (SIMS) is an important technique to investigate the compositional variations along the film thickness, which is commonly used to perform depth profiles of the absorber layer. Depth profiling is achieved by measuring surface composition and then using ions to sputter away a layer of material before making the next measurement. Sputter rates can vary significantly depending on the compositions within the material. If the similar samples were analysed under same conditions with the same equipment, the measurements for different samples are highly comparable. However, the composition profiling cannot be used to do quantitative compositional

analysis, which requires calibration references such as XRF measurements; mainly because each element has their own sensitivity factor corresponding to SIMS ion signals. There is a useful method of correlating the results of SIMS and XRD to assess the gallium grading profile and phase formation qualitatively [1.13].

Photoluminescence (PL) is used to understand the mechanisms of radiative recombination and defect nature of deposited CIGS films. PL can provide simultaneous information on many types of defects in a sample, but only the defects that can produce radiative recombination processes are detectable [1.70]. Low temperature measurements are normally applied to obtain the complete spectroscopic information by minimising thermally activated non-radiative recombination processes. Excitation power and temperature dependencies of the PL spectra along with the variation of peak positions are normally used to identify the radiation types and consequently locate the position of the defects. The peak shifts can result in a characteristic of types of recombination. For example, if a defect-related peak shifts towards higher photon energies with an excitation power increases (*j*-shift), this could be assigned to donor-acceptor recombination (D-A) or band-to-tail (BT) recombination. In case of increasing temperature, the peak shifts to lower energies that may be representing a band-to-tail (BT) recombination.

1.2.3.2 Device characterisation

Current density-voltage (*J-V*) measurements (*Section 1.1.1*) and external quantum efficiency (EQE) measurements are the most important and direct characterisation techniques to explore the quality of the solar cell devices. *J-V* measurements of the solar cells were performed under standard-test conditions (25˚C, 1000 Wm^{-2}, AM1.5G illumination). *J-V* measurements were undertaken as four-point probe measurements to reduce the effects from the contact resistance. The most valuable parameters that can be extracted from this measurement are open circuit voltage (V_{oc}), short circuit current (J_{sc}), fill factor (FF), as well as power conversion efficiency (η). Many other parameters can be determined also from *J-V* measurements in dark and illuminated conditions such as series resistance, shunt resistance, diode ideality factor and reverse saturation current.

External quantum efficiency (EQE) measurement is another technique to quantify the conversion of the illuminated light into current, which can be used to acquire some detailed information related to loss mechanisms, band gap properties, reflection losses

and losses arising from parasitic absorption. Due to the spectral mismatch of most solar simulators, an EQE measurement gives a more accurate value of the J_{sc} than a *J-V* measurement. In the typical EQE curve of a CIGS solar cell, the cut-off in the low-wavelength is caused by the band gap of the TCO layer. The wavelength region between 400-500 nm is determined by parasitic absorption in the CdS buffer layer. The maximum height of the EQE curve is related to the losses such as reflection, grid obscuration, parasitic absorption of window and buffer layers and carrier collection in the CIGS layer. If the EQE has decreased gradually in the range of 500-1000 nm wavelength, it can be correlated to the enhanced recombination losses and reduced carrier lifetimes within the CIGS layer. The region towards cut-off at high wavelength is strongly depended on the band gap profile, mainly determined by the compositional gradient along the absorber thickness. The cut-off wavelength is related to the minimum of the band gap of the CIGS layer and it can be calculated by plotting $(EQE*hv)^2$ against the photon energy *hv* [1.71].

1.3 Scope of this thesis

The aim of this work is to gain knowledge for transferring CIGS research into industrial scale process. The challenge is to develop a scale-up process which can achieve high power conversion efficiency cost-effectively within an industrially relevant framework.

Chapter 2 addresses the design and development work of a novel pilot scale, inline evaporation system which was developed jointly with Scientific Vacuum Systems (SVS) Ltd. UK. SVS was responsible for the build of the machine for high efficiency CIGS solar cells at a production level. A part of the effort in designing and testing was performed at Heriot-Watt University, where SVS Ltd. were informed of the modifications and changes to be brought out for effective control of the processing of CIGS solar cell development. A series of testing and optimisation of this system was carried out to ensure it could provide high quality, high throughput and high reproducible 30 cm × 30 cm CIGS PV modules. Most importantly, the optimisation of process parameters is investigated to generate and manipulate the recipe for the CIGS growth on 30 cm × 30 cm SLG substrates. The process parameters such as the evaporation flux and deposition uniformity of copper, indium, gallium and selenium were optimised with the help of a thickness distribution model. Another important process parameter is the temperature distribution, which has been optimised by

designing a suitable heating system. Infra-red lamps and a graphite heater were compared in this large area application. All the results are presented in Chapter 2.

Chapter 3 covers process development by utilising the inline co-evaporation system towards a three-stage process. The aim of this work was to develop a growth process that enables the production of highly efficient CIGS solar cells with low production cost. The thickness of the grown CIGS film was chosen to be around 1 μm which is less than half of the thickness of the standard high efficiency CIGS solar cell. Thinner CIGS layers would reduce material cost and directly enable higher throughput. A two-step process (CIG stack precursor and selenisation), simplified three-stage process, and a standard three-stage process were employed in this work to find the most crucial issues of the thinner CIGS prepared with above methods. After the CIGS layers were prepared, the films were brought to Empa, Switzerland to fabricate the CIGS devices and characterise their corresponding photovoltaic properties.

Chapter 4 of this thesis is concerned with the process development at an extreme condition. The aim of this work was to find a recovery technique to improve the low quality CIGS films. The CIG stack precursors were evaporated at room temperature and post annealing at low vacuum were performed to grow CIGS films. A simple mechanical compression was introduced to improve the morphological and electronic properties of CIGS film. The effect of compression was analysed using photoluminescence to explore the possible recombination mechanism of these highly doped and defect-prone CIGS films.

Finally, a novel approach focused on the preparation of chalcopyrite CIGS thin films using rapid thermal processing of the low temperature Cu-In-Ga-Se precursors in Chapter 5. Following the research direction towards the low-cost techniques, an optimised Cu-In-Ga-Se precursor was grown at the substrate temperature below 200 ℃ and rapidly annealed in a few minutes. This technique has great potential to reduce manufacturing cost significantly with acceptable high power conversion efficiency. Extensive material studies were done using *in-situ* and *ex-situ* XRD to understand the reaction mechanism through different preparation conditions.

All in all, the scope of this thesis is closely linked with the development and transfer of research knowledge from the laboratory in the field of cost-effective and efficient CIGS solar cells into industrial manufacturing.

References

[1.1] J. M. Barroso, "Energy priorities for Europe.," *Presentation to the European Council*, February 2011.

[1.2] A. Jäger-Waldau, "Photovoltaics, Status of," in *Encyclopedia of Sustainability Science and Technology*, R. A. Meyers, Ed., ed Springer New York Dordrecht Heidelberg London: Springer New York, 2012.

[1.3] M. A. Green, K. Emery, Y. Hishikawa, W. Warta, and E. D. Dunlop, "Solar cell efficiency tables (version 44)," *Progress in Photovoltaics: Research and Applications*, vol. 22, pp. 701-710, 2014.

[1.4] C. J. Hibberd, "Development of non-vacuum and low-cost techniques for Cu(In,Ga)(Se,S)$_2$ thin film solar cell processing," Doctoral thesis, Loughborough University, 2009.

[1.5] http://www.manz.com/products-services/manz-cigs-fab/overview, 2014.

[1.6] S. Benagli, D. Borrello, E. Vallat, J. Meier, U. Kroll, J. Hötzel, J. Bailat, J. Steinhauser, M. Marmelo, G. Monteduro and L. Castens, "High-Efficiency Amorphous Silicon Devices on LPCVD-ZnO TCO Prepared in Industrial KAI TM-M R&D Reactor," *Conference Record of the 24th European Photovoltaic Solar Energy Conference*, Hamburg, pp. 2293-2298, 2009.

[1.7] http://investor.firstsolar.com/releasedetail.cfm?ReleaseID=864426, "First solar builds the highest effciency thin film PV cell on record," 2014.

[1.8] http://www.zsw-bw.de/uploads/media/pr12-2014-ZSW-WorldrecordCIGS.pdf, "ZSW Brings World Record Back to Stuttgart New best mark in thin-film solar performance with 21.7 percent efficiency ", 2014.

[1.9] S. Mathew, A. Yella, P. Gao, R. Humphry-Baker, F. E. CurchodBasile, N. Ashari-Astani, I. Tavernelli, U. Rothlisberger, M. K. Nazeeruddin and M. Grätzel, "Dye-sensitized solar cells with 13% efficiency achieved through the molecular engineering of porphyrin sensitizers," *Nat Chem*, vol. 6, pp. 242-247, 2014.

[1.10] W. Wang, M. T. Winkler, O. Gunawan, T. Gokmen, T. K. Todorov, Y. Zhu, and D. B. Mitzi,"Device Characteristics of CZTSSe Thin-Film Solar Cells with 12.6% Efficiency," *Advanced Energy Materials*, vol. 4, pp. 1301465, 2014.

[1.11] L. Eldada, "Thin film CIGS photovoltaic modules: monolithic integration and advanced packaging for high performance, high reliability and low cost," *Conference Record of the SPIE 7942 Optoelectronic Integrated Circuits XIII*, San Francisco, 79420F, 2011.

[1.12] K. Moriwaki, M. Nomoto, S. Yuuya, N. Murakami, T. Ohgoh, K. Yamane, S. Ishizuka and S. Niki, "Monolithically integrated flexible Cu(In,Ga)Se$_2$ solar cells and submodules using newly developed structure metal foil substrate with a dielectric layer," *Solar Energy Materials and Solar Cells*, vol. 112, pp. 106-111, 2013.

[1.13] A. Chirilă, S. Buecheler, F. Pianezzi, P. Bloesch, C. Gretener, A. R. Uhl, C. Fella, L. Kranz, J. Perrenoud, S. Seyrling, R. Verma, S. Nishiwaki, Y. E. Romanyuk, G. Bilger and A. N. Tiwari, "Highly efficient Cu(In,Ga)Se$_2$ solar cells grown on flexible polymer films," *Nat Mater*, vol. 10, pp. 857-861, 2011.

[1.14] P. Reinhard, S. Buecheler, and A. N. Tiwari, "Technological status of Cu(In,Ga)(Se,S)$_2$-based photovoltaics," *Solar Energy Materials and Solar Cells*, vol. 119, pp. 287-290, 2013.

[1.15] R. Scheer and H.-W. Schock, "Design Rules for Heterostructure Solar Cells and Modules," in *Chalcogenide Photovoltaics*, ed: Wiley-VCH Verlag GmbH & Co. KGaA, pp. 129-174, 2011.
[1.16] M. J. de Wild-Scholten, "Energy payback time and carbon footprint of commercial photovoltaic systems," *Solar Energy Materials and Solar Cells*, vol. 119, pp. 296-305, 2013.
[1.17] A. Chirilă, P. Reinhard, F. Pianezzi, P. Bloesch, A. R. Uhl, C. Fella, L. Kranz, D. Keller, C. Gretener, H. Hagendorfer, D. Jaeger, R. Erni, S. Nishiwaki, S. Buecheler and A. N. Tiwari, "Potassium-induced surface modification of $Cu(In,Ga)Se_2$ thin films for high-efficiency solar cells," *Nat Mater*, vol. 12, pp. 1107-1111, 2013.
[1.18] P. Jackson, D. Hariskos, R. Wuerz, W. Wischmann, and M. Powalla, "Compositional investigation of potassium doped $Cu(In,Ga)Se_2$ solar cells with efficiencies up to 20.8%," *physica status solidi (RRL) – Rapid Research Letters*, vol. 8, pp. 219-222, 2014.
[1.19] http://www.solar-frontier.com/eng/news/2014/C031367.html, "Solar Frontier Sets Thin-Film PV World Record with 20.9% CIS Cell," ed, 2014.
[1.20] H.-W. SCHOCK, "Solar Cells , Chalcopyrite-Based Thin Film," in *Encyclopedia of Sustainability Science and Technology*, R. A. Meyers, Ed., ed Springer New York Dordrecht Heidelberg London: Springer New York, 2012.
[1.21] S.-H. Wei, S. B. Zhang, and A. Zunger, "Effects of Ga addition to $CuInSe_2$ on its electronic, structural, and defect properties," *Applied Physics Letters*, vol. 72, pp. 3199-3201, 1998.
[1.22] A. M. Gabor, J. R. Tuttle, M. H. Bode, A. Franz, A. L. Tennant, M. A. Contreras, R. Noufi, D. G. Jensen and A. M. Hermann, "Band-gap engineering in $Cu(In,Ga)Se_2$ thin films grown from $(In,Ga)_2Se_3$ precursors," *Solar Energy Materials and Solar Cells*, vol. 41–42, pp. 247-260, 1996.
[1.23] S. Minoura, K. Kodera, T. Maekawa, K. Miyazaki, S. Niki, and H. Fujiwara, "Dielectric function of $Cu(In, Ga)Se_2$-based polycrystalline materials," *Journal of Applied Physics*, vol. 113, pp. 063505, 2013.
[1.24] B. J. Stanbery, "Copper Indium Selenides and Related Materials for Photovoltaic Devices," *Critical Reviews in Solid State and Materials Sciences*, vol. 27, pp. 73-117, 2002.
[1.25] M. Powalla, P. Jackson, W. Witte, D. Hariskos, S. Paetel, C. Tschamber and W. Wischmann, "High-efficiency $Cu(In,Ga)Se_2$ cells and modules," *Solar Energy Materials and Solar Cells*, vol. 119, pp. 51-58, 2013.
[1.26] F. Kessler and D. Rudmann, "Technological aspects of flexible CIGS solar cells and modules," *Solar Energy*, vol. 77, pp. 685-695, 2004.
[1.27] A. M. Gabor, J. R. Tuttle, D. S. Albin, M. A. Contreras, R. Noufi, and A. M. Hermann, "High-efficiency $CuInxGa_{1-x}Se_2$ solar cells made from $(In_x,Ga_{1-x})_2Se_3$ precursor films," *Applied Physics Letters*, vol. 65, pp. 198-200, 1994.
[1.28] P. Jackson, R. Würz, U. Rau, J. Mattheis, M. Kurth, T. Schlötzer, G.Bilger and J. H. Werner, "High quality baseline for high efficiency, $Cu(In_{1-x}Ga_x)Se_2$ solar cells," *Progress in Photovoltaics: Research and Applications*, vol. 15, pp. 507-519, 2007.
[1.29] I. Repins, M. A. Contreras, B. Egaas, C. DeHart, J. Scharf, C. L. Perkins, B. To and R. Noufi, "19 9%-efficient $ZnO/CdS/CuInGaSe_2$ solar cell with 81 2% fill factor," *Progress in Photovoltaics: Research and Applications*, vol. 16, pp. 235-239, 2008.
[1.30] S. Chaisitsak, A. Yamada, and M. Konagai, "Preferred Orientation Control of $Cu(In_{1-x}Ga_x)Se_2$ ($x\approx0.28$) Thin Films and Its Influence on Solar Cell Characteristics," *Japanese Journal of Applied Physics*, vol. 41, p. 507, 2002.
[1.31] J. D. Wilson, B. E. McCandless, R. W. Birkmire and W. N. Shafarman, "In-situ post-deposition thermal annealing of co-evaporated $Cu(InGa)Se_2$ thin films deposited at low temperatures," *Conference Record of 34th IEEE Conference Photovoltaic Specialists*, Philadelphia, pp. 11444-1148, 2009.
[1.32] F. Karg, V. Probst, H. Harms, J. Rimmasch, W. Riedl, J. Kotschy, J. Holt, R. Treichler, O. Eibl, A. Mitwalsky and A. Kiendl, "Novel rapid-thermal-processing for CIS thin-film solar cells," *Conference Record of the 23rd IEEE Photovoltaic Specialists Conference*, Louisville, pp. 441-446, 1993.
[1.33] http://www.solar-frontier.com/eng/news/2013/C027438.html, 2013.

[1.34] http://www.hanergy.com/en/content/details_38_1322.html, "World's Most Advanced PV Technology Introduced at Caofeidian, Hebei Province, " 2014.

[1.35] G. Brown, P. Stone, J. Woodruff, B. Cardozo and D. Jackrel, "Device characteristics of a 17.1% efficient solar cell deposited by a non-vacuum printing method on flexible foil," *Conference Record of the 38th IEEE Photovoltaic Specialists Conference,* Austin, pp. 3230-3233, 2012.

[1.36] T. K. Todorov, O. Gunawan, T. Gokmen and D. B. Mitzi, "Solution-processed $Cu(In,Ga)(S,Se)_2$ absorber yielding a 15.2% efficient solar cell," *Progress in Photovoltaics: Research and Applications,* vol. 21, pp. 82-87, 2013.

[1.37] R. N. Bhattacharya, H. Wiesner, T. A. Berens, R. J. Matson, J. Keane, K. Ramanathan, A. Swartzlander, A. Mason and R. N. Noufi, "12.3% Efficient $CuIn_{1-x}Ga_xSe_2$-Based Device from Electrodeposited Precursor," *Journal of The Electrochemical Society,* vol. 144, pp. 1376-1379, 1997.

[1.38] T. Todorov and D. B. Mitzi, "Direct Liquid Coating of Chalcopyrite Light-Absorbing Layers for Photovoltaic Devices," *European Journal of Inorganic Chemistry,* vol. 2010, pp. 17-28, 2010.

[1.39] D. Hariskos, R. Menner, P. Jackson, S. Paetel, W. Witte, W. Wischmann, M. Powalla, L. Bürkert, T. Kolb, M. Oertel, B. Dimmler and B. Fuchs, "New reaction kinetics for a high-rate chemical bath deposition of the Zn(S,O) buffer layer for $Cu(In,Ga)Se_2$-based solar cells," *Progress in Photovoltaics: Research and Applications,* vol. 20, pp. 534-542, 2012.

[1.40] M. A. Contreras, L. M. Mansfield, B. Egaas, J. Li, M. Romero, R. Noufi, E. Rudiger-Voigt and W. Mannstadt, "Wide bandgap $Cu(In,Ga)Se_2$ solar cells with improved energy conversion efficiency," *Progress in Photovoltaics: Research and Applications,* vol. 20, pp. 843-850, 2012.

[1.41] J. Haarstrich, H. Metzner, M. Oertel, C. Ronning, T. Rissom, C. A. Kaufmann, T. Unold, H.W. Schock, J. Windeln, W. Mannstadt and E. Rudigier-Voigt, "Increased homogeneity and open-circuit voltage of $Cu(In,Ga)Se_2$ solar cells due to higher deposition temperature," *Solar Energy Materials and Solar Cells,* vol. 95, pp. 1028-1030, 2011.

[1.42] S. Ishizuka, A. Yamada, P. Fons, and S. Niki, "Texture and morphology variations in $(In,Ga)_2Se_3$ and $Cu(In,Ga)Se_2$ thin films grown with various Se source conditions," *Progress in Photovoltaics: Research and Applications,* vol. 21, pp. 544-553, 2013.

[1.43] Y. Kamikawa-Shimizu, H. Komaki, A. Yamada, S. Ishizuka, M. Iioka, H. Higuchi, M. Takano, K. Matsubara, H. Shibata and S. Niki, "Highly Efficient $Cu(In,Ga)Se_2$ Thin-Film Submodule Fabricated Using a Three-Stage Process," *Applied Physics Express,* vol. 6, p. 112303, 2013.

[1.44] J. Lindahl, U. Zimmermann, P. Szaniawski, T. Torndahl, A. Hultqvist, P. Salome, C. Platzer-Björkman and M. Edoff, "Inline $Cu(In,Ga)Se_2$ Co-evaporation for High-Efficiency Solar Cells and Modules," *Photovoltaics, IEEE Journal of,* vol. 3, pp. 1100-1105, 2013.

[1.45] E. Wallin, U. Malm, T. Jarmar, O. L. M. Edoff, and L. Stolt, "World-record $Cu(In,Ga)Se_2$-based thin-film sub-module with 17.4% efficiency," *Progress in Photovoltaics: Research and Applications,* vol. 20, pp. 851-854, 2012.

[1.46] M. Nakamura, Y. Kouji, Y. Chiba, H. Hakuma, T. Kobayashi and T. Nakada, "Achievement of 19.7% efficiency with a small-sized $Cu(InGa)(SeS)_2$ solar cells prepared by sulfurization after selenizaion process with Zn-based buffer," *Conference Record of the 39th IEEE Photovoltaic Specialists Conference,* Tampa, pp. 849-852, 2013.

[1.47] T. Kobayashi, H. Yamaguchi, and T. Nakada, "Effects of combined heat and light soaking on device performance of $Cu(In,Ga)Se_2$ solar cells with ZnS(O,OH) buffer layer," *Progress in Photovoltaics: Research and Applications,* vol. 22, pp. 115-121, 2014.

[1.48] G. M. Hanket, C. P. Thompson, J. K. Larsen, E. Eser and W. N. Shafarman, "Control of Ga profiles in $(AgCu)(InGa)Se_2$ absorber layers deposited on polyimide substrates," *Conference Record of the 38th IEEE Photovoltaic Specialists Conference,* Austin, pp. 662-667, 2012.

[1.49] http://www.hanergyamerica.com/newsSolibro.html. "Solibro Achieves 20.5% Efficiency for CIGS Solar Cell," 2014.
[1.50] M. A. Green, K. Emery, Y. Hishikawa, W. Warta and E. D. Dunlop, "Solar cell efficiency tables (version 43)," *Progress in Photovoltaics: Research and Applications,* vol. 22, pp. 1-9, 2014.
[1.51] http://www.manz.com/media/news/archive/2012/manz-presents-cigs-world-record-module-with-efficiency-of-146-at-pv-taiwan-425.
[1.52] http://www.xsunx.com/news13.php?nid=309, ed, 2011.
[1.53] S. Wiedeman, S. Albright, J. S. Britt, U. Schoop, S. Schuler, W. Stoss and D. Verebelyi, "Manufacturing ramp-up of flexible CIGS PV," *Conference Record of the 35th IEEE Photovoltaic Specialists Conference*, Honolulu, pp. 3485-3490, 2010.
[1.54] http://investors.ascentsolar.com/releasedetail.cfm?ReleaseID=437180, 2009.
[1.55] http://www.prnewswire.com/news-releases/siva-power-approaches-19-efficiency-in-record-time-adds-to-solar-companys-powerful-technical-advisory-board-243722021.html, 2014.
[1.56] http://www.avancis.de/en/press/press-releases/view/meldung/avancis-erzielt-neuen-zertifizierungsrekord-bei-duennschichtmodul-nrel-zertifiziert-wirkungsgrad-des/, "AVANCIS achieves new certification record for thin-film module NREL certified efficiency of CIS module with 16.6%," 2014.
[1.57] http://www.prnewswire.com/news-releases/tsmc-solar-commercial-size-modules-109-square-meters-set-cigs-157-efficiency-record-211932801.html, "TSMC Solar Commercial-size Modules (1.09 Square Meters) Set CIGS 15.7% Efficiency Record. "
[1.58] http://www.stion.com/stion-demonstrates-23-2-efficiency-thin-film-with-simply-better-tandem-technology/, "Stion Demonstrates 23.2% Efficiency Thin Film With Simply Better™ Tandem Technology," 2014.
[1.59] R. N. Bhattacharya, "CIGS-based solar cells prepared from electrodeposited stacked Cu/In/Ga layers," *Solar Energy Materials and Solar Cells,* vol. 113, pp. 96-99, 2013.
[1.60] R. N. Bhattacharya, W. Batchelor, H. Wiesner, F. Hasoon, J. E. Granata, K. Ramanathan, J. Alleman, J. Keane, A. Mason, R. J. Matson and R. Noufi, "14.1% $CuIn_{1-x}Ga_xSe_2$-Based Photovoltaic Cells from Electrodeposited Precursors," *Journal of The Electrochemical Society,* vol. 145, pp. 3435-3440, 1998.
[1.61] A. Duchatelet, G. Savidand, R. N. Vannier, E. Chassaing and D. Lincot, "A new deposition process for $Cu(In,Ga)(S,Se)_2$ solar cells by one-step electrodeposition of mixed oxide precursor films and thermochemical reduction," *Journal of Renewable and Sustainable Energy*, vol. 5, pp. 011203, 2013.
[1.62] J.F. Guillemoles, J. P. Connolly, O. Ramdani, O. Roussel, D. Guimard, V. Bermudez, N. Naghavi, P.P. Grand, L. Parissi, J. Kurdi, J. Kessler, O. Kerrec and D. Lincot, "Solution Processing Route to High Efficiency $CuIn(S,Se)_2$ Solar Cells," *Journal of Nano Research,* vol. 4, pp. 79-89, 2009.
[1.63] Q. Guo, G. M. Ford, R. Agrawal and H. W. Hillhouse, "Ink formulation and low-temperature incorporation of sodium to yield 12% efficient $Cu(In,Ga)(S,Se)_2$ solar cells from sulfide nanocrystal inks," *Progress in Photovoltaics: Research and Applications,* vol. 21, pp. 64-71, 2013.
[1.64] W. Zhao, Y. Cui and D. Pan, "Air-Stable, Low-Toxicity Precursors for $CuIn(SeS)_2$ Solar Cells with 10.1% Efficiency," *Energy Technology,* vol. 1, pp. 131-134, 2013.
[1.65] W. Wang, S.-Y. Han, S.-J. Sung, D.-H. Kim and C.-H. Chang, "8.01% $CuInGaSe_2$ solar cells fabricated by air-stable low-cost inks," *Physical Chemistry Chemical Physics,* vol. 14, pp. 11154-11159, 2012.
[1.66] S. J. Park, J. W. Cho, J. K. Lee, K. Shin, J.-H. Kim and B. K. Min, "Solution processed high band-gap $CuInGaS_2$ thin film for solar cell applications," *Progress in Photovoltaics: Research and Applications,* vol. 22, pp. 122-128, 2014.
[1.67] V. K. Kapur, A. Bansal, P. Le and O. I. Asensio, "Non-vacuum processing of $CuIn_{1-x}Ga_xSe_2$ solar cells on rigid and flexible substrates using nanoparticle precursor inks," *Thin Solid Films,* vol. 431–432, pp. 53-57, 2003.
[1.68] V. K. Kapur, V. K. Kapur, A. Bansal and S. Roth, "Roadmap for manufacturing cost competitive CIGS modules," *Conference Record of the 38th IEEE Photovoltaic Specialists Conference,* Austin, pp. 3343-3348, 2012.

[1.69] M. A. Contreras, B. Egaas, K. Ramanathan, J. Hiltner, A. Swartzlander, F. Hasoon and R. Noufi, "Progress toward 20% efficiency in Cu(In,Ga)Se_2 polycrystalline thin-film solar cells," *Progress in Photovoltaics: Research and Applications*, vol. 7, pp. 311-316, 1999.

[1.70] D. K. Schroder, *Semiconductor Material and Device Characterization, 3rd Edition*. Hoboken, New Jersey.: John Wiley & Sons, Inc., 2006.

[1.71] S. F. Buecheler, "Investigation of compound semiconductors as buffer-layer in thin film solar cells," Doctoral thesis, ETH, Zürich, 2010.

Chapter 2 – Design and optimisation of process parameters in an inline pilot evaporation system for growing $Cu(In,Ga)Se_2$ films

Abstract

$Cu(In,Ga)Se_2$ (CIGS) has been one of the most promising thin-film technologies for manufacturing the industrial level photovoltaic modules. Substantial efforts have been made globally towards improving $Cu(In,Ga)Se_2$ thin film solar cell efficiencies with several organisations successfully exceeding the 20% barrier on a research level using the three-stage CIGS process, but commercial mass production of the three-stage process has been limited due to the technological difficulties of scale-up. A recent contribution to produce a flexible world record efficiency CIGS solar cell also exceeding the 20% on polyimide foils using three-stage co-evaporation process [2.1] has provided further inspiration for both CIGS PV researchers and industries. An attempt has been made to identify the scale-up issues by designing and manufacturing an inline pilot production deposition system for the three-stage CIGS process which is capable of processing 30 cm × 30 cm modules. The development of an inline system in this investigation provides a unique opportunity to address engineering challenges related with CIGS technology – scale-up employing three-stage deposition process for uniform CIGS material deposition and development of novel industrially favourable process towards cost-effective CIGS solar cells. The optimisation of the process parameters such as source and substrate temperature, deposition uniformity, flux of copper, indium, gallium and selenium and thickness control has been presented in this investigation. A simple thickness distribution model of evaporated films was developed to predict the designed deposition process, which delivers a comparable simulation compared with the experimental data. These experiments also focused on the optimisation of the temperature uniformity across the 30 cm × 30 cm substrate using the proper heating system, which is crucial to form the correct α-phase CIGS in the desired time period. The following attempts were made to achieve a heating system design using: (i) rapid heating by infra-red (IR) lamps, (ii) IR lamps with a graphite susceptor and (iii) a specially designed graphite heater. A three-dimensional heat transfer model using COMSOL Multiphysics 4.2a software has been developed and validated with help of the experimental data.

2.1 Introduction

Physical vapour deposition (PVD) was widely used in the thin film growth area. Evaporation and sputtering were selected to produce $Cu(In,Ga)Se_2$ absorber. The development of CIGS thin film solar cells has gained significant importance due to better material utilization and reduction of the cost of the modules as compared to c-Si, in an attempt to achieve grid parity [2.1-2.3]. However, there has been fierce competition offered recently by the c-Si technology, which has brought the module cost well below $1/Wp [2.4]. Large area CIGS modules were normally deposited using two-step process including sputtering and selenisation to reach around 15% efficiency by some leading companies [2.5, 2.6]. PVD processed CIGS technology has all the advantages of thin film processes: the highest achievable efficiency, finest controllable manufacturing, low material usage and reliability. All of these factors offer higher possibility to make high efficiency CIGS modules with lower cost-per-Watt for the mass production.

Although, there is a good scope for thin film technologies such as CIGS to increase the efficiency and bring the cost down further, it still remains a challenge to scale up the technology to achieve high performance of the modules on a production scale. This mainly stems from the optimisation of the process conditions to achieve control on the morphology and electronic parameters of the thin film layers from batch to batch production. Some organisations have made good progress in transferring the state-of-the-art champion cell technologies to the industrial production. Solar frontier, Japan has achieved 20.9% efficiency on approximately 0.5 cm^2 area CIGS solar cell and 17.8% on 819 cm^2 CIGS module efficiency using the two-step process which requires toxic H_2Se and H_2S vapour for selenisation and sulphurisation, respectively [2.2, 2.5]. Manz has achieved a CIGS module efficiency of 14.6% with the help of a turn-key production line using the one-stage co-evaporation process [2.6]. In this simple single-step process all the source evaporation rates as well as the substrate temperature were kept constant through the deposition process [2.6, 2.7]. In the one-stage process manufacturing conditions can be easily controlled, but it renders less refined crystallisation and phase transition of CIGS. Sputtering of Cu, In and Ga metal precursors is a favourable technique for scale-up to module size, but H_2Se is highly toxic and requires special precautions for its use. Se and S are less complicated, but it hasn't reached 20% efficiency level of CIGS solar cells by using of Se or S for selenisation in the state-of-

the-art two-step technology. The reason may be more relevant to reaction chemistry and kinetics for conversion CIGS crystals [2.8].

The film uniformity is the key to scale up of CIGS solar cells. The thickness and composition uniformity are the primary requirements to achieve good optical and electronic properties for high performance solar cells. From a production point of view, uniformity directly impacts yield [2.9]. Therefore, for mass production of the high efficiency and large area modules, high throughput and reproducible uniformity are crucial. Towards the scale-up objective, necessary process modelling work has been developed to efficiently utilise material and time resources in this pilot scale system. A thickness distribution model from two-source evaporation has been developed to simulate the deposition process of each metal source and their thickness uniformity over a large area. This model was used to gain better understanding of the physical system and to predict the film growth. Another important requirement is the flux control which has been addressed as well with the help of the thickness distribution model. In this study, an attempt has been made towards the development of uniform CIGS layers deposited over a 30 cm × 30 cm area with three different heating systems. These heating systems were used to validate and optimise the heating uniformity: five-1 kW-IR-lamp array, five-1 kW-IR-lamp array with a piece of 4 mm-thick graphite sheet acting as a susceptor positioned on top of the glass substrate, and a specially designed graphite element heater. The experiments were designed to validate the operational feasibility of an in-line three-stage deposition process. The optimisation was focused on the substrate temperature control and its distribution, which is one of the most important scale-up requirements. To achieve uniform heating over 30 cm × 30 cm area, a thermal model based on the heat transfer module of COMSOL 4.2a was developed to simulate and guide the improvement for the further experimental work. A specially designed graphite heating systems was used to validate and optimise the heating uniformity. The temperature data were collected from six K-type thermocouples attached underneath the substrate at different locations.

2.2 Contributed design elements for the inline CIGS system

A novel pilot scale, inline evaporation system has been designed and developed for the high performance CIGS process at a production level; a photograph of this system is given in Fig. 2.1. The three-stage process has the potential to yield the highest efficiencies in production as compared with the standard one- and two-step processes,

because most of the champion cells are manufactured this way at a research level. However, it is the most difficult of the three processes to scale up due to its process complexities. As presented here the pilot production system has a few significant advantages over existing one-step and two-step CIGS production systems.

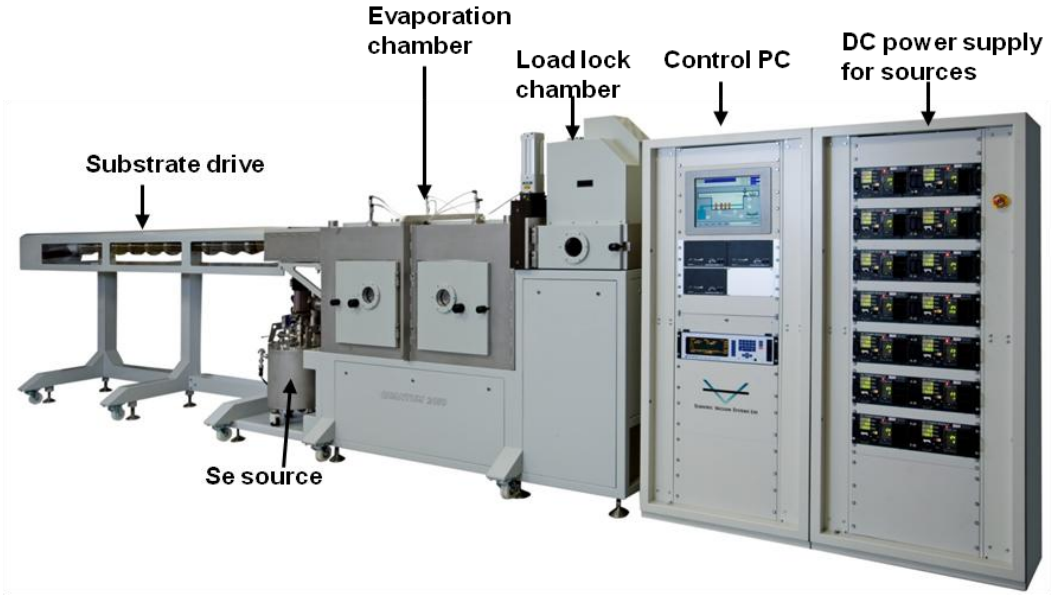

Figure 2.1: *A photograph of the inline pilot co-evaporation system for high performance CIGS, designed and developed jointly with SVS Ltd., UK.*

It has been designed to avoid the use of highly toxic reactant gas H_2Se, which requires robust maintenance of the exhaust and trapping system such as an expensive scrubber along with a gas sensor alarm system. Here a cold trapping system (Fig. 2.2a) was designed to effectively trap any residual hot Se vapour in the exhaust. This inline system has a built-in flash evaporation unit (Fig. 2.2b) which can be used to prepare the CdS or Cd-free buffer layer [2.10]. An obvious advantage lies in utilizing the vacuum deposition process for all five layer stacks for finishing the CIGS solar cells, thereby reducing the total deposition time, without having to break the vacuum.

The standard system configuration consists of three interconnecting chambers as shown in Fig. 2.1 and 2.3, comprising a central dealer chamber with an evaporation chamber and sputter chamber connected either side and separately pumped. The substrate loading is controlled by a robotic arm which picks the substrate mounted in a holder from the load lock, and moves it along with the heater to provide local heating of the substrate. The substrate drive is controlled by a servomotor and encoder which allows the substrates to be accurately positioned and oscillate over each of the deposition zones achieving optimum film uniformity. On completion of the process development work,

this system has the potential to be developed into an efficient industrially proven process for large scale production of CIGS which will yield a reduction in process time as compared with other energy intensive vacuum apparatus. Normally a significant amount of energy is wasted in breaking vacuum in order to transfer the substrates to perform other vacuum or non-vacuum processes. It may be noted that a separate sputtering chamber for the deposition of Mo, ZnO and ZnO:Al layers could not be built due to lack of resources but would be integrated with the existing evaporation chamber as per the design.

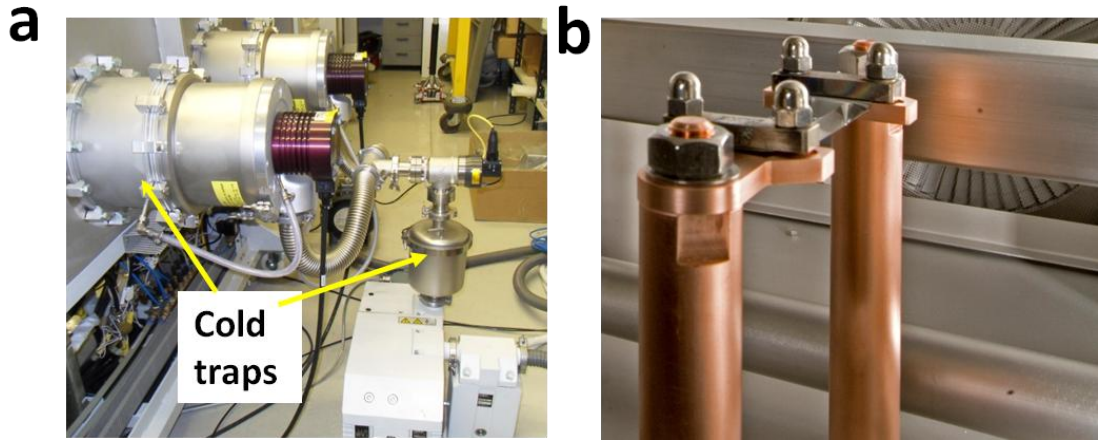

Figure 2.2: *The photographs showing (a) cold traps for selenium trapping, (b) flash evaporator for alternative buffer deposition.*

There are several process issues for scale-up of the three-stage process in an inline system such as heating the substrate to elevated temperatures whilst moving the substrate assembly to different areas of the process chamber for deposition of the various elements and the positioning of multiple deposition sources for each element to achieve uniform distribution of the deposition materials, as well as other process complexities such as maintaining the flux of elements in right proportion reaching on the substrate at desired temperature regimes. This inline pilot system has been developed to grow CIGS layers using a three-stage process on glass substrates to address these scale-up issues. The details about the process development are presented in Chapter 3.

2.3 Modelling and experiments

2.3.1 Thickness and temperature distribution modelling using MATLAB and COMSOL

A simple thickness distribution model from two-source evaporation has been developed using MATLAB 2008 software to simulate the deposition process of each metal source and its thickness uniformity across a large area. Some process parameters such as source temperature and chamber pressure in the presence of selenium vapour are considered in this model. Besides, a three-dimensional finite-element thermal model was developed for the heat transfer process applied to the substrate with localised heating using COMSOL Multiphysics 4.2a software. The theory, boundary conditions and modelling details for both the parameters are presented in *Section 2.4* of this chapter.

2.3.2 Experiments

The inline pilot scale co-evaporation system (Fig. 2.3) consists of two deposition zones which are separated by a metal shield. Ga and In sources in the second zone, while Cu sources are kept in the first zone. This has been done to avoid cross contamination. These metal effusion sources were supplied by Veeco Inc., USA. The base pressure of the evaporation chamber is kept at ~10^{-5} Pa with a processing pressure of ~10^{-3} Pa. Most of the samples for testing were 5 cm × 5 cm and 10 cm × 10 cm dimensions mounted on a graphite substrate holder as shown in Fig. 2.4. The modelled thickness distribution was experimentally validated. The thickness uniformity was controlled by the temperature of metal sources, temperature of substrates, and transverse speed of the substrate. A control thermocouple was used to monitor the substrate temperature. It was ensured that the thermocouple made a proper contact with the edge of a graphite substrate holder. It may be noted that with this arrangement the SLG substrates were not able to directly connect with thermocouple. Therefore in order to ensure more accurate temperature measurements for the SLG substrates, the temperature on the Mo coated SLG was measured with the help of other thermocouples which were allowed to contact the bottom of the mounted SLG. The temperature of the SLG was varied and measured using PID controls along with the temperature recorded by the control thermocouple, which was calibrated against the thermocouples underneath the SLG glass. An experiment was conducted without performing the actual process to avoid any complications as described as follows.

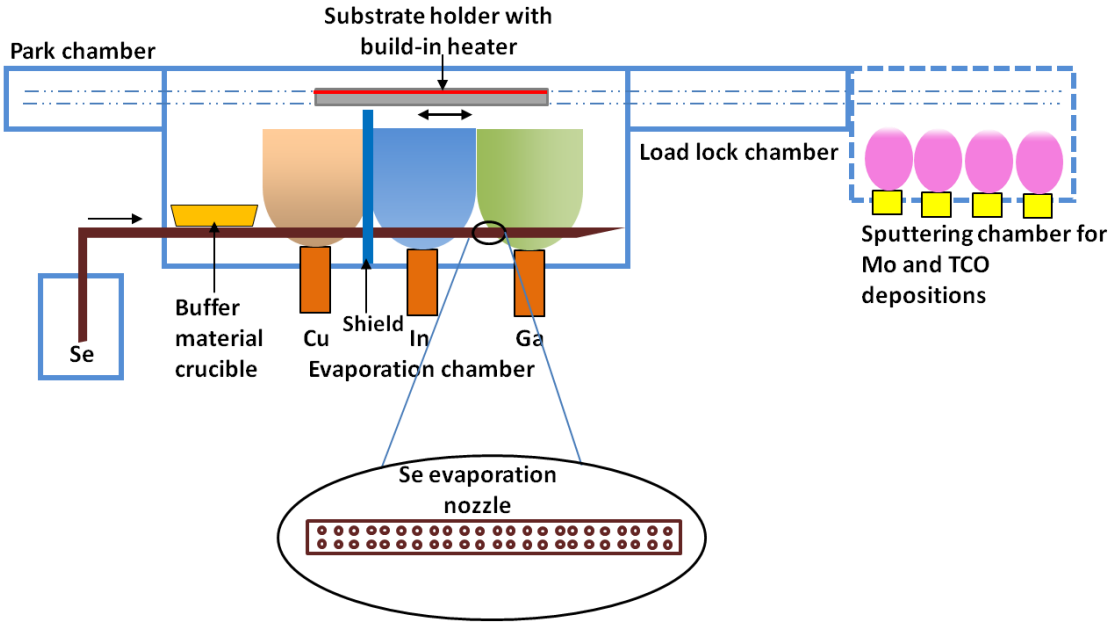

Figure 2.3: *A schematic of an inline co-evaporation CIGS system. The evaporation chamber is for absorber and buffer depositions, the sputtering chamber is for front and back contact depositions and load lock and park chamber are loading and unloading samples and transferring samples.*

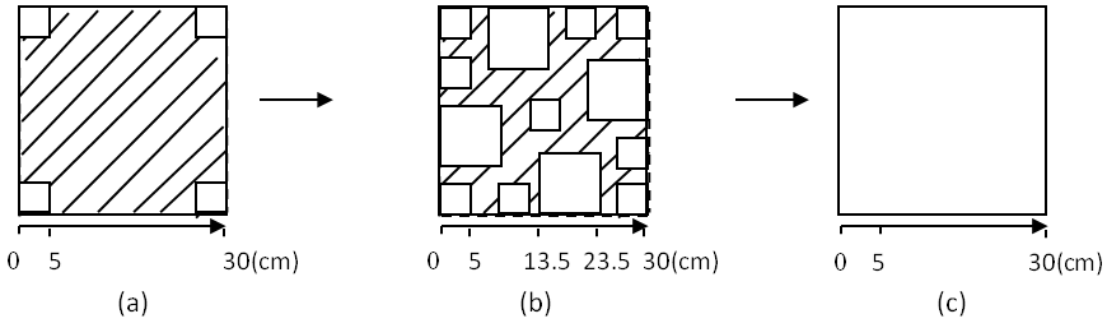

Figure 2.4: *Masks with capabilities to hold (a) 5 cm × 5 cm, (b) 10 cm × 10 cm and (c) 30 cm × 30 cm substrates for deposition of CIGS layers. The white squares in (a-c) are the substrates; the shaded area is un-coated area.*

The optimisation of the substrate temperature control and distribution is one of most important scale-up requirements, which has been focused in this study. The experiments were designed and carried out towards the uniform heating on 30 cm × 30 cm substrate using three different heating assemblies as shown in Fig. 2.4 through the following procedures (Fig. 2.5):

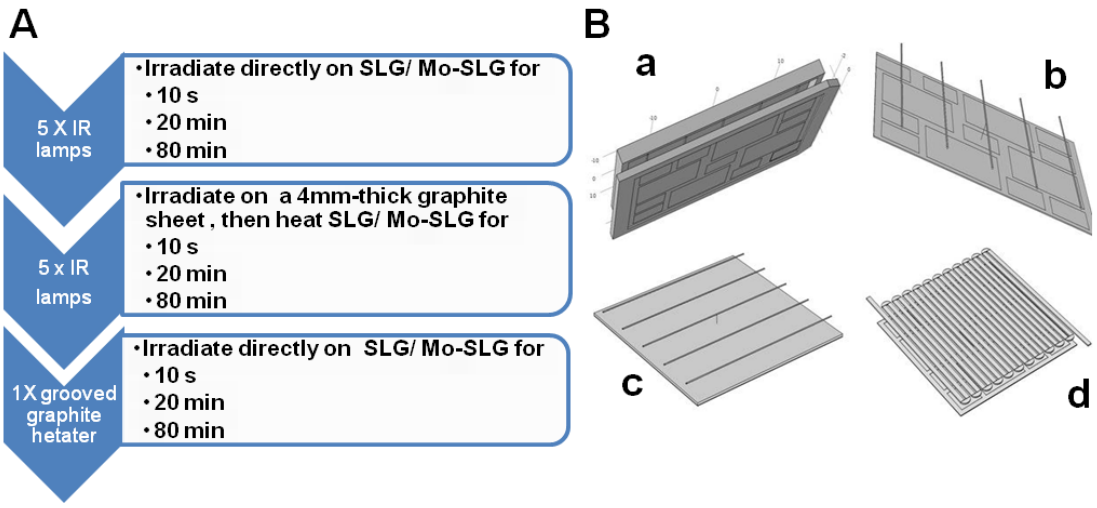

Figure 2.5: *The diagrams representing (A) A flow chart of the experimental procedures of the temperature validation work and (B) Geometry of heating assembly a), five-lamp array heater b), five-lamp array with a graphite susceptor c) and a specially designed graphite heater d).*

The modelled temperature distribution was also validated with the experimental data. The temperature data was collected by six K-type thermocouples using three designed multi-location stainless steel strips to cover the whole substrate area from the centre to the edge as shown in Fig. 2.6. There were fifteen points available for selection to mount the six thermocouples per run. Enough care was taken to ensure that proper contact between thermocouples and glass substrate was made by providing desired tension to the thermocouples. White ceramic layers were positioned between the three stainless steel straps and substrate holder, so that the holder can withstand temperature up to 800 ℃, which was used to avoid heat transfer from the chamber body to the thermocouples. The data was collected through 16-Channel thermocouple input module (National Instruments) installed with a LabVIEW program.

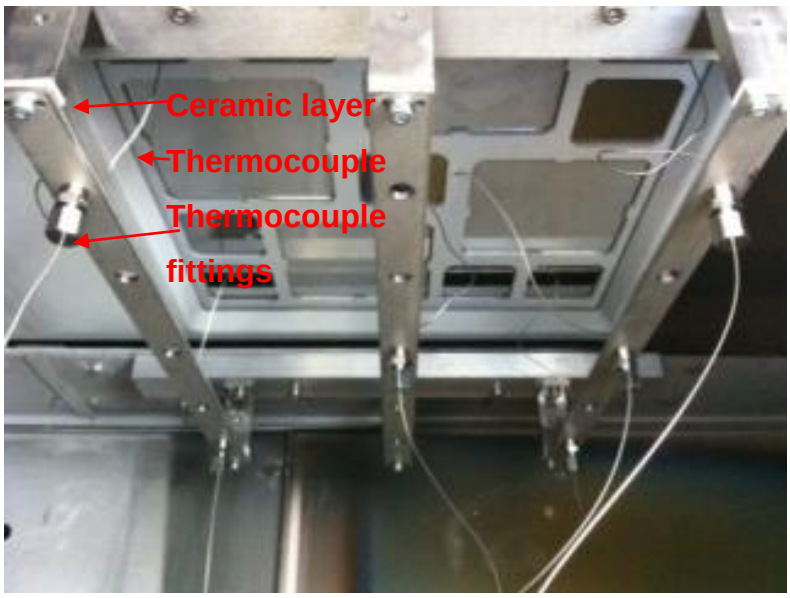

Figure 2.6: *A photograph of six thermocouples positioned underneath the glass substrate mounted on a movable heater stage assembly.*

2.4 Results and Discussion

2.4.1 Thickness distribution model of the evaporation process

In this PVD process, there are two deposition sub mechanisms: (A) evaporation from the effusion cells and (B) deposition of materials on the substrates. These mechanisms influence the final film quality, especially thickness uniformity and composition uniformity. The deposited copper, indium and gallium are used to validate and examine the modelling results. But the selenium is provided in excess, as it is hard to qualify the real deposited amount due to its high vapour pressure and low adsorption on the substrates. Glang describes comprehensively the general physical evaporation and deposition process [2.11]. Hanket *et al* adapted a method to derive the saturation pressures for copper, indium and gallium [2.12], which is in conjunction with the Glang's mathematical derivation. Junker *et al* developed a discrete dynamic model of the deposition process using the cinematic technique on a roll to roll moving substrate [2.13]. Mukati *et al.* modelled the source design and vapour flux control using a three-dimensional electro-thermal model towards a good uniformity distribution [2.14].

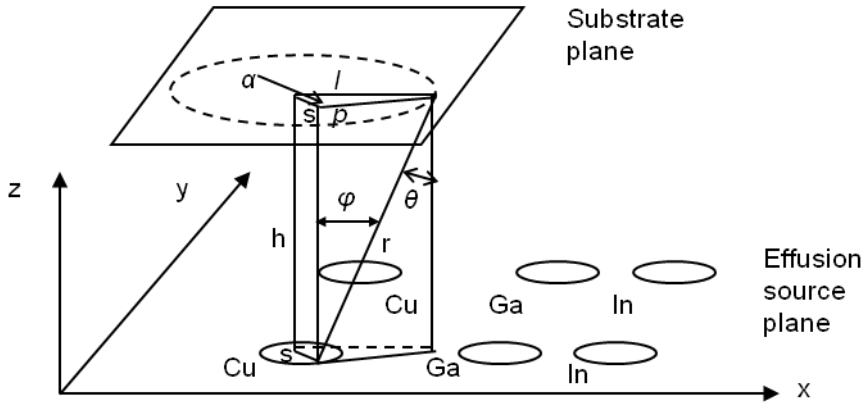

Figure 2.7: *Geometry of evaporation and deposition of various elements considered in the proposed model. Letters defined in the text.*

Inside the inline co-evaporation CIGS system, the thickness uniformity for each elemental source in the *x*-direction (along the movement of the substrates) and in *y*-direction (perpendicular to movement of the substrates), determines the final CIGS layer thickness and composition uniformity. Therefore, depositing uniform film thickness from each elemental source is the primary objective considered in this study. Specifically, in *x*-direction, there is only one source for each metal element. The uniformity is mostly dependent on stability of the substrate speed and evaporation rate. In the *y*-direction, there are two point effusion sources for each metal element which are heated by two separate DC power supplies. Fig. 2.7 describes the geometrical positioning of these elemental pair sources to ensure the better overlap of elemental flux resulting in good uniformity of the layers.

A preliminary mathematical model to describe the thickness distribution of the evaporation process of metals viz. Cu, In and Ga was developed. The validity of the model was restricted to the particular source design and acceptable stabilised evaporation temperatures. Due to the confidentiality of the Veeco's effusion source, the electrical power balance and thermal transition was not considered in this model. To reduce complexities of calculations and modelling, the following assumptions were made.

(1) It was assumed that the pair of the sources for each element was heated to the same evaporation temperature throughout the required deposition period.

(2) The change in the chamber pressure during the deposition was neglected.

(3) The deposition area was differentiated into small enough elements to be integrated.

(4) The heating of substrate didn't lead to the changes on the source temperature.

(5) The effects of mass losses of the source after every deposition on the deposition profile were neglected.

To achieve good thickness and composition uniformity, requires the optimised geometrical source design and the source operational temperature profile. A proper estimation of each source evaporation rate and deposition distribution is also needed. Hence, the source evaporation and deposition model was developed to propose the dynamic condition which allows analysing thickness uniformity of the deposited layers.

2.4.1.1 Mathematical model for the evaporation and deposition process

The evaporation theory [2.11] and previous semi-empirical models [2.14, 2.15] provide a fundamental understanding of the principle and mechanism of the deposition process as it applies to effusion sources and thickness-uniformity distribution. This model involves the problems concerned with the metals operated at high temperatures. The vapour pressure and rates of evaporation are essential in order to interpret results and predict the possible optimisation changes. As shown in Fig. 2.7, a Cartesian coordinate system (*x,y,z*) is used to define the locations and geometry of the whole deposition system. *h* is the source-to-substrate distance, *s* is the radius of the mouth of the source crucible, *l* is the radius of a circular deposition pattern, α is the angle between *l* and the projection of *s* on the substrate plane. The evaporation rate *F* represents the volume of the molecules striking the unit area per unit time [2.11], this can be described as:

$$F = \left(P_{sat}(T) - P_{cham}\right)\sqrt{\frac{M}{2\pi RT}} \tag{2.1}$$

where *R* is the ideal gas constant, *T* is the vapour temperature, *M* is the molar mass of the evaporated material, $P_{sat}(T)$ is the saturation pressure of the material which is derived according to Hanket's method [2.12] as:

$$\log P_{sat}(T) = A - \frac{B}{T} \tag{2.2}$$

where *A*, *B* are constant. P_{cham} is the partial pressure in the chamber. Thus, the thickness *d* received from a small disk source [2.11] can be given by:

$$d = \iiint_{t,s,\alpha} \frac{Fsd\alpha ds}{\pi\rho} \frac{h^4}{r^4} dt \tag{2.3}$$

where t is the deposition time, ρ is the density of the material, r is the deposition radius. Integrating α from 0 to 2π and as $r^2 = h^2 + l^2 + s^2 - 2ls\cos\alpha$, the resulting expression of d [2.11] is

$$d = \iint_{t,s} \frac{2Fh^2}{\rho} \frac{h^2 + l^2 + s^2}{\left[\left(h^2 - l^2 + s^2\right) + \left(2lh\right)^2\right]^{l,s}} sdsdt \tag{2.4}$$

The deposition from two Cu sources at a point on the substrate is calculated by the sum of the thicknesses from two individual sources.

2.4.1.2 Simulation results and experimental validation

Fig. 2.8A shows the simulated Cu fluxes in the *y*-direction, which determines the thickness distribution over the substrate. Fig. 2.8B shows the experimental results of the Cu deposition carried out at room temperature and its comparison with the simulated data. The modelling results show non-uniformity mainly at the edges of the 30 cm × 30 cm substrate geometry, which corresponded with experimental results as shown in Fig. 2.8B. The non-uniformity of the films at the edges was ±13%, which is an acceptable value for the deposition onto the substrates at room temperature. The non-uniformity between centre and edge has been reported to decrease with the increase in substrate temperature [2.16], which was observed in subsequent experimental trials.

Based on the validation of the Cu (Fig. 2.8B) deposition model over 30 cm × 30 cm area, it was assumed that the evaporation and deposition model could be extended for In and Ga deposition as well. The multiple source (Cu, In and Ga pair sources) deposition on to the substrates at room temperature showed the similar behaviour of thickness variation across the specified area of the substrate which corresponded with the simulation results as shown in Fig. 2.9. In this experiment, the substrates were located evenly on nine positions across the centre to the edge of the 30 cm × 30 cm area as shown in Fig. 2.4b. The measured non-uniformity was comparable with the simulated results. The non-uniformity was more pronounced at the edges along the *y*-direction, which was confirmed previously with Cu-source experiment as shown in Fig. 2.8B. The non-uniformity of the films at nine selected positions was ±8%.

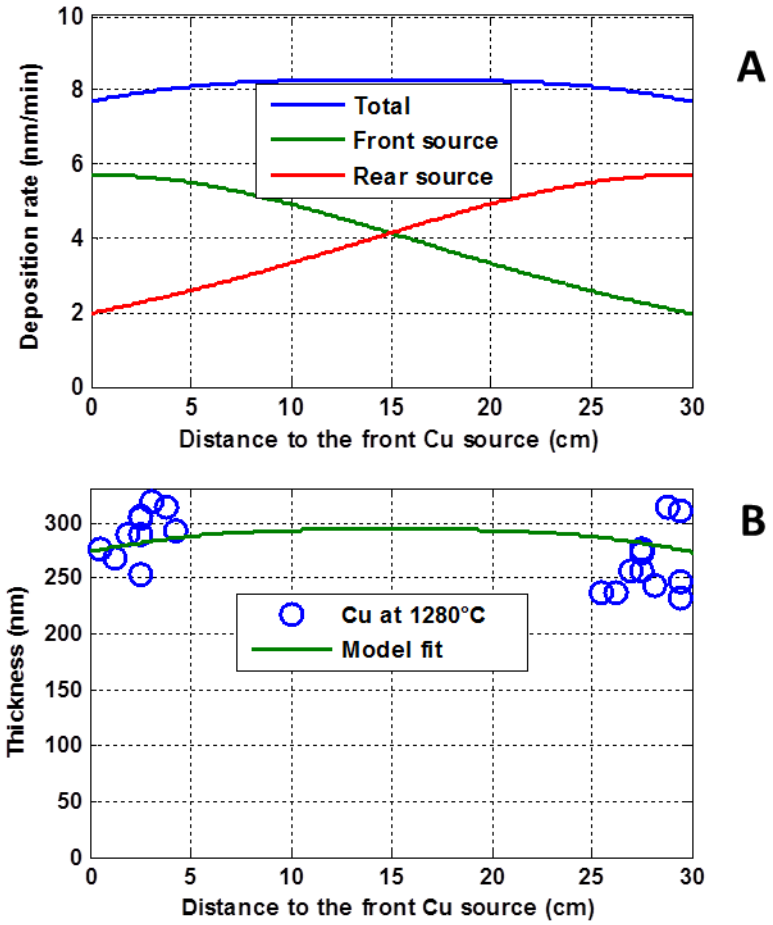

Figure 2.8: *(A) Modelled deposition rate of two copper sources at 1280 ℃ in the y-direction. (B) Measurements of Cu-coated four 5 cm × 5 cm samples and model-fit for film thickness*

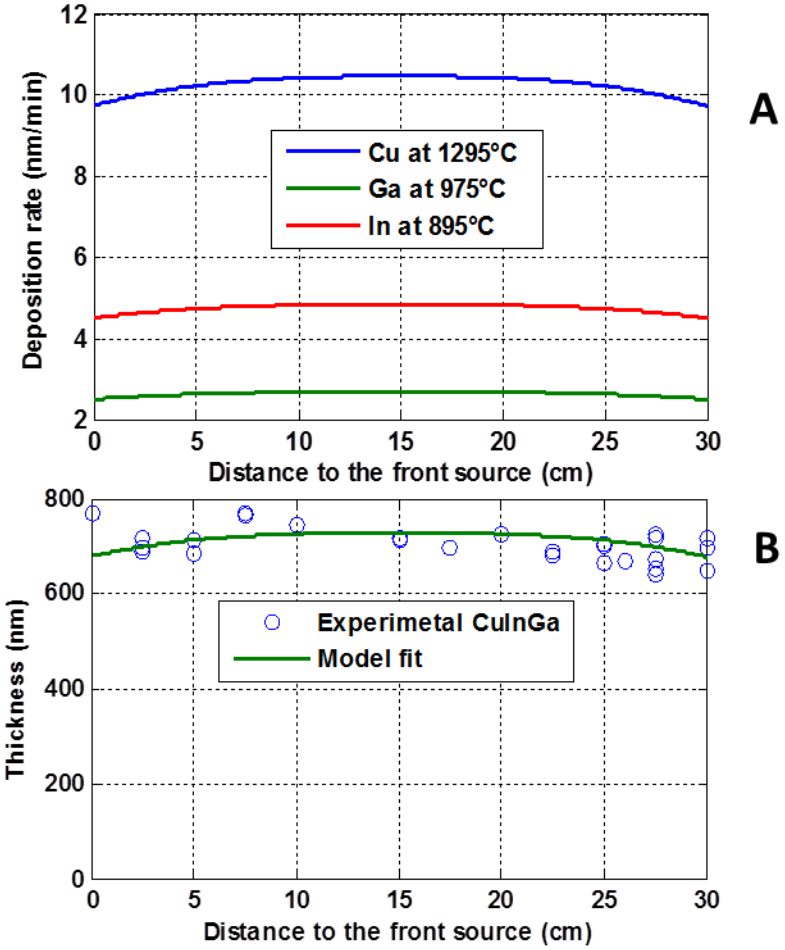

Figure 2.9: *(A) Modelled deposition rate of Cu, Ga and In sources at 1295 ℃, 975 ℃ and 895 ℃ respectively. (B) Measurements of CuGaIn-coated nine 5 cm × 5 cm samples and model-fitted film thickness. In this deposition run, Cu, Ga and In source temperature were at 1295 ℃, 975 ℃ and 895 ℃ respectively.*

2.4.1.3 Simulations on the effects of source temperature and chamber pressure in presence of selenium

The source temperature is considered as the most important variable in an evaporation process. The deposition rate of each effusion source was controlled by changing the source temperature at the same chamber pressure around ~10^{-3} Pa. The simulated deposition rates for copper, indium and gallium were calculated near the evaporation temperatures as shown in Fig. 2.10. This was used to fine tune the deposition rate in order to achieve good reproducibility. It was found that the change of the deposition rate was proportional to the change of the source temperatures for all Cu, In and Ga.

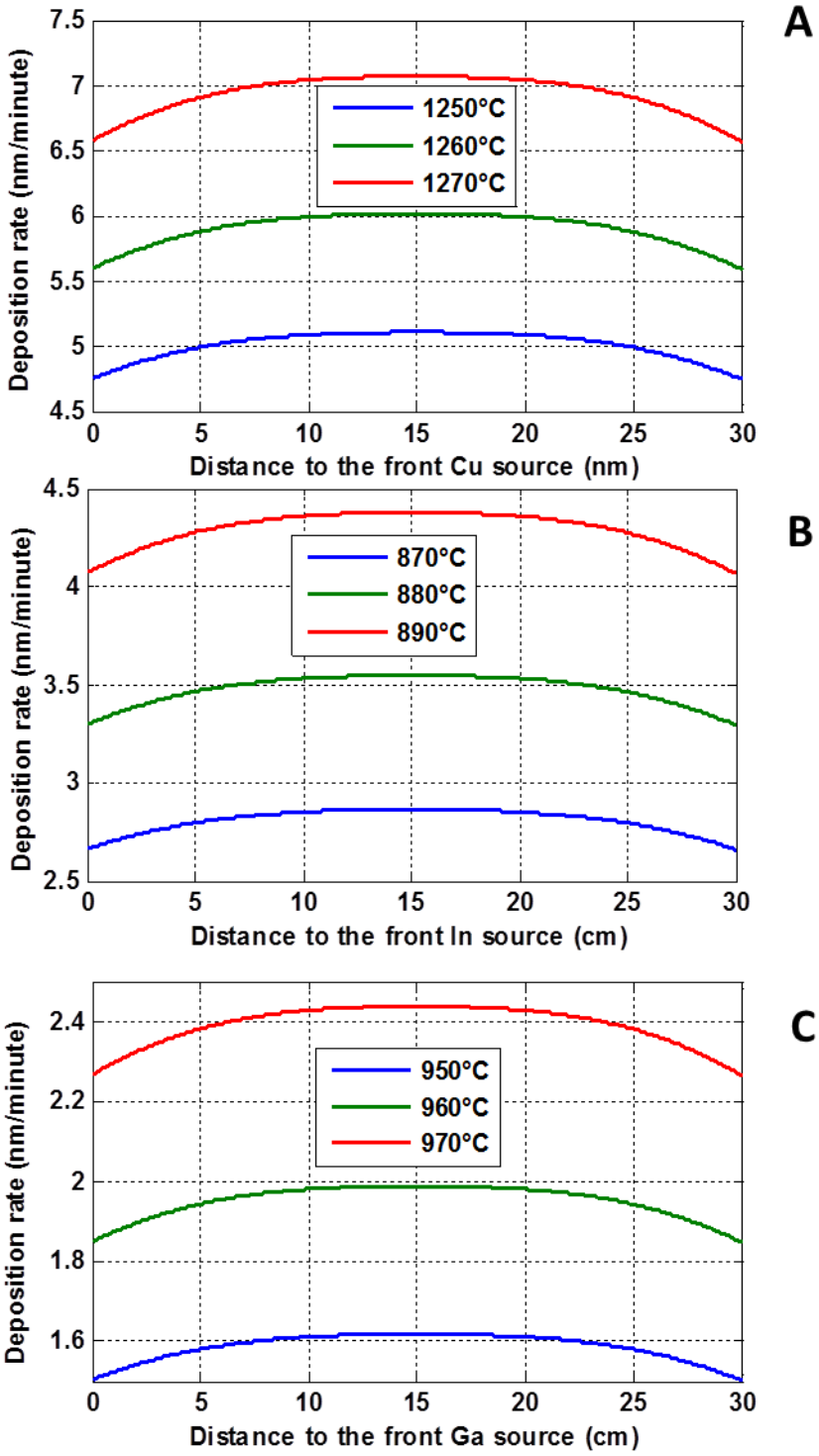

Figure 2.10: *Simulation results showing the variation of the deposition rate for different temperature of (A) copper source, (B) indium source and (C) gallium source.*

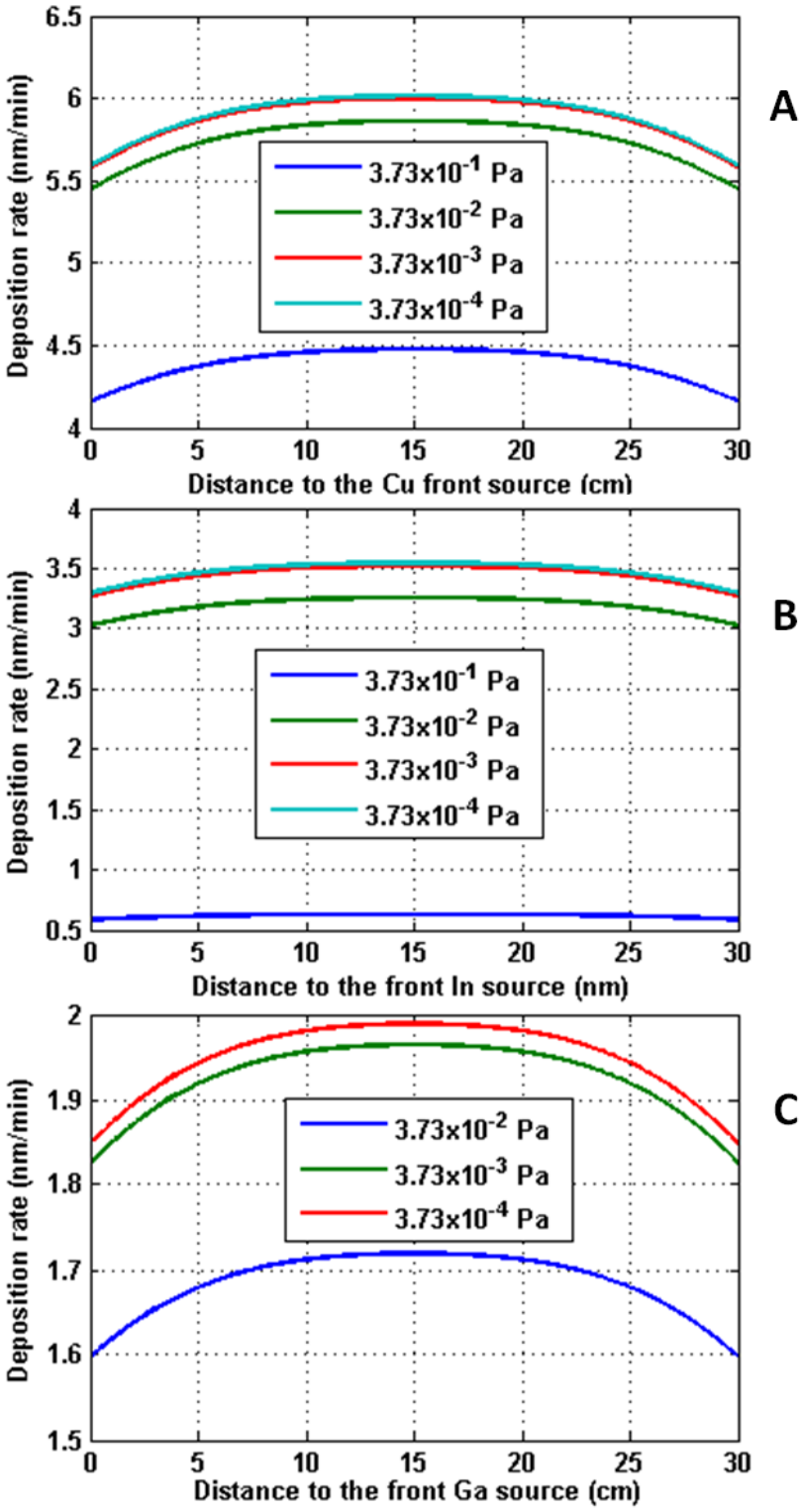

Figure 2.11: *Simulation results showing the variation of the deposition rate for different chamber pressures of (A) copper source at 1280 ℃, (B) indium source at 880 ℃ and (C) gallium source at 960 ℃.*

The pressure of the chamber is found to be another important parameter in determining the deposition rate of copper, indium and gallium sources as shown in Fig. 2.11. These results are useful to predict the variation in the evaporation rate after selenium vapour was introduced into the chamber. The presence of selenium vapour can increase the chamber pressure. A decrease in the deposition rate was observed as the chamber pressure increased for all these Cu, In and Ga sources. It showed the same trend for all three metal sources. When the chamber pressure was smaller than 10^{-5} Pa, there was no significant change on the deposition rate whilst keeping the same source temperature. For gallium source, at 10^{-1} Pa the calculated deposition rate was negative which indicates no evaporation taking place [2.13], hence the deposition rate curve could not be generated in the Fig. 2.11C.

2.4.1.4 Effects of other process parameters

$P_{sat}(T)$ is the saturation pressure of the material at temperature T as described in *Section 2.4.1.1*. This vapour pressure of the materials is always considered in the industrial development, because it directly decides the evaporation rate in this high vacuum process [2.17]. It can help to interpret results observed and also used to guide in choice of metals for specific temperature requirements [2.18].

Fig. 2.12A shows the calculated saturation pressure variation of Cu, Ga and In with increase in the temperature at constant pressure. In has highest saturation vapour pressure compared to Ga and Cu at the same temperature. In other words, the vapour pressure change per degree centigrade of In near its evaporation temperature is largest among these three elements. According to equation (2.1), the calculated evaporation fluxes versus temperatures of the materials were plotted in Fig. 2.12B. They showed the similar trends as vapour pressure variation. The flux of In was varied much quicker than Ga and Cu in the same temperature interval. These predictions were quite helpful in the practical control of these metal effusion sources.

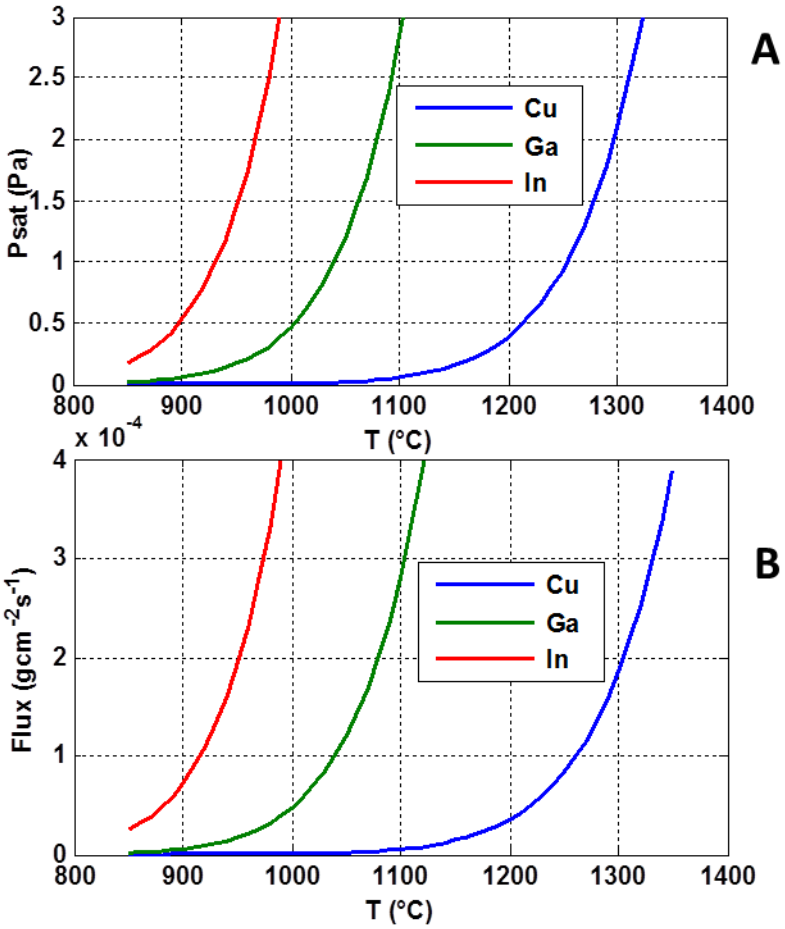

Figure 2.12: *(A) The calculated saturation pressure of Cu, Ga and In with increasing temperature at constant pressure, (B) the calculated evaporation flux of Cu, Ga and In with increasing temperature at constant pressure.*

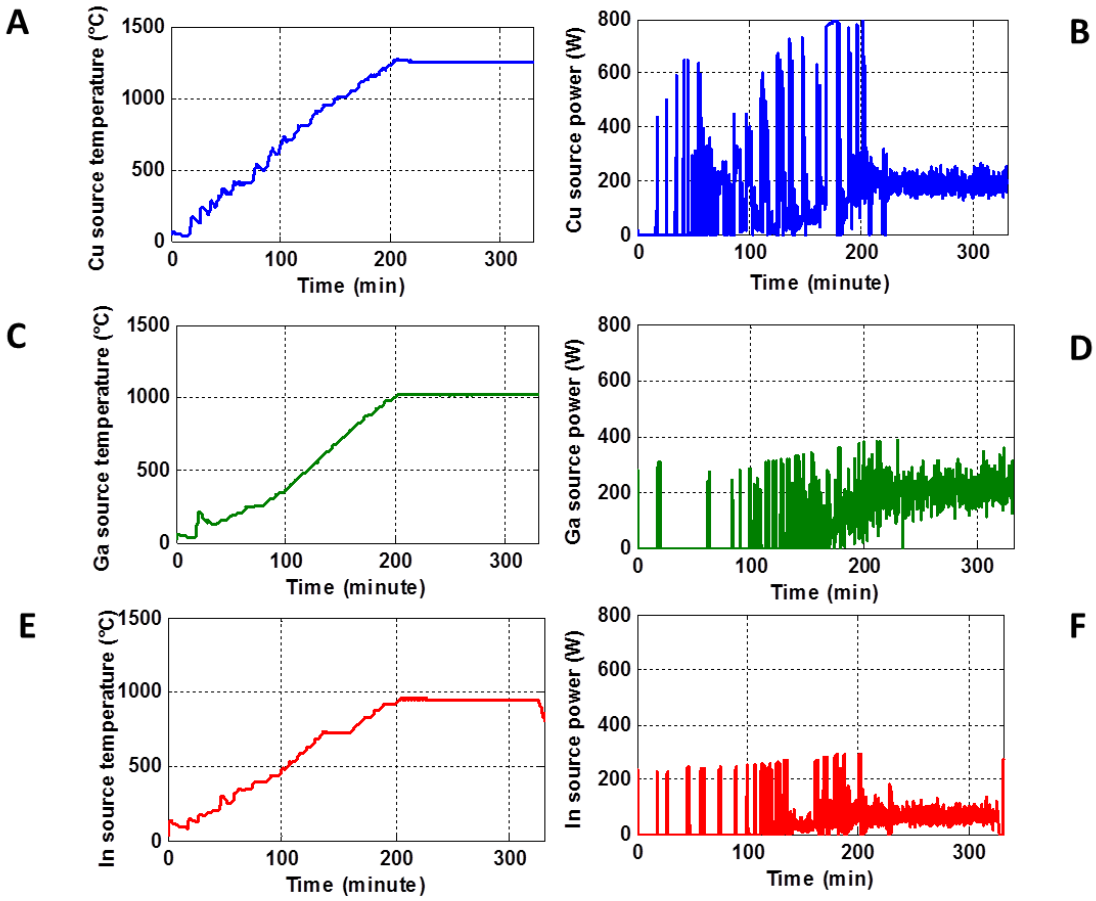

Figure 2.13: *System process parameters. (A), (C) and (E) are the heating profiles of Cu, Ga and In sources; (B), (D) and (F) are the power control of the Cu, Ga and In sources.*

The point metal effusion sources and DC power supplies were supplied by Veeco Inc. The control signal comes from a Eurotherm proportional-integral-derivative (PID) controller. An adjustable paddle switch is to set the desirable current limits for power input to these metal sources. The performance in this application went quite well during the heating and deposition process for all these sources in Fig. 2.13. The accuracy of measured source temperature is within ±5 ℃. The heating profiles for these sources were more than 3 hours due to fine tuning the parameters of three PIDs; the standard heating period to the desired source temperature should be controlled within 1.5 hours. In this case, there will be more fluctuations in the controlled power input.

2.4.2 The temperature distribution model for the heat transfer process

The temperature distribution model is a thermal model based on heat transfer effect mainly determined by radiation and conduction processes. In this model, the convection effects were not considered. The radiation covers heat transfer a) between the heater and substrates, b) from the external surface of the heater and substrates to the surrounding

environment. The conduction was considered between the substrate holders and different pieces of the substrates. The typical calculation by COMSOL is quite complex and time consuming. The following assumptions were made to simplify these computational problems.

(1) It was assumed that there is good heat transfer efficiency between the heater and the substrates.

(2) It was also assumed that the substrate edges and the graphite substrate holder were in a good thermal contact.

(3) The heat radiation to the internal surface of the heater assembly was neglected due to the proper insulation from the graphite holder.

(4) All the surfaces were opaque and radiated diffusively.

(5) The chamber was assumed as a blackbody at room temperature.

(6) The power input on the heater was stabilised during the process.

2.4.2.1 Mathematical model of heat transfer process

This model is based on heat transfer principle (diffusion equations), which is defined as the movement of energy due to the difference in temperature. In order to achieve the high process temperature uniformity on the glass substrate in a short period, the graphite radiation heater was selected in this system. The heat transfer mechanisms by radiation take place through the transport of photons. The first law of thermodynamics governs all heat transfer, which is known as the principle of conservation of energy. A simplified form of heat equation [2.19] is:

$$\rho C_p \frac{\partial T}{\partial t} + \rho C_p u \cdot \nabla T = \nabla \cdot (k \nabla T) + Q \tag{2.5}$$

where ρ is the density, C_p is the specific heat capacity at constant pressure, T is the absolute temperature, u is the velocity vector, Q represents the heat flux from the heat sources, and k is the thermal conductivity.

The total heat flux vector [2.19] is defined as:

$$Q_t = \nabla \cdot q_t = \nabla \cdot (\rho u U - k \nabla T + q_r) \tag{2.6}$$

where Q_t is the total heat flux from the heat source, q_t is the total heat flux, q_r is the radiative heat flux, and U is the internal energy.

For the heat transfer process, the heat fluxes and sources at the domain and boundary were computed respectively with the consideration of different physical variables. For domain heat flux, two main types of heat fluxes were considered: conductive heat flux in solid and radiative heat flux from non-conductive graphite heater. The domain heat fluxes can be derived from equation (2.6), which are also available as boundary heat fluxes. The boundary heat fluxes normally equal to the mean value of the adjacent domain such as graphite heater and substrate holder. The radiative heat flux on boundaries [2.19], r_{flux}, is a scalar quantity highlighted as:

$$r_{flux} = \varepsilon\sigma\left(T_{amb}^4 - T^4\right) + \varepsilon\sigma\left(G - T^4\right) + q_w \tag{2.7}$$

where the terms respectively account for surface-to-ambient radiative flux, surface-to-surface radiative flux and radiative in participating net flux, q_w. ε is known as surface emissivity, σ is the Stefen-Boltzmann constant, T_{amb} is the ambient temperature, and G is the total arriving radiative flux.

In this model, surface-to-surface radiation [2.19] can be described as the generalised equation of equation (2.6):

$$G = G_m + F_{amb}\sigma T_{amb}^4 \tag{2.8}$$

where G_m is the mutual irradiation arriving from other surfaces in the simulated geometry, and F_{amb} is the ambient view factor.

2.4.2.2 Simulation results and experimental validation of three heating assemblies

COMSOL software was used to solve the above heat transfer equations. The simulation of the temperature distribution was performed on bare soda-lime glass. COMSOL uses the proven finite element method (FEM) to solve the models with adaptive meshing. Three-dimensional (3-D) meshes were built with the sufficiently fine resolution to obtain an accurate solution as shown in Fig. 2.14.

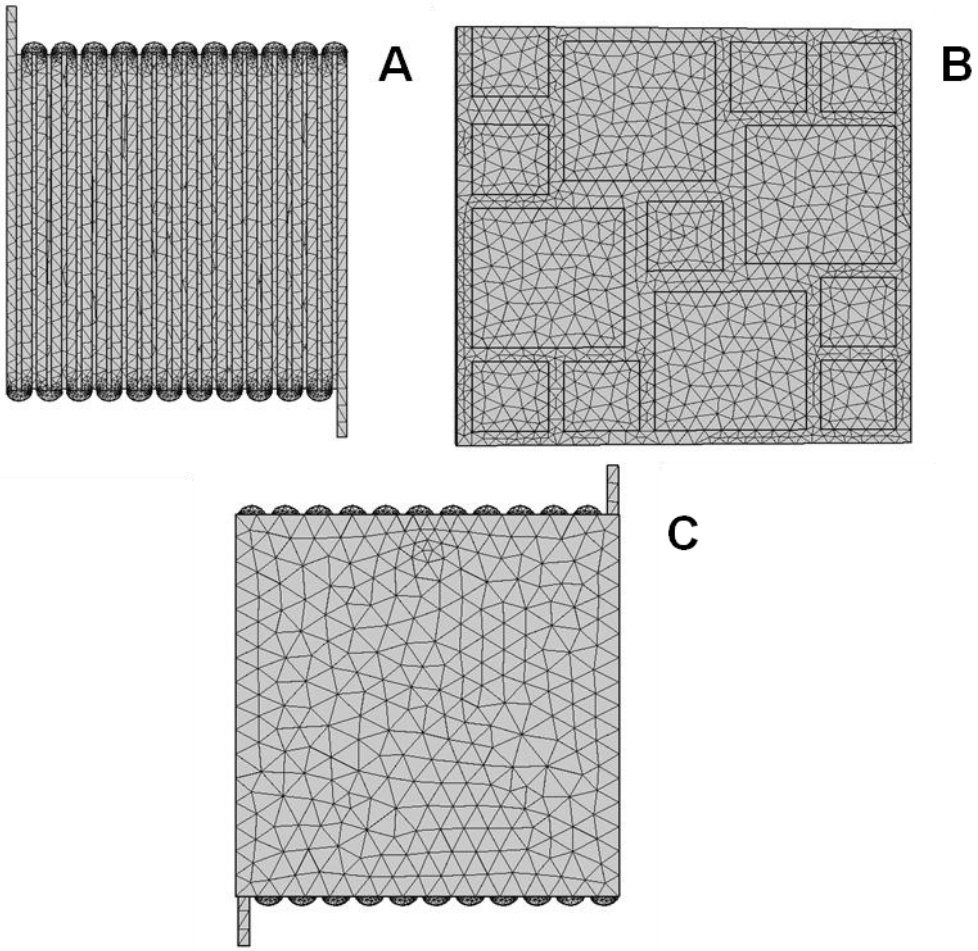

Figure 2.14: *The mesh elements of heating assembly and substrates: A) top view of heater elements, B) bottom view of the 5 cm × 5 cm and 10 cm × 10 cm SLG substrates with a graphite holder, C) bottom view of the 30 cm × 30 cm glass substrate.*

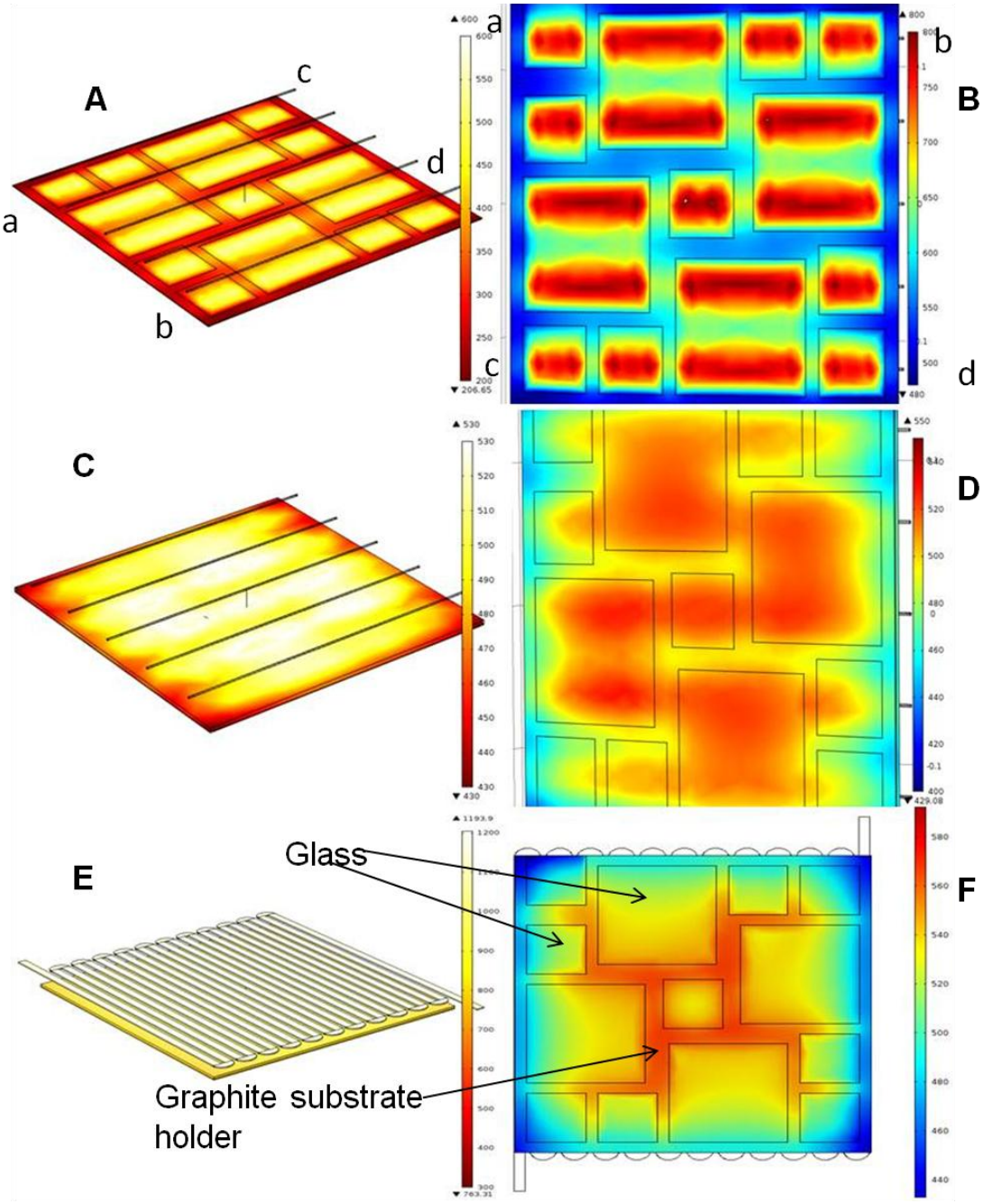

Figure 2.15: *Simulated temperature distribution for 10 s on the 30 cm × 30 cm substrate using IR lamp heater: A) IR heater assembly temperature; B) Mo-SLG substrates temperature. For an IR-lamps heater and a 4 mm thick graphite susceptor heated for 80 minutes: C) IR heater assembly temperature; D) Mo-SLG substrates temperature. For a specially designed graphite heater heated for 80 minutes: E) heater assembly temperature; F) Mo-SLG substrates temperature. The heater and substrate were coordinated using a, b, c and d in A and B, which are also applied to C-F. The temperature units are ℃ in this graph.*

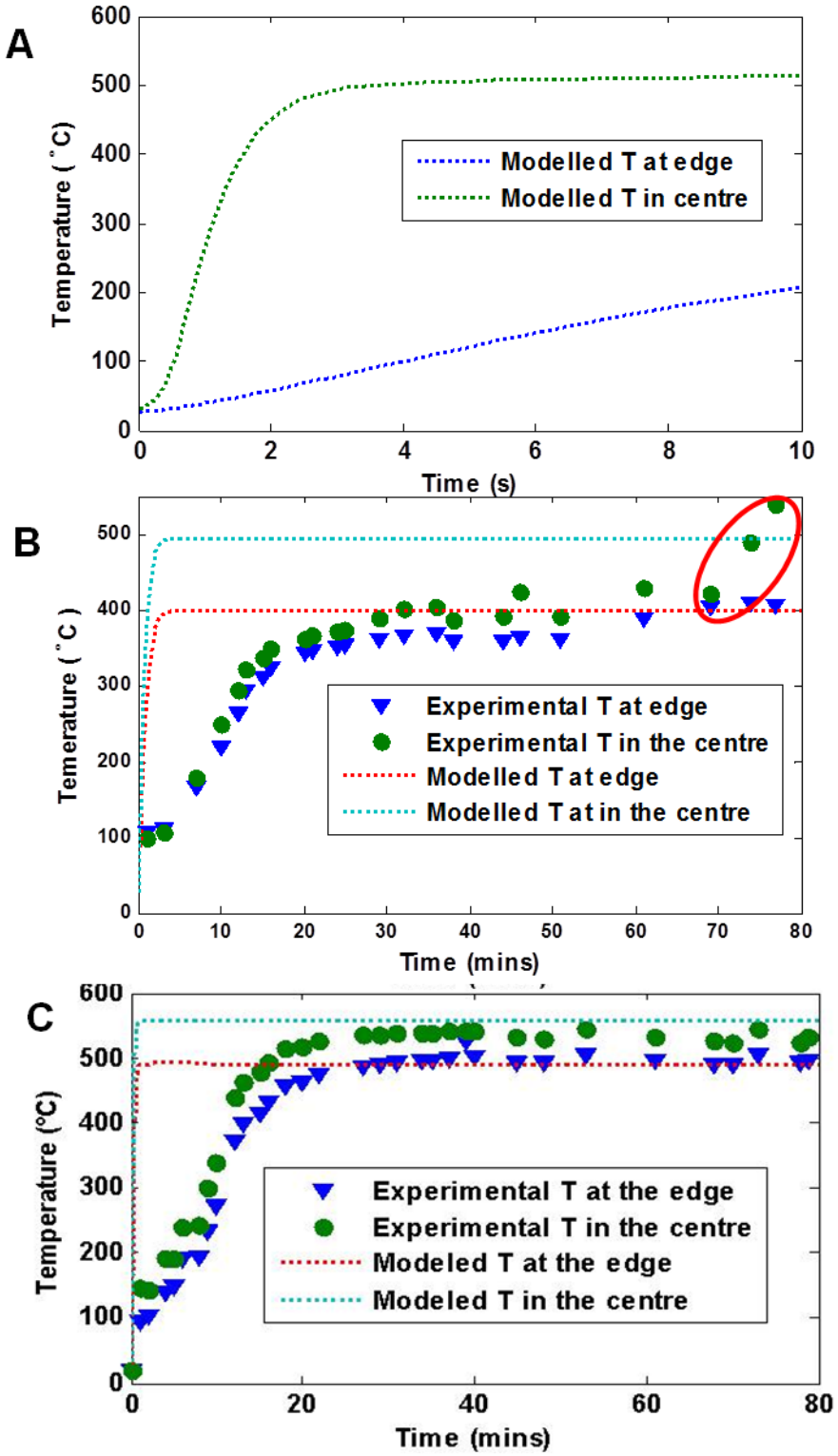

Figure 2.16: *The heating profiles of the edge and the centre of SLG substrates heated by: A) only IR lamps heater for 10 s; B) IR lamps and a graphite susceptor for 80 minutes, the temperature increase in the red circle is due to a sudden rise in temperature causing melting of the glass substrate; C) a specially designed graphite heater for 80 minutes.*

The results of a 3-D temperature profile and distribution on a 30 cm × 30 cm substrate with rapid heating IR lamps were calculated and presented in Fig. 2.15. IR lamps were normally used for rapid heating application for example the soda-lime glass (SLG) can be heated up to more than 500 ℃ in a few seconds. There is a 300 ℃ temperature-difference between the edge and the centre of 30 cm × 30 cm substrate area. This leads to non-uniformity of temperature distribution of ±21%, which is unacceptable for the CIGS co-evaporation deposition process. In order to reduce the non-uniformity of temperature distribution across the 30 cm × 30 cm substrate, a graphite susceptor was placed on top of the substrates to act as a heat homogenizer. This graphite susceptor can absorb the radiation from the IR lamps, and then transmits this through conduction to the glass substrate. The temperature difference between the edge and the centre of the 30 cm × 30 cm substrate area was reduced to less than 100 ℃, which leads to the non-uniformity of ±10%. Although this was an improvement, it is still below the industrial benchmark. However, for a small area (less than 10 cm × 10 cm), the non-uniformity can be reduced to ±5% as shown in Fig. 2.15D and 2.16B for 80 minutes run, which is an acceptable industrial value for this process, but certainly with the limitation of usable area of 10 cm × 10 cm, which is a drawback for an industrial cost-effective process. Besides, the temperature in the centre increases suddenly up to approximately 700 ℃ in a few seconds for ~80 minutes of heating. This may be due to the non-uniformity of temperature distribution across the whole area, which is highlighted in the red circle in Fig. 2.16B.

In order to form proper α-phase CIGS alloy, the substrate requires to be heated to >500 ℃ for a certain period of time depending on optimisation conditions set by various groups [2.20-2.22]. This requires the stabilised power output from the heater and flexible control on the fine tuning of temperature changes. A heater assembly system (Fig. 2.14) was used to carry out the temperature profiling measurements. The simulated and experimental temperature distributions were compared across 30 cm × 30 cm area with nine evenly positioned 5 cm × 5 cm soda-lime glasses substrates. The experimental data was the average of four thermocouples at four different locations. The non-uniformity of bare SLG substrates heated by the specially designed graphite heater was reduced to ±5% across the 30 cm × 30 cm area as shown in Fig. 2.15E, 2,15F and 2.16C. This provides a very promising solution toward the uniform heating of large area applications. In Fig. 2.15F, the small squares are glass substrates, which are held by a graphite holder. The values from Fig. 2.15F are obtained from the simulated results. The

temperature variation on the glass substrates were measured within 50 ℃. The temperature difference between graphite substrate holder and the glass substrates were larger than 50 ℃, this may be due to high thermal conductivity of the graphite. There was a discrepancy between the simulation and experimental data for the initial 15 min of heating. The simulated results were showing quick ramp-up time compared to the experimental measurement. This may be due to the following reasons:

1) Outgassing effect from the heater assembly can lead to overall pressure increases in the main chamber, which slows down the initial heating performance.
2) The accuracy of measurement of the K-type thermocouples may not be good enough at the temperature range between 20 to 500 ℃.
3) The contact between the control thermocouple of the PID controller and SLG edge may not be proper.
4) The boundary conditions of heat transfer model need to be improved especially the 'surface-to-ambient' to fit into the real heating process.

Based on the progress made using the graphite heater, a heat trial was performed to test the temperature distribution on a single piece of 30 cm × 30 cm glass substrate. This was a very important step to investigate the solution of overcoming the scale-up challenge. In Fig. 2.17, the temperature on the 30 cm × 30 cm substrate showed a rippled contour shape distribution. It shows good uniformity at the centre part of the substrate, non-uniformity at the corners. This leads to a non-uniformity of approximately ±5%.

The experimental results corresponded with the simulated results. However, the measured temperatures during the initial 15 minutes were lower than the simulated temperature as discussed above. Due to simplified modelling assumptions, there was an ambiguity in temperature rise results from experimental results. The equilibrium temperature was lagging behind by 15 minutes compared with the simulated results. It was observed that the single piece of glass was deformed (the centre of the glass bucked slightly) during the process as shown in Fig. 2.18. This may be due to the effect of gravity on the glass when it is molten. It may also be caused by the non-uniform heating experienced at the edges from the heater. Redesigning the heater reflector to improve the temperature uniformity at the edges would overcome this problem. An improved substrate holder design changing the orientation of the substrate assembly and

repositioning of the thermal sources may be required when increasing the substrate area as used for standard 120 cm ×60 cm modules.

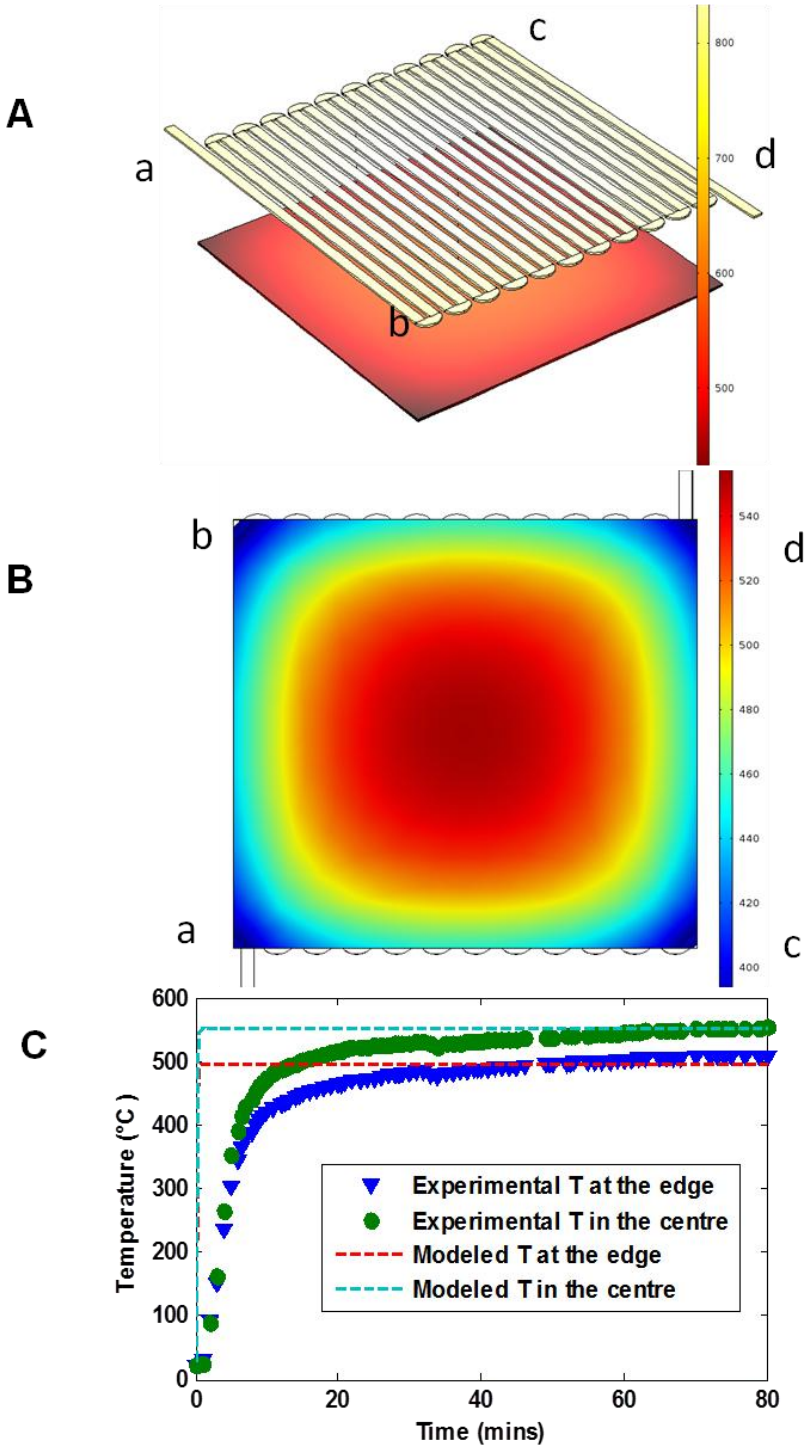

Figure 2.17: *Simulated temperature distribution on a 30 cm × 30 cm-area glass substrate with a specially designed graphite heater: (A) top view of the heater assembly, (B) bottom view of substrate temperature distribution, (C) simulated and experimental temperature distributions on the 30 cm × 30cm substrate using a specially designed graphite heater for 80 minutes. The heater and substrate were coordinated using a, b, c and d in A and B. The temperature units are ℃ in this graph.*

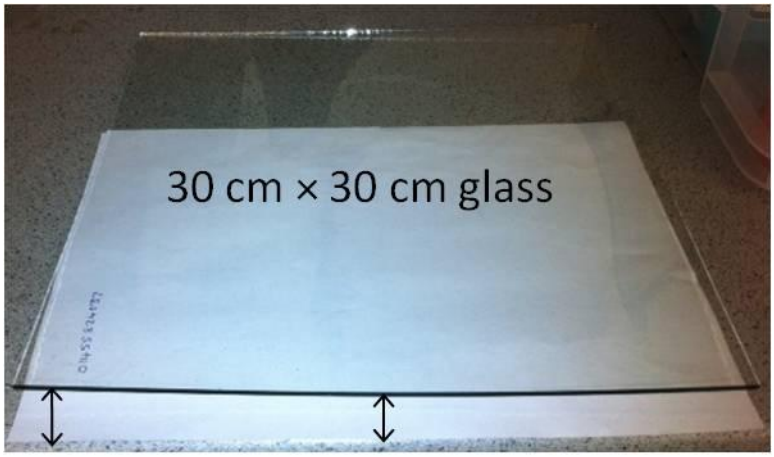

Figure 2.18: *The photograph shows the buckling of a 30 cm × 30 cm glass substrate*

2.4.2.3 Effects of the control thermocouple positions

The position of the control thermocouple was varied to get accurate measurements and effective heating power output from the heaters. Because direct measurement on the substrate surface was difficult due to the inline moving mechanism, the control thermocouple was placed to touch the edge of the substrate and near the lamps. All the experiments were carried out with lamps heater. Further comparison for the graphite heater is necessary for better temperature monitoring and control.

There is a clear temperature difference between control thermocouple and testing thermocouples (TC1, TC2, and TC3) as shown in Fig. 2.19A. This may be because there wasn't a proper contact between the control thermal and the edge of the glass substrate. The difference between the control thermocouple and the testing thermocouples were reduced by relocating the control thermocouple near the lamp heater, though it was not in contact with anything. The optimised distance between the heater and the control thermocouple is necessary to be calibrated to get the best power control of the heater.

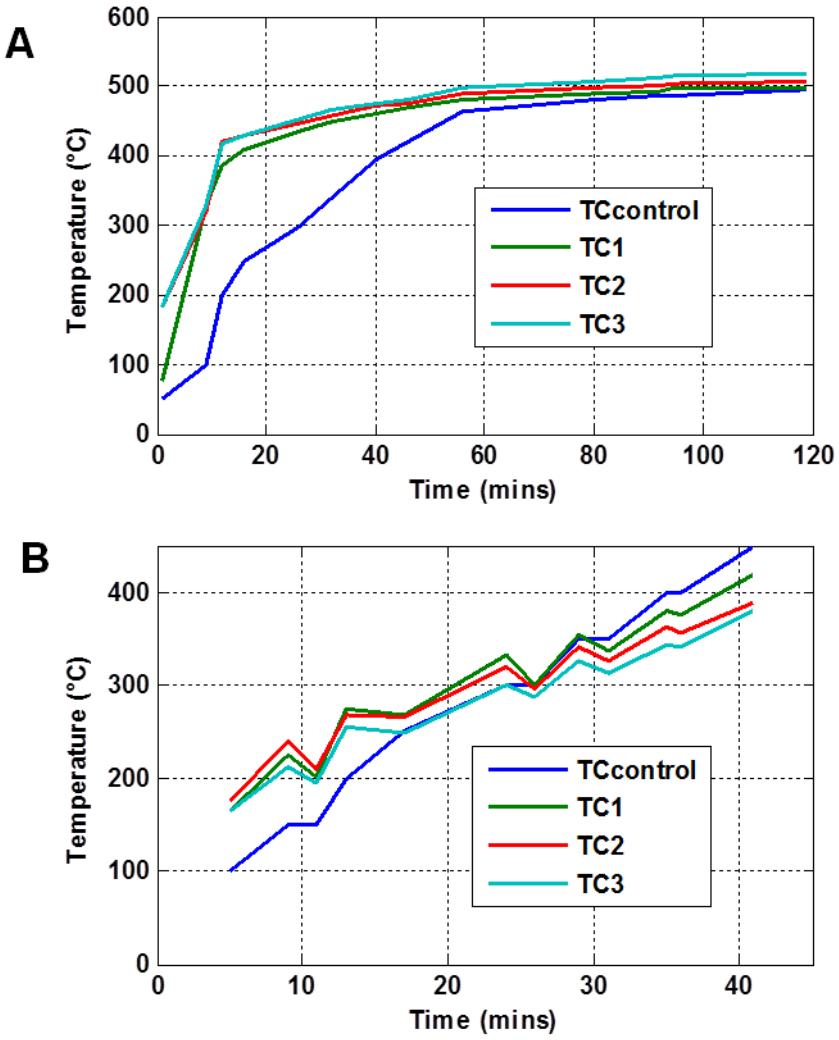

Figure 2.19: A) *Temperature distribution of four corners on 30 cm × 30 cm substrate when the control thermocouple touched on the edge of the substrate. B) Temperature distribution of four comers on the 30 cm × 30 cm substrate when the control thermocouple placed near lamps.*

2.5 Conclusion

This chapter covers the design and optimisation of an inline pilot scale co-evaporation system for CIGS solar cells. This work was conducted to investigate the challenges on the process optimization for large area high performance CIGS solar cells. Two scaling up challenges were targeted in this chapter. The first one was the Cu, In and Ga layers thickness uniformity over 30 cm × 30 cm area, deposited using an in-line evaporation system, which was predicted and validated using a simple evaporation model. These results were in agreement with the predicted data leading to a thickness uniformity of ±8%. The second challenge was the uniform temperature distribution over a 30 cm × 30 cm area substrate, which was heated using a specially designed graphite heater. Temperature mapping was conducted using K-type thermocouples and the simulated

results were calculated using a 3-D heat transfer model. A validation of the simulation results is in good agreement with the experimental measurements, which resulted in non-uniformity of ±5% from centre to edge across a 30 cm × 30 cm area. The results of this investigation provide a promising solution towards uniform heating of a 30 cm × 30 cm area for high performance solar cell application.

References

[2.1] A. Chirilă, P. Reinhard, F. Pianezzi, P. Bloesch, A. R. Uhl, C. Fella, L. Kranz, D. Keller, C. Gretener, H. Hagendorfer, D. Jaeger, R. Erni, S. Nishiwaki, S. Buecheler and A. N. Tiwari, "Potassium-induced surface modification of $Cu(In,Ga)Se_2$ thin films for high-efficiency solar cells," *Nat Mater,* vol. 12, pp. 1107-1111, 12, 2013.

[2.2] http://www.solar-frontier.com/eng/news/2014/C031367.html, "Solar Frontier Sets Thin-Film PV World Record with 20.9% CIS Cell," 2014.

[2.3] P. Jackson, D. Hariskos, R. Wuerz, W. Wischmann and M. Powalla, "Compositional investigation of potassium doped $Cu(In,Ga)Se_2$ solar cells with efficiencies up to 20.8%," *physica status solidi (RRL) – Rapid Research Letters,* vol. 8, pp. 219-222, 2014.

[2.4] Z. M. Beiley and M. D. McGehee, "Modeling low cost hybrid tandem photovoltaics with the potential for efficiencies exceeding 20%," *Energy & Environmental Science,* vol. 5, pp. 9173-9179, 2012.

[2.5] M. Nakamura, Y. Kouji, Y. Chiba, H. Hakuma, T. Kobayashi and T. Nakada, "Achievement of 19.7% efficiency with a small-sized $Cu(InGa)(SeS)_2$ solar cells prepared by sulfurization after selenizaion process with Zn-based buffer," *Conference Record of the IEEE 39th Photovoltaic Specialists Conference*, Tampa, 849-852, 2013.

[2.6] http://www.manz.com/media/news/archive/2012/manz-presents-cigs-world-record-module-with-efficiency-of-146-at-pv-taiwan-425, 2013.

[2.7] W. N. Shafarman and L. Stolt, "$Cu(InGa)Se_2$ Solar Cells," in *Handbook of Photovoltaic Science and Engineering*, ed: John Wiley & Sons, Ltd, pp. 567-616, 2005.

[2.8] J. J. Scragg, P. J. Dale, D. Colombara, and L. M. Peter, "Thermodynamic Aspects of the Synthesis of Thin-Film Materials for Solar Cells," *ChemPhysChem,* vol. 13, pp. 3035-3046, 2012.

[2.9] H. Sugimoto, Y. Kawaguchi, Y. Yasaki, T. Aramoto, Y. Tanaka, H. Hakuma, S. Kuriyagawa and K. Kushiya, "Challenge to 18% Efficiency with 30x30 cm_2-Sized $Cu(InGa)(SeS)_2$ Submodules in Solar Frontier," *Conference Record of the 26th European Photovoltaic Solar Energy Conference and Exhibition*, Hamburg, pp. 2307-2310, 2011.

[2.10] R. Verma, "Vacuum evaporated In_2S_3 buffer layer for $Cu(In,Ga)Se_2$ thin-film solar cell," Doctoral thesis, ETH, Zurich, 2010.

[2.11] R. Glang, "Vacuum Evaporation," in *Handbook of Thin Film Technology*, L. I. Maissel, Ed., ed New York: McGraw-Hill Book Co., pp. 1-87, 1983.

[2.12] G. M. Hanket, R. W. Birkmire, S. Fields and E. Eser, "Commercial-scale sources for the evaporation of elemental Cu, Ga, and In: Modeling, design, and validation," *Conference Record of the 35th IEEE Photovoltaic Specialists Conference*, Honolulu, pp. 770-775, 2010.

[2.13] S. T. Junker, R. W. Birkmire and F. J. Doyle, "Manufacture of Thin-Film Solar Cells: Modeling and Control of $Cu(InGa)Se_2$ Physical Vapor Deposition onto a Moving Substrate," *Industrial & Engineering Chemistry Research,* vol. 43, pp. 566-576, 2003.

[2.14] K. Mukati, B. A. Ogunnaike, E. Eser, S. Fields and R. W. Birkmire, "Scaleup of $Cu(InGa)Se_2$ Thin Film Coevaporative Physical Vapor Deposition Process, 1.

Evaporation Source Model Development," *Industrial & Engineering Chemistry Research*, vol. 48, pp. 5975-5991, 2009.

[2.15] G. M. Hanket, P. D. Paulson, U. Singh, S. T. Junker, R. W. Birkmire, F. J. Doyle, III, E. Eser and W. N. Shafarman, "Fabrication of graded Cu(InGa)Se_2 films by inline evaporation," *Conference Record of the 28th IEEE Photovoltaic Specialists Conference*, Anchorage, pp. 499-504, 2000.

[2.16] C. Guillén and J. Herrero, "Structure, morphology and photoelectrochemical activity of $CuInSe_2$ thin films as determined by the characteristics of evaporated metallic precursors," *Solar Energy Materials and Solar Cells*, vol. 73, pp. 141-149, 2002.

[2.17] S. Dushman, "Vapor pressures and rates of evaporation," in *Scientific Foundation of Vacuum Technique*, J. M. Lafferty, Ed., Second ed New York: John Wiley & Sons, pp. 691-737, 1949.

[2.18] R. W. Ditchburn and J. C. Gilmour, "The Vapor Pressures of Monatomic Vapors," *Reviews of Modern Physics*, vol. 13, pp. 310-327, 1941.

[2.19] COMSOL, *Heat Transfer Module User's Guide*, 2011.

[2.20] I. Repins, M. A. Contreras, B. Egaas, C. DeHart, J. Scharf, C. L. Perkins, B. To and R. Noufi, "19.9%-efficient ZnO/CdS/$CuInGaSe_2$ solar cell with 81.2% fill factor," *Progress in Photovoltaics: Research and Applications*, vol. 16, pp. 235-239, 2008.

[2.21] A. Chirilă, S. Seyrling, S. Buecheler, D. Guettler, S. Nishiwaki, Y. E. Romanyuk, G. Bilger and A. N. Tiwari, "Influence of high growth rates on evaporated Cu(In,Ga)Se_2 layers and solar cells," *Progress in Photovoltaics: Research and Applications*, vol. 20, pp. 209-216, 2012.

[2.22] R. Caballero, C. A. Kaufmann, V. Efimova, T. Rissom, V. Hoffmann and H.-W. Schock, "Investigation of Cu(In,Ga)Se_2 thin-film formation during the multi-stage co-evaporation process," *Progress in Photovoltaics: Research and Applications*, vol. 21, pp. 30-46, 2013.

Chapter 3 – Development of different processes for $Cu(In,Ga)Se_2$ thin film absorber using inline pilot scale co-evaporation system

Abstract

Polycrystalline $Cu(In,Ga)Se_2$ thin film solar cells were prepared by elemental co-evaporation process using an inline pilot scale production system on soda lime glass at a substrate temperature of 550 ℃. To develop high efficiency CIGS solar cells, the so called three-stage process [3.1] was modified. The CIG metal precursors were grown at room temperature to investigate the individual source performance, and then selenised at 550 ℃ for the CIGS formation. The substrates within each stage of the growth process were maintained at a constant temperature and varied temperatures between the first and second stages. The CIGS layers grown using the standard three-stage process with varied substrate temperatures showed the most condensed and uniform surface morphology. The composition of Cu and Ga content CGI and GGI are crucial for high efficiency CIGS solar cells. The Cu content was varied by changing the source evaporation rate; the best compositions were obtained at 0.8-0.9 for this inline deposition system. It was observed that an increased Ga content can increase the open circuit voltage for achieving better power conversion efficiency. Since a new inline pilot scale CIGS co-evaporation system was built, achieving high efficiency was the primary motivation of this work, and demonstrating the running of this system towards a large area and cost-effective CIGS solar cells was targeted in this time frame. Reducing the thickness of the CIGS layer was chosen in this work due to their unique advantages including shortening the manufacturing time, reducing material cost and increasing the throughput. To investigate critical issues of the thinner absorber layers, above two-step and modified three-stage processes were utilised to grow CIGS film with thickness of around 1 μm. It has been found that the current densities were significantly reduced, along with a notable reduction in fill factor and open circuit voltage. A better light absorption is required for the thinner absorber layer. A best CIGS solar cell device with ~1 μm reached up to 8.1% conversion efficiency (V_{oc} = 0.63 V, J_{sc} = 20.8 mA/cm^2 , FF = 68.8, total area = 0.09 cm^2 without grid and anti-reflection coating) under simulated AM1.5G standard test conditions.

3.1 Introduction

Polycrystalline CIGS materials have thinner total film thickness as compared to bulk crystalline materials, because the CIGS layer has a direct band gap with high light absorption coefficient [3.2]. Another main property in favour of polycrystalline CIGS is the intrinsic doping with native defects to control the conductivity of the material [3.3]. For the last ten years, the certified cell efficiency has steadily increased by nearly 2% absolute [3.4-3.6] to reach 21.7% [3.7] threshold value. Reasonable large grain size is not the only requirement for high efficiency cell [3.8], but also the intentional alkaline doping [3.9-3.11] can enhance the device performance.

Two crucial deposition parameters in the three-stage process for growing high efficiency CIGS solar cells are discussed in this chapter, which are the substrate temperature and composition variation. In general, the three-stage process includes a deposition stage of In and Ga in Se environment first. Then, Cu deposited in Se environment in the second stage. In the third stage, the growth of the material finished with In and Ga in presence of copious supply of Se. There are quite complex material formations and transitions in each stage, so the precisely controlled deposition parameters, especially substrate temperature and composition, at each stage will determine the final CIGS phases and film quality. The empirical composition ratios of $0.80 \leq CGI \leq 0.90$ (CGI) and $0.25 \leq GGI \leq 0.35$ (GGI) are the primary requirements to fabricate CIGS solar cell with an efficiency above 19% [3.8, 3.12].

The substrate temperature and its control play an important role in the growth of high quality CIGS solar cells. It was reported that CIGS films processed at 400 ℃ had lower efficiency and smaller grain size as compared to those grown at 550 ℃ [3.13, 3.14]. The higher substrate temperature brought more Cu-deficient defect phases during the second stage and increased In-Ga-interdiffusion, which led to a better crystallinity [3.9, 3.14]. This also indicates some benefits of the incorporation of Na in the CIGS layers to elevate the film properties at the high substrate temperature (>550 ℃) [3.15]. With the breakthrough of the 20% cell efficiency both from high substrate temperature (>550 ℃) on soda lime glass [3.11] and low substrate temperatures (~450 ℃) on polyimide [3.5], lowering the substrate temperature has been proven to be a possible way to make high performance CIGS solar cell devices more cost-effectively. Potassium and sodium fluoride were introduced after CIGS deposition in both champion devices have resulted in distinct improvements. Pianezzi *et al.* tried to analyse the beneficial effects of these

alkaline metals from the point of view of defect related recombination [3.10] such as increasing hole concentration and thinner CdS layer thickness to reduce CdS/CIGS interface recombination [3.16].

The thickness of the CIGS absorber is generally in the range of 2-3 μm. Reducing the CIGS layer thickness and maintaining high efficiency are very attractive to industrial production because it can reduce material cost and increase throughput. The main drawback of the thinner CIGS layer is the reduced light absorption, hence reducing efficiency. An application of an Au reflective back contact was used to increase the light trapping and lead to the power conversion efficiency of CIGS solar cells grown using co-evaporation process with thickness around 1 μm reaching more than 10% [3.17]. Alternatively, a backwall superstrate configuration based CIGS solar cell exceeding 10% efficiency with the CIGS layer thickness around 1 μm grown with single-stage co-evaporation process was demonstrated. This structure effectively increased the short-circuit current due to increased light absorption [3.18].

In the case of varied substrate temperature in the three-stage process, higher substrate temperature at the second and third stages would create a 'trough' shape gallium double graded composition profile. The formation of this Ga double-grading helps the light absorption due to a low minimum band gap, minority carrier collection at the back contact due to the introduction a back surface field, and to increase the open circuit voltage (V_{oc}) due to an elevated built-in voltage at the front contact [3.19]. However, it can form a much more pronounced double-gradient at the lower substrate temperatures or the constant substrate temperature, which results in the formation of a higher concentration of antisite or vacancy defects [3.10]. The defect orientated problems were recovered successfully by the PDT alkaline elements after the growth of CIGS layer [3.9].

This chapter starts with the preparation of defect pronounced CIGS films using a two-step process, which includes the growth of Cu, In and Ga stack layers as a precursor at room temperature using the inline co-evaporation system, and then post selenisation of the precursor using a tube furnace. Secondly, a simplified three-stage process was used to grow CIGS films in a three-stage sequence at a constant substrate temperature using the inline evaporation system. Finally, a full three-stage process was performed to deposit high quality CIGS films at varied substrate temperatures. This was done in order

to find the processing routes to attain lowering of the cost of producing CIGS material absorbers, without compromising their performance. Another strategy to lower the cost was adapted later on with Cu-In-Ga-Se precursors deposited at low temperature (<200 ℃) and then post annealed using rapid thermal processing, in a collaboration conducted at Empa, Switzerland, studies of which is detailed in Chapter 5.

3.2 Experimental techniques

3.2.1 Experiments

CIGS solar cells were grown on 1 mm thick soda-lime glasses (SLG). About 1 μm thick Mo back contacts were deposited by DC sputtering on the properly cleaned SLG substrates. The sheet resistance of the Mo film is around 0.2 Ω/square. The CIGS absorber layers and CIG stack layers were grown in a high vacuum chamber with the base pressure around 10^{-7} hPa. Around 1 μm thick CIGS layers were deposited on the Mo back contact using the inline system which uses Cu, In and Ga point sources in pairs for attaining better film uniformity. The CIGS films are yielding GGI ratios in the range of 0.20-0.30, and CGI ratios in the range of 0.70-1.00. On top of CIGS layers, a very thin CdS layer was deposited with the thickness of about 60 nm with the help of chemical bath deposition process. The i-ZnO layers with thickness around 50 nm and ZnO:Al layers with thickness of around 600nm were deposited by RF sputtering. The total sheet resistance of AZO layer is in the range of 20-30 Ω/square measured by four-point probe method. In the last step, single cells were defined by mechanical scribing.

In the present study, a series of experiments were carried out towards a successful accomplishment of a three-stage CIGS co-evaporation process using the inline pilot scale deposition system. Three main processes were performed to obtain CIGS absorber layers in a cost-effectively industrial route, which is described in detail as follows. The optimisation of some crucial process parameters such as the control of source evaporation rate, the temperature of the substrate, the heating uniformity etc. were performed for up to 30 cm × 30 cm substrates. These processes are shown in the Fig. 3.1 for the sake of clarity. A control thermocouple was used to monitor the substrate temperature.

In **Process A** (Fig. 3.1A), the Cu, Ga and In metal layers were evaporated separately using the inline system on a substrate at room temperature to calibrate the evaporation rate of effusion cells with the source temperature. Subsequently, these elemental layers

were grown into a stacked layer as a metal precursor to form CIGS using a two-step selenisation process.

Process B (Fig. 3.1B) was used to grow large area CIGS films using the inline system with a simplified three-stage process performed at a constant substrate temperature. This experiment applied the similar evaporation rates comparing with the standard three-stage process, but at the constant substrate temperature of 500˚C.

Process C (Fig. 3.1C), a standard three-stage process was adapted to grow good quality CIGS films. During the first stage, an $(In,Ga)_2Se_3$ layer was grown at a substrate temperature of 400˚C. In the second stage, the substrate temperature was increased to 550˚C to deposit $Cu_{2-x}Se$ and the film turned into Cu-rich. In the third stage, the In, Ga and Se were co-evaporated with the same evaporation rates and deposition time as in the first stage until the film turned into Cu-poor.

To investigate the effect of variation of CGI and GGI, the source evaporation temperature of Cu and In were varied. In the Process B and Process C, the CGI and GGI variations were found to be in the range of 0.59-0.89 and 0.19-0.24.

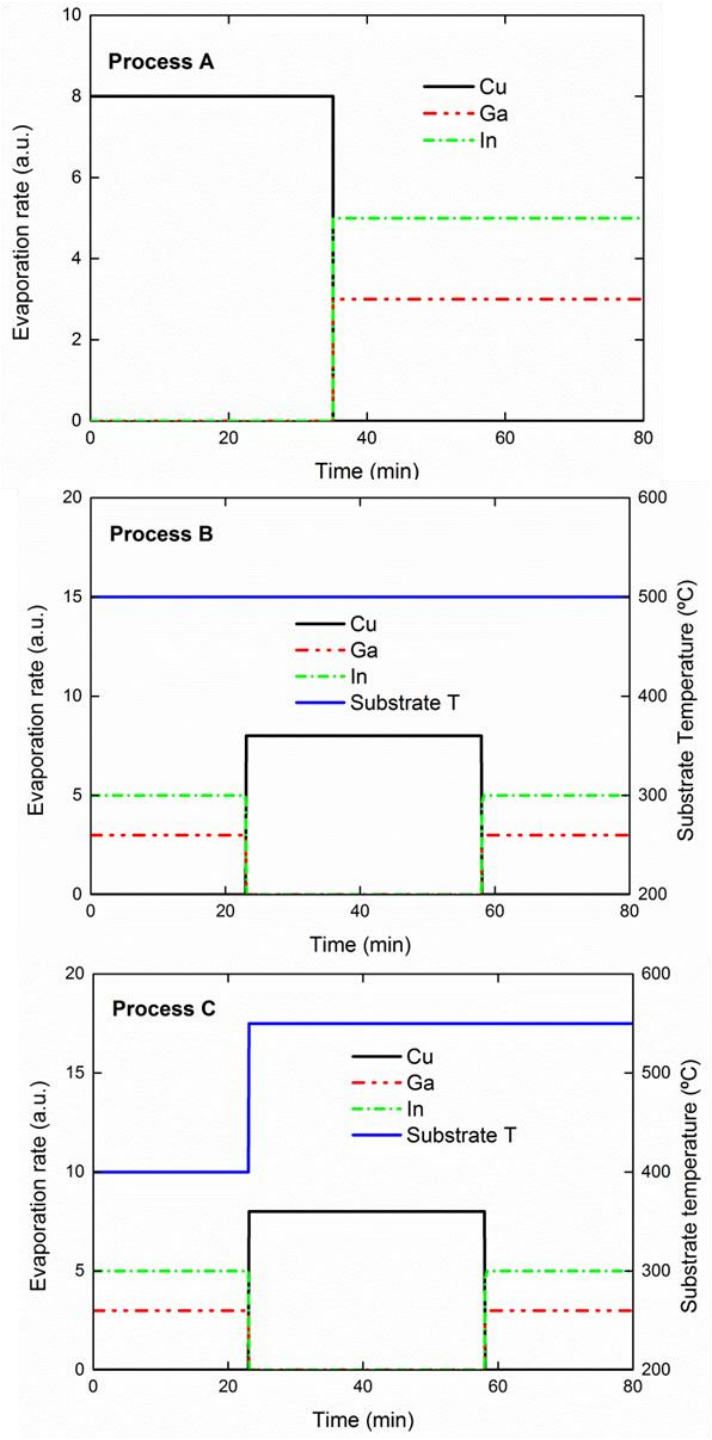

Figure 3.1: *Simulated metal deposition rates and substrate temperatures as a function of deposition time of the three deposition processes. A) Cu, Ga and In stack layers deposited at room temperature as a metal precursor, and then they were selenised in a tube furnace. B) A simplified three-stage process, Cu, Ga, In and Se were deposited in a three-stage sequence at the constant substrate temperature of 500˚C. C) CIGS films were grown in a standard three-stage process. $(In,Ga)_2Se_3$ was grown at 400˚C in the first stage and at 550 ˚C in the third stage. $Cu_{2-x}Se$ was grown at 550˚C in the second stage.*

3.2.2 Characterisations

The thickness of the layers was measured using a Dektak profilometer.

Scanning electron microscope (SEM) was used to investigate structural and morphological properties of the CIGS layers. The surface morphology of CIGS was studied with the help of an FEI Quanta 3D Dual Beam (Ion and Electron) field emission gun scanning electron microscope (FEG-SEM) at Heriot-Watt University, UK and a Hitachi S-4800 scanning electron microscope at Empa, Switzerland.

X-ray diffraction (XRD) is the other important technique to investigate the orientation of the grains in the polycrystalline CIGS films. The crystalline structure was measured using a Bruker D8 Discover X-ray Diffraction System with a step size of 0.02 ° in a 2θ range of 20 °to 60 °, voltage of 40 keV and current of 40 mA at Empa.

The average composition of the CIGS layers was determined by X-ray fluorescence measurements (XRF) at 45 kV at Empa. Kα lines together with calibrated standards were used to calculated the average GGI, CGI and at% Se.

Secondary ion mass spectroscopy (SIMS) was used to investigate the compositional variations along the film thickness. Depth profiling data were obtained with a time-of-flight SIMS 5 system from ION-TOF at Empa. Bi^+ ions were used as primary ions and positive ions were detected. Sputtering was performed using O_2^+ sputtering ions with 2 keV ion energy, 400 nA ion current and a 300 µm × 300 µm raster size. An area 100 µm × 100 µm was analysed using Bi^+ ions with 25 keV ion energy.

All current density-voltage (*J-V*) characteristics of the CIGS solar cell devices were measured under standard test conditions (1000 W m^{-2}, 25 ℃, AM1.5G illumination) with the help of a solar simulator at Empa. External quantum efficiency (EQE) of solar cells was used to correct the spectral mismatch of the solar simulator. EQE system combines a lock-in amplifier, a chopped white light source, and a dual grating monochromator at Empa. The beam size was adjusted to the illumination area was smaller than the device area. A certified monocrystalline Si solar cell from Fraunhofer ISE was used as the reference cell for both *J-V* and EQE system.

3.3 Results and discussion

3.3.1 Structural morphology and individual evaporation rate optimisation of Cu, Ga and In separate layers deposited on Mo at room temperature

The surface and cross-section of Cu, Ga and In films were investigated by SEM as shown in Fig. 3.2. These films were grown with similar evaporation rates as used in the three-stage process at room temperature.

A comparison of micrographs of the separate layers of Cu, Ga and In was shown in the Fig. 3.2. The Cu layer was evaporated at 1210˚C on the SLG at room temperature, which shows a very condensed surface morphology (Fig. 3.2A). It is very hard to detect the size of the grains of this Cu layer with the SEM. As compared to Cu layer, Ga particles evaporated at 940˚C tends to form large sphere shaped islands on the room temperature substrates as shown in Fig. 3.2B. The possible reason for this is the low melting point of Ga. When high energetic Ga atoms from high temperature source reach the different locations of the substrate, they would form a number of nucleation centres on the cold surface of the glass. However, the residual heat transferred from Ga atom to the cold substrate could raise the substrate temperature, which would keep the Ga in a liquid phase resulting in coalescence of the nucleation centres to form of a liquid drop. Then the non-uniform distribution of Ga atoms would create a pattern of Ga particles gathered into different size of small and giant spheres as shown in Fig. 3.2B. The formation mechanism of the In layer at room temperature SLG was assumed to combine some parts of the Cu and Ga deposition routines. In Fig. 3.2C, there are some small In spheres at the bottom of the In layer and a thick top In layer with some micron-sized line cracks. The growth of this structure starts from evaporating of In at 900˚C to condense on the cold substrate. More energetic In particles would heat up to the substrate and form a In layer in liquid phase. After deposition, the In film starts to solidify and thermal non-uniformity would create a thermal stress, which leads to form the In layer with the visible cracks.

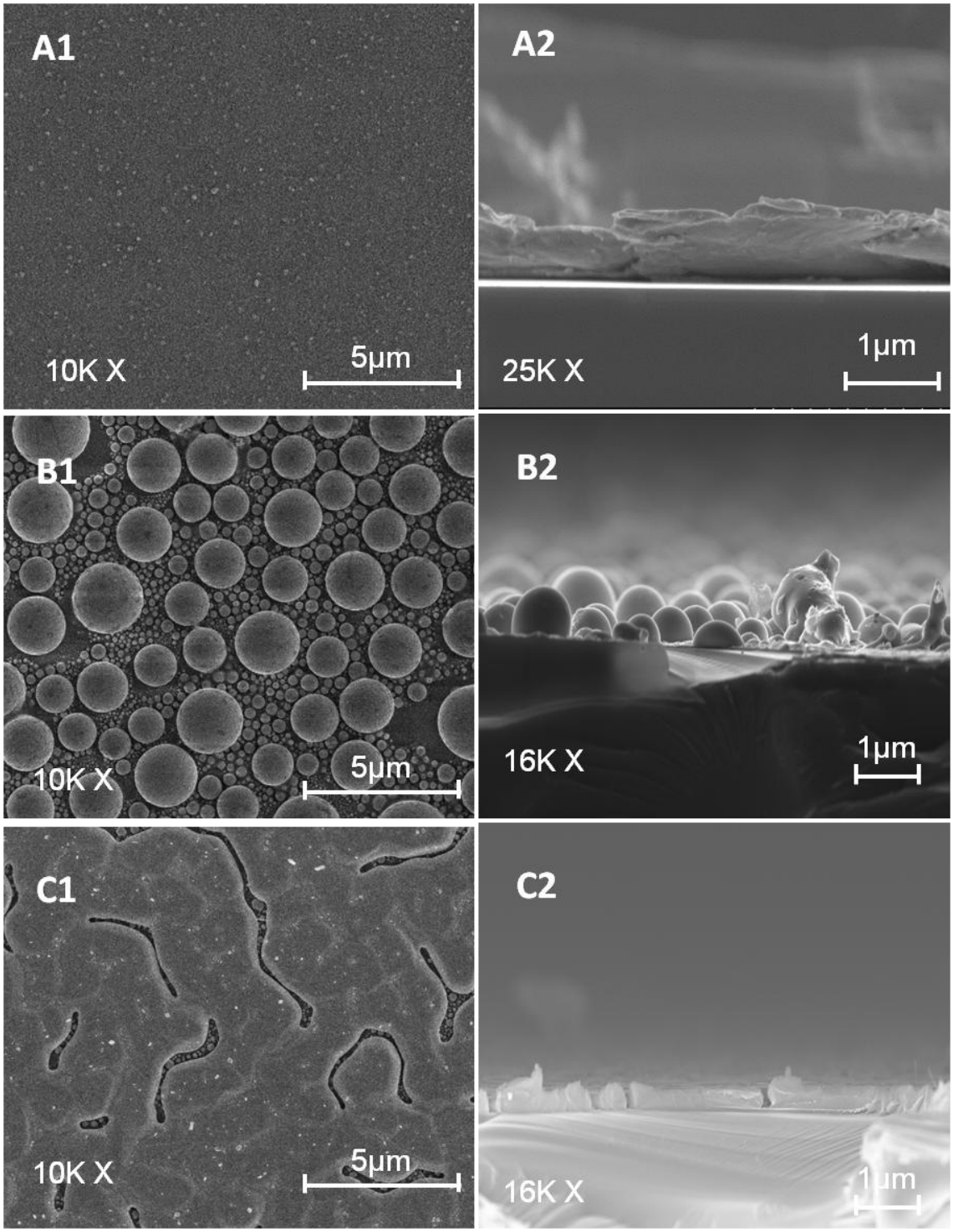

Figure 3.2: *SEM surfaces and cross-sections of the Cu (A), Ga (B) and In (C) single layers grown on SLG at room temperature. These layers deposited at similar running conditions of the effusion cells for the three-stage process. For Cu (A), a uniform and condensed film was formed. For Ga (B), a layer of big and small drop-shape spheres aggregated on the substrate. For In (C), an In layer was formed with big cracks.*

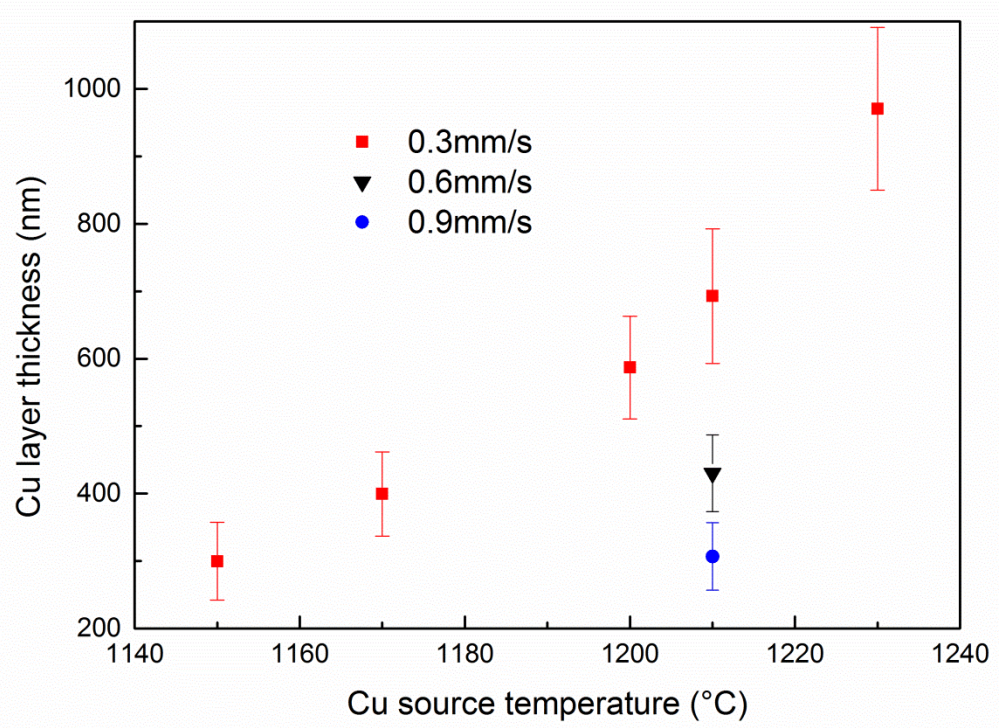

Figure 3.3: *The variation of Cu layer thickness by changing the Cu source temperatures and substrate holder traversal speeds of 0.3, 0.6 and 0.9 mm/s. The error margin was also indicated in the graph.*

To calibrate the deposition rate of the metal layers, several depositions of the Cu layer were carried out at different source temperatures and traversal speeds of the substrate holder assembly. The thickness of the layer was measured using a Dektak profilometer on various locations of the substrates. The evaporation rate was very sensitive to the source temperature and it can be doubled as the source temperature increased by only 50 ℃. This calibration was used for fine tuning the evaporation rate in the three-stage process. However, the error margins are quite high as plotted on the Fig. 3.3. These errors were caused by the non-uniformity of the thickness distribution estimated for Cu layer on the room temperature substrates. Due to the layer softness of In and Ga, the thickness calibration was mainly based on the computational calculations as described in Chapter 2, which was validated by the SEM measurements.

3.3.2 Growth of the CuGaIn stack layers on Mo at room temperature and post selenisation (Process A)

3.3.2.1 Material characterisation

The morphology and the microstructure of CIG precursors and selenised CIGS layers were compared in Fig. 3.4. Two types of CIG precursors were prepared on top of Mo coated SLG at room temperature using the inline system. The first precursor (Fig. 3.4A)

was grown from Cu layer and then finished with mixed Ga and In layer. This precursor showed relatively large grains and some voids between these grains. The second precursor (Fig. 3.4B) was grown in the opposite sequence as Cu layer on top of mixed Ga and In layer. On the surface of this film, very small grains aggregate in the form of some big islands. The size of these islands is comparable with the large grains in the first precursor. Deep valleys are visible between the islands.

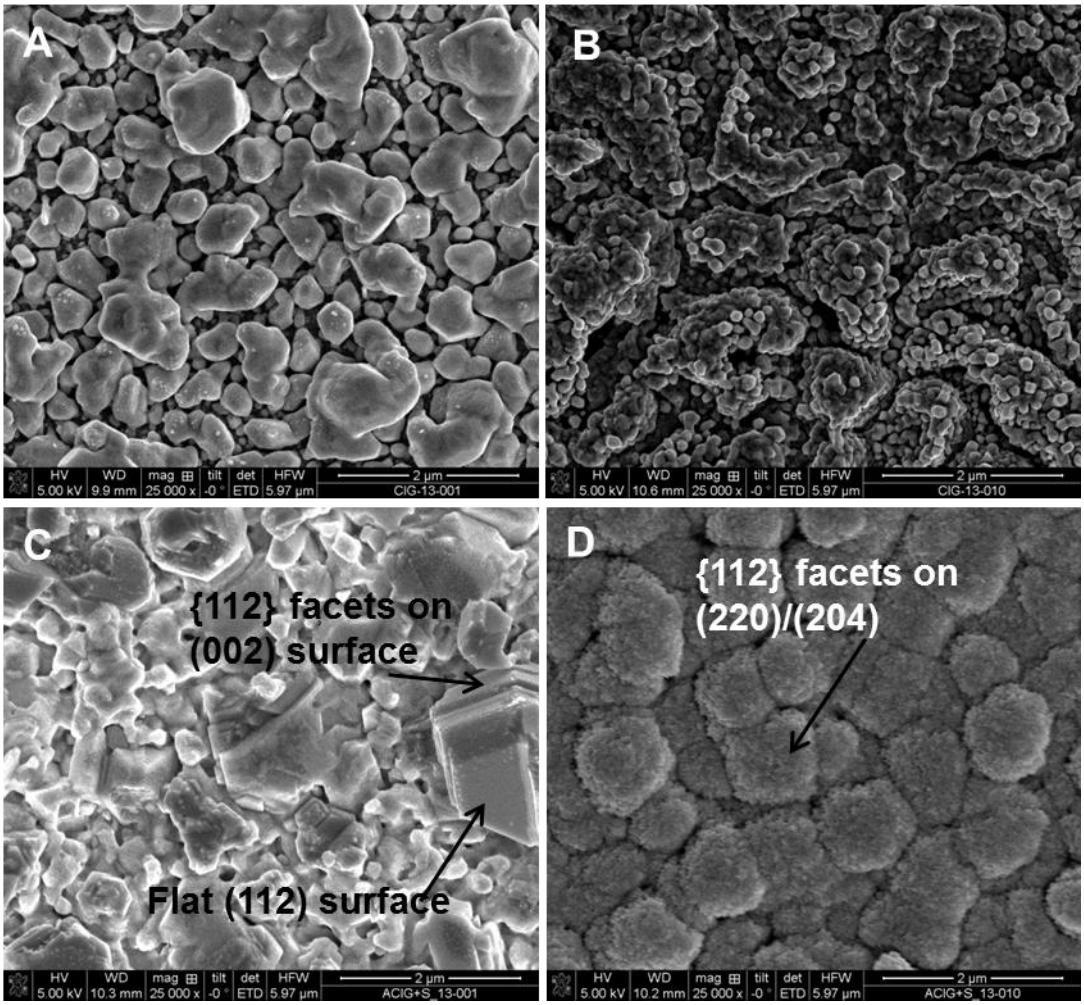

Figure 3.4: *SEM images of CuGaIn stacked layers grown under two sequences and their selenised CIGS films: (A) Cu underneath GaIn layer and (C) its selenised CIGS film; (B) Cu on top of GaIn layer and (D) its selenised film.*

The two bottom SEM images in the Fig. 3.4 describe the surface morphologies of two selenised metal precursors. The left hand side one (Fig. 3.4C) shows the CIGS film grown from CIG precursor with Cu underneath GaIn layer. The polycrystalline nature of the layer with the grain size up to one micron is clearly shown. (112) and (002) textures of the grain orientation are presented in this film. {112} facets are found and it is known as the most stable surface of the CIGS grains [3.20]. The second selenised CIG precursor is shown on the right hand side image (Fig. 3.4D). The whole layer is

covered by {112} facets on (220)/(204)-textured surface. This type of surface was found in the CIGS film prepared by epitaxial growth [3.20, 3.21], three-stage evaporation [3.22], sputtering and RTP selenisation [3.22] processes. The (220)/(204) notation is commonly used for the peaks obtained from the overlapping (220) and (204) textures in the XRD measurements. The different texture formation of the CIGS may be due to their precursor structures. The first precursor with a Cu-poor surface tends to form (112) and {112} facets dominated surface. The CIGS films grown from the second precursor with a Cu-rich surface present a (220)/(204) and {112} pronounced surface.

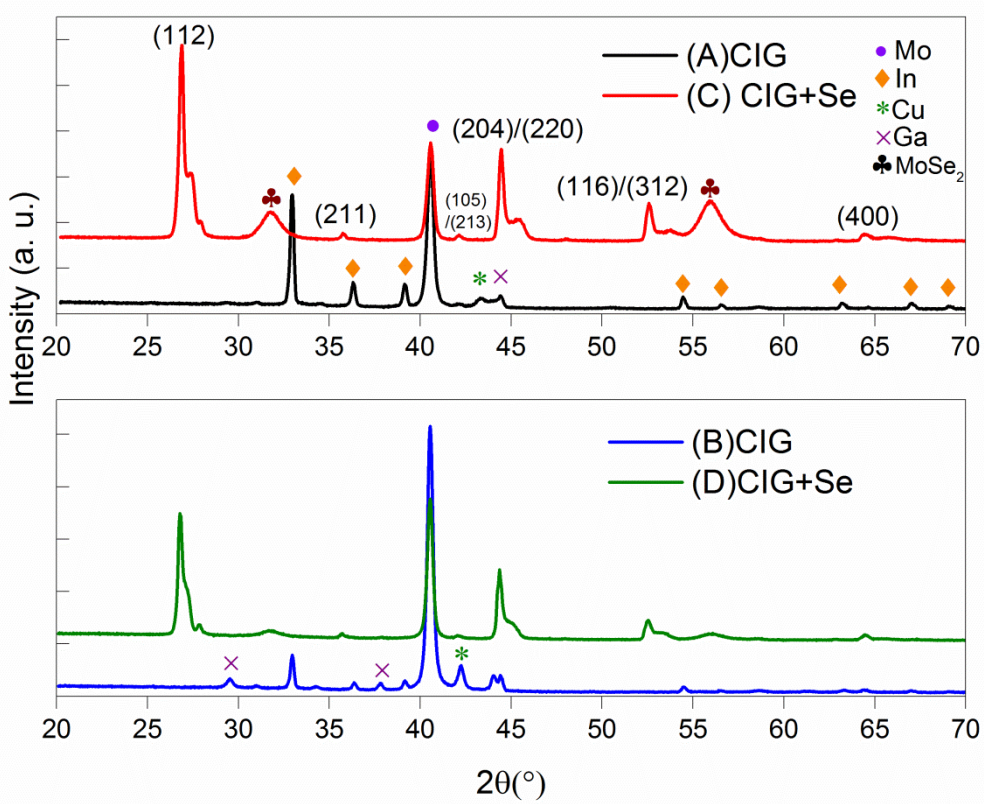

Figure 3.5: *The XRD patterns of CuGaIn stacked layers grown under two sequences and their selenised CIGS films: (A) Cu underneath GaIn layer and (C) its selenised CIGS film; (B) Cu on top of GaIn layer and (D) its selenised film.*

The XRD patterns in Fig. 3.5 were used to compare the phase formation of two metal precursors and their selenised CIGS films. All the detected peaks were evaluated to differentiate the desired CIGS phases and some impurity phases. For the first precursor (Fig. 3.5A), In (JCPDS 5-642), Ga (JCPDS 01-089-2884) and Cu (JCPDS 4-836) are identified. There are no detectable oxide phases appearing in the XRD pattern, which are beneficial for making efficient solar cell devices. Because the metal oxides such as Ga_2O_3 and In_2O_3 are very stable and resistive binary impurity phases, they can create

shunt paths in the final devices. A similar pattern in the Fig. 3.5B for the second precursor is shown, but another two Ga (JCPDS 5-601) peaks and one Cu (JCPDS 4-836) peak are more visible in this measurement. For both selenised precursor films, all the diffractograms (Fig. 3.5C and D) show Cu(In,Ga)Se_2 (JCPDS 35-1102) peaks without any detectable oxide phases. The intensity ratio between the two main CIGS peaks of (112)/(204/220) are 1.97 and 1.76 for selenised CIGS samples respectively. These values may indicate more (220)/(204) phases formed through the seleniseation of second precursor configuration. After selenisation of these CIG precursors, a higher $MoSe_2$ peak from selenised GaIn on top of Cu film rather than the one from the other CIG configured film. This pronounced additional $MoSe_2$ (JCPDS 29-914) layer may lead to a slightly worse device performance.

The GGI ratios of CIGS films grown from two metal precursors were obtained by XRF measurement are 0.26 and 0.24. The XRD patterns of the CIGS (220)/(204) peak for two-configuration precursors were used to investigate the incorporation of Ga into CIS crystals. The increased Ga content leads to a smaller lattice constant and thus a higher diffraction angle [3.9, 3.23]. For both CIGS spectra (Fig. 3.6), a sharp peak at a low diffraction angle and a broad shoulder towards higher diffraction angle mean a highly graded Ga profile in a wide region of films. The peak position of the CIGS grown from the first precursor (Fig. 3.6A) appears at a higher diffraction angle than the CIGS grown from the second precursor (Fig. 3.6B) indicates the CIGS grown from the first precursor with a higher Ga content. A shoulder towards higher diffraction angle with a very low intensity reveals a wide region of a pronounced Ga gradient. The depth profiling (Fig. 3.7) from SIMS was used to obtain the actual Ga grading profile. It shows a dramatic increase of Ga gradient from the film surface to the bottom.

As shown in the Fig. 3.7, an increasing GGI ratio towards the back contact would result in a highly graded band gap. In the band structure, the increasing Ga content leads to an increasing conduction band minimum, while the valence band maximum remains nearly same level [3.24]. This structure normally referred to a back-surface field (BSF), which can be designed to increase the collection efficiency of the minority carriers [3.25]. This BSF drives the photo-generated electrons towards the depletion region in the conduction band. This directly increases the possibility of the electron collection before they can recombine, and it also reduces the diffusion of electrons to the back contact to recombine.

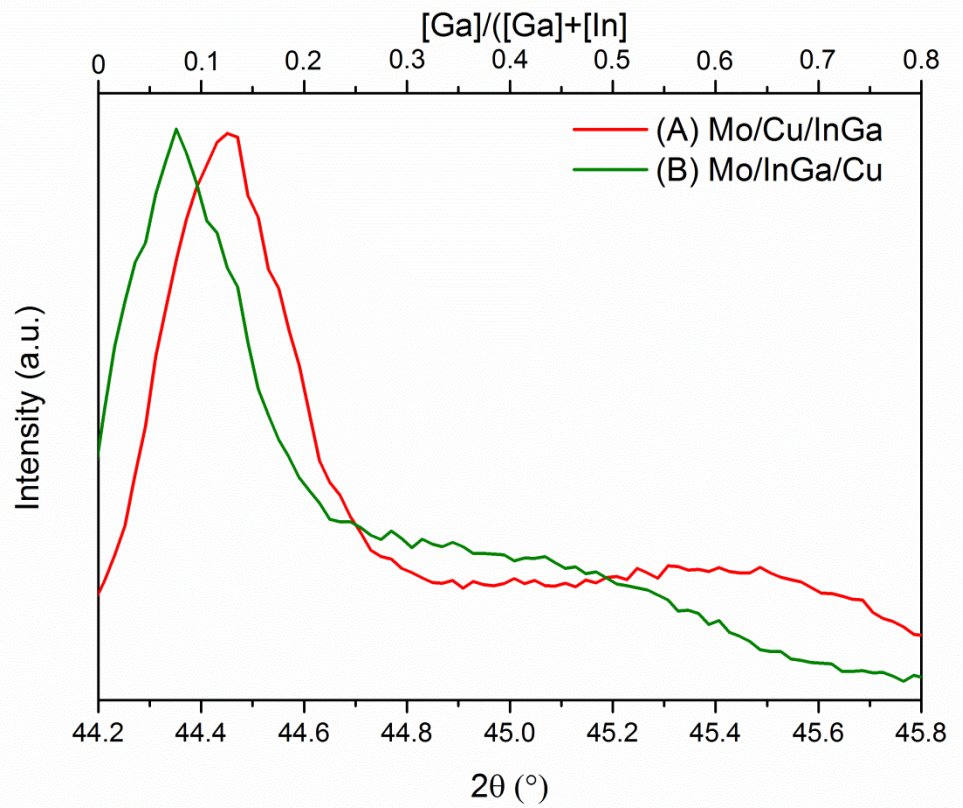

Figure 3.6: *Corresponding XRD spectra of the (220)/(204) peaks obtained from the selenised metal precursors: (A) CIGS grown from Cu underneath GaIn layer and (B) CIGS grown from Cu on top of GaIn layer.*

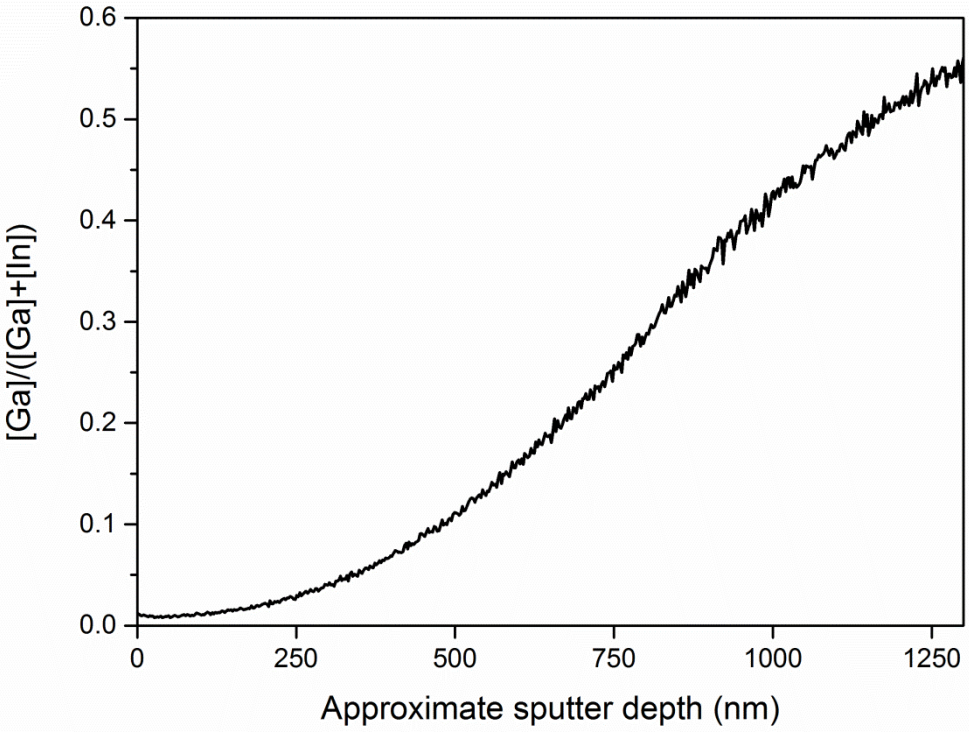

Figure 3.7: *A depth profile of the CIGS sample from Cu on top of GaIn layer showing the relative Ga content along the CIGS film depth as assessed by SIMS measurements.*

3.3.2.2 Solar cell devices and their photovoltaic properties

These two types of selenised CIGS films were used to fabricate CIGS solar cells in the standard solar cell structure described in the *Section 3.2.1*, but the top Ni/Al grid was not used here. As shown in the Fig. 3.8A and C, the CIGS solar cells made from the precursor with Cu underneath Ga/In layer and Cu on top of GaIn layer achieved 5% and 7.4% efficiencies respectively.

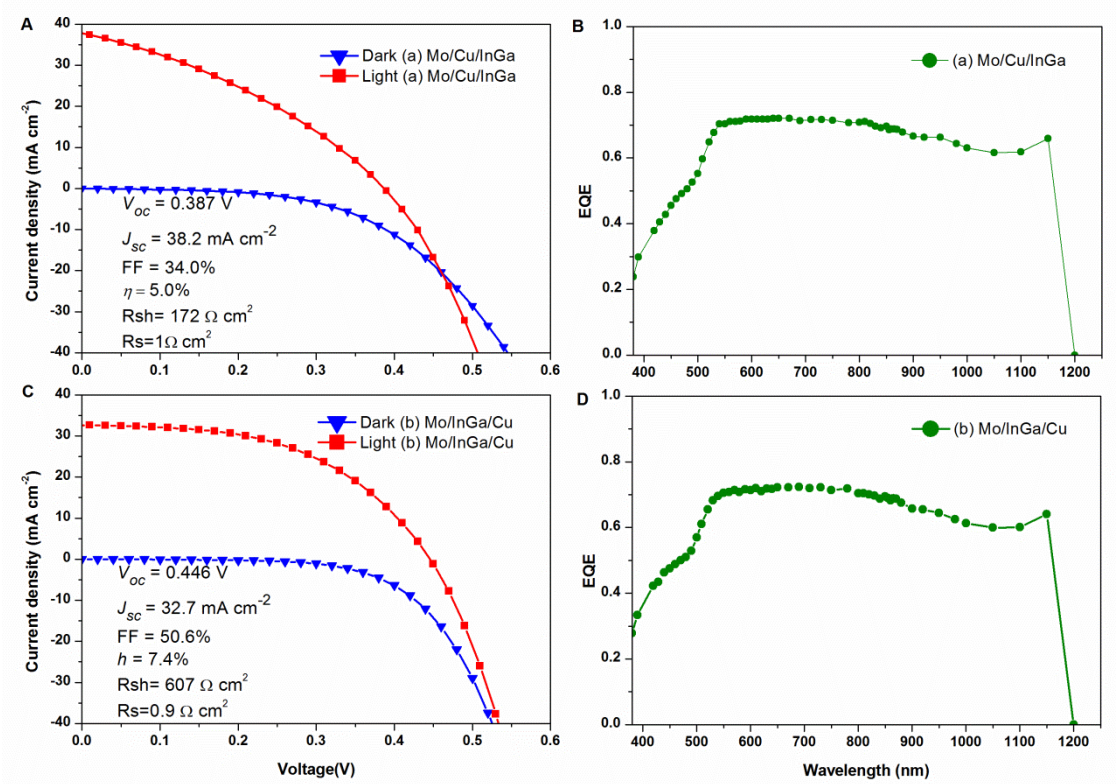

Figure 3.8: *J-V and EQE curves of CIGS solar cells deposited from two types of the CIG precursors: (A) J-V curve and (B) EQE curve for CIGS solar cells obtained from Cu underneath GaIn layer and (C) J-V curve and (D) EQE curve for CIGS solar cells obtained from Cu on top of GaIn layer.*

The very low V_{oc} for these CIGS devices as compared to those of the efficient devices reported in literature, could be associated with the low Ga incorporation and the high recombination losses associated with the defects in the CIGS layers grown in this study [3.5]. The CIGS solar cell grown with Cu on top of GaIn layer exhibited better V_{oc} than the one grown with the opposite configuration. However, the difference on V_{oc} is not in good agreement with the difference to the Ga content estimated from XRD and XRF (*Section 3.3.2.1*) for these two CIGS samples. The reason for the better V_{oc} of the CIGS solar cell grown with Cu on top of GaIn layer could be mainly due to less

recombination losses as compared to the other device. However, comparison of the EQE measured at different reverse bias condition is necessary to confirm that the losses are mainly electronic losses due to the recombination in the absorber layer [3.26]. The low FF for both CIGS solar cells may be due to the low shunt resistance. The voids between the grains (Fig. 3.4C and D) could lead to the pronounced shunt paths. The light-to-dark crossover (Fig. 3.8A) was observed for the CIGS solar cell grown with Cu underneath GaIn layer, which could be caused by photoconductive effects or a light-dependent electron barrier at the interface between the absorber and buffer layers [3.26].

The unusual sharp drops in the EQE curve at 1200 nm wavelength (due to limitation in the measured wavelength range) as shown in Fig. 3.8B and D, is different to the EQE curves for the CIGS solar cells in literature [3.5] and in *Section 3.3.3* and *3.3.4* of this chapter. This is possibly related to the lower minimum band gap, caused by the lower level of Ga-incorporation for both samples. The lower band gap could also be related to the slightly higher J_{sc} compared to the J_{sc} obtained with higher band gap CIGS films in *Section 3.3.3 and 3.3.4* of this chapter. This may be due to the lower band gap that would allow more low energy photons to be absorbed in the CIGS absorber layer.

3.3.3 Growth of the CIGS layers on Mo at the constant temperature – Simplified three-stage process towards the low cost approach (Process B)

3.3.3.1 Material characterisation

The cross-section and surface morphologies of the CIGS layers grown at the constant substrate temperature with different Cu composition (as referred to CGI ratio) of 0.80 and 0.89 were investigated with the help of SEM as shown in the Fig. 3.9. The thicknesses of the CIGS layer for the sample with CGI of 0.80 and 0.89 are around 1.6 μm and 1.0 μm, respectively (Fig. 3.9 A2 and B2). A comparison of the micrographs of the CIGS layers obtained for these two Cu contents films shows a significant improvement in the grain size and their compactness in CIGS films with CGI = 0.89. When the CGI ratio reduced to 0.80, the CIGS layer (Fig. 3.9A1) formed with a surface roughness of around 50 nm. There are some big grains (~ 1μm) formed at the bottom part of the CIGS layer and some voids located in the middle and on the surface of the layer (Fig. 3.9A2). The origin of these voids or crevices was discussed in the published literature [3.27-3.29]. It was assumed some $Cu_{2-x}Se$ compounds formed in between and around the CIGS grains in the Cu-rich film growth regime. These extra Cu-rich $Cu_{2-x}Se$

can be converted into CIGS in the third stage of the CIGS growth where there is lack of the direct Cu source [3.28].

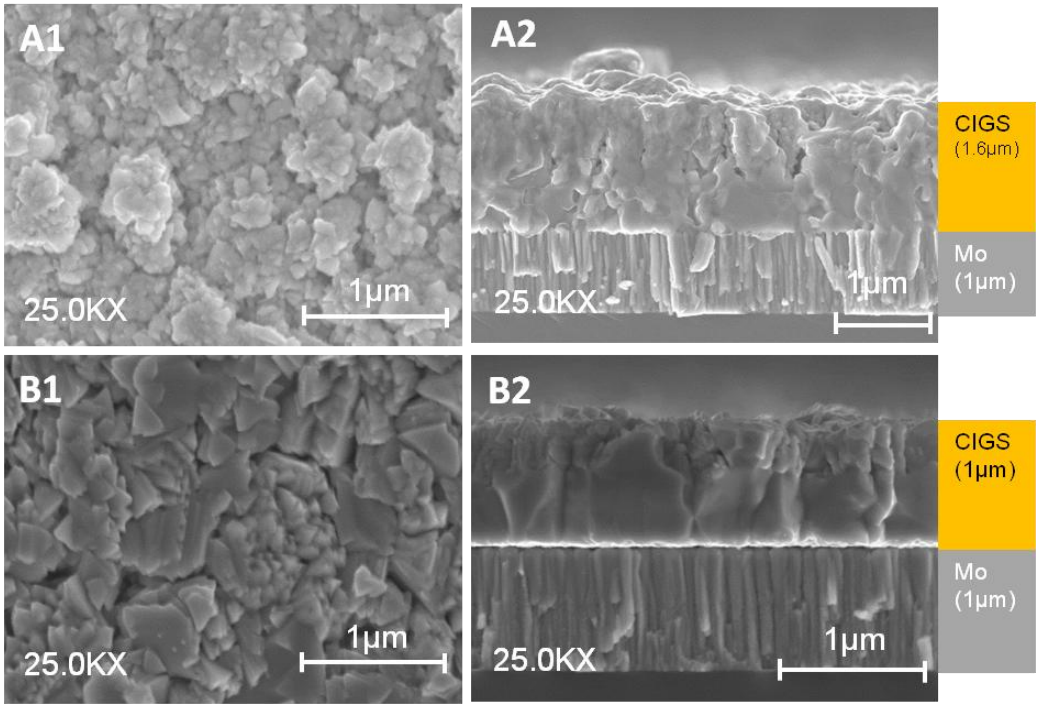

Figure 3.9: *SEM (A1) surface and (A2) cross-section micrographs of the CIGS absorber grown with CGI = 0.80 and SEM (B1) surface and (B2) cross-section micrographs of CIGS absorber grown with CGI = 0.89. The variation in the composition was changed by adjusting the metal source temperature.*

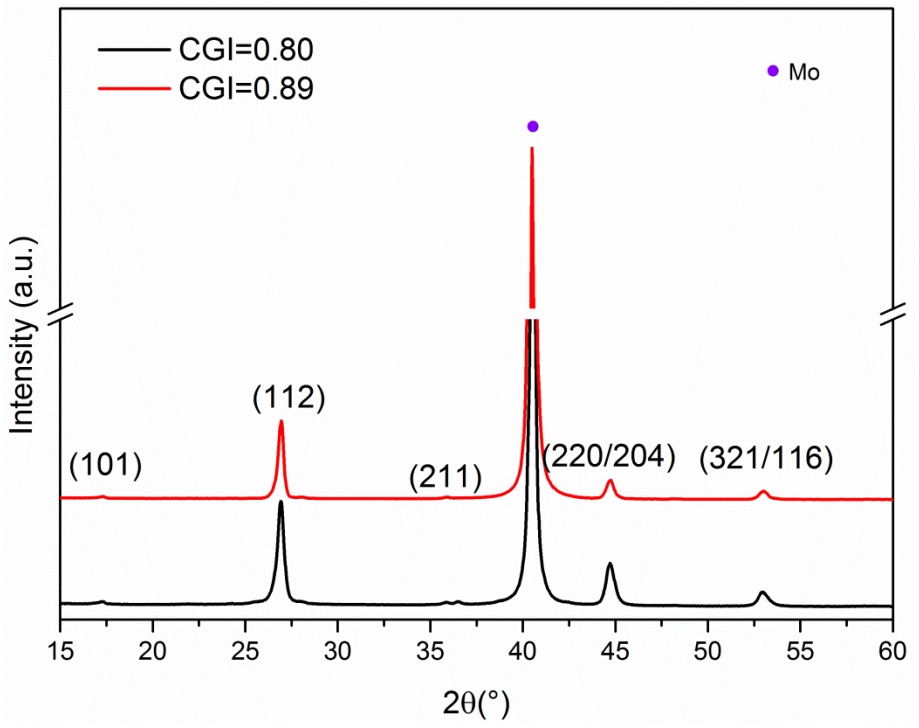

Figure 3.10: *XRD patterns of comparison of CIGS absorber grown with the different CGI ratios: (A) 0.80 and (B) 0.89.*

The SEM micrographs (Fig. 3.9B1) of the CIGS film with a CGI = 0.89 show the improved surface uniformity compared to the CIGS film with the lower Cu content. More big grains appear on the surface of the film and less voids formed on the cross-section (Fig. 3.9B2). This may be because more Cu source available can form the bigger and compact grains of CIGS in the third stage and they can distribute evenly into the grain structures [3.28]. The grain growth appears to be developing from the bottom end of the substrate whilst the growth towards the surface of the film appears to be composed of a 300 nm region of small grains, which may increase the surface roughness.

The XRD patterns of CIGS absorbers grown with different Cu contents of 0.80 and 0.89 were plotted in the Fig. 3.10 respectively. The main $Cu(In,Ga)Se_2$ (JCPDS 35-1102) peaks of (112) and (220/204) were obtained for these two samples. From XRF measurements, two absorbers have a similar Ga content of 0.24. A closer look in Fig. 3.11 at the (112) and (220/204) peaks gives the insight into the gallium incorporation and crystal quality. Comparing these two samples with the similar Ga content, it became quite apparent that the smaller full width at half maximum (FWHM) were obtained for the CIGS film with Cu content of 0.89.

The (112)/(220/204) peak intensity ratios for two samples with CGI of 0.80 and 0.89 are 2.35 and 3.91, respectively. The effect of the peak intensity ratio between (112) and (220/204) on the overall cell performance is still unclear, in terms of the dominance of one with the other. Both of these textures dominated CIGS films have been made into high efficiency devices [3.8]. In the three-stage process, [Se]/([In] + [Ga]) ratio during the first stage deposition of $(In,Ga)_2Se_3$ has a significant influence on the texture of the finished absorber [3.30]. The substrate temperature during the first stage could also influence the final texture of the CIGS film. The Se sticking coefficient decreases (Se-poor) with increase in substrate temperature [3.30]. Both of the CIGS films in this section grown at the constant temperature of 500 ℃ through three stages exhibit (112) dominant texture, which may be due to the high growth temperature at the first stage and hence the slightly Se-poor $(In,Ga)Se_x$ phases formed.

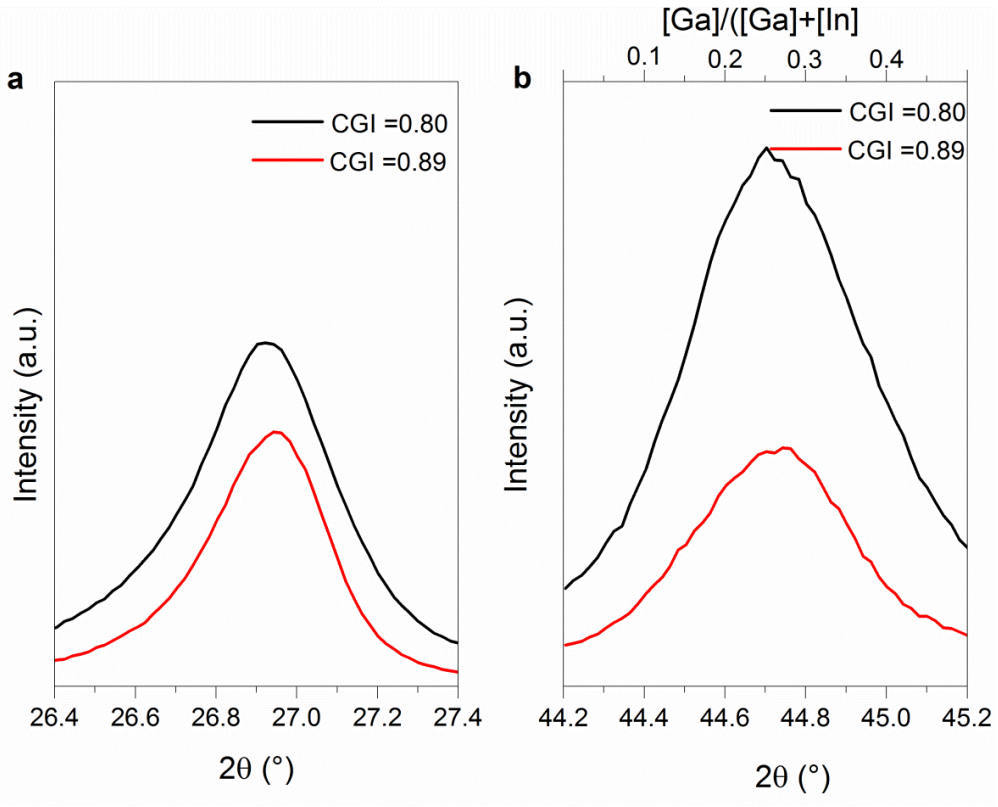

Figure 3.11: *XRD patterns of the CIGS (112) (a) and (220/204) (b) peaks for absorbers grown with the different CGI ratios. The smaller FWHM, which reflects a homogenous Ga incorporation and higher crystal quality, was obtained for CGI = 0.89.*

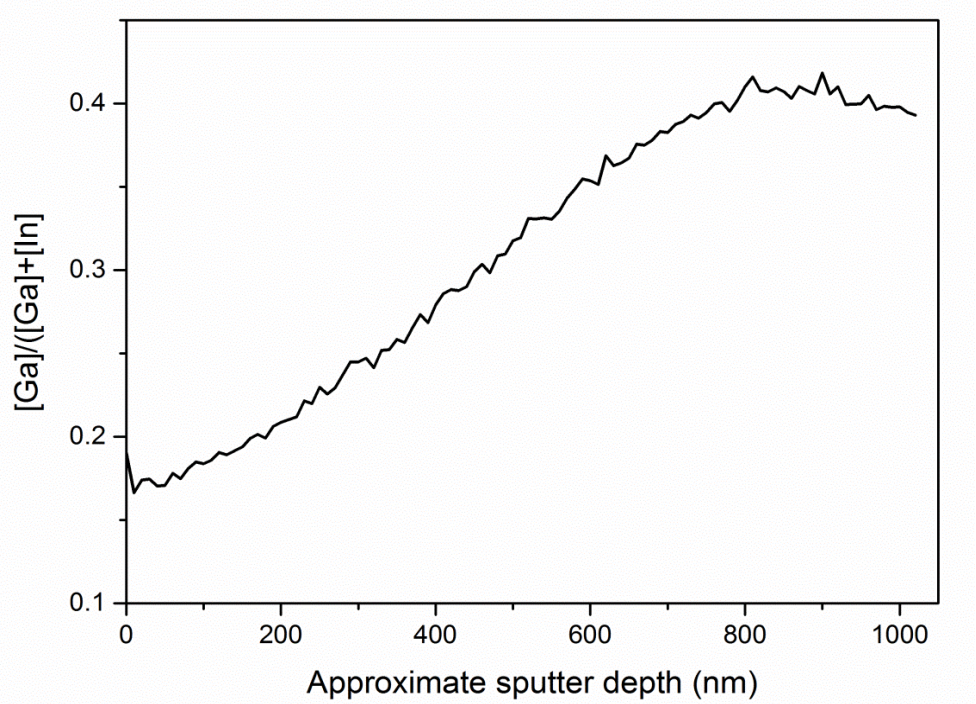

Figure 3.12: *Depth profiles of the CIGS sample grown at the constant substrate temperature with the CGI ratio of 0.89 showing a single Ga gradient along the CIGS film depth as assessed by SIMS measurements.*

The lateral distribution of the elemental compositional gradients of CIGS films was measured using SIMS. Fig. 3.12 depicts the Ga/III depth profiles with an average composition of GGI = 0.24. It shows a single Ga gradient with a strong increase towards the back contact. The surface composition is Ga-poor (Ga/III = 0.17), increases toward Ga/III = 0.4 at the back contact. This is quite common in the three-stage CIGS co-evaporation process and can be explained by the preferential out-diffusion of In relative to Ga in the CIGS alloy, and hence a CIS preferred formation over CGS [3.31]. This would create a spontaneous Ga gradient towards the back contact.

3.3.3.2 Solar cell devices and their photovoltaic properties

Solar cells were fabricated with CIGS absorbers grown with different Cu contents at the constant substrate temperature (500 ℃). Among the CIGS solar cells fabricated in this section, the champion devices exhibited the efficiencies of 3.5% and 7.7% with CGI ratio of 0.80 and 0.89, respectively as shown in the Fig. 3.13A and C.

All the solar cell parameters V_{oc}, J_{sc}, FF and η of the device with CGI = 0.89 are higher than the ones with CGI = 0.80. The main difference in the efficiencies is due to the improved V_{oc} along with the nearly doubled J_{sc} for the CIGS device with CGI = 0.89. The lower FF for the CIGS device with CGI = 0.80 as compared to the one with CGI = 0.89 could be due to the voids and crevices (as shown in Fig 3.9) in the CIGS absorber layer that can lead to lower values of shunt resistance. In this respect, a larger-grained and denser film of the absorber with CGI = 0.89 might contribute to the efficiency improvement. However, the light-to-dark crossover (Fig. 3.13A) was observed for the CIGS film grown with CGI = 0.89. Apart from the reasons for the crossover in *Section 3.3.2.2*, the origin of the crossover here could also be the reduced Ga grading towards the back contact, which may lead to a reverse photocurrent in the CIGS solar cell [3.32].

Comparing the EQE curves of the both devices, it is apparent that the absorbers with CGI = 0.89 exhibit a higher spectral response in the measured wavelength region resulting in a gain in short circuit current density J_{sc}. The band gap E_g of the absorber can be calculated from the EQE curve. The absorption coefficient is proportional to $\sqrt{h\nu - E_g}$ close to the absorption edge for a direct band gap semiconductor. Hence, the E_g can be extracted from a linear extrapolation of $(EQE \cdot h\nu)^2$ against photon energy $h\nu$. In practice, the calculated value of E_g from EQE is regarded as the minimum band gap of the absorber in a graded band gap. As shown in the inset graphs in Fig. 3.13B

and D, the minimum band gap of these two absorbers is 1.13 eV, which can be derived from the absorption onset. These values are in good agreement with the estimated average band gap values (1.14 eV) from XRD and XRF measurements (*Section 3.3.3.1*) reflected to the Ga incorporated into the absorber layer. The apparent lower EQE values for the sample with CGI of 0.80 at 400-500 nm region compared to sample with CGI of 0.89 may be caused by thicker CdS layer leading to more parasitic losses. The pronounced losses in the EQE curve at 500-900 nm region especially for sample with CGI of 0.80 (Fig. 3.13B) are possibly due to the high surface recombination and low diffusion length of the charge carriers which reduces the current collection [3.26]. The significant losses especially at the wavelength larger than 900 nm are maybe due to the thin absorber layers leading to an incomplete absorption of the absorber [3.26]. Comparable EQE values at these longer wavelength range for the thicker film with CGI of 0.80 as compared to the film with CGI of 0.89 (Fig. 3.9A2 and B2) could be suggested more recombination losses in the bulk of the lower CGI sample.

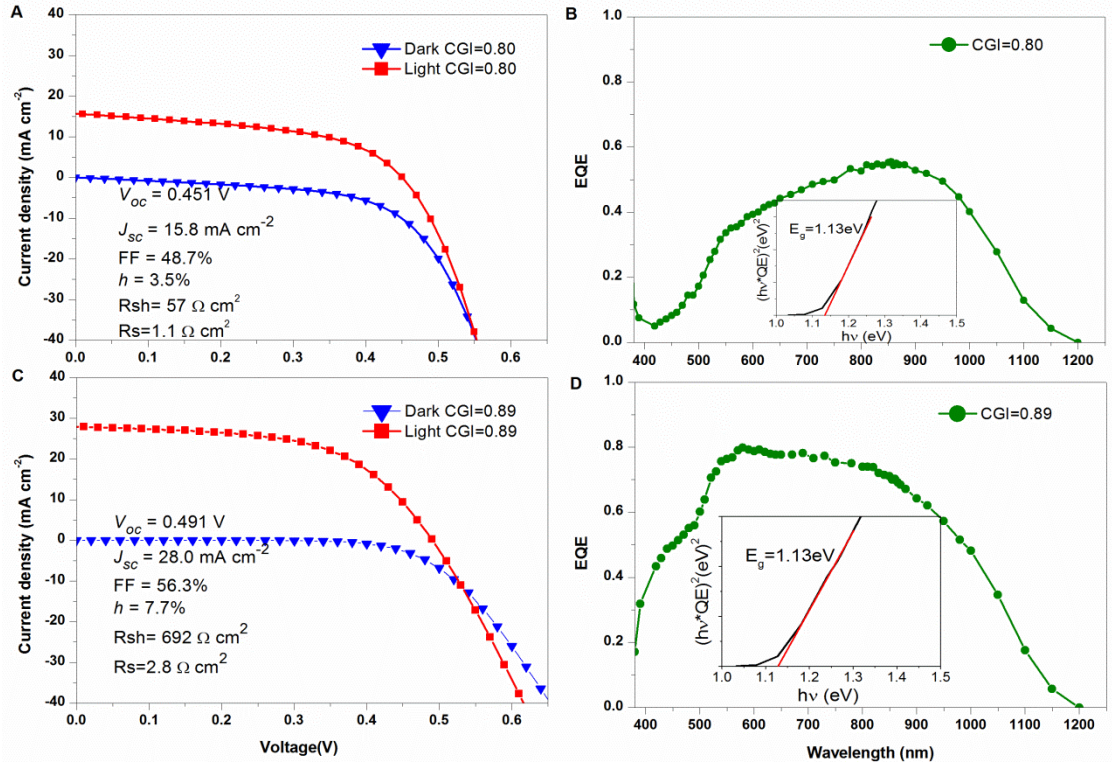

Figure 3.13: *J-V and EQE curves of CIGS solar cells grown with the different CGI ratios at the constant substrate temperature: (A) J-V curve and (B) EQE curve for CIGS solar cells with CGI = 0.80 and (C) J-V curve and (D) EQE curve for CIGS solar cells with CGI = 0.89.*

3.3.4 Growth of the CIGS layers on Mo using a three-stage process at varied substrate temperatures (Process C)

3.3.4.1 Material characterisation

3.3.4.1.1 Variations on the Cu content

The CIGS films with the varied CGI ratios were examined first in this series of experiments using the standard three-stage process. These CIGS films were grown at the CGI ratios of 0.59, 0.68 and 0.79. The Ga content of three selected samples was 0.24 as measured by XRF.

The structure and morphology of the as-grown CIGS films were investigated with SEM as shown in the Fig. 3.14. First of all, three films (Fig. 3.14A1, B1 and C1) all consist of very small grains with diameters well below 200 nm. This is reflected well in the cross-section images (Fig. 3.14A2, B2 and C2). The upper crust of the film shows the small grain accumulation resulting in a rough surface about 100 nm deep. With the growth performed for different CGI ratios, the extremely Cu-poor growth regime (CGI = 0.59) clearly consists of the small grains in the whole layer thickness of about 1.0 μm (Fig. 3.14A1 and A2), suggesting the fact that crystallinity was not improved for this condition and films appears more or less filled with small grains. For the CGI ratios of 0.68 (Fig. 3.14B2), the thickness of this layer is around 1.1μm and there is a marked increase in the compactness of the films with a comparatively bigger grains appearing underneath the surface. In the case of CGI ratio of 0.79 (Fig. 3.14C2), the thickness of this layer is around 1μm and a more compacted film accompanied with much bigger grains started to form from bottom of the film. The rough layer regions of small grains of the samples with CGI = 0.68 and CGI = 0.79 are ~300 nm and ~150 nm respectively. This may be a critical structural parameter for making an efficient solar cell device. A further feature correlating with the surface roughness is the appearance of the micron-sized voids and crevices. A crack from the top surface to the bottom of the layer observed (Fig. 3.14C2), which may form a shunt path to reduce the cell performance.

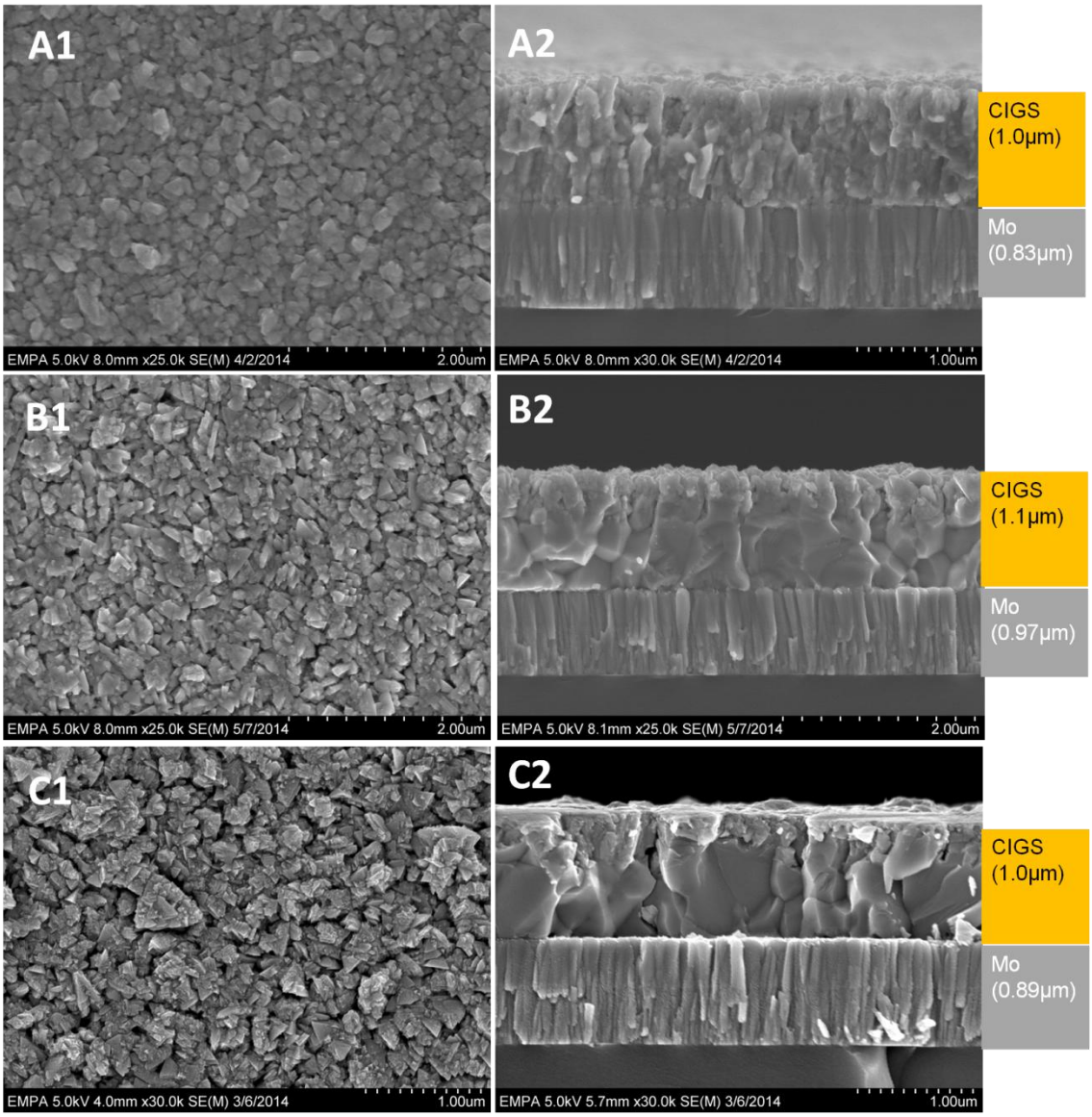

Figure 3.14: *SEM (A1) surface and (A2) cross-section micrographs of the CIGS absorber grown with CGI = 0.59, SEM (B1) surface and (B2) cross-section micrographs of the CIGS absorber grown with CGI = 0.68 and SEM (C1) surface and (C2) cross-section micrographs of the CIGS absorber grown with CGI = 0.79. The variation in the composition was changed by adjusting the metal source temperature.*

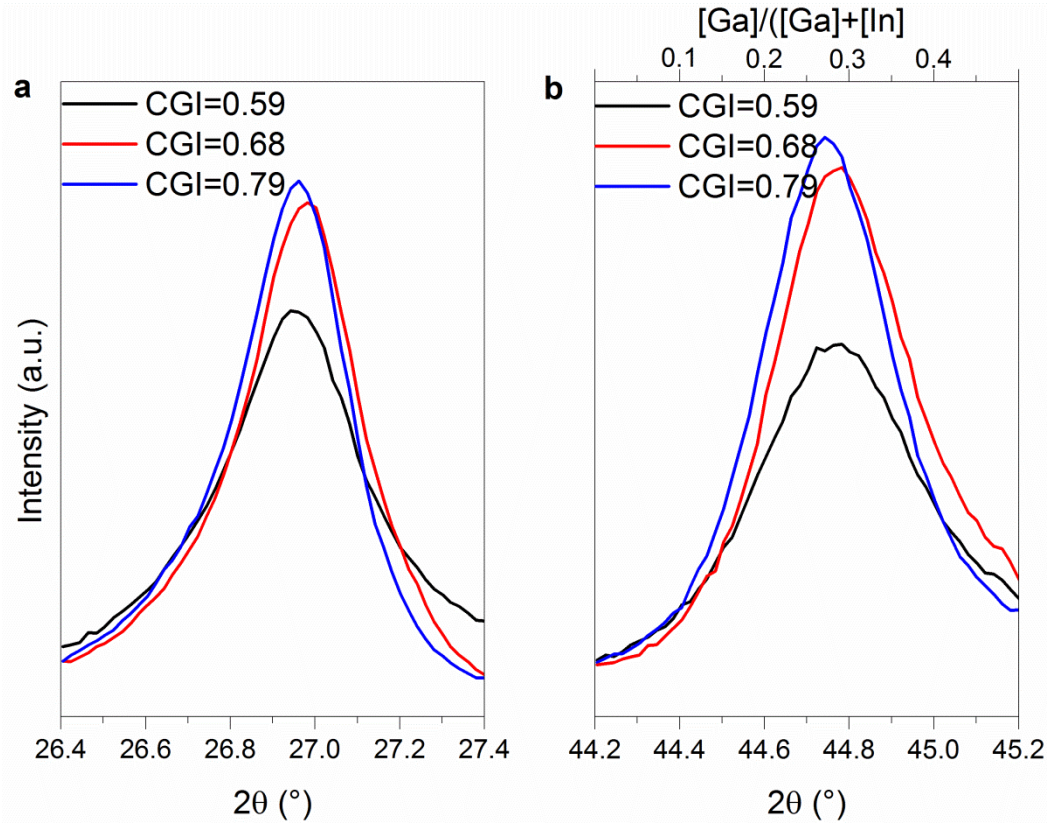

Figure 3.15: *XRD patterns of the CIGS (112) (a) and (220/204) (b) peaks for absorbers grown with different CGI ratios. The smallest FWHM, which reflects a homogenous Ga incorporation and higher crystal quality, was obtained for CGI = 0.79.*

A closer look on the (112) and (220)/(204) CIGS peaks (Fig. 3.15) was used to identify the Ga incorporation and crystal quality. Comparing three samples with the different Cu contents, the peaks of the sample with CGI = 0.79 show the smallest FWHM, which indicates the highest Ga incorporation. The sample with CGI = 0.68 is comparable but exhibits a slightly larger FWHM, whereas the sample with CGI = 0.59 appears a broadest FWHM. The largest FWHM of CGI = 0.59 can be correlated to lowest crystallinity of the film. The (112)/(220/204) ratios for three samples are 2.33, 2.00 and 1.99. As discussed in *Section 3.3.2*, the higher growth temperature in the first stage results in the Se-poor (In,Ga)Se_x compounds formation and hence a (112) dominated the final CIGS film.

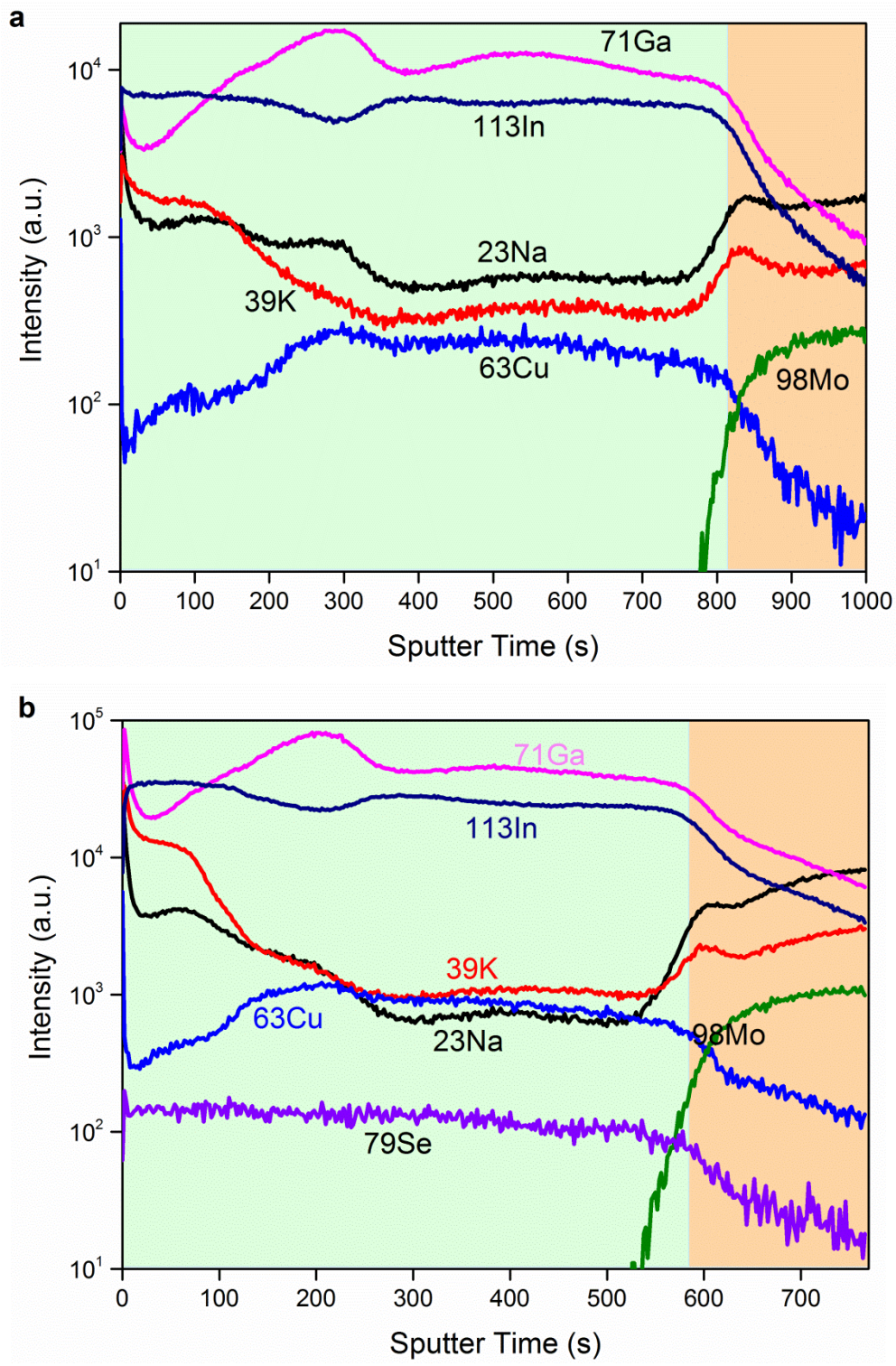

Figure 3.16: *Elemental depth profiling of the CIGS film grown with different CGI ratios: (a) 0.68 and (b) 0.79. SIMS profiles show all relevant elements from the CIGS absorber (green background) to the Mo back contact (orange background) obtained from the representative devices.*

SIMS profiles of the samples with the different CGI ratios (Fig. 3.16) reveal a relative higher count rate of Cu through the whole absorber layer of CGI = 0.79 compared to the sample with CGI = 0.68. The sputter time corresponds to the depth into the CIGS/Mo stack. The sputter rate for the sample with CGI = 0.68 is slower than the sample with CGI = 0.79, because those two samples have similar thicknesses as confirmed from the SEM images. For both samples, there is a clear drop at first 200s sputtering time region (surface region), which could indicate a Cu-poor composition at the surface. Apart from Cu, the count rates of In and Ga in the sample with CGI = 0.79 are also higher than the sample with CGI = 0.68. The count rate of Na remains almost in the same level in both samples due to the similar diffusion rate from the soda-lime glass.

3.3.4.1.2 Variations on the Ga content

The effects of the Cu content on the structural properties of the CIGS films were revealed in the previous section. The effects of the variation of the Ga content on the structural properties of the CIGS films are also performed and discussed as follows. Three GGI ratios of 0.19, 0.21 and 0.23 were grown intentionally to investigate the influence of the Ga content. The CGI ratios of three samples were kept at 0.78-0.80 as this ratio resulted in the better structural properties. The surface and cross-section morphologies of these films with the above GGI ratios are shown in the Fig. 3.17. The surface non-uniformity is the common feature for three of selected films. Some ~200 nm-sized voids or crevices were formed on all three films between the big and small grains at the surface. Some of these crevices extend to the bottom of the CIGS films. The possible origin of these crevices was assumed to be lack of direct Cu source in the third stage of the deposition [3.28] as discussed in *Section 3.3.2*. It also believed that the formation of these crevices is due to non-uniformly distributed thermal stress between the grains of CIGS. These crevices could be the source of the recombination centres at the grain boundaries leading to the shunt paths, and hence reducing the device performance of the solar cells.

From the closer view of the (112) and (220)/(204) peaks (Fig. 3.18), the sample with the GGI ratio of 0.24 has the smallest FMHW, which indicates the best crystal quality and the best Ga incorporation. The estimated Ga contents of three samples obtained from XRD are in good agreement with the XRF measurements as shown in Fig. 3.18b. There is an apparent right shift of the sample with GGI = 0.24 compared to the other two samples, indicating a lattice constant shift relating to a possible band gap increase. The

(112)/(220/204) intensity ratios for three samples are 2.36, 2.45 and 1.99. This also indicates the variation of the grain orientation of three samples.

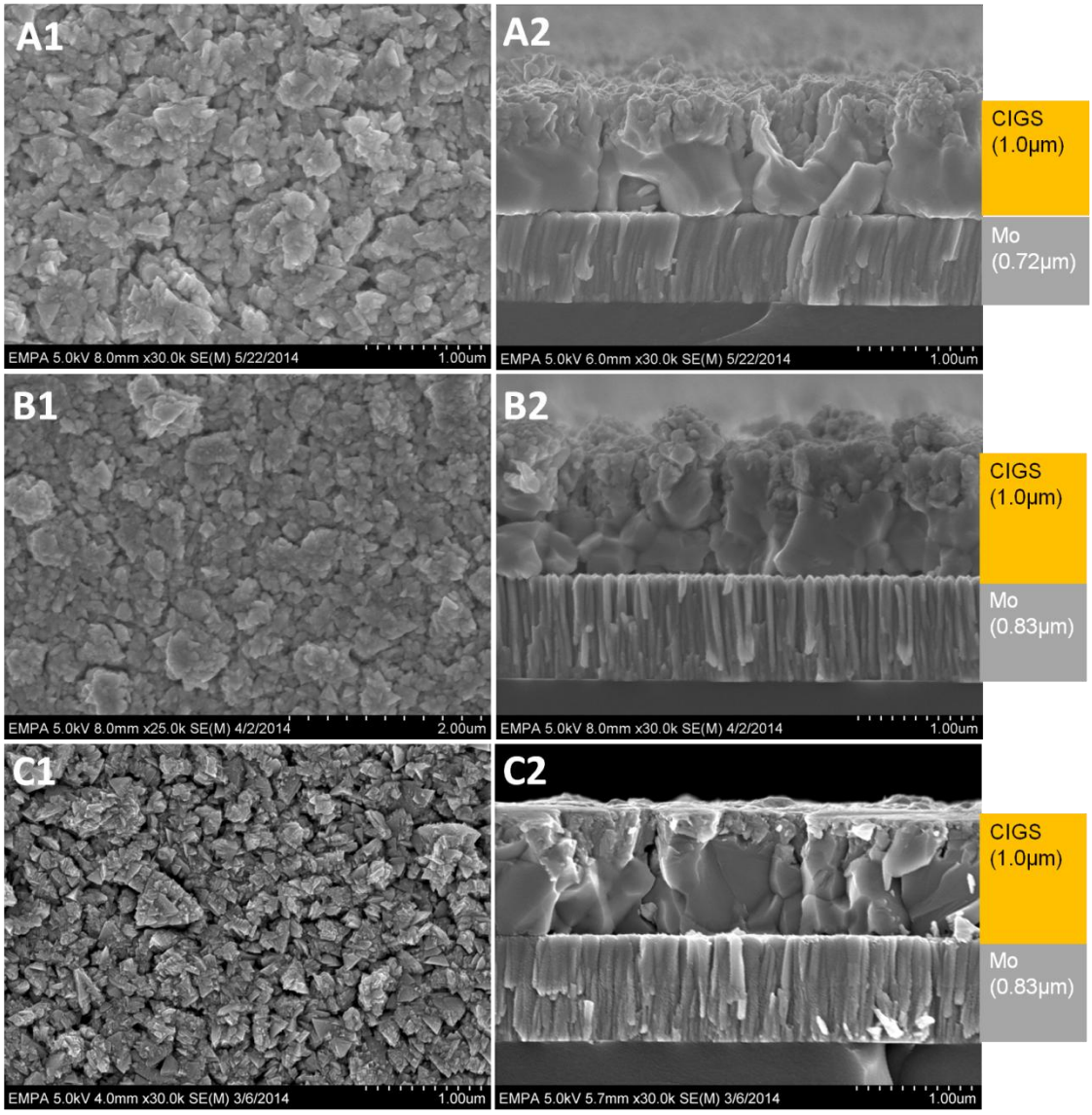

Figure 3.17: *SEM (A1) surface and (A2) cross-section micrographs of the CIGS absorber grown with GGI = 0.19, SEM (B1) surface and (B2) cross-section micrographs of the CIGS absorber grown with GGI = 0.21 and SEM (C1) surface and (C2) cross-section micrographs of the CIGS absorber grown with CGI = 0.24. The variation in the composition was changed by adjusting the metal source temperature.*

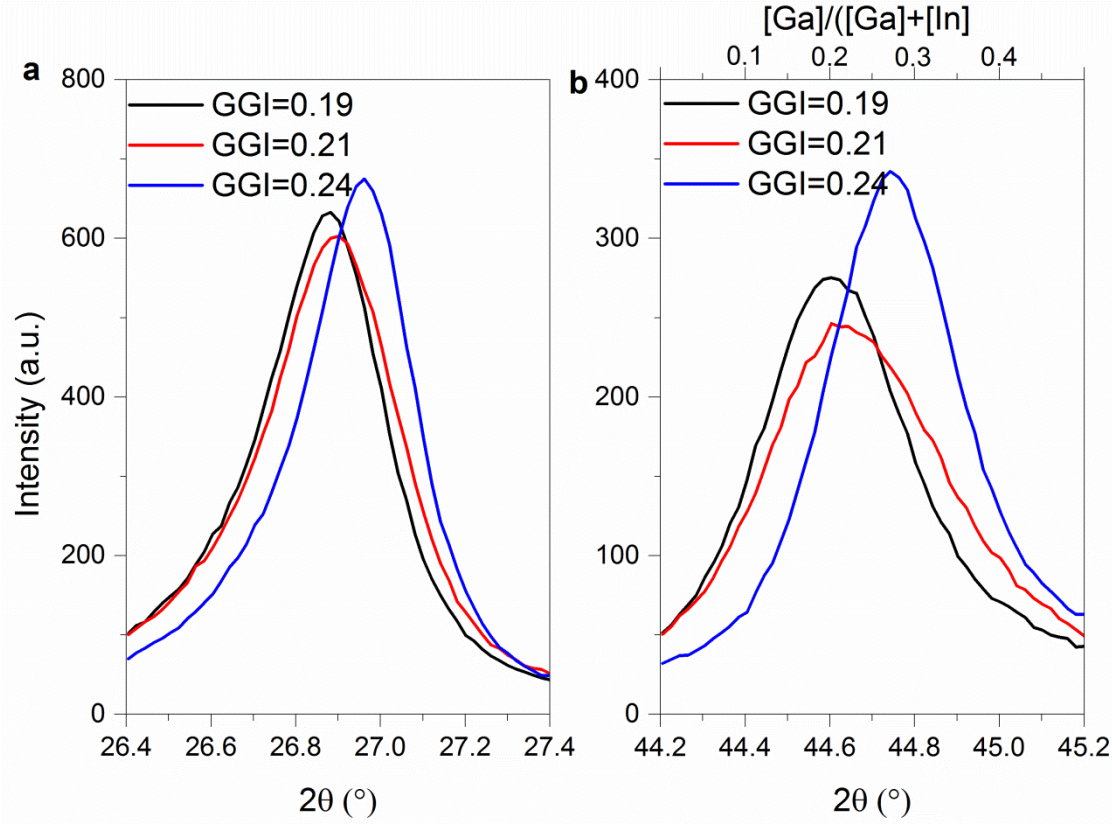

Figure 3.18: *XRD patterns of the CIGS (112) (a) and (220)/(204) (b) peaks for absorbers grown with the different GGI ratios. The smallest FWHM, which reflects a homogenous Ga incorporation and the higher crystal quality, was obtained for GGI = 0.24.*

To analyse the composition profiles, the CIGS layer with GGI = 0.24 was investigated using SIMS. The Ga profile of this sample was plotted in Fig. 3.19. The heights of the front, middle and back parts are labelled as Δx_{front}, Δx_{middle} and Δx_{back}. As compared to the high efficiency CIGS [3.9], the front Ga grading of this sample is much steeper and its trough appears in the first 100 nm. This dramatic change can be related to the rough surface in the SEM image (Fig. 3.17C). It shows a gradual increase of the Ga content through the middle of the absorber until 750 nm. The Ga content variation in the middle region results in a bigger grain and compacted layer (Fig. 3.17C). Finally, a small decrease of the Ga content appears at the back surface. There is no clear morphological change on the film can be correlated to this drop of Ga content. The total GGI value of this sample is lower than the ones fabricated into the high efficiency CIGS devices [3.5, 3.8, 3.11], and normally there is only one double-Ga-gradient in their CIGS absorber layers. A smoother Ga gradient would reduce the surface recombination and hence improve the efficiency [3.9].

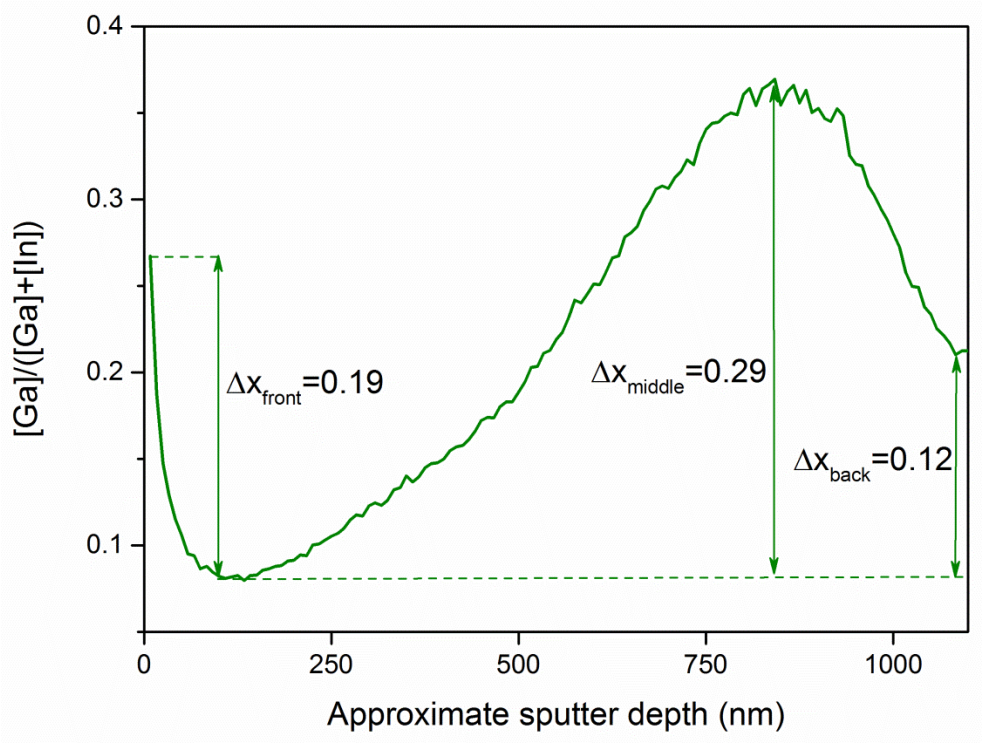

Figure 3.19: *Depth profiles of the CIGS sample grown using the standard three-stage process with GGI = 0.24 showing the relative Ga grading profile along the CIGS film depth as assessed by the SIMS measurements.*

3.3.4.2 Solar cell devices and their photovoltaic properties

3.3.4.2.1 Variation on the Cu content

The PV properties of the CIGS solar cells grown with the different CGI ratios of 0.59, 0.68 and 0.79 at the varied substrate temperatures using the three-stage process are presented and compared. These varied compositions were achieved by adjusting the metal source temperature. In table 3.1, the PV parameters are summarised corresponding to the Cu contents.

Table 3.1: PV parameters of the solar cells grown with the different CGI ratios of 0.59, 0.68 and 0.79 at varied substrate temperatures.

[Cu]/[III]	η (%)	V_{oc} (V)	J_{sc} (mA cm^{-2})	FF (%)	R_{sh} (Ω cm^2)	R_s (Ω cm^2)
0.59	3.7	0.520	12.4	57.5	352	1.3
0.68	3.6	0.444	14.6	55.7	255	0.6
0.79	8.1	0.563	20.8	68.8	196	0.9

A significant increase in J_{sc} for the CIGS device with CGI = 0.79 compared to CGI = 0.59 and 0.68 is observed. V_{oc} and FF also increase with the CGI ratio. The more Cu atoms are incorporated into the film, the better compactness of the CIGS layer as that is

evident from the SEM cross-section micrographs (*Section 3.3.4.1.1*, Fig. 3.14). This will result in the reduced recombination and hence the better power conversion efficiency can be achieved for this device. However, the lowest V_{oc}, FF and η were obtained for the CIGS device with CGI = 0.68. This is possibly due to the relatively complex Ga depth profiles (Fig. 3.16a) of the CIGS device with CGI = 0.68 as compared to the CIGS device with CGI = 0.79 (Fig. 3.16b). The dramatic changes in the Ga profile would contribute to the recombination losses since it may reduce the beneficial effects of the BSF as described in *Section 3.3.2.1*. The light-to-dark crossover (Fig. 3.13A) was observed for three CIGS films grown different CGI. As discussed in *Section 3.3.3.2*, the reduced Ga grading could possibly reduce the BSF, consequently, a decrease in photocurrent [3.32] .

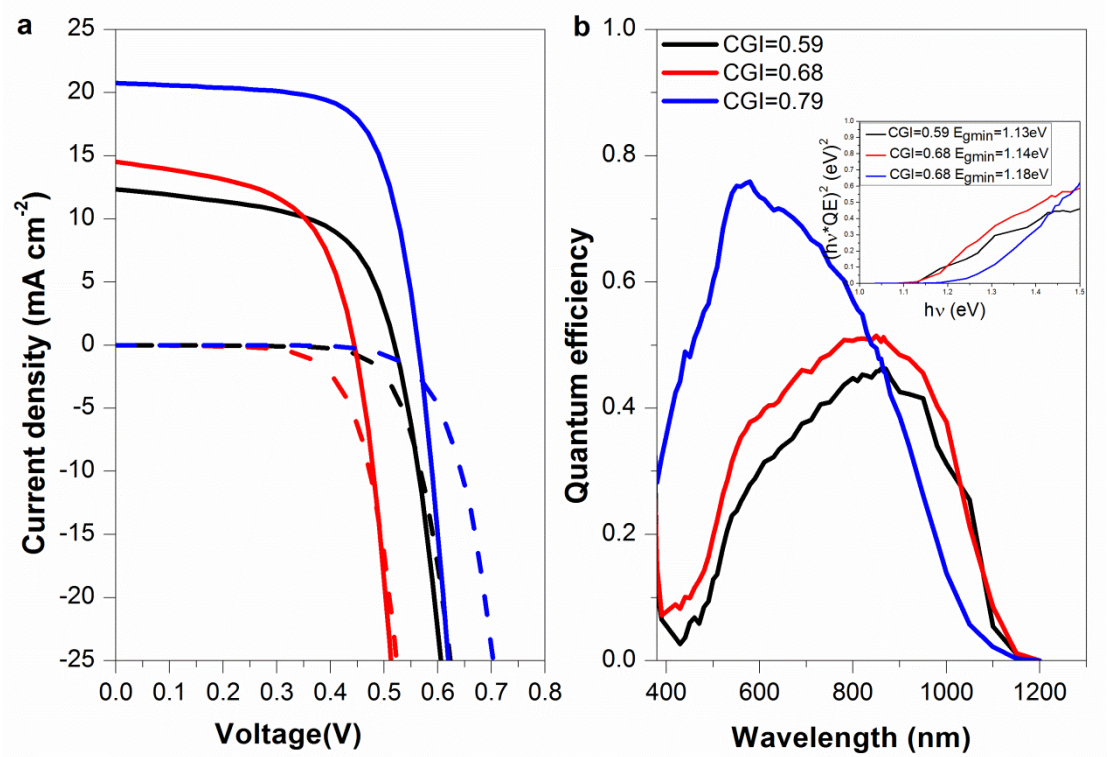

Figure 3.20: *(a) J-V characteristics of CIGS solar cells grown with the different CGI ratios of 0.59, 0.68 and 0.79 at the varied substrate temperatures. The dotted and solid lines represent the measurements in the dark and under illumination. (b) Corresponding EQE curves of the solar cells. The minimum band gaps were derived to be 1.13 eV, 1.14 eV and 1.18 eV for CIGS films with different CGI ratios of 0.59, 0.68 and 0.79, respectively.*

The EQE measurements as shown in Fig. 3.20b of the solar cells reveal that the current density increases over the short wavelength region (<850 nm) of the spectrum due to improved surface uniformity and crystallinity of the sample with CGI = 0.79 compared

to other two samples as observed from the SEM and XRD measurements (*Section 3.3.4.1.1*, Fig. 3.14 and 3.15). However, the EQE of these three samples are low as compared to the highly efficient CIGS solar cells reported in literature [3.5] possibly due to the incomplete absorption and collection in the thin absorber layers in this section as shown in Fig. 3.20b. These pronounced losses could be caused by the thinner absorber thickness, low diffusion length and complex Ga grading related recombination [3.9]. The minimum band gaps of the CIGS absorbers are also shown in the inset of Fig. 3.20b, which are in good agreement with the estimated average band gap values (1.14 eV) from XRF and XRD measurements (Fig. 3.15). The increase in In content and the decrease in Cu content for both samples in SIMS profiles (Fig, 3.16*a* and *b*) may lead to n-type ODC formation at the absorber surface, which could also reduce the minority carrier collection near the junction.

3.3.4.2.2 Variation on the Ga content

The PV properties of the CIGS solar cells grown with different GGI ratios of 0.19, 0.21 and 0.24 at varied substrate temperatures prepared by the three-stage process are compared (Fig. 3.21). These composition variations were achieved by adjusting the metal source temperature. In table 3.2, the PV parameters are summarised corresponding to the Ga contents.

Table 3.2: PV parameters of the solar cells grown with the different GGI ratios of 0.19, 0.21 and 0.24 at the varied substrate temperatures.

[Ga]/[III]	η (%)	V_{oc} (V)	J_{sc} (mA cm^{-2})	**FF** (%)	R_{sh} (Ω cm^2)	R_s (Ω cm^2)
0.19	5.6	0.468	21.7	55.2	323	1.1
0.21	5.7	0.492	19.8	58.9	382	1
0.24	8.1	0.563	20.8	68.8	196	0.9

J-V and EQE measurements were performed and the photovoltaic parameters of the best solar cells are shown in table 3.2 and Fig. 3.21. The first observation from the *J-V* parameters is that the V_{oc} increases significantly with increase in the Ga content. The increase of V_{oc} could be mainly due to the increased band gap of the CIGS absorber layer due to the increase in the Ga content [3.19]. However, the J_{sc} reduces slightly upon the change of the Ga contents due to less low-energy-photon that would be absorbed in the CIGS absorber layer (due to the increased band gap) [3.19]. An improved FF with

increase in the GGI is also obtained. This could be mainly due to the improved surface uniformity and film compactness of the CIGS layers (*Section 3.3.4.1.2*, Fig. 3.17).

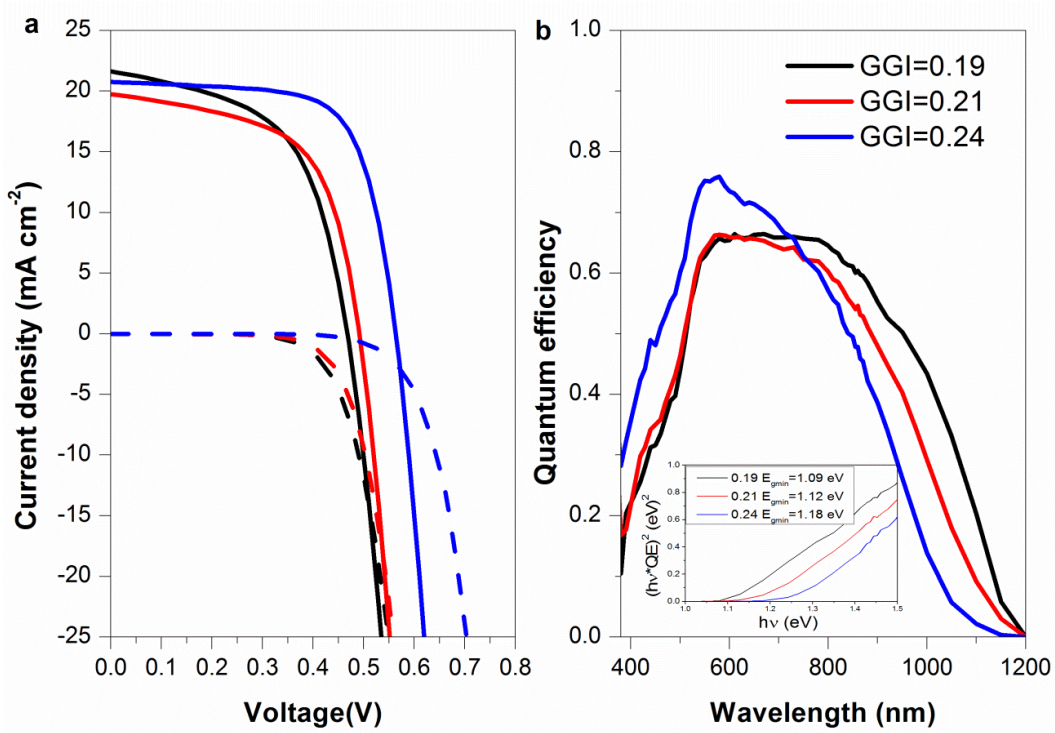

Figure 3.21: *(a) J-V characteristics of CIGS solar cells grown with different GGI ratios of 0.19, 0.21 and 0.24 at the varied substrate temperatures. The dotted and solid lines represent the measurements in the dark and under illumination. (b) Corresponding EQE curves of the solar cells. The minimum band gaps were derived to be 1.09 eV, 1.12 eV and 1.18 eV for the CIGS films with different GGI ratios of 0.19, 0.21 and 0.24, respectively.*

From the EQE measurement (Fig. 3.21b), The low blue response of the samples with GGI = 0.19 and 0.21 as compared to 0.24 is likely due to the increased surface recombination and minority carrier collection at the junction, which is reflected by the rougher surface in the SEM images in Fig. 3.17 and Cu-poor surface profile leading to form ordered defect compounds in SIMS measurement (Fig. 3.16b). The reduced current of the sample with GGI = 0.24 at the wavelength larger than 800 nm appears to be related to the incomplete carrier collection, thus, pointing to the increased recombination in the bulk and grain boundaries may be caused by the cracks in Fig. 3.17C. It shows that the samples with higher Ga contents have a lower cut-off wavelength, and hence a higher minimum band gap of the absorber. This could be related to the narrowest FWHM of the XRD peak corresponding to the (112) peak for the sample with GGI = 0.24 in the pattern (Fig. 3.18).

3.4 Conclusion

In this chapter, CIGS absorber layers have been grown with three different methods – grown CIG precursors at room temperature and selenisation, grown CIGS films at the constant substrate temperature in a three-stage sequence, and grown CIGS films at varied substrate temperatures in a standard three-stage process. Compared to 2-3 μm-thick standard high efficiency CIGS absorber, ~1 μm thickness was chosen to investigate the feasibility of the preparations of thinner absorber layers using above three methods. The influence of different growth paths on the material properties and device performance of the absorber were investigated.

In the first set of experiments, Cu, In and Ga layers were grown respectively on the room temperature substrates to investigate their thickness uniformity and structural properties. These results also provide a good calibration on the metal layer deposition rate at the desired source temperature and the speed of the substrate movement.

Thus the CIG stacked layers were deposited in the two different configurations: GaIn on top of Cu and Cu on top of GaIn. After selenisation of these CIG precursors, a higher $MoSe_2$ peak from the selenised GaIn on top of Cu film than the one from the other CIG configured film. The formation of excess $MoSe_2$ may lead to slightly worse device efficiency. Devices employing CIGS absorber layers from Cu on top of GaIn precursor exhibited up to 7.4% efficiency on a total area of 0.09 cm^2 without the top metal grid and the anti-reflection coating.

Next, a simplified three-stage process was employed to deposit the CIGS films at the constant substrate temperature in the three-stage sequence. The effect of different CGI ratios on the material properties and device efficiency was investigated. A 7.7% champion CIGS solar cell was obtained with CGI ratio of 0.89.

Finally, the CIGS films were prepared using a standard three-stage process at varied substrate temperatures. Furthermore, the influences of both CGI and CGI ratios were studied. The best device efficiency is 8.1% obtained from this set of experiment. From improved V_{oc} and FF, there is still room for further improvements on the material properties and the device efficiency by improving the film quality. Especially a more uniform CIGS surface with less voids and crevices and a smoother Ga grading profile are crucial to increase the CIGS film quality and the device efficiency.

References

[3.1] A. M. Gabor, J. R. Tuttle, D. S. Albin, M. A. Contreras, R. Noufi and A. M. Hermann, "High-efficiency $CuIn_xGa_{1-x}Se_2$ solar cells made from $(In_xGa_{1-x})_2Se_3$ precursor films," *Applied Physics Letters,* vol. 65, pp. 198-200, 1994.

[3.2] W. N. Shafarman and U. Rau, "Cu(In,Ga)Se_2 Solar Cells," in *Clean Electricity From Photovoltaics,* R. H. Mary D. Archer, Ed., ed London: Imperial College Press, pp. 277-346, 2001.

[3.3] R. Scheer and H.-W. Schock, "Design Rules for Heterostructure Solar Cells and Modules," in *Chalcogenide Photovoltaics,* ed: Wiley-VCH Verlag GmbH & Co. KGaA, pp. 129-174, 2011.

[3.4] P. Jackson, D. Hariskos, E. Lotter, S. Paetel, R. Wuerz, R. Menner, W. Wischmann and M. Powalla, "New world record efficiency for Cu(In,Ga)Se_2 thin-film solar cells beyond 20%," *Progress in Photovoltaics: Research and Applications,* vol. 19, pp. 894-897, 2011.

[3.5] A. Chirilă, P. Reinhard, F. Pianezzi, P. Bloesch, A. R. Uhl, C. Fella, L. Kranz, D. Keller, C. Gretener, H. Hagendorfer, D. Jaeger, R. Erni, S. Nishiwaki, S. Buecheler and A. N. Tiwari, "Potassium-induced surface modification of Cu(In,Ga)Se_2 thin films for high-efficiency solar cells," *Nat Mater,* vol. 12, pp. 1107-1111, 2013.

[3.6] I. Repins, M. A. Contreras, B. Egaas, C. DeHart, J. Scharf, C. L. Perkins, B. To and R. Noufi, "19.9%-efficient ZnO/CdS/$CuInGaSe_2$ solar cell with 81.2% fill factor," *Progress in Photovoltaics: Research and Applications,* vol. 16, pp. 235-239, 2008.

[3.7] http://www.zsw-bw.de/uploads/media/pr12-2014-ZSW-WorldrecordCIGS.pdf, "ZSW Brings World Record Back to Stuttgart New best mark in thin-film solar performance with 21.7 percent efficiency ", 2014.

[3.8] M. Powalla, P. Jackson, W. Witte, D. Hariskos, S. Paetel, C. Tschamber, W. Wischmann, "High-efficiency Cu(In,Ga)Se_2 cells and modules," *Solar Energy Materials and Solar Cells,* vol. 119, pp. 51-58, 2013.

[3.9] A. Chirilă, S. Buecheler, F. Pianezzi, P. Bloesch, C. Gretener, A. R. Uhl, C. Fella, L. Kranz, J. Perrenoud, S. Seyrling, R. Verma, S. Nishiwaki, Y. E. Romanyuk, G. Bilger and A. N. Tiwari, "Highly efficient Cu(In,Ga)Se_2 solar cells grown on flexible polymer films," *Nat Mater,* vol. 10, pp. 857-861, 2011.

[3.10] F. Pianezzi, P. Reinhard, A. Chirilă, S. Nishiwaki, B. Bissig, S. Buecheler and A. N. Tiwari, "Defect formation in Cu(In,Ga)Se_2 thin films due to the presence of potassium during growth by low temperature co-evaporation process," *Journal of Applied Physics,* vol. 114, pp. 194508, 2013.

[3.11] P. Jackson, D. Hariskos, R. Wuerz, W. Wischmann and M. Powalla, "Compositional investigation of potassium doped Cu(In,Ga)Se_2 solar cells with efficiencies up to 20.8%," *physica status solidi (RRL) – Rapid Research Letters,* vol. 8, pp. 219-222, 2014.

[3.12] P. Jackson, R. Würz, U. Rau, J. Mattheis, M. Kurth, T. Schlötzer, G.Bilger and J. H. Werner, "High quality baseline for high efficiency, $Cu(In_{1-x}Ga_x)Se_2$ solar cells," *Progress in Photovoltaics: Research and Applications,* vol. 15, pp. 507-519, 2007.

[3.13] W. N. Shafarman and J. Zhu, "Effect of substrate temperature and depostion profile on evaporated Cu(InGa)Se_2 films and devices," *Thin Solid Films,* vol. 361–362, pp. 473-477, 2000.

[3.14] C. A. Kaufmann, D. Greiner, H. Rodriguez-Alvarez, A. Weber, M. D. Heinemann, J. Lauche, M. Klaus, C. Genzel and H.-W. Shock, "Co-evaporation of Cu(In,Ga)Se_2 at low temperatures: An In-Situ x-ray growth analysis," *Conference Record of the 39th IEEE Photovoltaic Specialists Conference,* Tampa, pp. 3058-3061, 2013.

[3.15] H. Rodriguez-Alvarez, R. Mainz, R. Caballero, D. Abou-Ras, M. Klaus, S. Gledhill, A. Weber, C. A. Kaufmann and H.-W. Schock, "Real-time study of Ga diffusion processes during the formation of Cu(In,Ga)Se_2: The role of Cu and Na content," *Solar Energy Materials and Solar Cells,* vol. 116, pp. 102-109, 2013.

[3.16] F. Pianezzi, P. Reinhard, A. Chirila, B. Bissig, S. Nishiwaki, S. Buecheler and A. N. Tiwari, "Unveiling the effects of post-deposition treatment with different alkaline elements on the electronic properties of CIGS thin film solar cells," *Phys Chem Chem Phys*, vol. 16, pp. 8843-51, 2014.

[3.17] Z. J. Li-Kao, N. Naghavi, F. Erfurth, J. F. Guillemoles, I. Gérard, A. Etcheberry, J. L. Pelouard, S. Collin, G. Voorwinden and D. Lincot, "Towards ultrathin copper indium gallium diselenide solar cells: proof of concept study by chemical etching and gold back contact engineering," *Progress in Photovoltaics: Research and Applications*, vol. 20, pp. 582-587, 2012.

[3.18] J. K. Larsen, H. Simchi, P. Xin, K. Kim and W. N. Shafarman, "Backwall superstrate configuration for ultrathin Cu(In,Ga)Se_2 solar cells," *Applied Physics Letters*, vol. 104, pp. 033901, 2014.

[3.19] A. M. Gabor, J. R. Tuttle, A. Schwartzlander, A. L. Tennant, M. A. Contreras and R. Noufi, "Band-gap engineering in Cu(In,Ga)Se_2 thin films grown from $(In,Ga)_2Se_3$ precursors," *Conference Record of the Twenty Fourth IEEE Photovoltaic Specialists Conference/IEEE First World Conference on Photovoltaic Energy Conversion*, Hawaii, vol.1, pp. 83-86, 1994.

[3.20] S. Siebentritt, N. Papathanasiou, J. Albert and M. C. Lux-Steiner, "Stability of surfaces in the chalcopyrite system," *Applied Physics Letters*, vol. 88, pp. 151919, 2006.

[3.21] D. Liao and A. Rockett, "Epitaxial growth of Cu(In,Ga)Se_2 on GaAs(110)," *Journal of Applied Physics*, vol. 91, pp. 1978-1983, 2002.

[3.22] S. F. Buecheler, "Investigation of compound semiconductors as buffer-layer in thin film solar cells," Doctoral thesis, ETH, Zürich, 2010.

[3.23] M. Bodegård, O. Lundberg, J. Lu and L. Stolt, "Re-crystallisation and interdiffusion in CGS/CIS bilayers," *Thin Solid Films*, vol. 431–432, pp. 46-52, 2003.

[3.24] S.-H. Wei, S. B. Zhang and A. Zunger, "Effects of Ga addition to $CuInSe_2$ on its electronic, structural, and defect properties," *Applied Physics Letters*, vol. 72, pp. 3199-3201, 1998.

[3.25] D. Rudmann, "Effects of sodium on growth and properties of Cu(In,Ga)Se_2 thin films and solar cells," Doctoral thesis, ETH, Zürich, 2004.

[3.26] S. S. Hegedus and W. N. Shafarman, "Thin-film solar cells: device measurements and analysis," *Progress in Photovoltaics: Research and Applications*, vol. 12, pp. 155-176, 2004.

[3.27] R. Klenk, T. Walter, H.-W. Schock and D. Cahen, "A model for the successful growth of polycrystalline films of $CuInSe_2$ by multisource physical vacuum evaporation," *Advanced Materials*, vol. 5, pp. 114-119, 1993.

[3.28] J. Schöldström, J. Kessler and M. Edoff, "Two-stage growth of smooth Cu(In,Ga)Se_2 films using end-point detection," *Thin Solid Films*, vol. 480–481, pp. 61-66, 2005.

[3.29] T. Walter and H.-W. Schock, "Crystal growth and diffusion in Cu(In, Ga)Se_2 chalcopyrite thin films," *Thin Solid Films*, vol. 224, pp. 74-81, 1993.

[3.30] S. Chaisitsak, A. Yamada and M. Konagai, "Preferred Orientation Control of $Cu(In_{1-x}Ga_x)Se_2$($x \approx 0.28$) Thin Films and Its Influence on Solar Cell Characteristics," *Japanese Journal of Applied Physics*, vol. 41, p. 507, 2002.

[3.31] A. M. Gabor, J. R. Tuttle, M. H. Bode, A. Franz, A. L. Tennant, M. A. Contreras, R. Noufi, D. G. Jensen and A. M. Hermann, "Band-gap engineering in Cu(In,Ga)Se_2 thin films grown from $(In,Ga)_2Se_3$ precursors," *Solar Energy Materials and Solar Cells*, vol. 41–42, pp. 247-260, 1996.

[3.32] Y. Abe, T. Minemoto and H. Takakura, "Origin of Crossover in Current Density–Voltage Characteristics of Cu(In,Ga)Se_2 Thin Film Solar Cell Fabricated Using Lift-Off Process," *Japanese Journal of Applied Physics*, vol. 50, p. 040201, 2011.

Chapter 4 – Effect of mechanical compression on $Cu(In,Ga)Se_2$ films: micro-structural and photoluminescence analysis

Abstract

The motivation to conduct this study was generated from the previous chapter where $Cu(In,Ga)Se_2$ (CIGS) thin films were deposited by a two-step process on Mo-coated soda lime glass substrates. The CuInGa (CIG) precursors were prepared in an inline evaporation system at room temperature, and then selenised at 500 ℃. As expected, the quality of the CIGS films was compromised and the surface morphology and the texture revealed porosity in the films. The mechanical compression process was incorporated to reduce the apparent porosity and improve electronic property of the CIGS films. These two-step processed CIGS films were mechanically compressed at 25 MPa to improve their optoelectronic properties, which were verified by photoluminescence (PL). The surface and structural properties were compared before and after compression. The mechanical compression has brought changes in the surface morphology and porosity without changing its structural properties. The PL technique has been used to reveal the changes in the electronic properties of the films. PL spectra at different excitation laser powers and temperatures were measured for as-grown as well as compressed samples. The PL spectra of the as-grown films revealed three broad and intense bands shifting at a significant rate towards higher photon energies (*j*-shift) as the excitation power increase suggesting that the material is highly doped and compensated. With increasing temperature, the peaks shift towards lower photon energies, which is a characteristic of the band tails generated by spatial potential fluctuation. The compression increases the intensity of bands by an order of magnitude and reduces the *j*-shift confirming an improvement of the structural quality.

4.1 Introduction

Selenisation of the metallic precursors using Se/N_2 [4.1-4.4] or H_2Se [4.5-4.7] environment is considered as a simple and promising two-step approach to produce the good quality absorbers and high efficiency CIGS solar cells. The low-temperature, low-vacuum and mechanical compression methods have attracted attention in the two-step process of the CIGS preparation due to its advantage of scalability and improved quality of the thin film preparation [4.1, 4.3, 4.8-4.10]. The low temperature and low vacuum two-step CIGS process had been extensively studied to produce good quality absorber layers. However, in the scale-up process, the CIGS thin films often suffer from inhomogeneity problems over large area. These are the main deviations observed from the composition uniformity, which is attributed to the unwanted defects and defect clusters [4.11]. Such defects play an important role in reducing the conversion efficiency, as they become potential trap sites for the carriers. Moreover, the intermixing and alloy formation in the Cu–In precursor layers also cause the non-uniformity of the layers during the low temperature (130 ℃) and low pressure (10 mbar) deposition methods [4.1, 4.3]. Several methods such as hydrogen (H_2) annealing, chemical treatment and mechanical compression have been attempted to address these problems and to suppress the defects for a good quality CIGS absorber formation [4.9, 4.12-4.15].

Mechanical compression is generally used in the material processing engineering to achieve high uniformity and high compactness of the thin films, especially in the low temperature processed dye-sensitised solar cells. This technique improves the necking between the porous TiO_2 particles and brings an improvement in the adhesion of the materials on the flexible substrates for dye sensitised solar cells applications [4.16, 4.17].

Solar cells based on the CIGS films deposited using the two-step process (Process A, *Section 3.2.1*, Chapter 3) without compression showed a low solar cell efficiency of ~3% due to high level of defects and porosity present in the material [4.4]. A better device performance can be achieved using the CIGS films grown with less voids and cracking, larger grains and optimum composition and better thickness uniformity. The mechanical compression technique was previously used on the CIGS films which showed reduction in the films porosity and improvement in the layer uniformity [4.9]. Although the changes on surface morphology and crystallinity due to compression have

been investigated in previous studies, the electronic properties and defect nature of the compressed CIGS absorber layers were not fully addressed.

In this chapter, PL analysis was used to collect the important information on the defect nature and mechanisms of radiative recombination [4.18]. Furthermore, the influence of the mechanical compression on the structural and optoelectronic properties of the CIGS films has revealed some interesting facts which have been investigated and correlated with the PL data.

4.2 Experimental techniques

The CIG precursor layer was grown using the preparation method (Process A) as described in *Section 3.2.1*, Chapter 3. The CIG precursor layer was then selenised in a two-temperature-zone quartz tube furnace. The selenium vapours were generated from Se pellets (Sigma Aldrich 99.999%) at 300 ℃ in the first temperature zone. The nitrogen (N_2) gas was used as a carrier gas to transport the selenium vapours to the second deposition zone. The CIG precursor was selenised at 500 ℃ to form Cu(In,Ga)Se_2 layers. Then, the CIGS films were cut into 1 cm^2 samples and compressed using a mechanical compression machine to apply 2.5 tons force which equals 25 MPa pressure on to the samples. It may be noted that the mechanical compression performed on the CIGS films was limited by the glass substrate, which cannot bear more than 2.5 tons force and would crack.

The device fabrication process and characterisation techniques including SEM, XRD and *J-V* measurements were detailed in *Section 3.2.1 and 3.2.2*, Chapter 3. Temperature and excitation power resolved photoluminescence (PL) measurements before and after compression were carried out on the CIGS thin films to understand the mechanisms of radiative recombination, nature of the defects and effects of compression on the defect properties. The PL measurements were performed using a closed-cycle cryostat, at temperatures from 5 to 300 K. An Ar^+ laser (514nm) was used for excitation. PL emission was focused on to the entrance slits of a 1 m spectrometer and detected by an InGaAs photomultiplier tube (PMT sensitive within the range from 950 to 1650 nm). Laser excitation power was varied from 0.2 to 20 mW which corresponds to the power densities ramping from 0.16 to 16W cm^{-2}.

4.3 Results and Discussion

The as-grown CIGS films described in the previous section were used to make CIGS solar cells and the current density-voltage characteristics of the device are listed in table 4.1. Four single solar cells from different region of the CIGS layer show different *J-V* parameters indicate the non-uniformity of the layer. The finished devices showed low efficiency values. The resulting poor performance was believed to be caused by defect-related recombination. This may be assigned to the poor quality of CIGS formed, which was predominantly porous in nature, as shown in Fig. 4.1a. The room temperature grown CuInGa metal layer leads to higher composition non-uniformity, which could generate a highly porous grain structure. The porous structure will bring more defects into the CIGS film. Thus the compression was applied in this work to smoothen the surface of the films and PL was used to investigate the effect of compression on the electronic properties of CIGS films.

Table 4.1: Comparison of parameters extracted from *J–V* analysis of four single solar cells from different regions of a CIGS film layer before compression.

Device	V_{oc} ***(mV)***	J_{sc} ***(mA/cm^2)***	***FF(%)***	η***(%)***
a	381	10.0	25.1	1.0
b	438	17.4	27.5	2.1
c	368	24.3	25.6	2.3
d	416	20.6	35.3	3.0

4.3.1 Structural and morphological properties

The Fig. 4.1 shows the surface and cross-section morphologies of CIGS films before and after compression. The SEM picture (Fig. 4.1a) reveals the porous and less compact nature of the as-grown film. It is believed that the non-uniformity of the mixing of Cu, In and Ga atoms would lead to the different reaction rates across the sample in the presence of selenium. This leads to the regions of the non-homogeneous growth of the films. This unevenness in the growth pattern can lead to the significant stresses in the film, and the grain boundaries created between the bigger and smaller grains. The disordered nature of this porous growth can be seen in the SEM cross-section image (Fig. 4.1c). After the mechanical compression, the surface (Fig. 4.1b) becomes smoother and more condensed as expected. The randomly oriented granular structures were brought closer by compression of the as-grown films without changing its grain size. Their structure becomes a columnar structure and the surface morphology of the films becomes an arrangement of bundles of slender and small grains in a pillar shape

(Fig. 4.1d). Oriented grains after compression have become more apparent suggesting a change in the morphology of the samples. At the bottom of the compressed film, a thin jointed layer appears which is indicative of providing additional compactness and can increase the shunt resistance of the device. The compression on the loosely connected bundles of grains brings them together and reduces the porous nature of the as-grown films without changing its orientation.

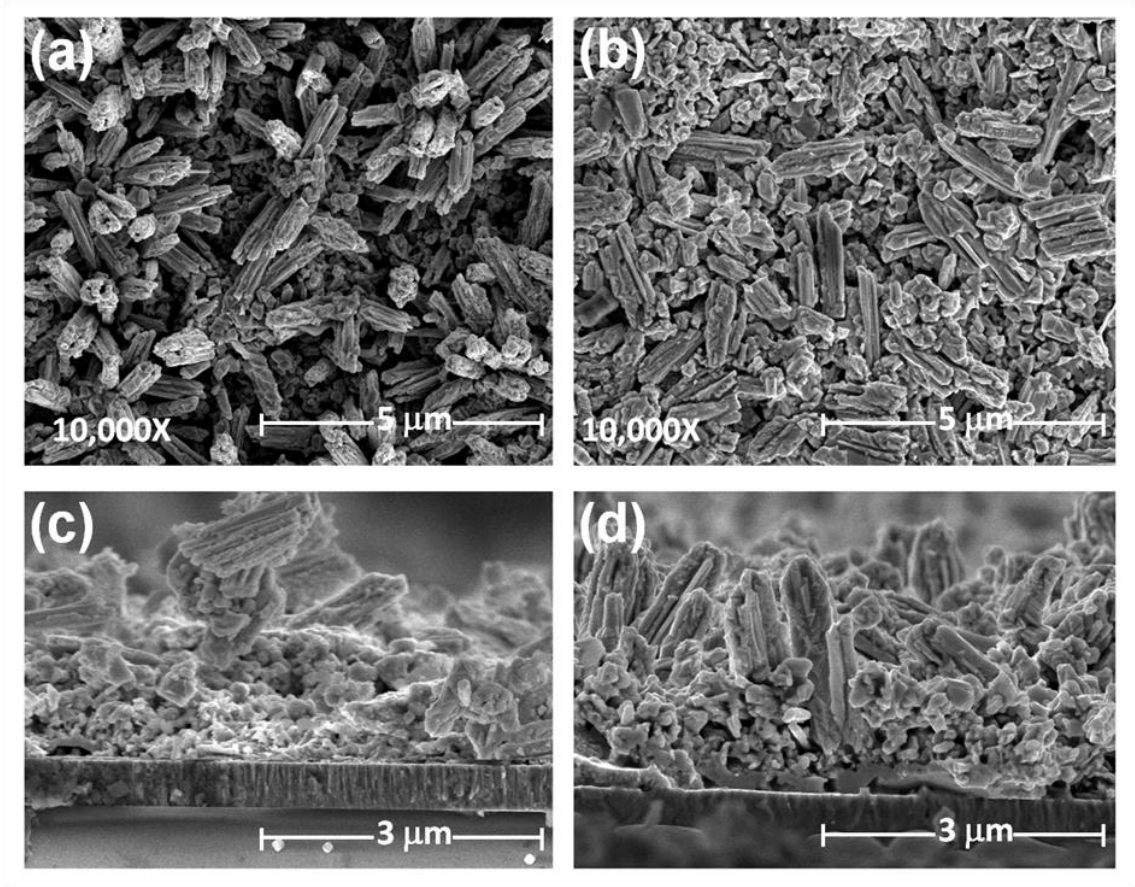

Figure 4.1: *SEM micrographs of the CIGS film surface and cross-section: (a and c) as grown film, (b and d) after compression.*

X-ray diffraction was performed on the CIGS film samples to detect any significant changes or appearance of new phases of CIGS under the effect of compression. The XRD spectra of CIGS grown on Mo coated glass substrates shows the preferential orientations along (112) and (220)/(204) planes confirming the formation of crystalline CIGS (JCPDS 35-1102). Fig. 4.2 shows the comparison of the XRD spectra of the CIGS films before and after compression. The XRD spectra of the CIGS films before and after compression reveal the similar widths of the peaks (full width at half maximum, FWHM). This suggests that the structural quality of the films has not been affected by the compression. The ratios of intensities of the peaks are also not affected by the compression demonstrating that compression does not change the main

orientation of the grains. It was also evident from XRD studies that the CIGS phases were unchanged after the compression.

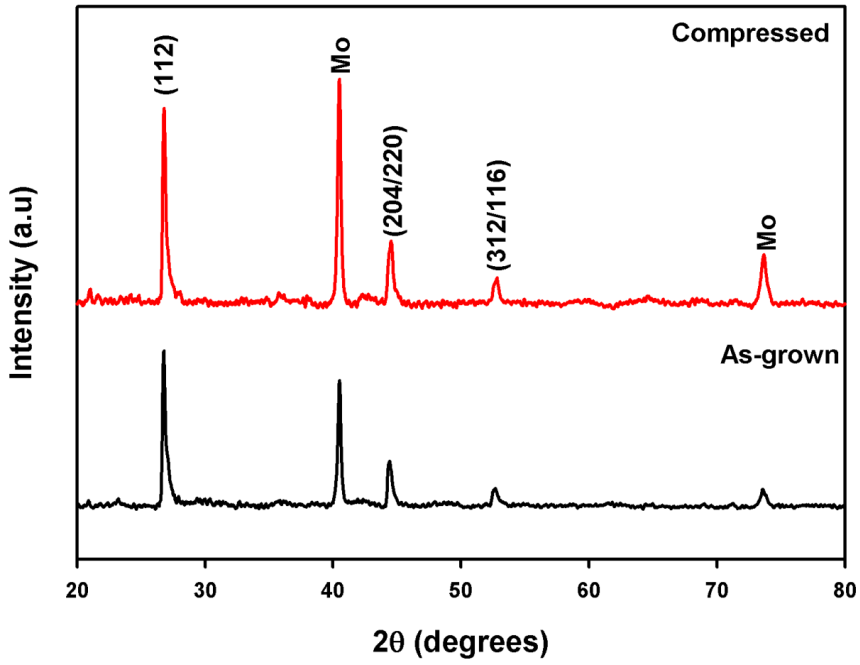

Figure 4.2: *The XRD patterns of the CIGS films before and after compression.*

4.3.2 PL analysis

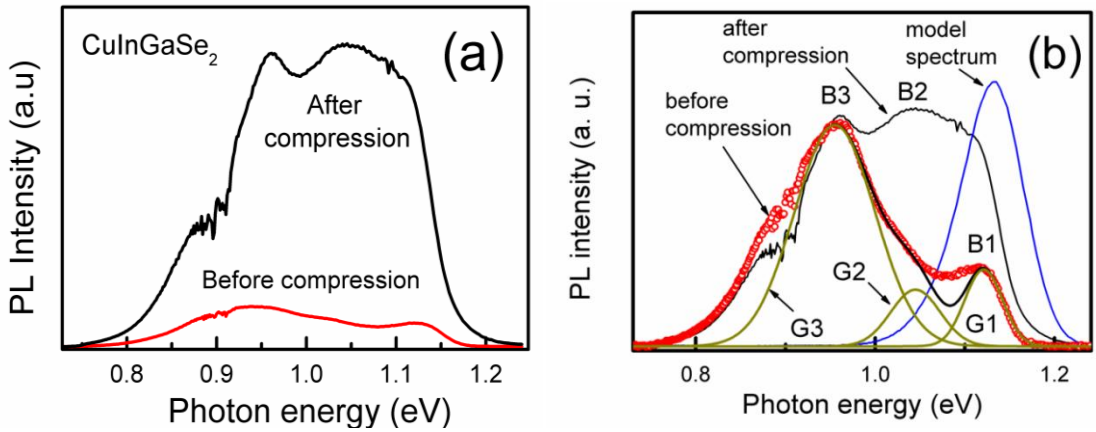

Figure 4.3: *(a) Comparison of the intensity of PL spectra of as-grown and compressed CIGS films (spectra recorded at 5 K, laser excitation power at 2 mW). (b) The same spectra with normalized intensities in comparison with a fit of the sum of 3 Gaussian shapes G1, G2, G3 for the spectrum before compression and a reference spectrum recorded at 10 K.*

Fig. 4.3a shows the PL spectra of the as-grown and compressed films compared films. It can be seen that compression significantly increases the intensity of the PL emission. In order to compare them at the same scale, the spectra from the as-grown films were

factored appropriately as shown in Fig. 4.3b. This figure also shows a PL spectrum measured in the $Cu(In,Ga)Se_2$ thin films with the similar gallium content GGI = 0.3, and used here as a reference (the blue curve referred to as 'model spectrum' in Fig. 4.3b). The reference films were deposited on Mo coated soda lime glass substrates to produce solar cells with power conversion efficiency of 15% [4.19]. Their PL spectra reveal a single high intensity recombination band with its maximum at 1.13 meV and the FWHM of 82 meV. The intensity of the reference spectrum is divided by a factor of 35 for a comparison.

Three broad PL bands B1, B2 and B3 are revealed at about 1.12, 1.04 and 0.94 eV as well as noticeable water absorption at 0.9 eV can be seen in the spectrum before the compression. The FWHM of the B1, B2 and B3 bands are approximated as 60, 80 and 140 meV by fitting three Gaussians, respectively, which have been indicated in the Fig. 4.3b. These Gaussians fit well into the high energy slopes of the B1, B2 and B3 bands whereas the low energy ones do not quite follow that of B1, B2 and B3 demonstrating a strong asymmetry of the band shapes. The dip between G1 and G2 suggests that the spectrum may contain one or more low intensity non-resolved bands. In this chapter, only the three higher intensity bands B1, B2 and B3 will be discussed. The relative intensities of these bands vary at different points on the samples, but their spectral positions remain the same. Amongst the three bands, the spectral position of B1 band is also in the range of the reference film. Therefore, we can expect the defects associated with the B1 band in our samples, to be similar to that in the reference film. The small differences in the spectral position and FWHM can be due to differences of the elemental composition and the structural quality, respectively.

The compression of the CIGS films generates changes in the film morphology and their electronic properties. Along with the significant increase in the total PL intensity, the compression increases the relative intensity of the higher energy part of the PL spectrum dramatically. However, the PL intensity after compression is still lower than that of the reference spectrum. The detailed investigation of the excitation power and temperature dependencies of the PL spectra will help to understand the changes in the electronic properties due to the compression. The compression study was also limited by the choice of the substrate, which is soda-lime glass in the present case. An attempt is necessary to be made to understand the effects of higher compression pressures on the

electronic properties of the film along with the studies performed with added variation of thermally assisted compression.

4.3.2.1 Excitation intensity dependence

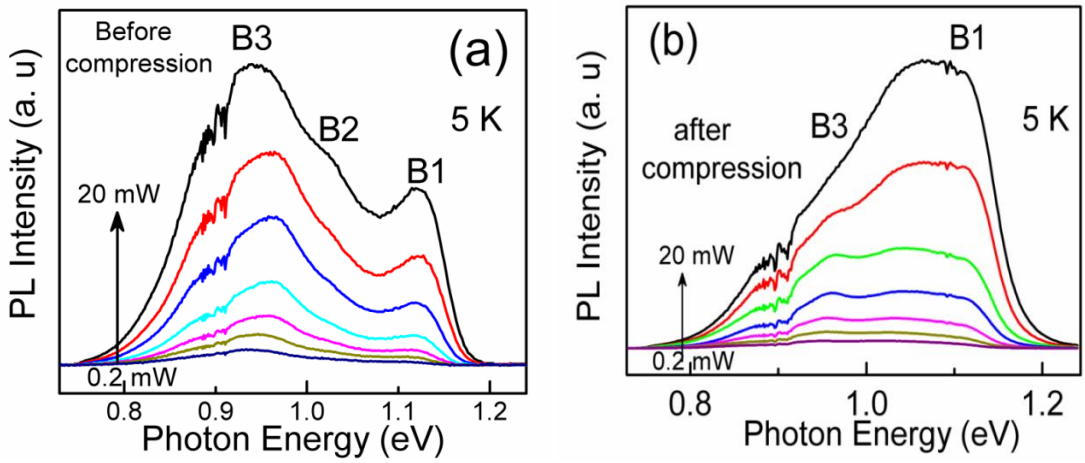

Figure 4.4: *Dependence of the PL spectra, measured (a) before compression and (b) after compression with different excitation laser power.*

Analysis of dependencies of the PL spectra on the laser excitation power can help to identify the recombination mechanisms involved. Such dependency of the PL spectra for the films before and after compression measured at 5 K for laser excitation powers ranging from 0.2 to 20 mW, are shown in Fig. 4.4a and b, respectively. It can be seen in Fig 4.4b in the PL spectra after the compression that the B1, B2 and B3 bands are significantly less resolved, although at excitation powers below 10 mW the B3 band can be seen better resolved in both Fig. 4.3b and 4.4b. The intensity of the B1 band emission, associated with the shallower defects, grows faster with increase in excitation power resulting in almost a disappearance of the B3 band at the laser excitation power of 20 mW.

The spectra measured at the different excitation intensities were normalised in order to quantify changes in the B1 and B3 bands, which are better resolved in the spectra than B2. The spectra normalised to compare the B3 band are shown in Fig. 4.5a. It can be seen that the B3 band shifts with the increasing excitation power towards the higher energies. The rate of the shifts is 25 meV per decade of the laser power change. The PL spectra equalised to analyse the B1 band shifts are shown in Fig. 4.5c. The B1 band also shifts with the increasing excitation power towards the higher energies although the rate of the shift is j = 14 meV per decade, which is close to that of the reference band suggesting a similarity of their nature.

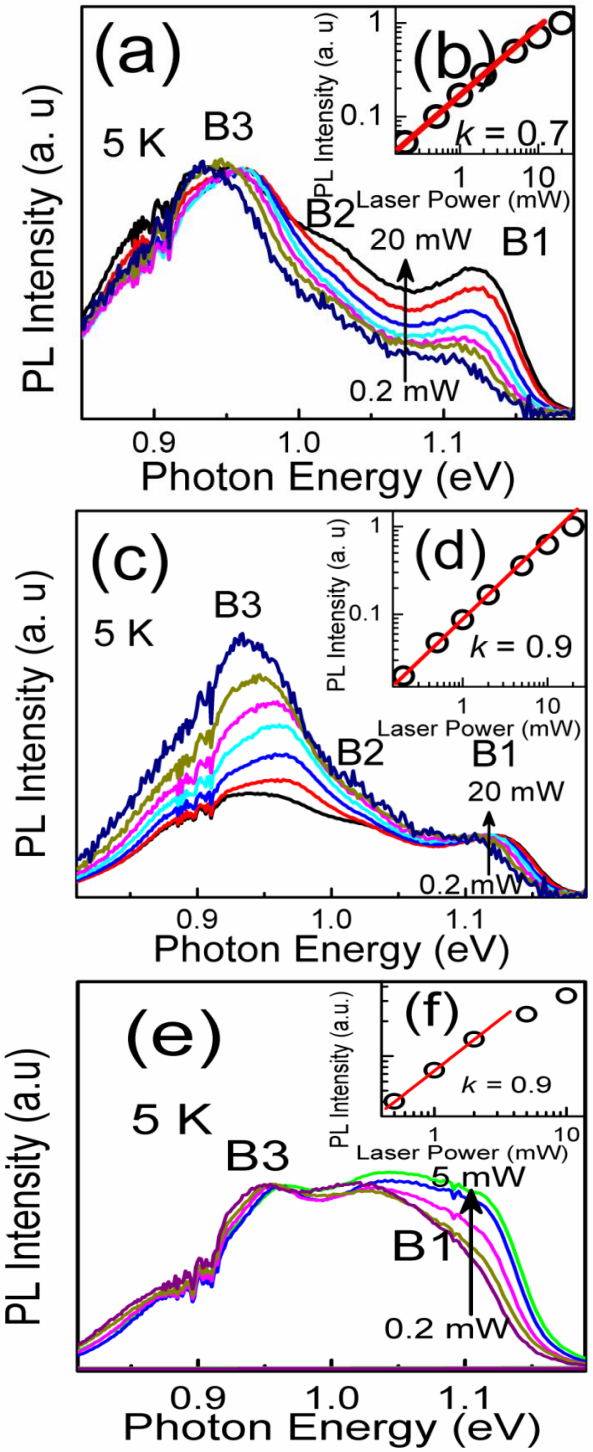

Figure 4.5: *Dependencies of the PL spectra on the excitation laser power, measured at 5 K for the films before compression (a, b, c, d). (a) The spectra for the films before compression normalised to B3 band, (b) log-log dependence of the B3 band intensity on the laser power. (c) The spectra for the films before compression normalised to the B1 band, (d) log-log dependence of the B1 band intensity on the laser power. (e) Dependence of the PL spectra, measured after compression, on the excitation laser power normalised to B3, (f) log-log dependence of the B3 band intensity on the laser power.*

Dependence of the PL spectra on the laser excitation power after the compression measured at 5 K for the laser excitation powers ranging from 0.2 to 20 mW is shown in Fig. 4.5e. The B1, B2 and B3 bands in these spectra are significantly less resolved than those before the compression. However the *j*-shift of the B3 band can be analysed at the lower excitation powers. The rate of the shift for the B3 band is estimated to be of about 14 meV per decade. Thus after the compression the B3 band demonstrates a significant reduction of the *j*-shift rate from 25 to 14 meV per decade.

The blue shift of PL bands with the increasing excitation power is often used to identify the recombination mechanism as donor – acceptor pair (DAP) one [4.20]. Wave functions of the closely located donors and acceptors overlap making the recombination of localised electrons and holes. In this case, the rate of *j*-shift cannot exceed a few meV per decade. The observed values of *j-shift* in this study for the B1, B3 bands and as well for the reference band exceed such a limit significantly. This is suggesting that the radiative recombination mechanisms of these bands which are more likely to be associated with band tails generated by high concentrations of clusters of charged defects [4.21, 4.22]. The asymmetrical shape of the bands showing more abrupt high energy slopes and longer low energy tails also can be taken as evidence of band-to-tail (BT) related recombination mechanisms [4.21]. Such BT related transitions are often observed in the PL spectra of the ternary and quaternary chalcopyrite single crystals and thin films [4.22-4.25]. Spatial potential fluctuations in CIGS and related compounds are generated by clusters of charged defects. These defects are due to the randomly distributed spatial deviations from the stoichiometry, and result in the band tails [4.21, 4.26].

According to the theory of heavily doped semiconductors with spatial potential fluctuations [4.21] and its application to PL analysis [4.26] of the radiative recombination can arise from several different channels. In the p-type material, it can be a recombination of a free electron and a hole localised in the valence band tail acting like acceptor. Because of potential fluctuations each band tail can represent not a single acceptor level but a distribution of acceptor states. The mean amplitude of potential fluctuations strongly depends on the level of doping and compensation, which determines the spectral positions of the band and the *j*-shift magnitude. The greater observed *j*-shift is related to the higher the potential fluctuation amplitude. It can occur through the acceptor state (band-to-impurity, BI-transition) that is deep enough not to

overlap with the valence band tail [4.27]. In the highly compensated semiconductors, the recombination can be between the deep donor and acceptor pairs also affected by the presence of the band tails [4.21].

The dependencies of the PL intensity (I) on the increasing laser power (P) for the B1 and B3 bands were fitted with equation $I \sim P^k$ [4.28] and plotted on a log-log scale in Fig. 4.5b and d for films before compression and 4.5f for films after compression. The slope (k) of these log-log dependencies can help to understand the nature of the transitions associated with B1 and B3. The slopes for the B3 log-log dependence before (Fig. 4.5b) and after (Fig. 4.5f) compression are measured to be $k \approx 0.7$ and $k \approx 0.9$, respectively. The k slope values are smaller than unity suggesting that the B1 and B3 bands before and after compression are associated with the defect related transitions [4.28]. The deviations from linearity in Fig. 4.5 (b, d, f) for the laser powers above 2 mW indicate that the laser beam increased the sample temperature.

4.3.2.2 Temperature dependence

In order to study the effect of temperature, the sample temperature has been varied from 5 K to 170 K. Fig. 4.6 shows the effect of temperature on the PL spectra. The spectral positions of all the three bands (B1, B2 and B3) in the spectra, measured before compression are shown (Fig. 4.6a), demonstrate shifts towards lower energies with increase in temperature. The B1 band quenches first then the B3 band quenches whereas the B2 band quenches the least at temperatures of about 170 K. The merged bands in the PL spectra of the film measured after compression (Fig. 4.6b) reveal the similar trend. At the central part of the spectra, the B2 band is quenching the least whereas the higher energy part is quenching first.

The red shifts with increase in temperature are also evidence that these transitions are associated with band tails. Such shifts have been reported for similar bands in the PL spectra of the thin films and the single crystals [4.19, 4.22, 4.24, 4.25]. The band in the reference spectrum also demonstrates the very similar red shifts with increase in temperature, which confirms the similarity of the defect nature associated with this band.

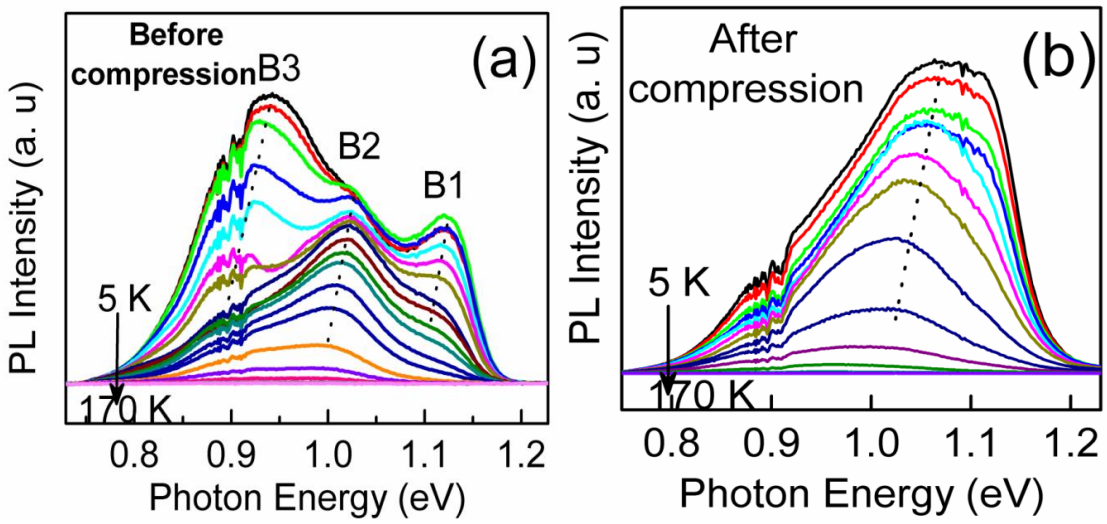

Figure 4.6: *Dependence of the PL spectra, measured before (a), and after (b) compression, on temperature. The shifts of the bands towards lower energies are shown by dot lines.*

The red shift of the bands with increase in temperature shown in Fig. 4.6, and significant *j*-shifts with the change in the excitation power changes suggests that all the three observed bands B1, B2 and B3 are associated with the BT recombination. The B1 band could be preliminarily assigned to the BT type recombination, a recombination of free electrons in the conduction band with holes localised at the valence band tail. The B2 and B3 are quite deep suggesting the presence of a range of additional deep defects and can be assigned to the DAP recombination influenced by the band tails.

Thus the results of both the excitation intensity and temperature analysis suggest that the studied CIGS thin films are highly doped and compensated. They contain high concentrations of the charged defects generating the significant band tails in the films before and after the compression. The B1 band is likely to be similar to the band observed in the PL spectra of the reference sample and the other high quality thin films fabricated by the traditional techniques [4.29, 4.30] and used to fabricate the high efficiency solar cells. The similarity is supported by its spectral position, FWHM, *j*-shift value and red shift with increasing temperatures. However, the PL intensity of B1 is still significantly lower than the reference sample suggesting the presence of significant non-radiative recombination and radiative recombination associated with deeper, unwanted defects. Some of these defects are represented by the B2 and B3 bands.

The compression induces the beneficial influences in the interfacial properties and hence in the PL spectra of the films. It increases the general PL intensity by an order of magnitude, suggesting a reduction of non-radiative recombination, the increased intensity of the B1 band whereas the unwanted B2 and B3 bands increase their intensity at a lower degree. The micro-structural quality improvement due to applied compression is also evident from *j*-shift from 25 meV to 14 meV per decade for the B3 band suggesting a reduction of the average depth of the potential fluctuations.

The proposed explanations of the changes in the PL spectra are based on analysis of the SEM micrographs. The branched tree structure of the grains before the compression can be seen in Fig 4.1a and 4.1c. After compression, the CIGS films appear to be more compact and dense columnar. From the micrographs it looks like the compression mostly affects the position of the larger grains pressing them closer to the substrate and to each other, and probably breaking some of them. This breakage reveals freshly cleaved surfaces of CIGS generating the observed high intensity the PL emission and its redistribution towards higher energy bands.

Although a comparison of the PL spectra of the CIGS films before and after compression along with the CIGS solar cell devices would have added more information to this investigation [4.31].

4.4 Conclusion

$Cu(In,Ga)Se_2$ (CIGS) thin films deposited on the Mo-coated soda-lime glass substrates by selenisation of metallic precursors at 500 ℃ were found to be porous in nature resulting in the poor efficiency values. An approach of reducing the porosity was applied by mechanically compression at 25 MPa. The following conclusions were drawn:

(i) The compression reduces the porosity without changing the preferential orientation and elemental composition of the CIGS films.

(ii) The PL spectra reveal three broad and intense bands shifting towards the higher energies (*j*-shift) with increase in the excitation power indicating the high level of doping and compensation. With increasing temperature, a red shift in the band positions is revealed, which is a characteristic of the band tails generated by the spatial potential fluctuations.

(iii) The compression increases PL intensity by an order of magnitude, mostly increasing the relative intensities of the higher energy bands suggesting a reduction of non-radiative recombination. It also reduces the *j*-shift demonstrating an improvement of the structural quality.

The above observations clearly reflect an improvement in the CIGS film quality upon compression. However, a full range of mechanical compression applied on the CIGS films and its consequent impact on the electronic quality of the CIGS films can be studied with the use of metal foils to avoid the limitation of glass substrate due to cracking.

References

[4.1] C. Guillén and J. Herrero, "Structure, morphology and photoelectrochemical activity of $CuInSe_2$ thin films as determined by the characteristics of evaporated metallic precursors," *Solar Energy Materials and Solar Cells*, vol. 73, pp. 141-149, 2002.

[4.2] C. J. Hibberd, E. Chassaing, W. Liu, D. B. Mitzi, D. Lincot and A. N. Tiwari, "Non-vacuum methods for formation of $Cu(In,Ga)(Se,S)_2$ thin film photovoltaic absorbers," *Progress in Photovoltaics: Research and Applications*, vol. 18, pp. 434-452, 2010.

[4.3] M. Kaelin, D. Rudmann, F. Kurdesau, H. Zogg, T. Meyer and A. N. Tiwari, "Low-cost CIGS solar cells by paste coating and selenization," *Thin Solid Films*, vol. 480–481, pp. 486-490, 2005.

[4.4] Z. Wei, T. Shimell and H. M. Upadhyaya, "Optimisation Towards High-Efficiency 30cmx30cm-Size $Cu(In,Ga)Se_2$ Solar Cells Using an In-Line Co-Evaporation System," *Conference Record of the 26th European Photovoltaic Solar Energy Conference and Exhibition*, Hamburg, pp. 2840-2844, 2011.

[4.5] V. Alberts, J. Bekker, M. J. Witcomb, J. H. Schön and E. Bucher, "Control of VSe-defect levels in $CuInSe_2$ prepared by rapid thermal processing of metallic alloys," *Thin Solid Films*, vol. 361–362, pp. 432-436, 2000.

[4.6] H. Sugimoto, Y. Kawaguchi, Y. Yasaki, T. Aramoto, Y. Tanaka, H. Hakuma, S. Kuriyagawa and K. Kushiya, "Challenge to 18% Efficiency with $30x30cm_2$-Sized $Cu(InGa)(SeS)_2$ Submodules in Solar Frontier," *Conference Record of 26th European Photovoltaic Solar Energy Conference and Exhibition*, Hamburg, pp. 2307-2310, 2011.

[4.7] S. Verma, N. Orbey, R. W. Birkmire and T. W. F. Russell, "Chemical reaction analysis of copper indium selenization," *Progress in Photovoltaics: Research and Applications*, vol. 4, pp. 341-353, 1996.

[4.8] S. F. Chichibu, M. Sugiyama, M. Ohbasami, A. Hayakawa, T. Mizutani, H. Nakanishi, T. Negami and T. Wada, "Use of diethylselenide as a less-hazardous source for preparation of $CuInSe_2$ photo-absorbers by selenization of metal precursors," *Journal of Crystal Growth*, vol. 243, pp. 404-409, 2002.

[4.9] D. L. Schulz, C. J. Curtis, A. Cram, J. L. Alleman, A. Mason, R. J. Matson, J.D. Perkins and D.S. Ginley, "CIGS films via nanoparticle spray deposition: attempts at densifying a porous precursor," *Conference Record of the 26th IEEE Photovoltaic Specialists Conference*, California, pp. 483-486, 1997.

[4.10] T. Wada, J. Kubo, S. Yamazoe, A. Yamada and M. Konagai,"Fabrication of High Density $Cu(In,Ga)Se_2$ Films by Combination of Printing and Sintering Processes," *Conference Record of the 25th European Photovoltaic Solar Energy Conference and*

Exhibition/5th World Conference on Photovoltaic Energy Conversion, Valencia, pp. 3465-3467, 2010.

[4.11] S. B. Zhang, S.-H. Wei, A. Zunger and H. Katayama-Yoshida, "Defect physics of the $CuInSe_2$ chalcopyrite semiconductor," *Physical Review B*, vol. 57, pp. 9642-9656, 1998.

[4.12] A. Darga, D. Mencaraglia, Z. Djebbour, A. Migan Dubois, J. F. Guillemoles, J. P. Connolly, O. Roussel, D. Lincot, B. Canava and A. Etcheberry, "Two-step wet surface treatment influence on the electronic properties of $Cu(In,Ga)Se_2$ solar cells," *Thin Solid Films*, vol. 517, pp. 2550-2553, 2009.

[4.13] D. W. Lee, M. S. Seol, D. W. Kwak, J. S. Oh, J. H. Jeong and H. Y. Cho, "Hydrogen effects on deep level defects in proton implanted $Cu(In,Ga)Se_2$ based thin films," *Thin Solid Films*, vol. 520, pp. 6382-6385, 2012.

[4.14] M. V. Yakushev, R. W. Martin, F. Urquhart, A. V. Mudriy, H. W. Schock, J. Krustok, R. D. Pilkington, A. E. Hill and R. D. Tomlinson, "A Photoluminescence Study of Hydrogen-Implanted $Cu(InGa)Se_2$ Thin Films," *Japanese Journal of Applied Physics*, vol. 39S1, p. 320, 2000.

[4.15] M. V. Yakushev, R. W. Martin, J. Krustok, H. W. Schock, R. D. Pilkington, A. E. Hill and R. D. Tomlinson, "A PL study of CIGS thin films implanted with He and D ions," *Thin Solid Films*, vol. 361–362, pp. 488-493, 2000.

[4.16] S. Senthilarasu, T. A. N. Peiris, J. Garcá-Cañadas, and K. G. U. Wijayantha, "Preparation of Nanocrystalline TiO_2 Electrodes for Flexible Dye-Sensitized Solar Cells: Influence of Mechanical Compression," *The Journal of Physical Chemistry C*, vol. 116, pp. 19053-19061, 2012.

[4.17] H. M. Upadhyaya, N. Hirata, S. A. Haque, M.-A. de Paoli and J. R. Durrant, "Kinetic competition in flexible dye sensitised solar cells employing a series of polymer electrolytes," *Chemical Communications*, vol. 0, pp. 877-879, 2006.

[4.18] U. Rau and H. W. Schock, "Electronic properties of $Cu(In,Ga)Se_2$ heterojunction solar cells–recent achievements, current understanding, and future challenges," *Applied Physics A*, vol. 69, pp. 131-147, 1999.

[4.19] M. V. Yakushev, A. V. Mudryi, V. F. Gremenok, E. P. Zaretskaya, V. B. Zalesski, Y. Feofanov and R. W. Martin, "Influence of growth conditions on the structural quality of $Cu(InGa)Se_2$ and $CuInSe_2$ thin films," *Thin Solid Films*, vol. 451–452, pp. 133-136, 2004.

[4.20] J. J. Hopfield, D. G. Thomas and M. Gershenzon, "Pair Spectra in GaP," *Physical Review Letters*, vol. 10, pp. 162-164, 1963.

[4.21] B. I. Shklovskii and A. L. Efros, Translated by S. Luryi, *Electronic Properties of Doped Semiconductors*. Berlin: Springer, 1984.

[4.22] P. W. Yu, "Radiative recombination in melt-grown and Cd-implanted $CuInSe_2$," *Journal of Applied Physics*, vol. 47, pp. 677-684, 1976.

[4.23] I. Dirnstorfer, M. Wagner, D. M. Hofmann, M. D. Lampert, F. Karg and B. K. Meyer, "Characterization of $CuIn(Ga)Se_2$ Thin Films," *physica status solidi (a)*, vol. 168, pp. 163-175, 1998.

[4.24] J. Krustok, H. Collan, M.Yakushev and K. Hjelt, "The role of spatial potential fluctuations in the shape of the PL bands of multinary semiconductor compounds," *Physica Scripta*, vol. 1999, p. 179, 1999.

[4.25] S. A. Schumacher, J. R. Botha and V. Alberts, "Photoluminescence study of potential fluctuations in thin layers of $Cu(In_{0.75}Ga_{0.25})(S_ySe_{1-y})_2$," *Journal of Applied Physics*, vol. 99, pp. 063508-8, 2006.

[4.26] A. P. Levanyuk and V. V. Osipov, "Edge luminescence of direct-gap semiconductors," *Soviet Physics Uspekhi*, vol. 24, p. 187, 1981.

[4.27] A. Jagomägi, J. Krustok, J. Raudoja, M. Grossberg, M. Danilson and M. Yakushev, "Photoluminescence studies of heavily doped $CuInTe_2$ crystals," *Physica B: Condensed Matter*, vol. 337, pp. 369-374, 2003.

[4.28] T. Schmidt, K. Lischka and W. Zulehner, "Excitation-power dependence of the near-band-edge photoluminescence of semiconductors," *Physical Review B*, vol. 45, pp. 8989-8994, 1992.

[4.29] I. Repins, M. A. Contreras, B. Egaas, C. DeHart, J. Scharf, C. L. Perkins, B. To and R. Noufi, "19 9%-efficient ZnO/CdS/CuInGaSe$_2$ solar cell with 81 2% fill factor," *Progress in Photovoltaics: Research and Applications,* vol. 16, pp. 235-239, 2008.

[4.30] P. Jackson, D. Hariskos, E. Lotter, S. Paetel, R. Wuerz, R. Menner, W. Wischmann and M. Powalla, "New world record efficiency for Cu(In,Ga)Se$_2$ thin-film solar cells beyond 20%," *Progress in Photovoltaics: Research and Applications,* vol. 19, pp. 894-897, 2011.

[4.31] S. Shirakata and T. Nakada, "Time-resolved photoluminescence in Cu(In,Ga)Se$_2$ thin films and solar cells," *Thin Solid Films,* vol. 515, pp. 6151-6154, 2007.

Chapter 5 – Low temperature evaporated precursors and rapid thermal processing for CIGS solar cells

Abstract

An economic approach to prepare chalcopyrite Cu(In,Ga)Se_2 (CIGS) thin films using rapid thermal processing (RTP) of Cu-In-Ga-Se precursor grown with the help of standard effusion cells for the deposition of Cu, In, Ga and Se at low substrate temperature (<200 ℃) has the potential to reduce the manufacturing cost of solar cells significantly. This strategy was adapted for the first time to help simplify the control complexity and increase the production throughput in an industry environment. Annealing CIGS precursors using RTP in an excess Se environment enables CIGS films with remarkable large grain size and good crystallinity. Different ramping rates, precursor composition, annealing temperature and Na doping were investigated, especially from the point of view of tuning the reaction mechanism for the chalcopyrite formation. It has been found that the process parameters of the rapid thermal processing strongly depended on the composition of the precursor. Structural and compositional properties of CIGS layers were characterised with the scanning electron microscopy, X-ray fluorescence, *in-situ* and *ex-situ* X-ray diffraction. The photovoltaic properties of the CIGS solar cell devices were characterised with the current density-voltage and quantum efficiency measurements. CIGS solar cells with power conversion efficiencies up to 10.8% (without the top grid and anti-reflection coatings) have been achieved using rapid thermal processing. Analysis of material and photovoltaic properties suggest a further potential for optimisation of the process for an enhanced performance of the CIGS solar cells with lowering of the production cost.

5.1 Introduction

The simplified two-step process could possibly further improve the performance and lower the cost of the devices through volume production with some modifications such as preparation method of precursor, rapid thermal processing (RTP) [5.1-5.3], adjusting Ga grading profile [5.4, 5.5], alkaline elements (Na, K) incorporation [5.6, 5.7]. The CIGS precursors for the RTP application have been prepared in different ways to improve the film quality and device efficiency. The common methods are the sputtering of Cu-In-Ga and Na-compound and thermal evaporation of selenium (Se) [5.8, 5.9], co-evaporation of CIGS films at low temperature [5.10], co-sputtering of Cu-In-Ga [5.2, 5.11], electro-deposition of Cu-In-Ga [5.12], co-evaporation of $(In,Ga)_2Se_3$-NaF-CuSe (450 ℃/25 ℃/150 ℃) [5.13], printing of Cu-In-Ga-Se nanoparticle ink [5.14]. Certainly, the selection of the preparation method is focused on lowering the cost of the device. Although non-vacuum methods to prepare precursor for RTP application such as electro-deposition and printed inks are inexpensive to make, they suffer breaking the vacuum to load the samples into the RTP vacuum chamber which is not ideal for the inline large scale production. Thus, a novel precursor using the co-evaporation of two-layer structure of In-Ga-Se/Cu-Ga-Se(-NaF) (<200 ℃) (abbreviated as Cu-In-Ga-Se or C-I-G-S) has been designed and deposited in this work. The success of this work would provide a scope to design an inline system consisting of three interconnecting chambers comprising of a central load-lock chamber with an evaporation chamber and a RTP chamber connected either side. This configuration would avoid wasting energy to break the vacuum and exposing the samples in the open air.

From a commercial point of view, RTP is considered as an industrially favourable technology because it can offer low thermal budget, short process cycle and atmospheric processing pressure. The above advantages of RTP are crucial for the process development towards scale-up of the low cost and high throughput inline module fabrication. RTP is known as a method for achieving better quality of chalcopyrite layers by using extremely high ramping rates with or without the presence of chalcogens [5.2]. The RTP system (Fig. 5.1) normally uses the lamps to generate a fast ramping rate by the thermal radiation and a graphite or quartz susceptor to effectively absorb and uniformly distribute the thermal energy inside the chamber. From a material point of view, the advantages of RTP have been understood as the reduction of undesired phase formation for the phase-pure CIGS growth [5.15, 5.16], the

avoidance of overdose of Na from soda lime glass (SLG) [5.9, 5.17] and the improvement on the electronic properties of CIGS films and devices [5.2, 5.17].

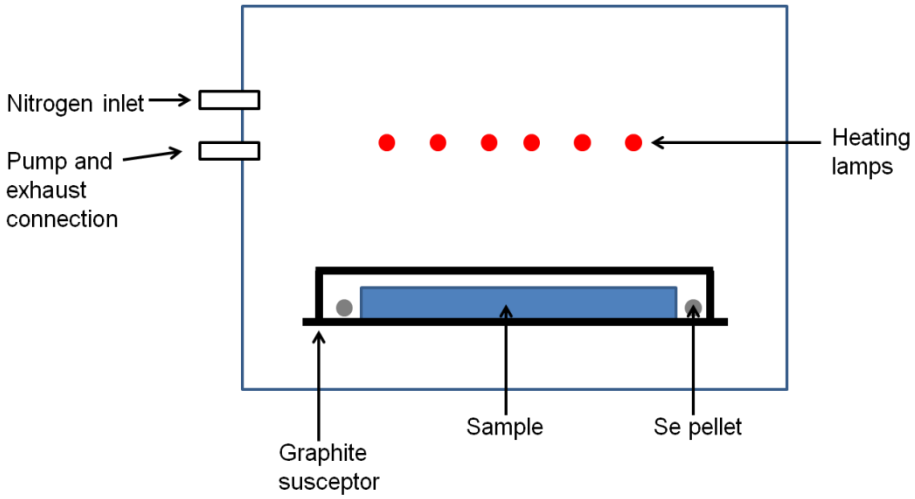

Figure 5.1: *Schematic of the rapid thermal processing system used to anneal the Cu-In-Ga-Se precursor layers.*

Apart from the ramping rates, the substrate temperature during annealing is another important process parameter for the chalcopyrite formation. In general, the efficiency of CIGS solar cells could be boosted by increasing the substrate temperature [5.10, 5.18, 5.19]. One major influence of the substrate temperature on the CIGS layers is changing the Ga grading profile [5.6, 5.20, 5.21], consequently, engineering of the band gap [5.22]. The CIGS layers with the optimally graded band gap normally have a superior device performance than those with the uniform band gap or highly graded band gap [5.5, 5.22]. An optimised Ga grading corresponds to a well graded band gap that could establish a quasi-electric field providing a drift field for carriers generated outside the depletion region to move towards the junction to be collected [5.22]. Another point that needs to be taken into account is the overheating of the substrate, which may create serious stress problems due to softening and bending of the glass [5.23].

Generally, high efficiency CIGS solar cells were grown preferably on SLG at substrate temperatures up to 600 ℃, because Na is introduced into CIGS by diffusion from SLG through Mo back contact. A huge amount of research works has been focused on the effects of Na-induced changes of the chalcopyrite formation. The beneficial effects of Na incorporation include changes of crystallinity and preferred grain orientation [5.24], an enhancement in p-type conductivity, passivation of defects [5.25, 5.26], and reduction of the inter-diffusions of Ga and In [5.24, 5.27], which enable a higher open

circuit voltage and fill factor. However, higher Na concentration (> 0.1 at%) could reduce the crystallinity of CIGS and grain size, and degrade the device performance [5.26, 5.28, 5.29]. The formation of Na_2Se_x during CIGS growth has been proposed to assist the reactions especially at the grain boundaries [5.30]. Rudmann reported the co-evaporation of the different amount of NaF during 1st stage or 2nd stage on both alkaline-free glass and soda lime glass using the standard three-stage process [5.27]. The lowest Na concentrations are found typically corresponding to the lowest [Ga]/[In] concentration ratio, where the largest grains are located. Apparently, this observation confirms the grain-boundary density through the absorber is closely related to the Na profiles. Based on the above, a novel approach was proposed in this work using slight amount of Na doping in the two-layer precursors. The addition of Na into C-I-G-S precursors could reduce the crystallinity and grain size for a better re-crystallisation using RTP in the presence of Se [5.31, 5.32].

This chapter presents the chalcopyrite CIGS formation using a two-step process including the preparation of Cu-In-Ga-Se precursors through evaporation and subsequently rapid annealing processing of the precursors. The importance of fast ramping rates, presence of Se, high annealing temperature for achieving large grain, phase-pure and highly crystallinity of CIGS films have been discussed. The role of sodium in re-crystallisation of CIGS was demonstrated taking into account several binary and ternary reaction mechanisms.

5.2 Experimental techniques

5.2.1 Experiments

All devices were grown on 1 mm thick soda lime glass. 600 nm thick Mo back contacts were deposited by DC sputtering with sheet resistance ~0.2 Ω/square. The two-layer structure of In-Ga-Se/Cu-Ga-Se (with or without co-evaporated NaF) (<200 ℃) (abbreviated as C-I-G-S) precursor layers were grown in a high-vacuum evaporation chamber at the base pressure ~10^{-8} hPa with multiple effusion cells capable for the deposition of Cu, In, Ga, Se and NaF. The CIGS films were formed by employing rapid thermal processing in a graphite box at an atmospheric pressure approximately. Annealing at 500-550 ℃ for 5-10 minutes was performed by IR-radiation using halogen lamps that enable heating rates up to 10 ℃/s. A homogeneous temperature distribution inside the graphite box was measured using four thermocouples across the heating region. The p-n junction was completed by chemical bath deposition of 60 nm thick

CdS. An i-ZnO/ZnO:Al window layer as top contact was grown using RF sputtering. The finished solar cell was defined into several single cells by mechanical scribing.

5.2.2 Characterisations

The characterisation techniques including XRF, SEM, XRD, *J-V* and EQE measurements were described in details in *Section 3.2.1 and 3.2.2*, Chapter 3. *In-situ* XRD was carried out using a PANalytical X'Pert ProMPD system with Ni-filtered Cu-K_α radiation in grazing angle geometry at an incident angle of 5 ° and 10 °. The substrate heating at 20 ℃/min from room temperature to 550 ℃ under N_2 atmosphere was performed using an Anton-Paar XRK 900 heating chamber. XRD patterns were recorded every 10 ℃ in the temperature range of 100-550 ℃ and each scan covers the 2θ in the range of 15-60 ° for about 15 minutes.

5.3 Results and discussion

5.3.1 Rapid thermal processing assisted chalcopyrite grain growth

5.3.1.1 Effects of ramping rates of annealing on structural and compositional properties

SEM is used to characterise the structural properties of the CIGS precursor grown at low substrate temperature (<200 ℃) and annealed CIGS layers in both N_2 and Se environment using rapid thermal processing (RTP) at 500 ℃. Fig. 5.2 shows the images of the cross-section and surface morphologies of CIGS films.

Typical thicknesses of the CIGS layers were in the range of 1.8–2.1 μm for all devices presented here. The structural morphologies of an evaporated C-I-G-S precursor (Fig. 5.2a) show a narrow columnar grain structure at the bottom part of the layer and a relative rough surface accompanied with small grains. A comparison of micrographs of CIGS films obtained by RTP of the C-I-G-S precursors in N_2 at atmospheric pressure with the ramping rates in the range of 0.25-8 ℃/s (Fig. 5.2b-e) shows a quite pronounced reduction in the grain size with decrease in the ramping rates. Remarkably, a very uniform film with large grains (>2 μm) and only a few voids on the surface (Fig. 5.2b) was grown with the ramping rate of 8 ℃/s. This indicates that it is possible to prepare CIGS films easily using this two-step process approach with the size of larger grains up to 2 μm. Concerning the grain boundaries, one of the most important features is that more horizontal grain boundaries were formed in the CIGS layer as the ramping rates of RTP decreased. These horizontal grain boundaries have been predicted to be

detrimental to the solar cell performance, which should be avoided in the absorber layer [5.33, 5.34]. There are voids and crevices appearing at the surface of the CIGS absorbers (Fig. 5.2b-e). This may be caused by the conversion of the $Cu_{2-x}Se$ into chalcopyrites as an indirect Cu source [5.35]. Fig. 5.2f presents the CIGS formation using RTP to anneal the precursors in Se at atmospheric pressure with the ramping rate of 8 ℃/s. The grain size is comparable to the CIGS processed in N_2, but it shows a better defined grain structure than the one in Fig. 5.2b. The cross-section and surface images of Fig. 5.2b suggests that there are lamellar arrangements within the large grain. In case of Fig. 5.2f, the grains become much larger with small grains resting on the top surface adding to the surface roughness. This may be expected as Fig. 5.2f images are representative microstructure of the RTP conducted under Se atmosphere which would ensure better conversion of CIGS phase.

Table 5.1: The composition parameters [Ga]/([Ga]+[In]), [Cu]/([Ga]+[In]) and at% Se as determined by XRF of (a) C-I-G-S precursor and annealed CIGS films obtained by different ramping rates using RTP annealing: (b) 8 ℃/s in N_2, (c) 3 ℃/s in N_2, (d) 1 ℃/s in N_2, (e) 0.25 ℃/s in N_2 and (f) 8 ℃/s in Se.

Sample	[Ga]/([Ga]+[In])	[Cu]/([Ga]+[In])	at% Se
a (precursor)	0.39	0.85	51
b	0.39	0.82	51
c	0.39	0.82	50
d	0.37	0.79	50
e	0.37	0.78	51
f	0.37	0.80	53

In table 5.1, the compositional ratios GGI, CGI and at% Se of the C-I-G-S precursor and the CIGS films in this sections as measured by XRF are summarised. The Ga contents are in the range of 0.37-0.39, which are slightly higher than the highly efficient devices in literature [5.4, 5.36]. Cu content is in the range of 0.78-0.82, which doesn't vary much for all these CIGS films. However, the Se composition of the film annealed in the Se ambient is 2-3 at% higher than the ones annealed in N_2. This could be an indication of Se-deficiency in CIGS films grown under N_2 atmosphere.

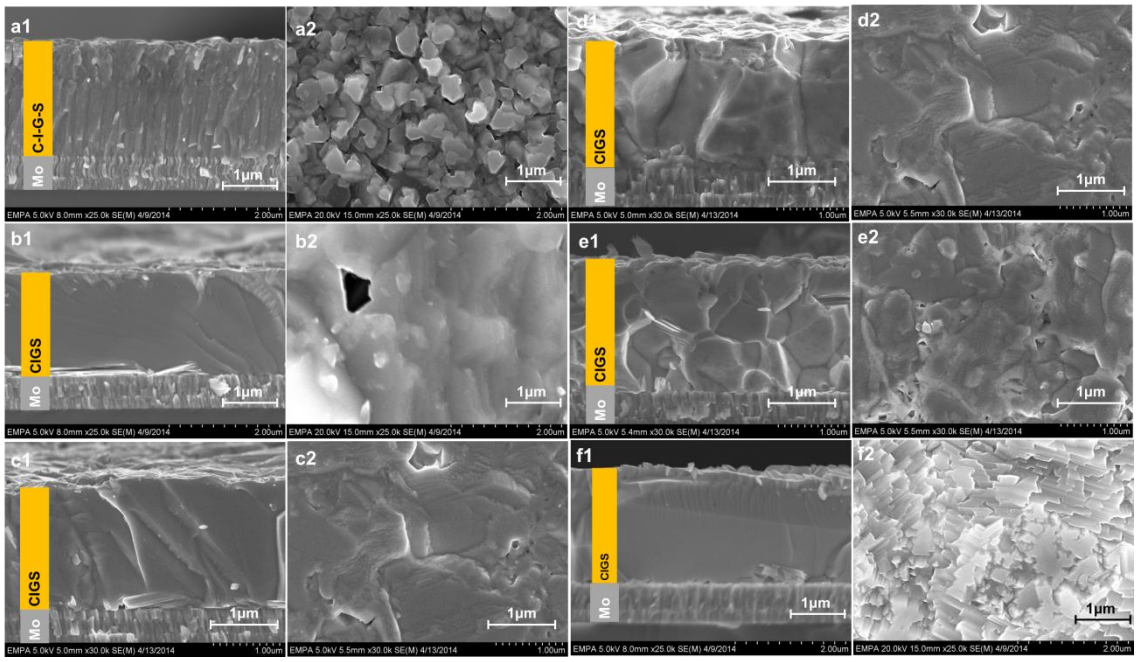

Figure 5.2: *SEM (a1) cross-sections and (a2) corresponding surface morphologies of the bare C-I-G-S precursor. SEM of CIGS layers on Mo coated glass obtained by different ramping rates using RTP annealing at 500 ℃ for 10 minutes: (b1) cross-section and (b2) surface of CIGS with 8 ℃/s in N_2, (c1) cross-section and (c2) surface of CIGS with 3 ℃/s in N_2, (d1) cross-section and (d2) surface of CIGS with 1 ℃/s in N_2, (e1) cross-section and (e2) surface of CIGS with 0.25 ℃/s in N_2 and (f1) cross-section and (f2) surface of CIGS with 8 ℃/s in Se. The black area in (b2) is a micron-size void.*

The XRD patterns of the CIGS absorber grown with different ramping rates in the range of 0.25-8 ℃/s using a RTP furnace are shown in Fig. 5.3. The two main Cu(In,Ga)Se_2 (JCPDS 35-1102) peaks of (112) and (220)/(204) are found in all these films. A pronounced γ-InSe (JCPDS 01-071-0354) peak appears in the films annealed in N_2, which may suggest insufficient Se for the complete chalcopyrite formation. The intensity of the InSe peak decreases as the ramping rate decreases. The InSe may also lead to formation of voids as shown in Fig. 5.2b, which could form shunt paths in the solar cell device. A closer look in Fig. 5.3 at the peak position of (220)/(204) CIGS peaks could be used to give an insight into the gallium incorporation into the CIGS films [5.4, 5.20]. Therefore, the estimation on the graded Ga profiles could be carried out with the help of XRD studies. All the patterns revealed that the GGI ratio was in the range of 0.3-0.4. The sample (c) in Fig. 5.3 has the narrowest peak width as compared to other samples. The overall variation appears to be a characteristic smooth Ga grading profile. However, the further investigation with other techniques such as the secondary

ion mass spectrometry (SIMS) would be necessary to confirm the actual depth profile of these metal ratios.

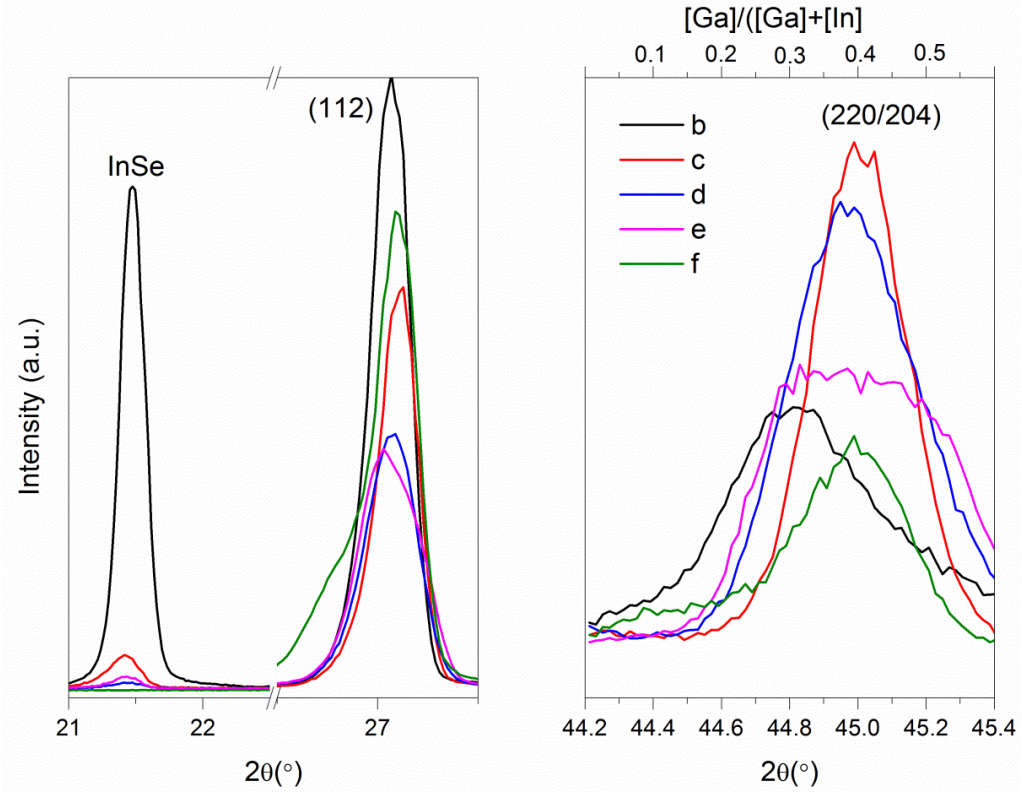

Figure 5.3: *Corresponding XRD patterns of the CIGS layers on Mo coated glass with different ramping rates using RTP annealing: (b) 8 ℃/s in N_2, (c) 3 ℃/s in N_2, (d) 1 ℃/s in N_2, (e) 0.25 ℃/s in N_2, and (f) 8 ℃/s in Se. The two main peaks (112) and (220)/(204) of CIGS films are indicated.*

5.3.1.2 Reaction mechanisms

To elucidate the origin of morphological changes and impurity phases, *in-situ* XRD measurements were employed for the C-I-G-S precursor. Due to the limitation of the maximum ramping rate and the highest scanning speed of the *in-situ* XRD set-up, only slow ramping (20 ℃/minute ≈ 0.33 ℃/s) could be performed in this set of experiments. The secondary phases formed in this ramping rate may not appear in the RTP process with the quicker ramping rates. Fig. 5.4 shows the temperature dependent phase evolution within the CIGS films with of the help of respective diffractograms. Two pressure conditions of 5 mbar and N_2 atmospheric pressure were selected to mimic the pressure condition used in the RTP process. No additional Se was supplied in the annealing chamber.

Firstly, the low temperature regime from 100 to 230 ℃ is dominated by the crystallisation of cubic $Cu_{2-x}Se$ (JCPDS 06-680) in both pressure conditions.

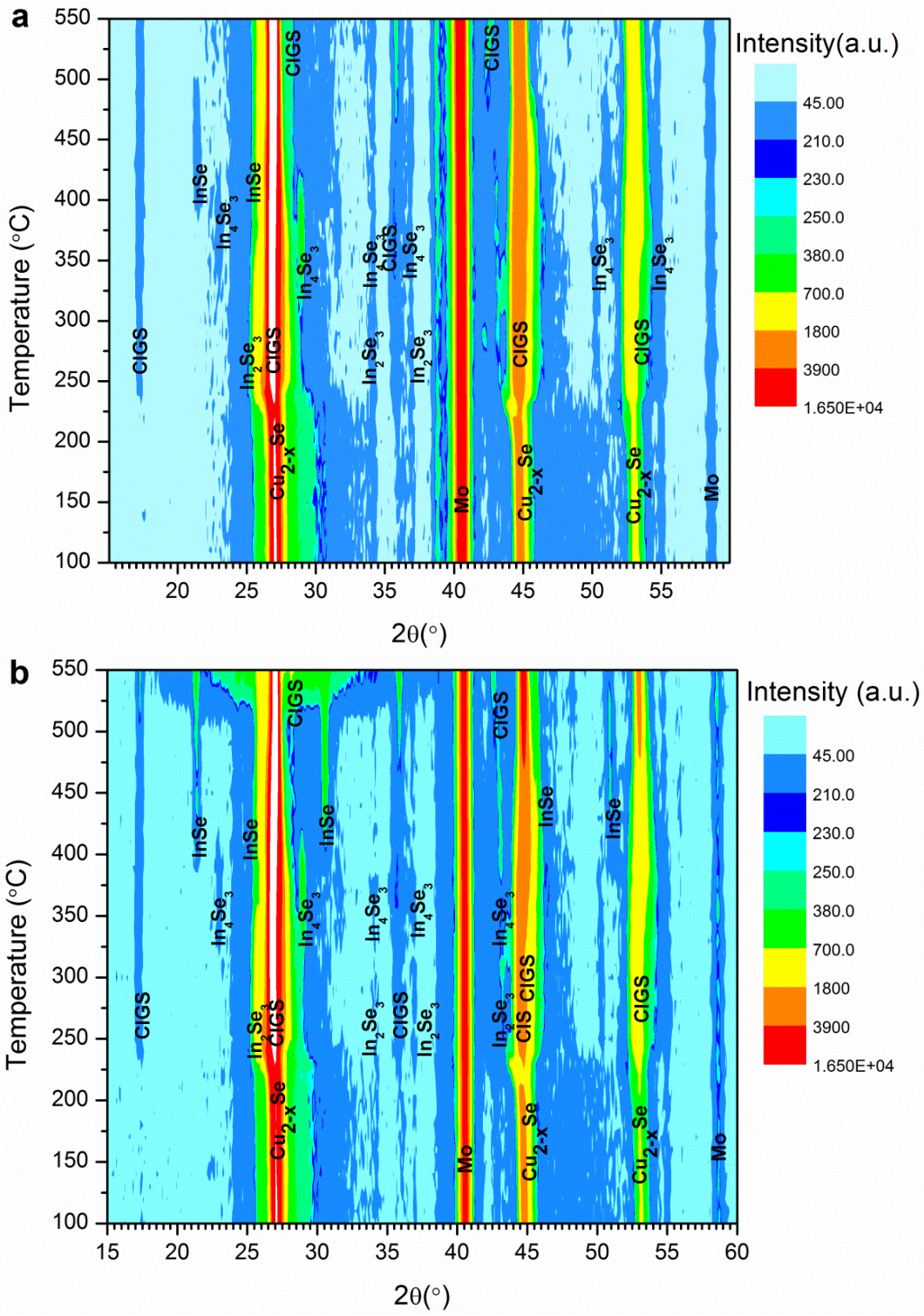

Figure 5.4: *In-situ XRD measurements during annealing of C-I-G-S precursor from 100 to 550 ℃ in N_2 at different pressure: (a) 5 mbar and (b) atmospheric pressure. Pronounced $Cu_{2-x}Se$ phases formed in the precursor and persist until around 250 ℃. At around 230 ℃, the first peaks of CIGS/CIS evolve. Between 250 and 500 ℃, In-Se phases react with the residual Cu-Se to form CIGS alloy.*

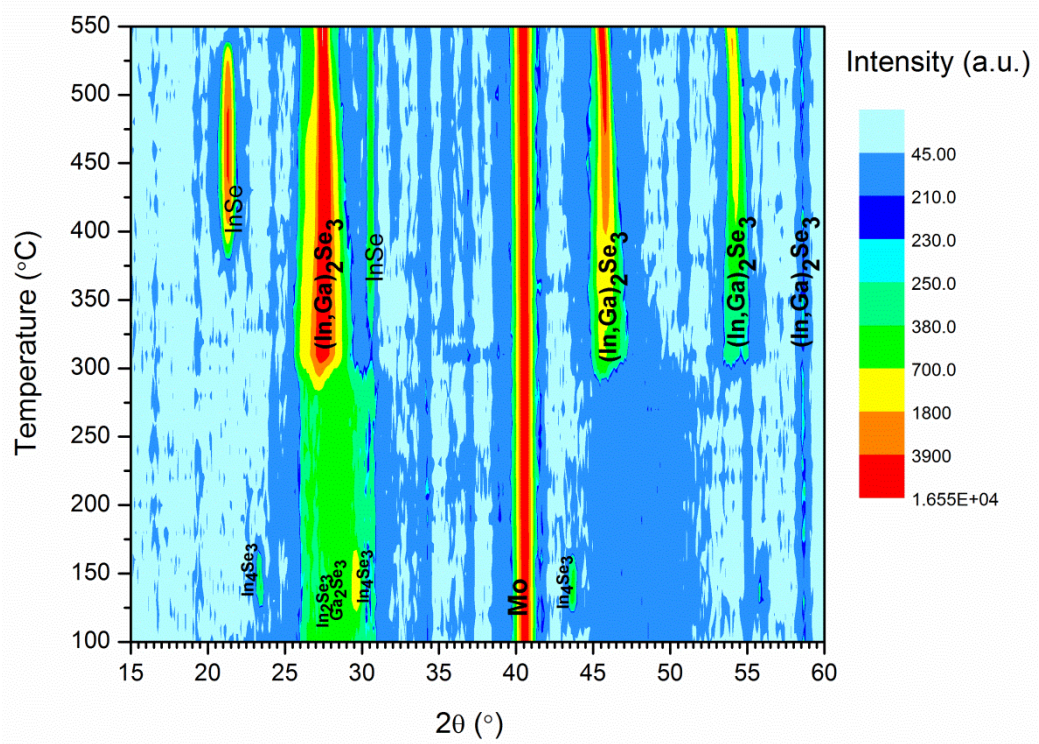

Figure 5.5: *In-situ XRD measurements during annealing of bottom InGaSe precursor from 100 to 550 ℃ in N_2 at the pressure of 5 mbar. A broad peak contains In_2Se_3 and Ga_2Se_3 phases formed in the precursor and persist until around 300 ℃. From 130 to 160 ℃, three In_4Se_3 peaks existed in the film. Approaching 300 ℃, the first peaks of $(In,Ga)_2Se_3$ evolve. Above 325 ℃, In-Se phases co-exist with the dominate $(In,Ga)_2Se_3$ phases of the film.*

In the pressure of 5 mbar, the formation of hexagonal γ-In_2Se_3 (JCPDS 01-089-0658) is visible starting at around 210°C until 300°C whereas γ-In_2Se_3 exists from 220 to 350 ℃ at atmospheric pressure. The first CIS (JCPDS 40-1487) or Cu(In,Ga)Se_2 (JCPDS 35-1102) peaks appear as tetragonal crystal structure around 250 ℃ at 5 mbar, which is 20 ℃ higher than the sample annealed in the N_2 atmospheric pressure. Almost simultaneous appearance of the γ-In_2Se_3 and CIS/CIGS phases suggests the possible reaction taking place in the films [5.31, 5.37]:

$$Cu_2Se + In_2Se_3 \rightarrow 2\ CuInSe_2 \quad (5.1)$$

$$Cu_2Se + Ga_2Se_3 \rightarrow 2\ CuGaSe_2 \quad (5.2)$$

After the formation of CIS and CGS as shown in reactions (5.1) and (5.2), the CIGS alloy could be formed by inter-diffusion of In and Ga. For both cases, the In_4Se_3 is prevailing as orthorhombic lattice (JCPDS 48-1575) from 320–420 ℃. At 390 ℃, In_4Se_3

seems to be converted into γ-InSe (JCPDS 01-071-0354) as trigonal form for both cases. InSe exists until 490 ℃ at 5 mbar. In the case of atmospheric pressure, InSe appears as a secondary phase in the CIGS film even after 550 ℃. These InSe peaks are also obtained from RTP processed CIGS films as shown in Fig. 5.3. Thus, it suggests the possible reactions at the high temperature regime as follows [5.31, 5.37, 5.38]:

$$In_4Se_3 + Se \rightarrow 4\ InSe \quad (5.3)$$

$$Cu_2Se + 2\ InSe + Se \rightarrow 2\ CuInSe_2 \quad (5.4)$$

The reaction (5.2) may apply to explain the formation of CIGS rather than pure CIS or CGS. The CGS or secondary phases of Ga compounds were not directly obtained due to the very limited amount of these compounds. Then a bottom layer of the C-I-G-S precursor contains only In-Ga-Se that was annealed to reveal the possible existence of the Ga. It is thought that this additional experiment can provide further insight into the reaction mechanism for the CIGS formation in the applied techniques.

The phase evolution of the bottom layer of the C-I-G-S precursor was analysed using *in-situ* XRD as shown in Fig. 5.5. From 100 to 300 ℃, the hexagonal γ-In_2Se_3 (JCPDS 01-089-0658) and the monoclinic β-Ga_2Se_3 (JCPDS 14-1012) are prevailing as a mixed broad peak. Three peaks of the In_4Se_3 as orthorhombic form (JCPDS 48-1575) appears for a short while from 130 to 160 ℃. The targeted ternary compound $(In,Ga)_2Se_3$ (JCPDS 01-070-6611) dominates the phases of the film after 300 ℃. γ-InSe (JCPDS 01-071-0354) as the trigonal form is prevailing at 320 ℃ and remains until 550 ℃. A confirmation could be drawn here that the presence of Ga in the precursor film did appear in the CIGS precursor as Ga_2Se_3 and $(In,Ga)_2Se_3$. Thus, the proposed reaction (5.2) is valid in the CIGS formation.

The other possible reaction routes through annealing of the complete C-I-G-S precursors are:

$$3\ (In,Ga)_2Se_3 + 2\ Cu + Se \rightarrow 2\ Cu(In,Ga)_3Se_5 \quad (5.5)$$

$$Cu(In,Ga)_3Se_5 + 2\ Cu + Se \rightarrow 3\ Cu(In,Ga)\ Se_2 \quad (5.6)$$

Reactions (5.5) and (5.6) normally appear the chalcopyrite phase formation in the three-stage process [5.39]. Nevertheless, it may not happen in the present investigation using

RTP process with the low temperature precursors. For precursors grown at low substrate temperature and rapid ramping in the RTP, the potential mechanism may be proposed as:

$$(In,Ga)_2Se_3+Cu_2Se \rightarrow 2\ Cu(In,Ga)Se_2 \quad (5.7)$$

The above phase transformations and reaction mechanisms are most suitable for the slow ramping rate; some reactions may not apply to or only existed for extremely short time in the RTP process. However, the rapid heating could avoid the formation of some secondary phases, and hence directly form well crystallised CIGS films [5.2, 5.16, 5.40, 5.41].

5.3.1.3 Device performance and photovoltaic properties

The samples (b-f) were used to fabricate the solar cell devices. However, all the samples (b-e) annealed in the N_2 were shunted, only sample f prepared in the Se atmosphere showed a photovoltaic response. This suggests the degradation of CIGS absorber in N_2 may be caused by the re-evaporation of Se from the precursor, due to the high vapour pressure of Se.

Solar cells employing the absorber layers from this process annealed in Se exhibited a maximum efficiency of 3.9% on a total area of 0.09 cm^2 without top grid and AR-coating as shown in Fig. 5.6. Although the absorber layer annealed in Se exhibits good crystallinity, consists of fairly big grains (Fig. 5.2f), and have quite high Ga content of 0.37 (as determined by XRF studies in *Section 5.3.1.1*, table 5.1), all the photovoltaic parameters are low compared to the solar cell prepared in the standard three-stage process reported in literature [5.3]. The low efficiency is mainly due to the very low open-circuit voltage of 0.307 V. The light-to-dark crossover (Fig. 5.6A) was observed for this CIGS solar cell which could be caused by photoconductive effects or a light-dependent electron barrier at the interface between the absorber and buffer layers, and hence increase the recombination at the interface [5.45].

From EQE measurements (Fig. 5.6b), the low current collection at the long wavelength region is clearly evident, which could be correlated to the low diffusion length of carriers. Other reasons such as high interface and bulk recombination caused by pronounced defects in the absorber layers may also be responsible for the low efficiency. The minimum band gap of 1.17 eV can be calculated from the absorption

onset of the EQE curve (as shown in the inset of Fig. 5.6b), which is lower than the average band gap value (1.21 eV) estimated from XRF measurement (table 5.1). Further experiments have been carried out to optimise the device performance with the introduction of more Se during the RTP annealing process, as discussed in the following sections.

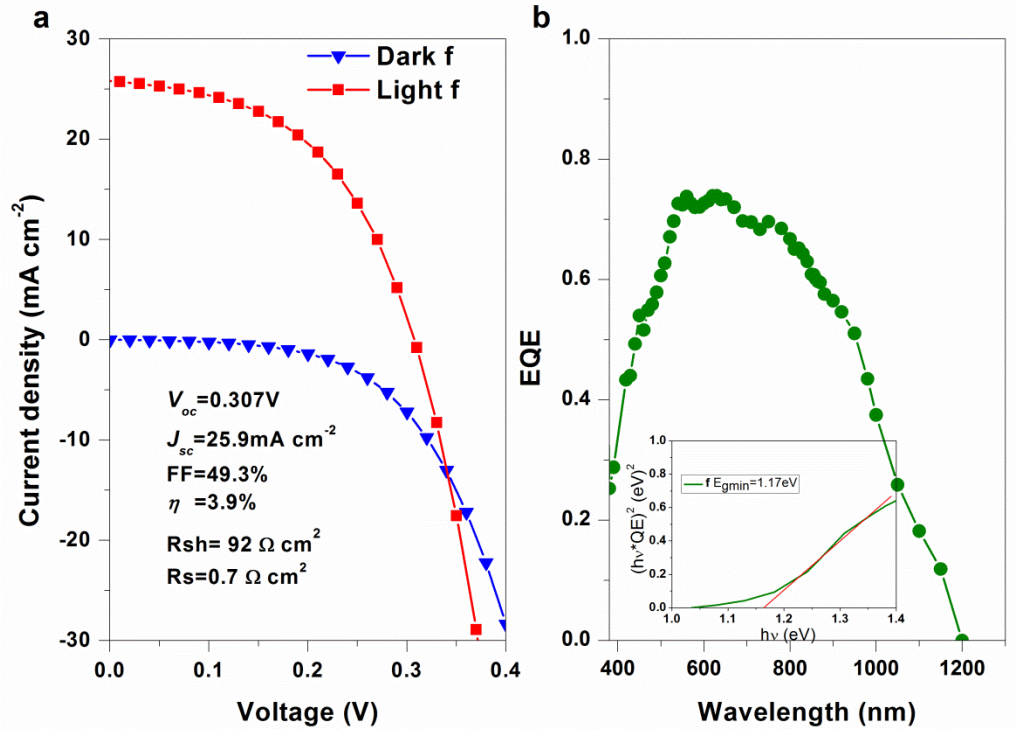

Figure 5.6: *J-V (a) and EQE (b) curves of CIGS solar cells grown with the annealed precursor in Se at atmospheric pressure. The minimum band gap was derived to be 1.17 eV.*

5.3.2 Effects of the higher annealing temperature and the precursor composition

5.3.2.1 Higher ramping rate and higher annealing temperatures

In this section, the effects of the higher ramping rate (10 ℃/s) and the higher temperatures (>500 ℃) on the CIGS film annealed from the low temperature C-I-G-S precursor were investigated. From the previous section, the Se can re-evaporate from the precursor layer during RTP. Hence, more Se had to be used to compensate the loss during RTP.

In table 5.2, the compositional ratios GGI, CGI and at% Se of the C-I-G-S precursor and the CIGS films annealed at 500 ℃, 525 ℃ and 550 ℃ with the ramping rate of 10 ℃/s as measured by XRF have been summarised. The GGI of the precursor and the annealed films are maintained at around 0.39. However, CGI of the annealed films are

reduced from 0.85 to about 0.80. For Se composition, only sample *d* annealed at 550 ℃ shows 2% higher than sample *a*-*c*. The band gap can be derived from Ga composition values using equation 1.4 as 1.23 eV for all three samples.

Table 5.2: The composition parameters [Ga]/([Ga]+[In]), [Cu]/([Ga]+[In]) and at% Se as determined by XRF of (a) C-I-G-S precursor and annealed CIGS films obtained at different substrate temperatures using the RTP annealing with the ramping rate of 10 ℃/s for 5 minutes: (b) 500 ℃ in Se, (c) 525 ℃ in Se and (d) 550 ℃ in Se.

Sample	[Ga]/([Ga]+[In])	[Cu]/([Ga]+[In])	at% Se
a (precursor)	0.39	0.85	54
b	0.39	0.81	54
c	0.38	0.80	54
d	0.39	0.80	56

The cross-section and surface morphologies of CIGS films (samples *b*, *c* and *d*) obtained by RTP of the C-I-G-S precursor (*a* in table 5.2) with ramping rate of 10 ℃/s at 500 ℃, 525 ℃ and 550 ℃ in Se are shown in Fig. 5.7, respectively. A pronounced increase in the grain size with increased annealing temperature has been obtained. In Fig. 5.7b2, the CIGS film with thickness of around 2 μm prepared at 500 ℃ shows a two-layer structure. The upper part of the absorber appeared to be a combination of large grains (~1μm) and small grains (~ 300 nm). The bottom part of the absorber contains a compact layer of small grains with the grain size below 200 nm. The small grains normally stem from Ga-rich CIGS phases [5.27]. The formation of this two-layer structure has been assumed to be due to overdose of Se in the film [5.32]. Fig. 5.7b2 shows a relatively rough surface of the CIGS film prepared at 500 ℃. The CIGS film with the thickness of around 1.7 μm grown at 525 ℃ (Fig. 5.7c2) shows a significantly increased grain size up to 2 μm and improved surface uniformity. The two-layer structure is still visible and some voids appear at the boundary between these two layers. However, some parts of larger grains from the upper layer extend to the bottom layer towards the Mo (Fig. 5.7c1). For the CIGS films with the thickness of around 2 μm (Fig. 5.7d) grown at 550 ℃, a uniform film is obtained with the largest grains up to 3 μm as compared to sample *b* and *c* (Fig. 5.7b and c). The voids and horizontal grain boundaries are visible in the cross-section of this film (Fig. 5.7d1).

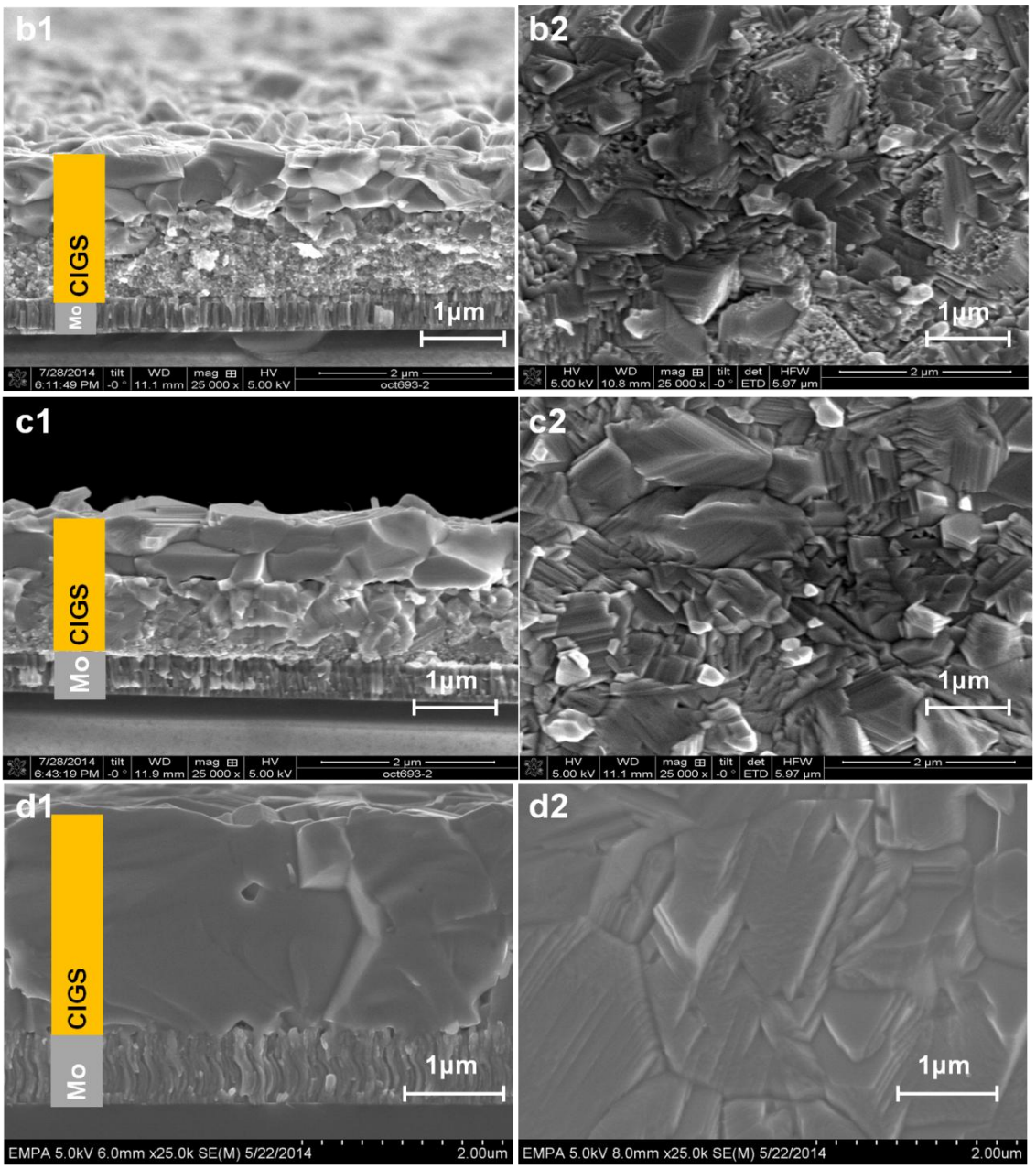

Figure 5.7: *SEM micrographs of CIGS films obtained at different substrate temperatures using the RTP annealing with the ramping rate of 10 ℃/s for 5 minutes: (b1) cross-section and (b2) surface at 500 ℃ in Se,(b1) cross-section and (b2) surface at 525 ℃ in Se and (d1) cross-section and (d2) surface at 550 ℃ in Se.*

X-ray diffraction (XRD) is used to characterise the structural and compositional properties of the CIGS layers. Fig. 5.8 shows the main peaks (112) and (220)/(204) of the CIGS phases from the films grown with different substrate temperatures. The intensity ratios between (112) and (220)/(204) peaks are 4.4, 4.4 and 4.3 for sample *b*, *c* and *d* respectively. Main focus for better device performance was on the crystallinity of films and Ga incorporation of these films as follows.

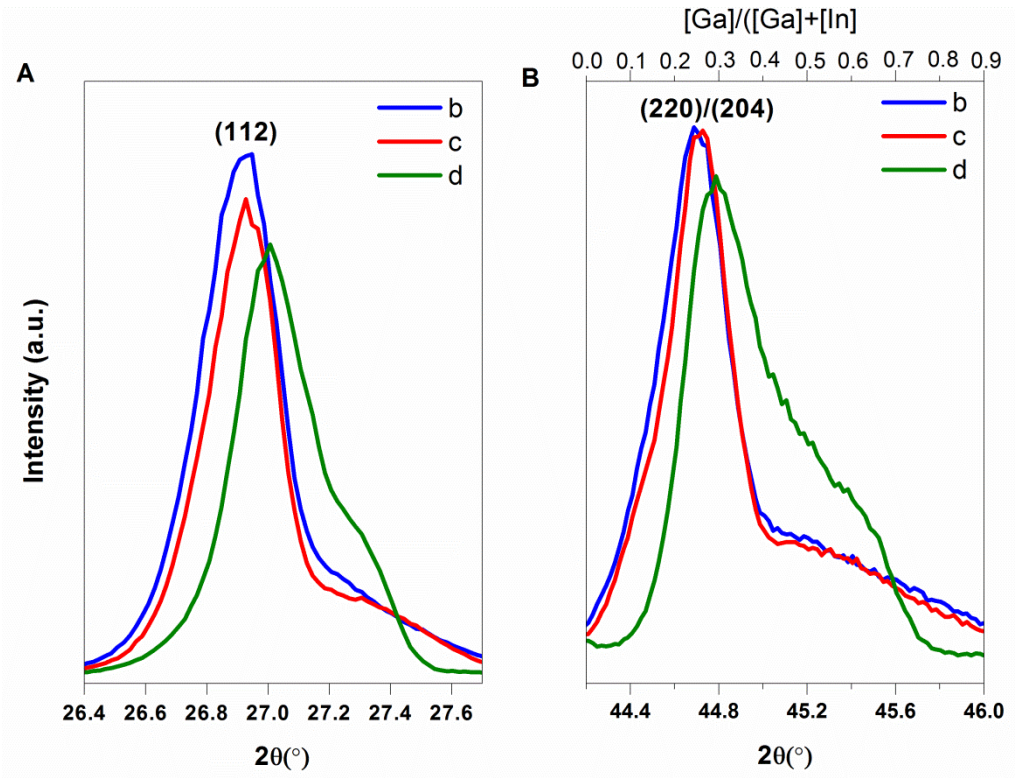

Figure 5.8: *XRD patterns of CIGS films obtained at different substrate temperatures using the RTP with the ramping rate of 10 ℃/s for 5 minutes: (b) 500 ℃ in Se, (c) 525 ℃ in Se and (d) 550 ℃ in Se. The two main peaks (112) (A) and (220)/(204) (B) of the CIGS films were indicated.*

For a closer look at the (112) CIGS peaks (Fig. 5.8A), sample *c* with the annealing temperature of 525 ℃ exhibits the smallest FWHM, which normally means the highest Ga incorporation and crystal quality. However, (112) peak of sample *d* are located at higher diffraction angle, which could indicate a higher Ga composition [5.4]. In Fig. 5.8B, a more pronounced shift of (220)/(204) peaks was observed towards higher diffraction angles for sample *d* as compared to sample *b* and *c*. In case of sample *b* and *c*, a shoulder towards higher diffraction angles indicates almost no intermixing of In and Ga has happened and most of the Ga remained in the lower layer with only very small grains as shown in Fig. 5.7b1. For sample *d*, the shoulder is higher and closer to the main peak, indicating a smoother Ga grading profile. However, investigation with other techniques such as the SIMS is again necessary to confirm the actual depth profile of these metal ratios.

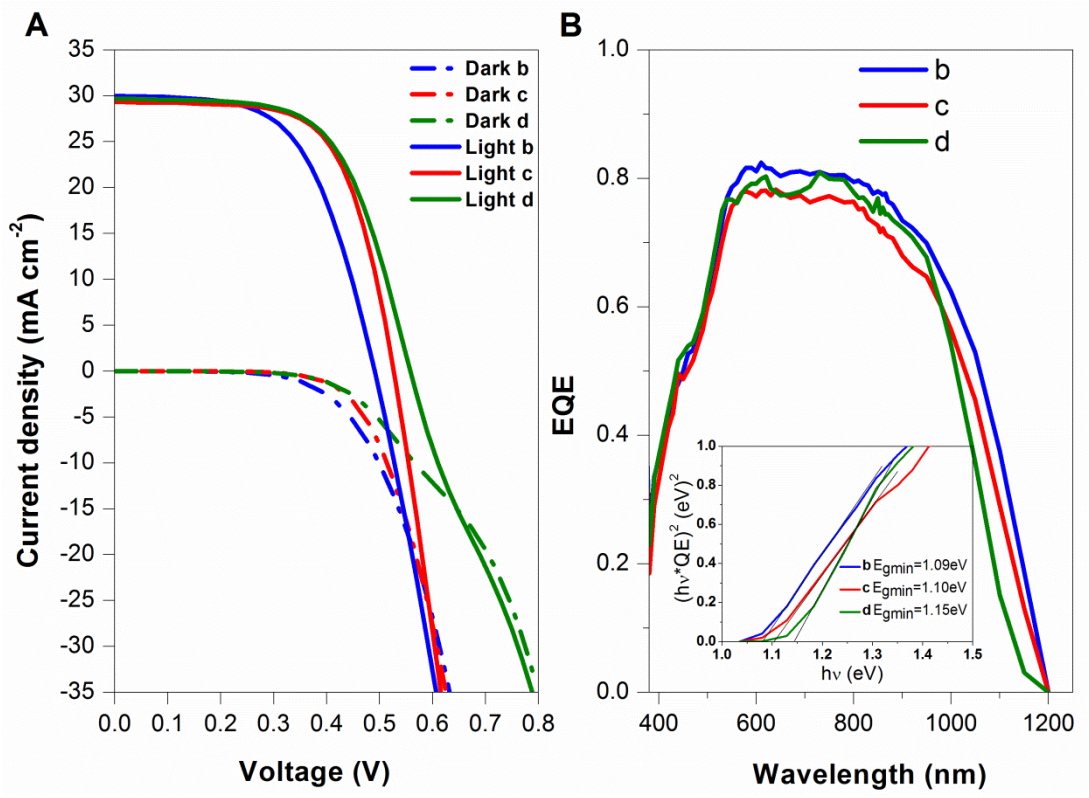

Figure 5.9: *(A) J-V and (B) EQE measurements for three champion devices of absorbers from annealed C-I-G-S precursor layers with the substrate temperatures of (b) 500 ℃, (c) 525 ℃ and (d) 550 ℃ show up to 8.5%, 10.1% and 10.2% efficiencies, respectively. The minimum band gaps were derived to be 1.09 eV, 1.10 eV and 1.15 eV for CIGS solar cells b, c and d, respectively.*

Table 5.3: PV parameters of solar cells grown with the substrate temperatures of (b) 500 ℃, (c) 525 ℃ and (d) 550 ℃.

Sample	η (%)	V_{oc} (V)	J_{sc} (mA cm^{-2})	FF (%)	R_{sh} (Ω cm^2)	R_s (Ω cm^2)
b	8.5	0.491	30.0	57.8	1624	2
c	10.1	0.527	29.3	65.1	2500	1.1
d	10.2	0.558	29.7	61.4	3623	5.2

The current-voltage characteristics of the solar cells grown with the different substrate temperatures using the RTP are shown in Fig. 5.9A. The corresponding photovoltaic parameters are given in table 5.3. The device with the CIGS absorber grown at 550 ℃ exhibits an efficiency of 10.2% without the antireflection coating. This device stands out of the three mainly due to the highest open-circuit voltage (V_{oc}) and highest shunt resistance (R_{sh}). The very high series resistance (R_s) may reduce the fill factor (FF) and short-circuit current (J_{sc}). While sample *c* has a comparable performance with sample *d*, the smallest R_s and best FF but lower V_{oc} result in a slightly lower efficiency. Sample *b*

grown at 500 ℃ exhibits the lowest V_{oc} and FF, which has not enough J_{sc} to compensate the gross loss, and hence the lowest efficiency has been obtained. It has been observed that the superior performance for devices with the CIGS absorber grown at 550 ℃ is likely to be related with the increased substrate temperatures at the same ramping rate using RTP. The highest annealing temperature provides the significantly improved V_{oc}, which may be due to the better intermixing of In and Ga (better Ga incorporated into CIGS) as confirmed from the XRD (Fig. 5.8). The light-to-dark crossover (Fig. 5.9A) was observed for three CIGS solar cell devices which lead to increased interface recombination as discussed in *Section 5.3.1.3* and Chapter 3.

Fig. 5.9B shows the external quantum efficiency measurements of solar cells obtained with different substrate temperature. The low response in the short wavelength below 500 nm may probably be due to a relative thick CdS buffer layer (70-80 nm). At the wavelength below 1000 nm, the reduced EQE is mainly attributed to the parasitic absorption and reflection losses of thicker TCO layers (~650 nm) as compared to the thickness of TCO layer (~250 nm) in the highly efficient CIGS devices [5.4]. At the wavelength in the range of 600-900 nm, the EQE of sample *c* is slightly lower than sample *b* and *d* due to lower thickness of the sample *c*. A clear difference in the spectra appears in the near infrared region above 1000 nm. The cut-off wavelength in this region corresponds to the region with the lowest Ga content. The minimum band gaps were calculated from the absorption onset of the EQE (inset in Fig. 5.9B) as 1.09 eV for sample *b*, 1.10 eV for sample *c*, and 1.15 eV for sample *d*.

However, all the PV parameters of the champion device are still lower than the highly efficient devices reported in literature [5.7]. Further optimisation is required to improve the device performance, which suffers from the low V_{oc} and relatively less J_{sc} values. The results are encouraging considering the novel approach utilised in the present study and the investigation performed are only at very initial phase. This suggests that the improvement on the device performance through RTP processed CIGS precursor can be expected by modifying the Ga content and grading profile in the precursor layers.

5.3.2.2 Variation of the precursor composition

Following the indications of the results from *Section 5.3.2.1*, a new C-I-G-S precursor was prepared with different composition: lower Ga and Cu contents for a better Ga incorporation as compared with the precursor in *Section 5.3.2.1*. The best CIGS solar

cell was achieved at 550 ℃ with the ramping rate of 1 ℃/s in Se. Because the similar results obtained for the effects of the ramping rate and substrate temperature, the analysis of the material and device characterisation for this best device was selectively chosen in this section. In table 5.4, the compositional ratios GGI, CGI and at% Se of the C-I-G-S precursors (a) and the CIGS films (b) prepared by annealing the precursor (a) are summarised. Comparing precursor (a) and its annealed film (b) at 550 ℃ with the ramping rate of 1 ℃/s in Se, all the compositional ratios changed marginally, but an increase of Se composition is observed.

Table 5.4: The composition parameters [Ga]/([Ga]+[In]), [Cu]/([Ga]+[In]) and at% Se as determined by XRF of (a) the C-I-G-S precursor with the lower Ga and Cu contents as compared with the reference precursor in *Section 5.3.2.1*; (b) CIGS film grown from annealing precursor (a) at 550 ℃ with the ramping rate of 1 ℃/s in Se.

Sample	[Ga]/([Ga]+[In])	[Cu]/([Ga]+[In])	at% Se
a (precursor)	0.31	0.79	53
b	0.32	0.76	55

The cross-section and surface morphologies of the CIGS film *b* annealed at 550 ℃ with the ramping rate of 1 ℃/s obtained using SEM are shown in Fig. 5.10b1 and b2. A compact film consists of larger grains (~2 μm) mainly at the top part and smaller grains (~200 nm) at the bottom 300 nm region (Fig. 5.10b1). The small grains normally stem from Ga-rich CIGS phases [5.27]. The voids at the surface of this CIGS film contribute to the surface non-uniformity of this layer (Fig. 5.10b2).

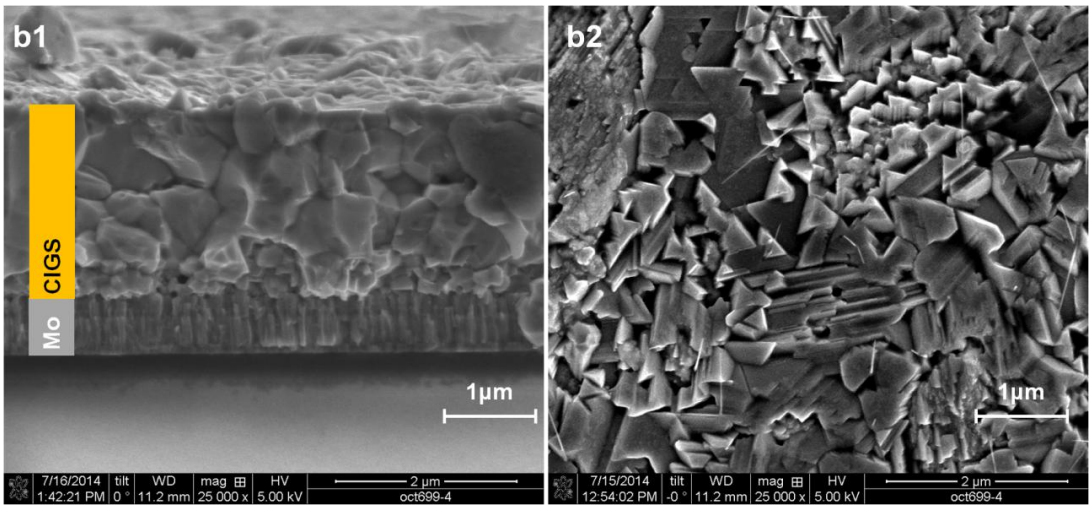

Figure 5.10: *SEM of CIGS films obtained using the RTP at the substrate temperatures of 550 ℃ in Se annealing with the ramping rate of 1 ℃/s for 5 minutes: (b1) cross-section and (b2) surface at 500 ℃.*

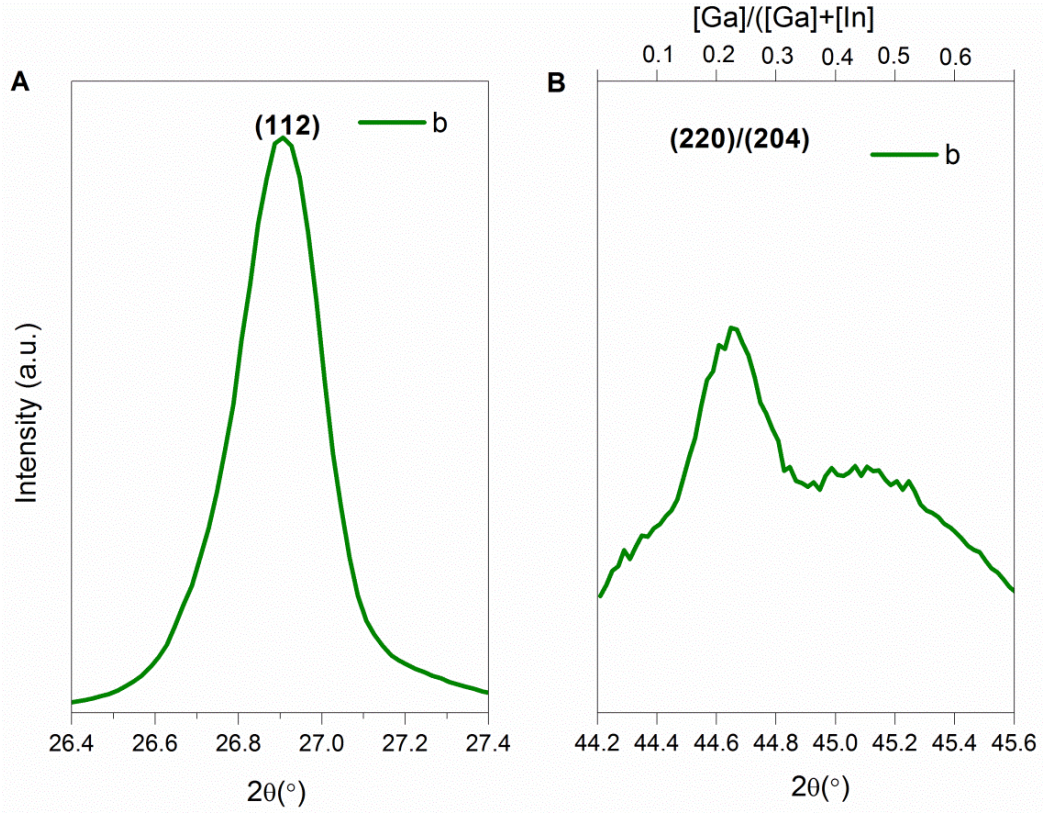

Figure 5.11: *XRD pattern of CIGS film (b) obtained using RTP by annealing precursor (a) at 550 ℃ for 5 minutes with the ramping rate of 1 ℃/s in Se. The two main peaks of (112) (A) and (220)/(204) (B) of the CIGS film were indicated.*

To analyse the structural and compositional properties, the CIGS film *b* was investigated with XRD as shown in Fig. 5.11. The intensity ratio between two main peaks of (112) and (220)/(204) is 59.8, indicating this CIGS film is strongly (112) peak dominated. For the (220)/(204) peak (Fig. 5.11B), a shoulder towards higher diffraction angle (sample *b*) indicates a relatively wide region of Ga-rich composition in the film, this could also be correlated to the Ga-rich small grains at the bottom of the CIGS absorber layer [5.27] (Fig. 5.10a).

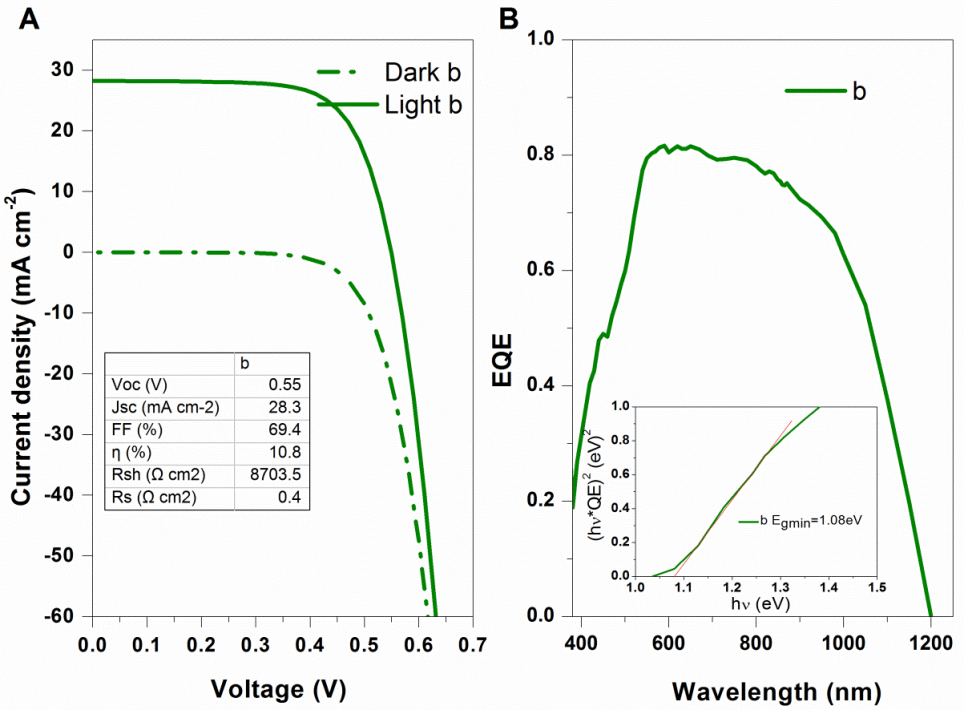

Figure 5.12: *(A) J-V and (B) EQE measurements for the champion device from the CIGS film (b) annealed C-I-G-S precursor layers (a) at 550 ℃ with the ramping rate of 1 ℃/s in Se. The CIGS solar cell shows up to 10.8% efficiency without antireflection coating. The minimum band gap was derived to be 1.08 eV.*

Fig 5.12 shows the *J-V* (A) and EQE (B) measurements for the CIGS device grown from the annealed precursor *a* (table 5.4). Comparing the photovoltaic parameters (Fig. 5.12A) of this device with devices shown in *Section 5.3.2.1*, FF, R_s and R_{sh} of device *b* are contributed most to the superior performance. Sample *b* with lower Ga and Cu contents was processed at the higher substrate temperature (550 ℃) with the lower ramping rate (1 ℃/s) and showed a slightly better efficiency than the best device with the precursor composition in *Section 5.3.2.1*. This suggests the annealing conditions such as the substrate temperature, ramping rate and extra Se amount which are important for improving the device performance are dependant on the precursor composition. External quantum efficiency (EQE) measurements of solar cells grown from precursors with modified compositions are shown in Fig. 5.12B. The minimum band gaps of sample *b* can be calculated as 1.08 eV (shown in the inset 5.12B), which is lower than the average band gap value (1.18 eV) calculated from XRF compositional analysis (table 5.4).

5.3.3 Re-crystallisation using sodium doped precursor

5.3.3.1 Structural comparison of annealed film with fast and slow ramping rates

Based on the results from previous sections, the recipe of the precursor was adjusted to increase the Se composition and co-evaporated a very light dose of NaF into the precursor. The purposes of those modifications are to compensate the Se loss during RTP and to reduce the crystallinity of the precursor film for a better re-crystallisation of CIGS. Cross-sections and surface morphologies (Fig. 5.13) of the CIGS films grown from annealing of the Na-doped C-I-G-S precursor using RTP with different ramping rates were investigated by SEM. The micrographs of the precursor (Fig. 5.13a) are compared with the CIGS films grown with the ramping rates of 8 ℃/s (Fig. 5.13b) and 1 ℃/s (Fig. 5.13c) using RTP at 500 ℃. The reason for choosing 500 ℃ is to avoid the overdose of Na in the final CIGS. A comparison of Na-doped precursor (Fig. 5.13a) and Na-free precursor (Fig. 5.1a) shows significant changes on the surface morphologies, especially on the shapes of the grains.

All the CIGS films prepared in this section were annealed in the Se atmosphere using RTP at different ramping rates. A fast (8 ℃/s) and a slow (1 ℃/s) ramping rates were selected to demonstrate the influence of the ramping rates on the structural properties of the CIGS films. In Fig. 5.13b, the large grains were obtained with the fast ramping rate, however it appears some voids and crevices along with some horizontal grain boundaries located in a depth of about 800 nm. The location of these 'horizontal separations' is approximately along with the boundaries of two precursor layers (Fig. 5.13a). It is noted that there are some nanowires with a diameter of a few tens of nanometres appearing at the surface of CIGS film (Fig. 5.13b). A similar vertical bundle of CIGS nanorod [5.43] in a pillar shape with a diameter of a few hundreds of nanometres were observed in Chapter 4. The origin of the formation of these nanowires could be $Cu_{2-x}Se$ or CuSe nanowires in the Na-doped precursor [5.44] (Fig. 5.13a). This type of chalcopyrite nanowires was obtained from liquid based precursors in the Na citrate solution [5.45], but they have been also formed in this vacuum based process. The beneficial effect of these nanowires in the solar cell application is enhancing the optical absorption [5.45], which has not been the focus of this work. In Fig. 5.13c, the CIGS film prepared with the slow ramping rate shows a two-layer structure. The upper part of the absorber appeared to be more compacted with larger grains than the bottom layer. The formation of this type of structure is due to the insufficient Cu or overdose of

Se in the film [5.32]. The CIGS/CIS nanowire was not observed on the sample processed with the slow ramping rate.

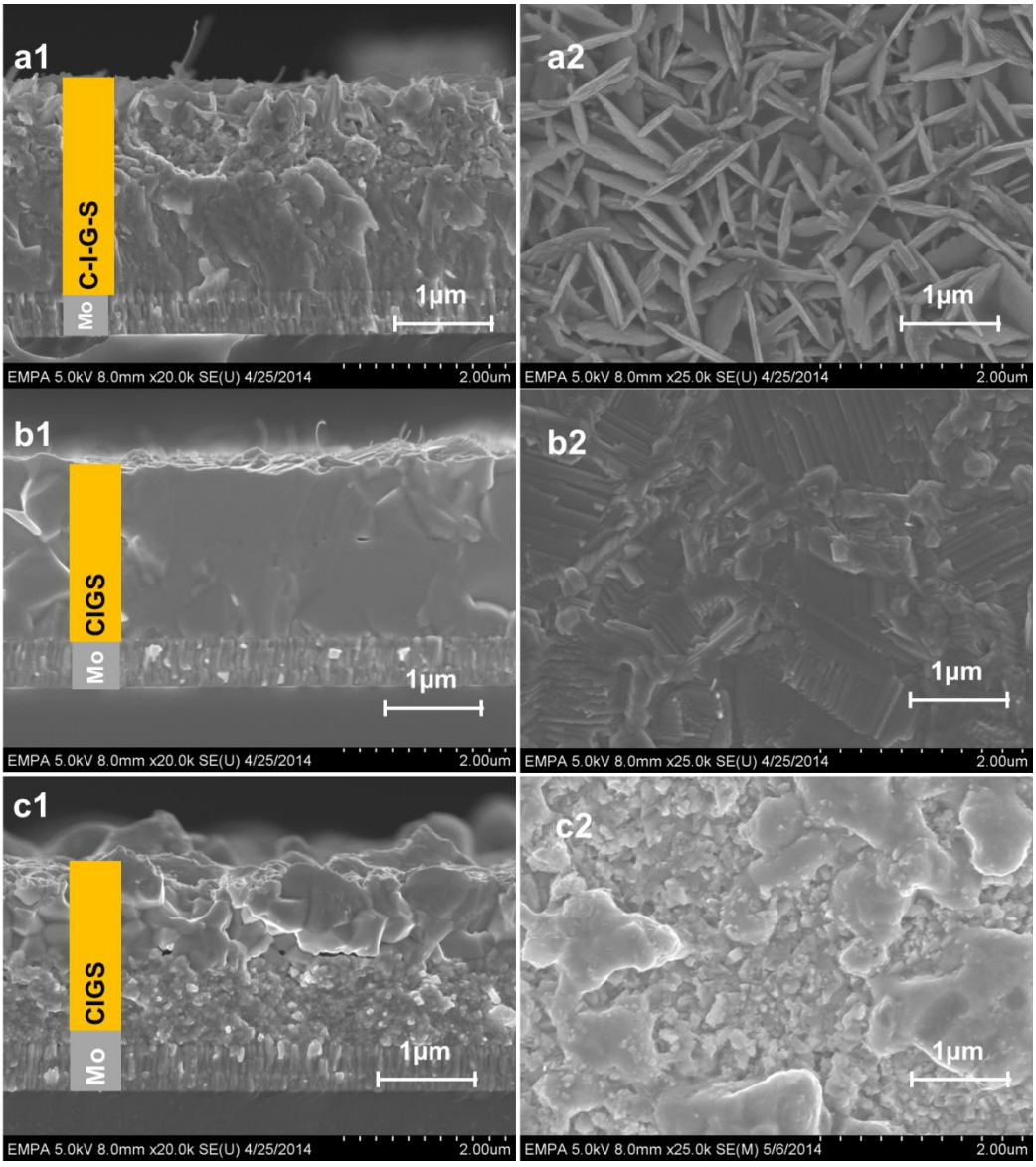

Figure 5.13: *SEM (a1) cross-sections and (a2) corresponding surface morphologies of the bare Na-doped C-I-G-S precursor. SEM of CIGS layers on Mo coated glass obtained by selected ramping rates using the RTP annealing at 500 ℃ for 10 minutes: (b1) cross-section and (b2) surface of CIGS with 8 ℃/s in Se and (c1) cross-section and (c2) surface of CIGS 1 ℃/s in Se.*

A comparison of XRD patterns of the Na-doped precursor with Na-free precursor shows a significant difference in the formed material phases. Na-free precursor exhibits a $Cu_{2-x}Se$ (JCPDS 06-680) dominated crystallisation as shown in Fig. 5.14. After intentional increasing Se composition and adding Na, the peak intensity of $Cu_{2-x}Se$ (JCPDS 06-680) phases has been reduced drastically. More secondary phases such as hexagonal α-CuSe (klockmannite (KM), JCPDS 34-0171) and orthorhombic $CuSe_2$ (JCPDS 19-

0400) become pronounced in the XRD pattern. Na-doped precursor showed reduced crystallinity, which is favoured as the lower energy required for re-crystallisation to form chalcopyrite [5.31, 5.32].

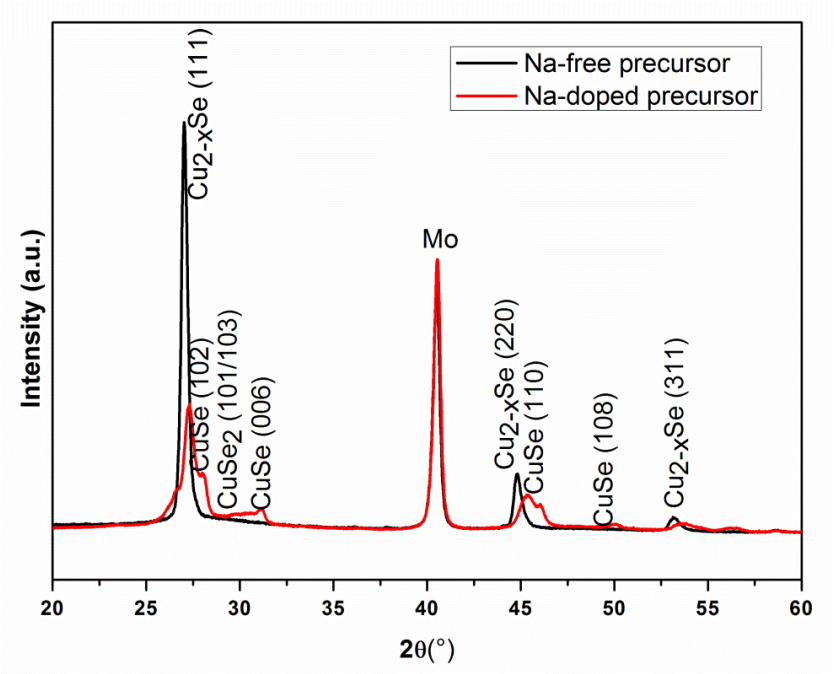

Figure 5.14: *XRD patterns of Na-free C-I-G-S precursor and Na-doped C-I-G-S precursor films.*

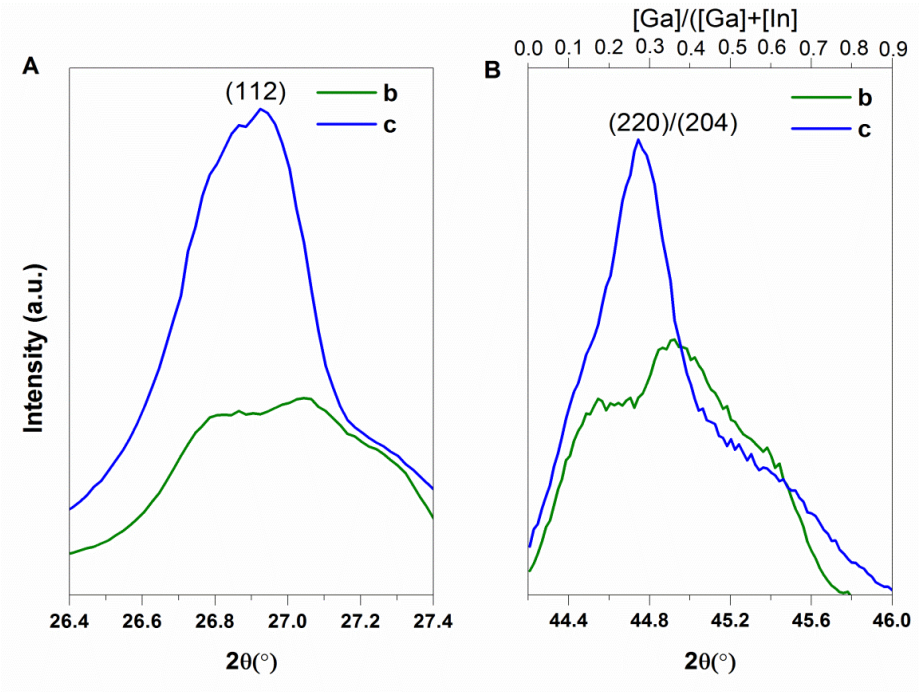

Figure 5.15: *Corresponding XRD spectra of the CIGS layers grown from Na-doped C-I-G-S on Mo coated glass with selected ramping rates using the RTP annealing: (b) 8 ℃/s in Se and (c) 1 ℃/s in Se. The two main peaks (112) and (220)/(204) of CIGS film were indicated as A and B.*

The Ga content, Cu content and Se composition of the Na-doped precursor, annealed CIGS film with ramping rates of 8 ℃/s and 1 ℃/s were summarised in table 5.5. It is clearly seen that the increased atomic percentage of Se both in the precursor and annealed CIGS films as compared to the ones in *Section 5.3.1.1* (table 5.1).

Table 5.5: The composition parameters [Ga]/([Ga]+[In]), [Cu]/([Ga]+[In]) and at% Se as determined by XRF of (a) Na-doped C-I-G-S precursor and annealed CIGS films obtained using RTP annealing with different ramping rates: (b) 8 ℃/s in Se and (c) 1 ℃/s in Se.

Sample	[Ga]/([Ga]+[In])	[Cu]/([Ga]+[In])	at% Se
a (precursor)	0.40	0.86	56
b	0.39	0.81	53
c	0.39	0.80	53

A closer look at the XRD patterns of the (112) and (220)/(204) peaks for CIGS (JCPDS 35-1102) is shown in Fig. 5.15. Both (112) and (220)/(204) peaks for sample *b* with a shoulder towards lower diffraction angles indicates a relatively wide region of Ga-poor composition in the film. Due to the overlap of the main and shoulder peaks, it is hard to estimate the FWHM and the crystallinity. Although the sample *c* shows a two-layer structure with big and small grains, the two main peaks from XRD patterns are relatively narrow, indicating the overall smoother Ga grading profile. This may be due to Na-assisted reduction of In/Ga inter-diffusion [5.27]. The dominate (112) reflection to (220)/(204) ratios for both sample *b* and c are 4.2 and 6.9 respectively, which are closer to the ratios from the high efficiency (112) pronounced CIGS solar cells [5.36].

5.3.3.2 Evaluation of sodium induced phase changes

The growth mechanism of $Cu(In,Ga)Se_2$ by the RTP annealing of Na-doped Cu-In-Ga-Se precursors was investigated by *in-situ* XRD. The temperature dependent formation of the phases during the RTP process in the presence of Se at the pressure of 5 mbar and N_2 atmosphere are depicted in Fig. 5.16. Three Cu-Se phases appear together in the precursor as shown in Fig. 5.14 and 5.16. The existence of $Cu_{2-x}Se$ (JCPDS 06-680), α-CuSe (JCPDS 34-0171) and $CuSe_2$ (JCPDS 19-0400) lasted until 270 ℃ at 5 mbar, while it can be detected at atmospheric pressure until 320 ℃. Thus, the γ-In_2Se_3 (JCPDS 01-089-0658) peaks exist from around 270 ℃ until 350 ℃, together with the appearance of first CIS (JCPDS 40-1487) or $Cu(In,Ga)Se_2$ (JCPDS 35-1102) at the pressure of 5 mbar.

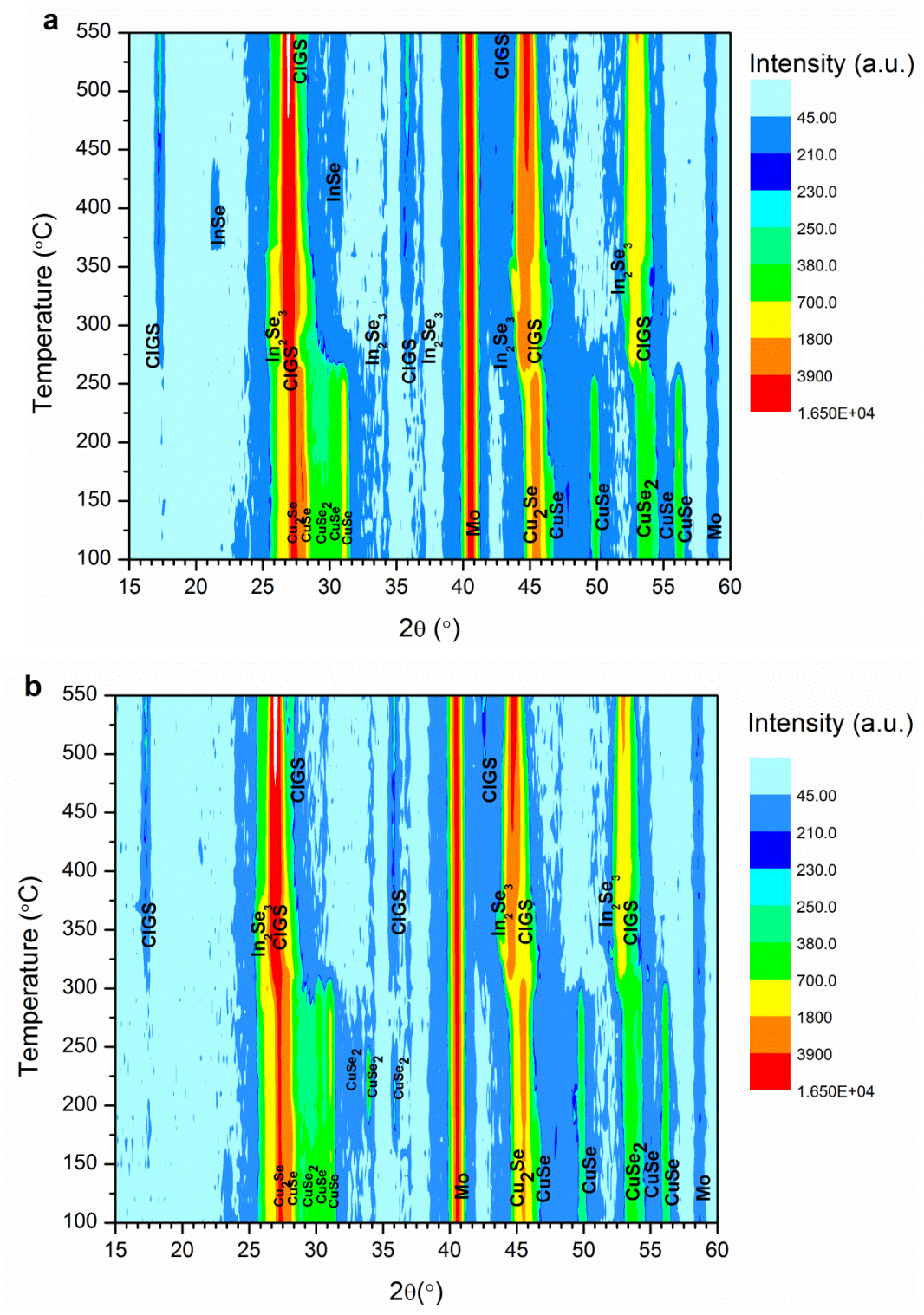

Figure 5.16: *In-situ XRD measurements during annealing Na-doped C-I-G-S precursor from 100 to 550 ℃ at different pressure: (a) 5 mbar and (b) N_2 atmospheric pressure. Pronounced $Cu_{2-x}Se$, CuSe and $CuSe_2$ phases formed in the precursor and persist until around 250/270 ℃. At around 250 ℃, the first peaks of CIGS/CIS evolve. Between 250 and 500 ℃, the formation of In-Se phases that reacts with the residual Cu-Se to form the CIGS alloy.*

Similarly, the γ-In_2Se_3 and CIS/CIGS phases appear simultaneously from 330 ℃ to 370 ℃ in the annealed sample at atmospheric pressure. This suggests that the reaction process was delayed to the higher temperature at the higher chamber pressure. The possible reactions can be estimated as [5.31, 5.38]:

$$CuSe_2 \rightarrow CuSe + Se \quad (5.8)$$

$$2\,CuSe \leftrightarrow Cu_2Se + Se \quad (5.9)$$

$$Cu_2Se + In_2Se_3 \rightarrow 2\,CuInSe_2 \quad (5.10)$$

$$2\,CuSe + In_2Se_3 \rightarrow 2\,CuInSe_2 + Se \quad (5.11)$$

The reaction (5.11) is a slow reaction, which may be taken over by (5.9) (5.10). The Ga incorporation comes from reaction (5.2). The formation of γ-InSe (JCPDS 01-071-0354) as trigonal can be seen with the precursor annealing at 5 mbar from 370 ℃ onwards, and it is being completely removed at 450 ℃. The reaction (5.4) incorporates to produce CIGS. At this high temperature regime, no InSe phase is observed in the precursor annealed at atmospheric pressure.

5.3.3.3 Model for the role of Na during CIGS-film formation

The previous sections (*Section 5.3.3.1 and 5.3.3.2*) showed a significant influence of the sodium doping on the structural, morphological properties and crystallinity of the annealed CIGS films using RTP. Based on the experimental observations, a model for the re-crystallisation mechanism during the film growth is proposed here. Fig. 5.17 shows schematically the interactions of Na, Se with C-I-G-S precursor to achieve well crystallised CIGS films using RTP.

A possible binary compound Na_2Se_x could assist the CIGS grain growth [5.28, 5.30], which is introduced in the proposed reaction mechanisms. However, the polyselenide phase Na_2Se_x was not directly confirmed by XRD due to the low quantity in the film, it is possible to detect with the help of X-ray photoelectron spectroscopy (XPS) [5.30, 5.46]. The reaction startes from the preparation of the C-I-G-S-NaF precursor (Fig. 5.17a). Cu, In, Ga, Se and NaF were co-evaporated in the sequences of In/Ga/Se/NaF and Cu/Ga/Se/NaF at the substrate temperature less than 200 ℃. The NaF could be decomposed into Na ions and then reacts with existing compounds in the precursor at high Se vapour pressure. As a result, the Na atoms typically present at the grain boundaries and surfaces due to low solubility of the Na in the CIGS [5.27, 5.47].

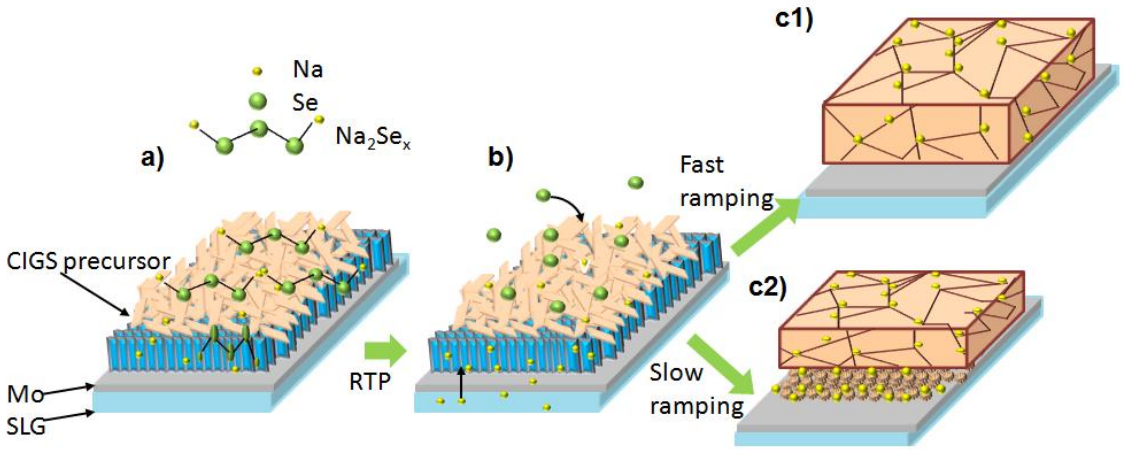

Figure 5.17: *Schematic view of re-crystallisation mechanism of Na-doped C-I-G-S using RTP with (c1) the fast ramping rate and (c2) the slow ramping rate. (a) Na-doped CIGS precursor is grown using co-evaporated Cu, In, Ga, Se and NaF at the low substrate temperature ($T_{sub.}$<200 ℃). (b) Na-doped CIGS precursor is annealed in the presence of Se using RTP, extra sodium diffuses from bottom SLG. (c1) Well crystallised CIGS film formed through RTP with the fast ramping rate, (c2) two layers of CIGS film formed through RTP with the slow ramping rate: the upper layer with large CIGS grains and the lower layer with small CIGS grains.*

A benign effect of Na is observed that reduces the crystallinity (Fig. 5.14) of the C-I-G-S precursor film which could give a better re-crystallisation of the final CIGS. Fig 5.17b shows a dynamic reaction process during RTP annealing at 500 ℃. Extra Se comes into the precursor and reacts with metal selenides, which may enhance the grain size and occupy the grain boundaries and voids to obtain a uniform CIGS film. More Na diffused from the bottom SLG into the CIGS films, and hence an increased gradient of Na towards the back contact Mo is normally observed [5.27, 5.28]. Finally, a significant morphological difference of CIGS films can be obtained from those films grown by the fast (8 ℃/s) and the slow (1 ℃/s) ramping rates of the RTP (Fig. 5.13). For the fast ramping rate, all the materials in the precursor were heated up to 500 ℃ rapidly and less Na could diffuse into the top part of the CIGS film from the bottom SLG due to the low solubility of Na in the CIGS. A uniform CIGS layer with large grains is achieved (Fig. 5.17c1). On the other hand, low ramping rate means a relatively longer ramping time leaded to more Na diffuses into the CIGS films especially at the bottom part of the film. A two-layer configuration is formed in the film with big grains at the top and small grains at the bottom depending on the variation of the Na composition (Fig. 5.17c2).

Therefore, it is found that the RTP is an effective method to obtain the big grain size of the chalcopyrite CIGS film and Na is a possible doping material to reduce the crystallinity of the precursor, which may result in a better re-crystallisation for the formation of the final chalcopyrite.

5.3.3.4 Device performance and photovoltaic properties

Absorbers from annealed Na-doped precursor layers with the ramping rates of 8 and 1 ℃/s were processed into CIGS solar cells of 0.09 cm^2 area without anti-reflection coating.

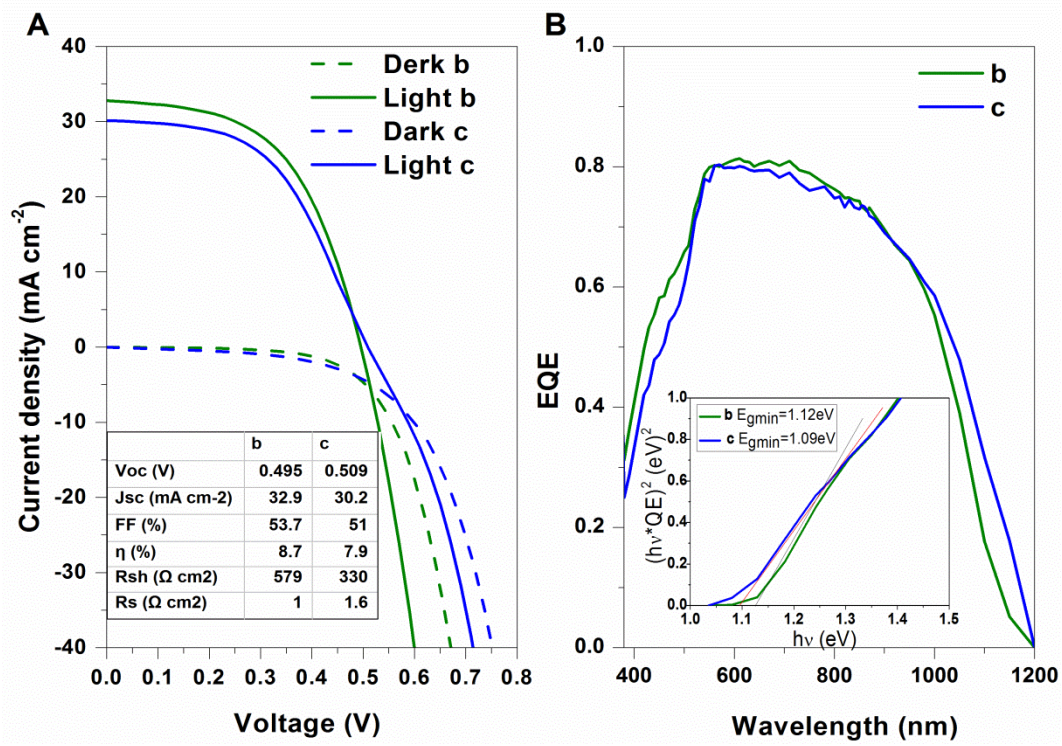

Figure 5.18: *J-V (A) and EQE (B) measurements for two champion devices of absorbers from annealed Na-doped precursor layers with the ramping rates of 8 ℃/s (b) and 1 ℃/s (c) show up to 8.7% and 7.9% efficiencies, respectively. The minimum band gaps were derived to be 1.12 eV and 1.09 eV for CIGS solar cells b and c respectively.*

Fig. 5.18 shows the current density-voltage (*J-V*) and the external quantum efficiency (EQE) of two champion devices. Comparing device parameters of absorber layers annealed at 8 ℃/s with 1 ℃/s, the gain in the efficiency is mainly due to improved shunt resistance and reduced series resistance next to increased J_{sc} and FF. But most of the PV parameters of both devices are much lower than the high efficiency devices [5.7] and CIGS solar cells fabricated in the *Section 5.3.2*. The nanowires on the surface of CIGS absorber with the ramping rate of 8 ℃/s (Fig. 5.13b) and the porosity of the absorber

with the ramping rate of 1 ℃/s (Fig. 5.13c) could generate small shunt resistance (R_{sh}) and high series resistance (R_s) and hence low FF. However, relatively high J_{sc} is obtained as compared to CIGS solar cells fabricated in the *Section 5.3.2*. The horizontal grain boundaries in both of the films could lead to the pronounced recombination loss, which may be the reason for the low V_{oc} [5.33]. These horizontal grain boundaries can increase the possibility of the recombination and the recombination mechanism is similar to the interface recombination. This will lead to a diode factor close to 2 [5.33]. The light-to-dark crossover (Fig. 5.18A) was observed for both CIGS solar cell devices grown from Na-doped precursor which could result in increased interface recombination as discussed in *Section 5.3.1* and Chapter 3. It is apparent that absorber with the ramping rate of 8 ℃/s exhibits a higher spectral response in the short-wavelength region resulting in a gain in the short circuit current. The minimum band gaps of 1.12 eV and 1.09 eV can be calculated from the absorption onset for the absorber annealed at 8 ℃/s and 1 ℃/s, respectively. These minimum band gaps are lower than the average band gap value (1.21 eV) estimated from XRF measurement (table 5.5).

5.4 Conclusion

Growth of the CIGS chalcopyrite films was performed using a novel co-evaporated precursor with two-layer structure of In-Ga-Se/Cu-Ga-Se(-NaF) (<200 ℃) and subsequent rapid thermal annealing. This work showed the CIGS film quality greatly depended on the process parameters of RTP and the composition of the precursor.

The compact absorber layers with grains up to 5 μm were facilitated using fast ramping rates (> 8 ℃/s). Smaller grains formed with decreased ramping rates. Voids and crevices appeared in most CIGS films along with the horizontal grain boundaries at the surface and cross-section of the layers, which contribute to the losses of the power conversion efficiency of the devices due to the defect related recombination. *In-situ* XRD results provided insight into the reaction mechanisms of CIGS grown from the low temperature evaporated C-I-G-S precursors. The detected binary phases may not form in the CIGS formation using RTP. Higher substrate temperatures lead to a better performance CIGS device mainly from the improvement on V_{oc} and FF. A smoother Ga grading profile means a reduced band gap grading may be one of the reasons for gaining the efficiency by increased temperature, however, it is not fully understood. Two champion devices were obtained with efficiencies of 10.2% and 10.8% grown with different composition

of the C-I-G-S precursors using RTP at ramping rates of 10 and 1 ℃/s respectively. Process parameters are dependent on the composition of the precursor.

Na was used as a doping material to reduce the crystallinity of the C-I-G-S precursor, consequently, to obtain a better CIGS re-crystallisation. A comparable efficiency of 8.7% was achieved and a vast amount of nanowires appeared in the CIGS film grown with the ramping rate of 8 ℃/s. These unexpected nanowire may create shunt paths, thus lower the efficiency value as compared to the CIGS film from Na-free C-I-G-S precursor. *In-situ* XRD results indicated more Cu-binary phases formed in the precursor, which may lead to the CIGS formation activated at 50 ℃-higher temperature. Na_2Se_x was proposed to assist the grain growth by reducing the In/Ga interdiffusion. The overdose of Na resulted in a small grain layer of CIGS. The chalcopyrite growth through low temperature precursors and RTP was proven to be an effective preparation method, which has the potential to further improve the efficiency of the solar cells devices.

References

[5.1] P. Reinhard, S. Buecheler and A. N. Tiwari, "Technological status of $Cu(In,Ga)(Se,S)_2$-based photovoltaics," *Solar Energy Materials and Solar Cells*, vol. 119, pp. 287-290, 2013.

[5.2] F. Karg, V. Probst, H. Harms, J. Rimmasch, W. Riedl, J. Kotschy, R. Treichler, O. Eibl, A. Mitwalsky and A. Kiendl, "Novel rapid-thermal-processing for CIS thin-film solar cells," *Conference Record of the 23rd IEEE Photovoltaic Specialists Conference*, Louisville, pp.4441-446, 1993.

[5.3] http://www.avancis.de/en/press/press-releases/view/meldung/avancis-erzielt-neuen-zertifizierungsrekord-bei-duennschichtmodul-nrel-zertifiziert-wirkungsgrad-des/, "AVANCIS achieves new certification record for thin-film module NREL certified efficiency of CIS module with 16.6%," 2014.

[5.4] A. Chirilă, S. Buecheler, F. Pianezzi, P. Bloesch, C. Gretener, A. R. Uhl, C. Fella, L. Kranz, J. Perrenoud, S. Seyrling, R. Verma, S. Nishiwaki, Y. E. Romanyuk, G. Bilger and A. N. Tiwari, "Highly efficient $Cu(In,Ga)Se_2$ solar cells grown on flexible polymer films," *Nat Mater*, vol. 10, pp. 857-861, 2011.

[5.5] J. Song, S. S. Li, C. H. Huang, O. D. Crisalle, and T. J. Anderson, "Device modeling and simulation of the performance of $Cu(In_{1-x},Ga_x)Se_2$ solar cells," *Solid-State Electronics*, vol. 48, pp. 73-79, 2004.

[5.6] D. Rudmann, D. Brémaud, H. Zogg and A. N. Tiwari, "Na incorporation into $Cu(In,Ga)Se_2$ for high-efficiency flexible solar cells on polymer foils," *Journal of Applied Physics*, vol. 97, pp. 084903, 2005.

[5.7] A. Chirilă, P. Reinhard, F. Pianezzi, P. Bloesch, A. R. Uhl, C. Fella, L. Kranz, D. Keller, C. Gretener, H. Hagendorfer, D. Jaeger, R. Erni, S. Nishiwaki, S. Buecheler and A. N.

Tiwari, "Potassium-induced surface modification of $Cu(In,Ga)Se_2$ thin films for high-efficiency solar cells," *Nat Mater*, vol. 12, pp. 1107-1111, 2013.

[5.8] T. Dalibor, S. Jost, H. Vogt, A. Heiß, S. Visbeck, T. Happ, J. Palm, A. Avellán, T. Niesen and F. Karg, "Towards Module Efficiencies of 16% with an Improved CIGSSe Device Design," *Conference Record of the 26th European Photovoltaic Solar Energy Conference and Exhibition*, Hamburg, pp. 240702411, 2011.

[5.9] J. Palm, V. Probst, A. Brummer, W. Stetter, R. Tölle, T. P. Niesen, S. Visbeck, O. Hernandez, M. Wendl, H. Vogt, H. Calwer, B. Freienstein and F. Karg, "CIS module pilot processing applying concurrent rapid selenization and sulfurization of large area thin film precursors," *Thin Solid Films*, vol. 431–432, pp. 514-522, 2003.

[5.10] J. D. Wilson, B. E. McCandless, R. W. Birkmire and W. N. Shafarman, "In-situ post-deposition thermal annealing of co-evaporated $Cu(InGa)Se_2$ thin films deposited at low temperatures," *Conference Record of the 34th IEEE Photovoltaic Specialists Conference*, Philadelphia, pp. 1144-1148, 2009.

[5.11] S. Merdes, D. Abou-Ras, R. Mainz, R. Klenk, M. C. Lux-Steiner, A. Meeder, H.-W. Shock and J. Klaer, "$CdS/Cu(In,Ga)S_2$ based solar cells with efficiencies reaching 12.9% prepared by a rapid thermal process," *Progress in Photovoltaics: Research and Applications*, vol. 21, pp. 88-93, 2013.

[5.12] C. M. Ruiz, X. Fontané, A. Fairbrother, V. Izquierdo-Roca, C. Broussillou, S. Bodnar, Pérez-Rodríguez and A. and Bermúdez, "Impact of electronic defects on the Raman spectra from electrodeposited $Cu(In,Ga)Se_2$ solar cells: Application for non-destructive defect assessment," *Applied Physics Letters*, vol. 102, pp. 091106, 2013.

[5.13] S. C. Kim, J. Koo and W. K. Kim, "Rapid thermal processing of Cu-rich $(InGa)_2Se_3/CuSe$ bilayer precursors with an inset NaF layer," *Thin Solid Films*, vol. 531, pp. 233-237, 2013.

[5.14] I. Klugius, R. Miller, A. Quintilla, T. M. Friedlmeier, D. Blázquez-Sánchez, E. Ahlswede and M. Powalla, "Growth mechanism of thermally processed $Cu(In,Ga)S_2$ precursors for printed $Cu(In,Ga)(S,Se)_2$ solar cells," *physica status solidi (RRL) – Rapid Research Letters*, vol. 6, pp. 297-299, 2012.

[5.15] C. J. Hibberd, "Development of non-vacuum and low-cost techniques for $Cu(In,Ga)(Se,S)_2$ thin film solar cell processing," Doctoral thesis, Loughborough University, 2009.

[5.16] H. Simchi, B. E. McCandless, K. Kim, J. H. Boyle and W. N. Shafarman, "Effect of Rapid Thermal Processing on the structural and device properties of $(Ag,Cu)(In,Ga)Se_2$ thin film solar cells," *Thin Solid Films*, vol. 535, pp. 102-106, 2013.

[5.17] X. Wang, S. S. Li, W. K. Kim, S. Yoon, V. Craciun, J. M. Howard, S. Easwaran, O. Manasreh, O. D. Crisalle and T. J. Anderson, "Investigation of rapid thermal annealing on $Cu(In,Ga)Se_2$ films and solar cells," *Solar Energy Materials and Solar Cells*, vol. 90, pp. 2855-2866, 2006.

[5.18] W. N. Shafarman and J. Zhu, "Effect of substrate temperature and depostion profile on evaporated $Cu(InGa)Se_2$ films and devices," *Thin Solid Films*, vol. 361–362, pp. 473-477, 2000.

[5.19] W. N. Sharaman, R. W. Birkmire, S. Marsillac, M. Marudachalam, N. Orbey and T. W. F. Russell, "Effect of reduced deposition temperature, time, and thickness on $Cu(InGa)Se_2$ films and devices," *Conference Record of the* 26th *IEEE Photovoltaic Specialists Conference*, Anaheim, pp. 331-334, 1997.

[5.20] M. Bodegård, O. Lundberg, J. Lu and L. Stolt, "Re-crystallisation and interdiffusion in CGS/CIS bilayers," *Thin Solid Films*, vol. 431–432, pp. 46-52, 2003.

[5.21] A. Chirilă, A., D. Guettler, P. Bloesch, S. Nishiwaki, S. Seyrling, S. Buecheler, R. Verma, F. Pianezzi, Y. E. Romanyuk, G. Bilger, R. Ziltener, D. Brémaud and A. N. Tiwari, "Optimization of composition grading in $Cu(In,Ga)Se_2$ for flexible solar cells and modules," *Conference Record of the 35th IEEE Photovoltaic Specialists Conference*, Honolulu, 656-660, 2010.

[5.22] A. M. Gabor, J. R. Tuttle, M. H. Bode, A. Franz, A. L. Tennant, M. A. Contreras, R. Noufi, D. G. Jensen and A. M. Hermann, "Band-gap engineering in $Cu(In,Ga)Se_2$ thin films grown from $(In,Ga)_2Se_3$ precursors," *Solar Energy Materials and Solar Cells*, vol. 41–42, pp. 247-260, 1996.

[5.23] V. Probst, W. Stetter, W. Riedl, H. Vogt, M. Wendl, H. Calwer, S. Zweigart, K.-D Ufert, B. Freienstein, H. Cerva and F.H. Karg, "Rapid CIS-process for high efficiency PV-modules: development towards large area processing," *Thin Solid Films,* vol. 387, pp. 262-267, 2001.

[5.24] S. Ishizuka, A. Yamada, M. M. Islam, H. Shibata, P. Fons, T. Sakurai, K. Akimoto and S. Niki, "Na-induced variations in the structural, optical, and electrical properties of Cu(In,Ga)Se2 thin films," *Journal of Applied Physics,* vol. 106, pp. 034908, 2009.

[5.25] S.-H. Wei, S. B. Zhang and A. Zunger, "Effects of Na on the electrical and structural properties of $CuInSe_2$," *Journal of Applied Physics,* vol. 85, pp. 7214-7218, 1999.

[5.26] F. Pianezzi, P. Reinhard, A. Chirila, B. Bissig, S. Nishiwaki, S. Buecheler and A. N. Tiwari, "Unveiling the effects of post-deposition treatment with different alkaline elements on the electronic properties of CIGS thin film solar cells," *Phys Chem Chem Phys,* vol. 16, pp. 8843-51, 2014.

[5.27] D. Rudmann, "Effects of sodium on growth and properties of $Cu(In,Ga)Se_2$ thin films and solar cells," Doctoral thesis, ETH, Zürich, 2004.

[5.28] C. M. Sutter-Fella, J. A. Stückelberger, H. Hagendorfer, F. La Mattina, L. Kranz, S. Nishiwaki, A. R. Uhl, Y. E. Romanyuk and A. N. Tiwari, "Sodium Assisted Sintering of Chalcogenides and Its Application to Solution Processed $Cu_2ZnSn(S,Se)_4$ Thin Film Solar Cells," *Chemistry of Materials,* vol. 26, pp. 1420-1425, 2014.

[5.29] R. Caballero, C. A. Kaufmann, T. Eisenbarth, M. Cancela, R. Hesse, T. Unold, A. Eicke, R. Klenk and H.-W. Schock, "The influence of Na on low temperature growth of CIGS thin film solar cells on polyimide substrates," *Thin Solid Films,* vol. 517, pp. 2187-2190, 2009.

[5.30] D. Braunger, D. Hariskos, G. Bilger, U. Rau and H. W. Schock, "Influence of sodium on the growth of polycrystalline $Cu(In,Ga)Se_2$ thin films," *Thin Solid Films,* vol. 361–362, pp. 161-166, 2000.

[5.31] F. Hergert, S. Jost, R. Hock and M. Purwins, "A crystallographic description of experimentally identified formation reactions of $Cu(In,Ga)Se_2$," *Journal of Solid State Chemistry,* vol. 179, pp. 2394-2415, 2006.

[5.32] S. Chaisitsak, A. Yamada and M. Konagai, "Preferred Orientation Control of $Cu(In_{1-x}Ga_x)Se_2$ ($x\approx0.28$) Thin Films and Its Influence on Solar Cell Characteristics," *Japanese Journal of Applied Physics,* vol. 41, p. 507, 2002.

[5.33] R. Scheer and H.-W. Schock, "Design Rules for Heterostructure Solar Cells and Modules," in *Chalcogenide Photovoltaics,* ed: Wiley-VCH Verlag GmbH & Co. KGaA, pp. 129-174, 2011.

[5.34] M. Gloeckler, J. R. Sites and W. K. Metzger, "Grain-boundary recombination in $Cu(In,Ga)Se_2$ solar cells," *Journal of Applied Physics,* vol. 98, pp. 113704, 2005.

[5.35] J. Scholdström, J. Kessler and M. Edoff, "Two-stage growth of smooth $Cu(In,Ga)Se_2$ films using end-point detection," *Thin Solid Films,* vol. 480–481, pp. 61-66, 2005.

[5.36] M. Powalla, P. Jackson, W. Witte, D. Hariskos, S. Paetel, C. Tschamber and W. Wischmann, "High-efficiency $Cu(In,Ga)Se_2$ cells and modules," *Solar Energy Materials and Solar Cells,* vol. 119, pp. 51-58, 2013.

[5.37] F. Hergert, R. Hock, A. Weber, M. Purwins, J. Palm and V. Probst, "In situ investigation of the formation of $Cu(In,Ga)Se_2$ from selenised metallic precursors by X-ray diffraction-The impact of Gallium, Sodium and Selenium excess," *Journal of Physics and Chemistry of Solids,* vol. 66, pp. 1903-1907, 2005.

[5.38] F. Oliva, C. Broussillou, M. Annibaliano, N. Frederich, P. P. Grand, A. Roussy, P. Collot and S. Bodnar, "Formation mechanisms of $Cu(In,Ga)Se_2$ solar cells prepared from electrodeposited precursors," *Thin Solid Films,* vol. 535, pp. 127-132, 2013.

[5.39] S. Nishiwaki, T. Satoh, S. Hayashi, Y. Hashimoto, T. Negami and T. Wada, "Preparation of $Cu(In,Ga)Se_2$ thin films from In–Ga–Se precursors for high-efficiency solar cells," *Journal of Materials Research,* vol. 14, pp. 4514-4520, 1999.

[5.40] K. Siemer, J. Klaer, I. Luck, J. Bruns, R. Klenk and D. Bräunig, "Efficient $CuInS_2$ solar cells from a rapid thermal process (RTP)," *Solar Energy Materials and Solar Cells,* vol. 67, pp. 159-166, 2001.

[5.41] S. S. Kulkarni, J. S. Shirolikar and N. G. Dhere, "Preparation of CIGSS Thin-Film Solar Cells by Rapid Thermal Processing," *Journal of Solar Energy Engineering,* vol. 129, pp. 323-326, 2006.

[5.42] S. S. Hegedus and W. N. Shafarman, "Thin-film solar cells: device measurements and analysis," *Progress in Photovoltaics: Research and Applications,* vol. 12, pp. 155-176, 2004.

[5.43] Z. Wei, S. Senthilarasu, M. V. Yakushev, R. W. Martin and H. M. Upadhyaya, "Effect of mechanical compression on $Cu(In,Ga)Se_2$ films: micro-structural and photoluminescence analysis," *RSC Advances,* vol. 4, pp. 5141-5147, 2014.

[5.44] J. Xu, W. Zhang, Z. Yang, S. Ding, C. Zeng, L. Chen, Q. Wang and S. Yang, "Large-Scale Synthesis of Long Crystalline $Cu_{2-x}Se$ Nanowire Bundles by Water-Evaporation-Induced Self-Assembly and Their Application in Gas Sensing," *Advanced Functional Materials,* vol. 19, pp. 1759-1766, 2009.

[5.45] J. Xu, C.-S. Lee, Y.-B. Tang, X. Chen, Z.-H. Chen, W.-J. Zhang, S.-T. Lee, W. Zhang and Z. Yang, "Large-Scale Synthesis and Phase Transformation of CuSe, $CuInSe_2$, and $CuInSe_2/CuInS_2$ Core/Shell Nanowire Bundles," *ACS Nano,* vol. 4, pp. 1845-1850, 2010.

[5.46] A. Schellenberger, R. Schlaf, C. Pettenkofer and W. Jaegermann, "XPS and SXPS studies on in-situ prepared Na/InSe insertion compounds," *Solid State Ionics,* vol. 66, pp. 307-312, 1993.

[5.47] L. Kronik, D. Cahen and H. W. Schock, "Effects of Sodium on Polycrystalline $Cu(In,Ga)Se_2$ and Its Solar Cell Performance," *Advanced Materials,* vol. 10, pp. 31-36, 1998.

Chapter 6– Conclusion and outlook

6.1 Conclusions

In this thesis, several aspects of CIGS layers grown by different techniques have been investigated. The main focus was on the process development for scaling up of efficient CIGS solar cells into industrial manufacturing. The first important step was the development and optimisation of a pilot scale inline evaporation system for high efficiency CIGS solar cells towards a production potential. Attempts were made to explore the challenges of scale-up of CIGS technology focusing on the development of more cost-effective processes for the high efficient solar cells. This motivation was translated into second step for the development and exploration of three different processes towards an industrially capable three-stage process using the inline system. Thirdly, the effects of the mechanical compression on the improvements of the morphological and electronic properties of the low quality porous CIGS films were attempted. Finally, a two-step process was employed to form high quality CIGS through low temperature Na-free and Na-doped Cu-In-Ga-Se precursors in conjunction with the rapid thermal processing.

Some highlights reflect the blends of scientific and engineering aspects of the CIGS technology which involved the design and development of an advanced tool referred to the pilot scale inline co-evaporation system along with the optimisation of processes for high efficiency and low cost CIGS solar cells. These have been summarised as follows:

1. A thickness distribution model using MATLAB software and a temperature distribution model using COMSOL software were built to simulate the actual running conditions of the inline system. The simulations carried out using the above software, showed a good validation with the experimental results. These models provided extensive information on the modifications of the inline system for more cost-effective and industrially favourable process development.
2. The challenges in the optimisation of various process parameters in the inline system are widely different from a laboratory based system. The success of the optimisation studies was realised in obtaining some good quality CIGS films over a large area (30 cm × 30 cm) through this inline system. A systematic study conducted showed a variation in the performance of the CIGS solar cells with

respect to the change in the relative Cu and Ga compositions. This provided the confidence of following the approach of developing cheaper and industrially favourable process such as evaporation of CIG precursors at room temperature followed by selenisation with some significant success in achieving good device performance (7.4%) in a few initial trials only.

3. The thickness of the CIGS films was kept at ~1 μm for the studies conducted throughout Chapter 3 and 4. Whilst in Chapter 5, a thickness about 2-3 μm was used in an attempt to achieve high efficiency with a low cost processing approach. This provided an opportunity to investigate the issues for thinner absorbers in the CIGS solar cells. Considering the losses, the insufficient absorption of the light in such thin absorber and increased recombination at the surface lead to comparatively less efficient solar cells as compared to the state-of-the-art values.
4. Mechanical compression was employed as a recovery technique to improve morphological and electronic properties of the low quality CIGS prepared through CIG precursors grown at room temperature and subsequent selenisation. The morphological and electronic properties of the CIGS films have been improved significantly as observed by SEM and PL investigations. This was the first attempt to correlate successfully the effect of compression on CIGS films with the change in the PL spectra.
5. A novel cost-effective process using low temperature (<200 ℃) evaporated Cu-In-Ga-Se precursors and RTP brought a remarkable improvement in the quality of the CIGS films using laboratory size tools. With further optimisation trials, this low cost method would have great potential to combine with the inline system for further process optimisation with further improvement of the efficiency towards the state-of-the-art values.
6. Na doping has been investigated as an effective method to reduce the crystallinity of the Cu-In-Ga-Se precursor, which leads to a better re-crystallisation of the CIGS films.

6.2 Outlook and further directions

In the previous sections, the highlights of the research output of the present thesis have been summarised. A list of possible suggestions for further research is described in this section:

1. For better deposition uniformity, a line source for Cu, In, or Ga would be able to distribute the material more evenly for larger area (> 1 m × 1 m) industrial application. A possible improvement is to use a better pump arrangement such as the cryogenic pump that can be used to improve the chamber pressure and reduce the pressure turbulence caused by the temperature overshoot. The water cooled cold traps can be replaced with a liquid nitrogen cold trap to improve trap efficiency especially in large scale manufacturing. Furthermore, an advanced *in-situ* XRF monitoring system attached on the inline machine can greatly improve the composition control and uniformity for single-stage or multi-stage co-evaporation process, and hence increasing the yield.
2. A proper end-point detection method (EPD) for the inline co-evaporation needs to be developed for day to day running of the system. For this work, a simple *in-situ* monitoring technique that would indicate layer composition, would greatly enhance the optimisation possibility and hence improve the quality of CIGS films.
3. The process needs to be optimised to achieve a desired increase in the thickness of CIGS layers (2-3 μm) to achieve enough light absorption and hence enhance the efficiency. Alternatively, a bifacial CIGS solar cell can be used to artificially double the light absorption with even thinner absorbers (<1 μm). Further development of this work needs to focus on increasing the absorption using some advanced optical enhancement techniques such as adding a surface texture layer and using a concentrated light source. Another improvement is tailoring the compositional gradient which determines the electronic band-gap structure of the device. In particular, engineering the band-gap in a highly controlled way and correlating the properties of the resulting films and solar cells to the particular growth recipe should be carefully addressed.
4. For further research on compression techniques, a comparison of the device efficiency to establish a mechanical compression-assisted CIGS growth process is requried to provide greater understanding.
5. To obtain real-time CIGS formation, a synchrotron-based XRD and XRF measurement needs to be carried out to understand the phase transition of the CIGS layers grown with three-stage process or two-step process.
6. Further work needed to find the beneficial doping level of Na in the precursor, because the overdose of Na leads to reduced solar cell efficiency. Fine tuning of

the RTP parameters such ramping rates and multiple ramping stages should be carried out with the corresponding precursor composition.